



HAL
open science

An optical Solution for Simultaneous in-situ Sea Water Salinity and Turbidity Measurements

Bo Hou

► **To cite this version:**

Bo Hou. An optical Solution for Simultaneous in-situ Sea Water Salinity and Turbidity Measurements. Optics [physics.optics]. Télécom Bretagne, Université de Bretagne-Sud, 2012. English. NNT : . tel-00719584

HAL Id: tel-00719584

<https://theses.hal.science/tel-00719584>

Submitted on 20 Jul 2012

HAL is a multi-disciplinary open access archive for the deposit and dissemination of scientific research documents, whether they are published or not. The documents may come from teaching and research institutions in France or abroad, or from public or private research centers.

L'archive ouverte pluridisciplinaire **HAL**, est destinée au dépôt et à la diffusion de documents scientifiques de niveau recherche, publiés ou non, émanant des établissements d'enseignement et de recherche français ou étrangers, des laboratoires publics ou privés.

Sous le sceau de l'Université européenne de Bretagne

Télécom Bretagne

En habilitation conjointe avec l'Université de Bretagne-Sud

Ecole Doctorale - sicma

**An optical solution for simultaneous in-situ sea water salinity
and turbidity measurements**

**Une solution optique pour la mesure simultanée in-situ de la
salinité et la turbidité de l'eau de mer**

Thèse de Doctorat

Mention : STIC

Présentée par **Bo Hou**

Département : OPTIQUE

Directeur de thèse : Jean-Louis de Bougrenet de La Tocnaye

Soutenance le 11 janvier 2012

Jury :

- M. Patrick Juncar, Professeur, CNAM (Rapporteur)
- M. Marc Le Menn, Docteur, SHOM (Rapporteur)
- M. Jean-Louis de Bougrenet de la Tocnaye, Professeur, Télécom Bretagne (Directeur de thèse)
- M. Marc Sevaux, Professeur, UBS (Examineur)
- M. Philippe Grosso, Enseignant chercheur, Télécom Bretagne (Invité)
- M. Patrice Brault, Ingénieur de recherche, NKE (Invité)
- M. Laurent Delauney, Ingénieur de recherche, Ifremer (Invité)

Acknowledgements

First of all, I would like to thank Mr. Jean-Louis De Bougrenet De La Tocnaye, the director of my thesis, for kindly accepting me as his PhD student and for his precious help, understanding and trust during the three years of work. I am very grateful to him for leading me to the right direction of the research works, for his valuable advice, and for his help in reading and correcting my articles and his pertinent remarks.

I am very thankful to Mr. Philippe Grosso, my supervisor, for his great help in the three years of work. Mr Philippe Grosso helped me with much advice and numerous ideas, and taught me a lot of concepts and helped me to resolve many problems and questions. I would never forget the days of the interesting discussions and the days of working together in the laboratory.

I am particularly grateful to Mr. Zong Yan Wu, my supervisor. Without him, I could not have the chance to start my study in France and in TELECOM Bretagne. He helped me not only in work but also in my daily life. His advice and idea inspired me to find the right way at the beginning of my PhD study. His help and support last even after his retirement. I would always remember his kindness, precious help and support.

I gratefully acknowledge Mr. Damien Malardé for his great work in the first version of the refractometer, which inspired me to continue my work. Mr. Damien Malardé helped me to get familiar with the project and everything about the school, gave me a lot of advice and help of working in the laboratory. I will always remember his kindness, for which he was always such a pleasant co-worker.

I would like to thank the project NOSS (NkeElectronics Optical Salinity Sensor) for the financial support of my thesis.

I would like to express my deep gratitude to Mr. Patrick Juncar, director of Institut de Métrologie au Centre National des Arts et Métiers and Mr. Marc Le Menn, director of Laboratoire de Métrologie of Service Hydrographique et Océanographique de la Marine, who kindly agreed to be the reviewers of this work.

My sincere appreciation to Mr. Marc Servaux of Université de Bretagne Sud, Mr. Patrice Brault of NKE electronics, Mr. Laurent Delauney of Ifremer, Mr. Philippe Grosso of TELECOM Bretagne, and Mr. Jean Louis De Bougrenet De La Tocnaye, who kindly agreed to be the members of the defence jury of my thesis.

I would also like to thank all the members of NKE electronics, SHOM and Ifremer, for their contributions to my work of thesis, especially Mr. Patrice Brault and Mr. Olivier Guillaume of NKE, Mr. Marc Le Menn of SHOM, Mr. Laurent Delauney and Mr. Christian Podeur of Ifremer.

I am grateful to the administrative team and technical team of TELECOM Bretagne. More precisely, I would like to express my deep gratitude to Ms. Anne-Catherine Cariou and Ms. Jennifer Romer for their effective management of the administrative affaires associated with their great kindness and precious help, to Mr. Jean-Pierre Clère for his fantastic work of the mechanics, and to Ms. Aimée Johansen for her precious help in correcting my english writing.

I would like to thank my parents for their endless care and support during my three years of life overseas. Their understanding, encouragement and support helped me through many difficult times.

Finally, I would like to express my thanks to all the professors, students and colleagues at TELECOM Bretagne, for their kindness and support during my stay in Brest.

Brest, February 2012

Bo HOU

Abstract

Salinity and turbidity are two important seawater properties for the physical oceanography. The study of physical oceanography requires a compact high-resolution *in-situ* salino-turbidi-meter. The main objective of this work is to propose, design and implement an optical solution to simultaneously measure the seawater salinity and turbidity. Our first study is carried out to design a high-resolution refractometer based on a laser beam deviation measurement by a Position Sensitive Device (PSD). The refractive index measurements obtained by the voltage value delivered by PSD have been evaluated to quantify the performances of the sensor. According to the obtained results, it is clear that this PSD-based refractometer is attractive for innovative applications in metrology. However, PSD lacks the capability to retrieve the power distribution information of laser beam, which is related to the turbidity measurements. On the contrary, Charge-Coupled Device (CCD) gives much more information of laser beam than PSD. In the second part of the thesis, a performance comparison between PSD and CCD combined with a centroid algorithm are discussed with special attention paid to the CCD-based refractometer. According to the operating principle of CCD-based system, five factors of CCD-based system: image window size, number of processed images, threshold, binning and saturation are evaluated to optimize the CCD-based refractometer. By applying the optimized parameters, the performance of CCD-based refractometer is better than PSD-based refractometer in measuring the refractive index. Furthermore, by applying different post-processing algorithms, CCD-based system possesses the capability of measuring the power distribution sensitive quantities. To show this advantage of CCD-based system, the attenuation measurement method is used to measure turbidity without modifying the refractometer configuration. The turbidity measurement and salinity measurements influence each other in a refractometer. To overcome these influences, a CCD combined with a new location algorithm is used to measure both the refractive index and the attenuation. Several simulations and experiments are carried out to evaluate this new method. According to the results, the way to improve the resolution is discussed as well. Comparing to the nephelometer specified by the NTU standard, our method has been proved as a valid method to measure turbidity. By studying the performances of CCD-based refracto-turbidi-meter, 3 new prototypes are proposed to improve the salinity and turbidity measurement performance at the end of this thesis. They are expected to be applied in the current researches of physical oceanography.

Keywords: salinity, turbidity, refractometer, turbidimeter, position sensitive device, charge-coupled device, seawater, refractive index, attenuation, scattering

Résumé court

La salinité et la turbidité sont deux propriétés importantes pour comprendre le comportement physique des océans. L'étude de l'océanographie physique a besoin d'un salino-turbidi-mètre in-situ, haute résolution. L'objectif de ce travail de recherche est de proposer, concevoir et réaliser de nouvelles solutions optiques dédiées aux mesures simultanées de salinité et de turbidité de l'eau de mer. Une première étude est menée, afin de démontrer la conception d'un réfractomètre à haute résolution basé sur une mesure de la déviation d'un faisceau laser par un dispositif de détection de position (PSD). La mise en place d'une plateforme de caractérisation des mesures d'indice de réfraction à l'aide d'une lecture de tension délivrée par le capteur de position a permis de quantifier les performances du capteur en terme de sensibilité. Au vu des résultats obtenus, il apparaît que ce réfractomètre basé sur la mesure de position du faisceau réfracté se présente comme particulièrement avantageux pour des applications en métrologie comme la salinité. Cependant, le PSD n'a pas la capacité de récupérer les informations de la distribution de puissance du faisceau laser, qui est liée à la mesure de la turbidité. Par contre, le dispositif à transfert de charge (CCD) donne beaucoup plus d'informations sur la distribution de la puissance du faisceau laser. Dans la deuxième partie de la thèse, une comparaison des performances entre le système avec PSD et le système avec CCD combiné à un algorithme de calcul du centre de gravité est discuté avec une attention particulière pour le réfractomètre avec CCD. Selon le principe du système basé sur CCD, cinq paramètres du système avec CCD: la taille de la fenêtre d'image, le nombre d'images traitées, le seuil, le «binning» et la saturation sont évalués afin d'optimiser le réfractomètre équipé d'un CCD. En appliquant les paramètres optimisés, les performances du système avec CCD sont meilleures que les performances du système avec PSD pour mesurer l'indice de réfraction. Par ailleurs, en appliquant les différents algorithmes de post-traitements, le système avec CCD possède la capacité de mesurer les propriétés, qui sont sensibles à la distribution de puissance. Pour montrer cet avantage du système avec CCD, une méthode basée sur la mesure d'atténuation de la lumière est utilisée pour mesurer la turbidité sans modifier la configuration du réfractomètre. Cependant, les mesures de salinité et turbidité s'influencent mutuellement dans un réfractomètre. Pour surmonter ces influences, un CCD combiné à un nouvel algorithme est utilisé pour mesurer l'indice de réfraction et l'atténuation. Plusieurs simulations et expérimentations sont menées pour évaluer cette nouvelle méthode. Selon les résultats, la façon d'améliorer la résolution est aussi discutée. La validation de notre méthode est montrée par la comparaison de nos résultats avec ceux du néphélomètre spécifié par le standard NTU. En étudiant les performances du réfracto-turbidi-mètre basé sur CCD, 3 nouveaux prototypes sont proposés pour améliorer les performances des mesures de salinité et de turbidité à la fin de cette thèse.

Mots clés: salinité, turbidité, réfractomètre, turbidimètre, PSD, CCD, eau de mer, indice de réfraction, atténuation, diffusion

Résumé

Introduction

L'océanographie est une science qui étudie et décrit les océans de la Terre. Cette discipline a la particularité d'être à cheval sur plusieurs domaines. On distingue en effet l'océanographie physique, biologique, chimique et géologique, mais on retrouve souvent des interactions très fortes entre ces différents domaines. Nous distinguons principalement l'océanographie physique, qui est l'étude des mouvements dans les océans, à toutes les échelles, des courants océaniques, jusqu'aux vagues en passant par les courants côtiers et les courants de marée. La méthode qu'elle utilise pour l'étude de ces phénomènes est d'étudier les propriétés physiques de l'eau de mer et leur distribution, par exemple, dans les zones côtière, offshore, et hauturière. Parmi ces propriétés physiques, la salinité, la température, et la pression sont les propriétés fondamentales. Une autre propriété très importante pour les recherches océaniques dans la zone côtière est la turbidité, elle est liée à des particules en suspension. L'étude de l'océan réclame un capteur in-situ en haute résolution pour mesurer simultanément la salinité et la turbidité.

La salinité

Si intuitivement, la salinité représente le contenu en sels dissous dans l'eau de mer, il faut se rendre à l'évidence qu'il est impossible de la mesurer précisément, de manière simple et globale. La première définition précise de la salinité de l'eau de mer date de 1902 et elle se définit comme la masse totale des substances solides dissoutes (en grammes) contenu dans un kilogramme d'eau de mer.

Cette définition est celle de la salinité absolue S_a , que l'on exprime en $g.kg^{-1}$. Jusqu'en 1978, la salinité était évaluée à partir de la chlorinité de l'eau. La relation entre la salinité et la chlorinité a été définie en 1902 comme suivant:

$$S_a = 0,03 + 1,805 Cl \quad (1)$$

L'inconvénient majeur de cette définition est que cette formule donne une salinité de 0,03‰ pour une chlorinité nulle. Une nouvelle formule est proposée en 1969:

$$S_a = 1,80655 Cl \quad (2)$$

Celle-ci ne prenait toujours pas en compte un équivalent de masse par kilogramme. En 1978, la salinité a donc été une nouvelle fois redéfinie, qui s'appelle «*practical salinity scale*» ou «*PSS-78*». Elle permet de calculer une salinité pratique S_P à partir de la mesure simultanée de la température, de la pression et de la conductivité électrique de l'eau de mer.

$$S_P = 0,0080 - 0,1692K_{15}^{1/2} + 25,3851K_{15} + 14,0941K_{15}^{3/2} - 7,0261K_{15}^2 + 2,7081K_{15}^{5/2} \quad (3)$$

où K_{15} est un rapport de la conductivité de l'eau de mer à la conductivité de référence. Le problème de cette définition est que le rapport K_{15} est en dehors du système international d'unité (SI). En 2009, le terme «*Salinité Absolue*» est réutilisé. Elle a été redéfinie comme «*Density Salinity*». De plus, plusieurs méthodes qui sont traçables au SI standard pour mesurer la «*Salinité Absolue*» directement, sont proposées, y compris la vitesse du son, l'indice de réfraction, et l'analyse chimique. Parmi ces méthodes, l'indice de réfraction correspond le mieux à nos exigences d'élaborer un capteur in-situ en haute résolution pour mesurer la salinité.

Les méthodes les plus avancées pour mesurer la salinité peuvent être divisées en deux catégories, l'une basée sur la mesure de conductivité et l'autre basée sur la mesure de l'indice de réfraction. La méthode basée sur la mesure de conductivité dépend fortement de la température et elle est affectée par les signaux électromagnétiques. De plus, les capteurs de conductivité se heurtent au problème majeur des mesures océaniques de longue durée: le «*fouling*», qu'il soit d'origine chimique ou biologique. Par rapport aux capteurs de conductivité, les capteurs de l'indice de réfraction basés sur le SI standard sont insensibles aux interférences électromagnétiques et le «*fouling*». Parmi les méthodes basées sur la mesure de l'indice de réfraction, le réfractomètre a beaucoup de fonctionnalités pour répondre à nos exigences de mesure de la salinité. C'est pour cela que nous souhaitons concevoir et mettre en oeuvre un réfractomètre pour mesurer la salinité de la mer dans cette thèse.

La turbidité

La turbidité se définit comme «*l'expression de la propriété optique qui fait que la lumière est dispersé et absorbé plutôt que transmise en ligne droite à travers l'échantillon*». Lorsque la lumière rencontre une particule, elle est dispersée dans toutes les directions. La dispersion est liée à la taille des particules, leur forme, leur composition et la longueur d'onde de la lumière. Plus la particule est grande, plus la lumière est dispersée vers l'avant. Dans un volume d'eau, la lumière diffusée par une particule sera dispersée par les autres particules, ce phénomène est appelé «*multi-scattering*». La mesure de turbidité est une mesure de l'effet de cette dispersion de un volume de l'eau.

Puisque la lumière est dispersée dans toutes les directions, la turbidité peut être mesurée à différents angles. La figure 1 montre le turbidimètre le plus avancé avec 4 détecteurs à des angles différents.

La turbidité est calculée par la formule:

$$T = \frac{I_{90}}{d_0 I_t + d_1 I_{fs} + d_2 I_{bs} + d_3 I_{90}} \quad (4)$$

Parmi ces angles, l'angle de 90° est particulier, il répond à deux standards: «*USEPA Method 180.1*» et «*ISO 7027*». La valeur de turbidité obtenu par ces deux méthodes a une unité, le NTU. Il faut mentionner que le standard primaire de turbidité est un matériau appelé Formazine. Il est utilisé pour calibrer tous les dispositifs de mesure de turbidité.

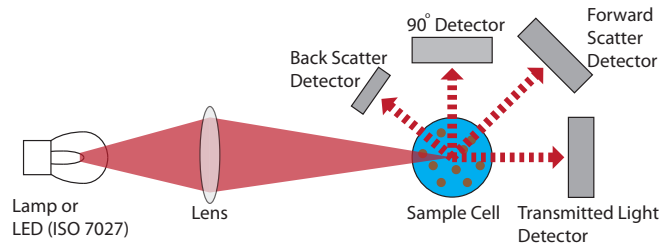


Figure 1: Le turbidimètre le plus avancé

Elaboration d'un réfractomètre à base de PSD

Principe du réfractomètre

Le principe du réfractomètre est montré dans la figure 2. Il est composé de quatre parties. Une source de lumière génère un faisceau de lumière, qui est réfractée à l'interface «verre-eau de mer». La réfraction provoque une déviation du faisceau, qui est mesurée par un capteur de position.

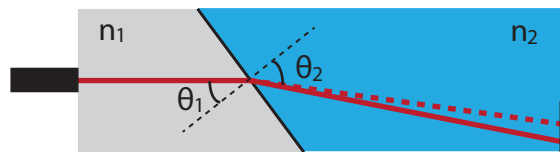


Figure 2: Le principe du réfractomètre

L'indice de réfraction de l'eau de mer peut être calculée en appliquant la relation de Snell-Descartes.

$$n_1 \times \sin(\theta_1) = n_2 \times \sin(\theta_2) \quad (5)$$

Analyse de la résolution

En étudiant l'interférence de la température, nous avons trouvé deux types de verres, de même coefficient thermo-optique mais de signes opposés qui permettent l'auto-compensation thermique du réfractomètre.

Avec ces deux verres, nous avons conçu un réfractomètre sous la forme d'un bi-prisme (figure 3). Il se compose donc de deux prismes (K7 et N-FK51). Un module laser est utilisé comme source lumineuse pour limiter la bande de longueur d'onde. Un «Position Sensitive Device» (PSD) est choisi pour mesurer la déviation du faisceau laser. Il mesure la position du faisceau laser après réfraction.

Par une méthode géométrique et une méthode différentielle, une relation entre l'indice de réfraction de l'eau de mer et la position du spot laser est obtenue. Basée sur cette relation, la gamme et la sensibilité requise du PSD sont calculées. Si l'indice de réfraction est dans une gamme de 1,336 (eau douce) à 1,345 (eau très salée), la longueur du PSD doit être au moins 10 mm. Pour atteindre une résolution de 10^{-7} sur l'indice de réfraction,

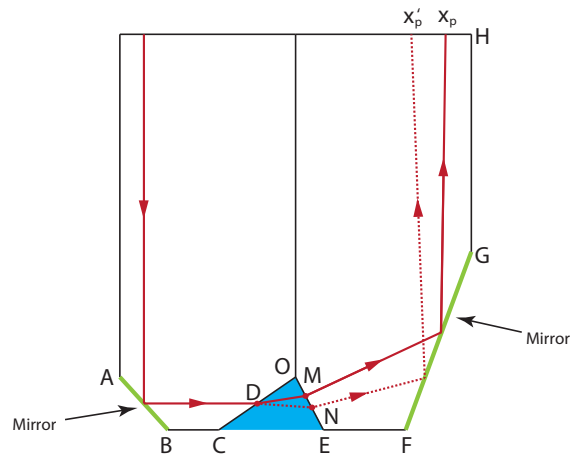


Figure 3: Le principe de réfractomètre «prototype I»

la résolution du PSD doit atteindre $0,3 \mu m$. Avec ces deux exigences, nous avons choisi un PSD de $12 mm$ avec une résolution étiquetée de $0,3 \mu m$.

Réalisation d'un réfractomètre à base de PSD

Ensuite, nous assemblons les pièces optiques et optoélectroniques pour fabriquer le réfractomètre. Le processus d'assemblage s'effectue en quatre étapes:

- Collage des blocs optiques
- Collage du module laser
- Collage du PSD
- Vérification et l'étalonnage

La résolution du réfractomètre dépend de la sensibilité du PSD. Bien que la résolution annoncée soit de $0,3 \mu m$, la résolution réelle peut être meilleure ou pire que cette valeur. Il est nécessaire d'évaluer la résolution réelle du PSD. Nous avons conçu pour cela un montage de haute résolution (Fig. 4).

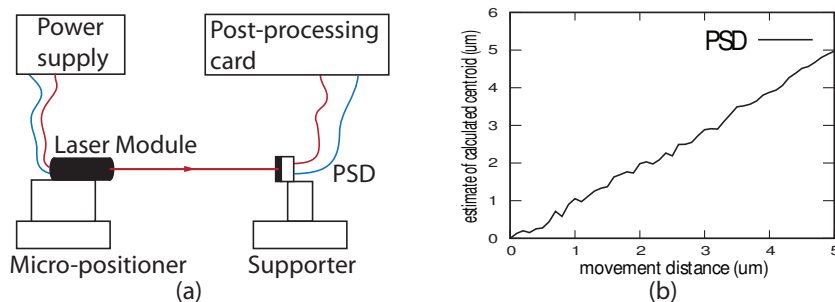


Figure 4: L'installation pour la vérification de la résolution du PSD

Le module laser est monté sur un micro-positionneur à 3-dimension avec une résolution de $0,1 \mu m$. Le faisceau laser pointe directement sur le PSD. Les signaux du PSD sont acquis par un ordinateur lorsque le faisceau laser se déplace sur une distance de 50 pas. Selon les résultats, la résolution expérimentale du PSD est de $0,11 \mu m$, la résolution de l'indice de réfraction correspondant est 3×10^{-7} , équivalent à la salinité absolue de $1 mg.kg^{-1}$.

Limitation du PSD

Le PSD est un capteur de haute performance pour mesurer la position de la lumière dans l'eau claire. Cependant, dans l'eau turbide, la lumière est diffusée hors de la direction transmise, et la distribution de la lumière est changée. Cette distribution contient beaucoup d'informations, telles que la position du spot laser. Toutefois, le PSD est conçu pour mesurer la position du spot laser, il ne peut pas être utilisé pour mesurer l'intensité lumineuse. Cela rend les techniques de post-traitement difficiles. Pour récupérer ces informations, par exemple, la turbidité de l'eau de mer, il est nécessaire d'utiliser un détecteur pour enregistrer la distribution d'intensité lumineuse, par exemple, un CCD (Charge-Coupled Device). Avant de commencer à mesurer les propriétés de distribution connexes, nous avons besoin de prouver que le réfractomètre équipé d'un CCD peut obtenir au moins la même résolution que le réfractomètre équipé d'un PSD.

Le réfractomètre à base de CCD: prêt à construire un capteur multi-fonctionnel

Principe du réfractomètre avec CCD

Le CCD n'enregistre que la distribution d'intensité de la lumière, il a besoin d'un algorithme de post-traitement pour récupérer les informations. L'algorithme qui peut nous fournir l'information du spot laser s'appelle «image location algorithm». Basé sur des définitions différentes, il existe 3 algorithmes:

- L'algorithme recherche du «centre de gravité»
- L'algorithme «transformée de Fourier»
- L'algorithme «détection du bord»

Tous les algorithmes permettent d'obtenir une résolution sub-pixel. Puisque nous voulons comparer les réfractomètres à base de PSD et CCD, l'algorithme de centroïde est utilisé car il mesure le centre de la gravité de l'intensité du spot comme le PSD.

Analyse de performance

La résolution du réfractomètre basé sur CCD est liée à l'erreur systématique. La première erreur systématique est provoquée par l'échantillonnage, la quantification du CCD, et l'algorithme de gravité. Cette erreur ne peut pas être évitée, mais peut être corrigée. Une autre erreur est provoquée par les bruits. Il y a trois sortes de bruits:

- Bruit de lecture (affecte tous les pixels)
 - Bruit de fond (affecte tous les pixels)
-

- Bruit photonique liée à l'intensité de la lumière incidente.

L'image capturée par le CCD est la somme des bruits et du spot original. L'algorithme de calcul du centre de gravité calcule la position du centre du spot et des bruits. Pour éliminer ou réduire les bruits de lecture et de fond, un seuil ou plusieurs images peuvent être utilisés. Le bruit photonique peut être réduits en appliquant un filtre passe-bas à l'image.

La vitesse est un autre indicateur de performance. Le réfractomètre basé sur l'utilisation d'un PSD a un temps de réponse très court. Toutefois, pour obtenir une résolution élevée, des signaux multiples doivent être capturés. La vitesse du système à base de PSD dépend de la fréquence d'échantillonnage. Le réfractomètre basé sur l'utilisation d'un CCD est plus compliqué. Pour parvenir à haute résolution, des images multiples doivent d'abord être capturées et mémorisées dans un dispositif de stockage, par exemple, le disque dur. L'algorithme doit charger ces images, et puis calculer la position. En conclusion, la vitesse du système à base de CCD dépend du nombre d'images traitées et de la taille de l'image.

La saturation du CCD est définie comme le montant maximum des charges qu'un pixel peut recueillir. Quand un pixel atteint ce niveau, la lumière reçue et les charges converties ne satisfont pas une relation linéaire. De plus, les charges qui ne peuvent pas être transférées vont polluer les pixels adjacents et former un «blooming». Pour cette raison, la saturation doit être évitée lors de la mesure.

L'évaluation des paramètres

Avant de commencer à comparer ces deux types de réfractomètres, nous avons besoin d'évaluer les paramètres du réfractomètre basé sur l'utilisation du CCD:

- nombre d'images traitées.
- seuil
- taille de la fenêtre
- puissance de la lumière

Nous avons fait une expérimentation pour évaluer ces paramètres. Dans l'expérimentation, la position du module laser est fixe et il pointe directement sur le CCD. 5 000 images sont capturées pour calculer la référence du centre et celle de la taille du spot. Le niveau de bruits peut être également obtenu par ces 5 000 images: soit 9 (valeur de pixel).

Selon les résultats expérimentaux, nous pouvons déduire les paramètres optimisés pour l'utilisation du CCD. Le nombre d'images traitées est un paramètre critique pour la vitesse, mais pas critique pour la résolution. Le seuil doit être supérieur au niveau de bruit. La taille de la fenêtre «image» est un paramètre critique pour la résolution et la vitesse. Pour obtenir une bonne résolution, la taille de la fenêtre doit être plus grande que la taille du spot. Pour réduire l'erreur systématique, la saturation doit absolument être évitée lors de la mesure.

Comparaison entre les solutions - CCD et PSD

Avec les paramètres optimisés, nous avons conçu une expérimentation pour comparer les systèmes CCD et PSD. Le module laser est monté sur un micro-positionneur à 3-dimensions

avec une résolution de $0,1 \mu m$. Pour mettre les deux systèmes dans les mêmes conditions, le CCD utilise seulement une fenêtre de 267 pixels, soit $1 mm$, égale à la hauteur du PSD. Cinq zones sont choisies pour mettre en oeuvre les comparaisons. Dans chaque zone, le module laser est déplacé d'une distance de $5 \mu m$ par le micro-positionneur avec un pas de $0,1 \mu m$. Dans chaque étape, 64 images sont capturées en 1 seconde, et le centre est calculé à partir de la moyenne des 64 centres de l'image. Pour le réfractomètre à base de PSD, 10 000 échantillons sont acquis avec une fréquence de 10 000 Hz. La position est calculée par la moyenne de ces 10 000 échantillons.

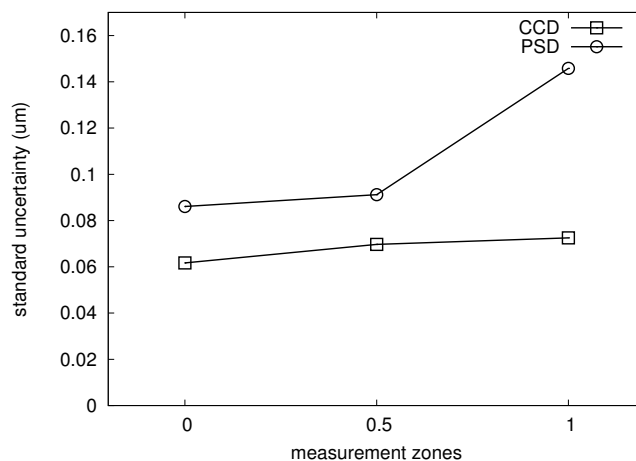


Figure 5: Résultats expérimentaux pour la comparaison entre les systèmes basés sur CCD et PSD

La figure 5 montre les résultats expérimentaux pour la comparaison entre les solutions CCD et PSD. Pour chaque zone, la solution CCD ($0,07 \mu m$) a une meilleure résolution que la solution PSD ($0,11 \mu m$). Il faut noter que la résolution du système à base de PSD repose sur la position du spot. Plus il est loin du centre, plus la résolution est mauvaise. Par contre, la solution CCD est indépendante de la position du spot.

La mesure de turbidité basée sur le réfractomètre

Le réfractomètre à base de CCD peut obtenir une meilleure résolution que le réfractomètre à base de PSD. De plus, le système basé sur CCD peut être utilisé pour mesurer les propriétés liées à la distribution de l'intensité de la lumière en appliquant des algorithmes différents à l'image. Pour prouver l'avantage du système CCD, la mesure de turbidité, sans modifier la configuration de notre réfractomètre, est étudiée dans cette thèse.

La première étape est de choisir les méthodes de mesure de la turbidité. Puisque nous voulons montrer les avantages du post-traitement du CCD, la méthode que nous choisissons doit présenter le moins de modifications possible dans notre réfractomètre. En considérant les méthodes différentes, l'angle de transmission est le bon choix.

Principe de la mesure de turbidité à l'angle de transmission

La figure 6 illustre le principe de la mesure de turbidité à l'angle de transmission. Lorsque la lumière se propage dans un milieu turbide, la lumière est absorbée et diffusée. Il y a

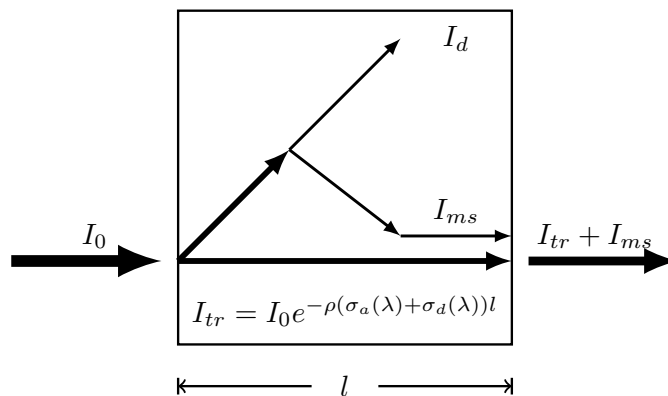


Figure 6: Principe de la mesure de turbidité à l'angle de transmission

trois sortes de lumières. La première appelée lumière transmise I_{tr} peut être calculée par la formule:

$$I_{tr} = I_0 e^{-\rho(\sigma_a(\lambda) + \sigma_d(\lambda))l} \quad (6)$$

où ρ est la densité de particule, σ_a décrit la partie de lumière absorbée par une particule et σ_d décrit la partie de lumière diffusée hors de la direction transmise. Outre la lumière transmise, une autre partie de la lumière est diffusée hors de la direction de transmission, et une partie est re-dispersée dans le sens de transmission. Cette dernière partie de lumière s'appelle I_{ms} . Selon l'équation 6, la partie $\rho(\sigma_a(\lambda) + \sigma_d(\lambda))$ et le coefficient d'atténuation, peut être utilisé pour décrire la turbidité:

$$T = \frac{\ln(I_m - I_{ms}) - \ln(I_0)}{l} \quad (7)$$

De cette équation, nous pouvons dériver la sensibilité de la mesure de la turbidité. Elle est proportionnelle à la sensibilité du capteur d'intensité lumineuse et inversement proportionnelle à la longueur du chemin parcouru par la lumière dans l'eau. Cette mesure est favorable en milieu à faible turbidité.

L'influence entre la mesure de la turbidité et la mesure de l'indice de réfraction

La lumière diffuse dans toutes les directions dans un milieu turbide. Cela conduit à un problème, la lumière transmise et la lumière diffusée sont mélangées comme on peut le voir dans la figure. 7.

Nous pouvons aussi observer les «speckles» dans l'image ci-dessus, qui sont provoqué par des interférences. Le PSD ne peut pas séparer la lumière transmise de la lumière diffusée. Par conséquent, il ne peut pas être utilisé pour mesurer la turbidité. De plus, la lumière diffusée et les interférences affectent la position du centre de gravité en intensité du spot, ce qui signifie que le PSD ne peut pas fournir la position correctement dans un milieu turbide. Cependant, avec le CCD, il est possible de récupérer le spot d'origine avec le post-traitement des algorithmes. En étudiant la transformée de Fourier de l'image, la lumière diffusée et les interférences existent à hautes fréquences. Une filtre passe-bas d'image permet d'éliminer efficacement les interférences et la lumière diffusée.

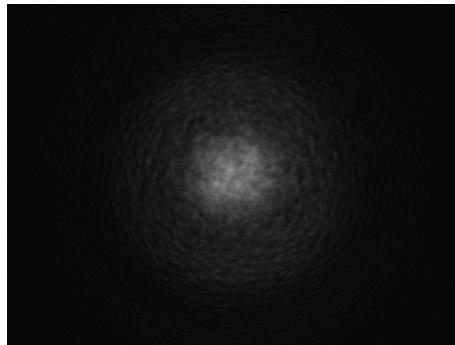


Figure 7: La lumière transmise et la lumière diffusée sont mélangés



Figure 8: Le spot asymétrique provoqué par la divergence et la diffusion

L'indice de réfraction rencontre un défi en milieu turbide aussi. La divergence du faisceau et la diffusion rendent le spot asymétrique comme on le voit dans la figure 8. Cela conduit à une conséquence que le PSD ne peut pas indiquer la bonne position du spot, et le CCD avec l'algorithme centroïde non plus. Cependant, le CCD peut bénéficier des techniques de post-traitement. Pour résoudre le problème, un nouvel algorithme est développé. Il cherche la position où les parties de deux cotés ont la même masse. En milieu claire, peu importe le nombre de divergences, la position reste au même endroit. En milieu turbide, cette règle fonctionne après avoir éliminé la lumière diffusée par un filtre passe-bas.

En étudiant la position du spot en milieu turbide, nous avons établi une loi de variation de centre: «En milieu turbide, le spot de projection d'un faisceau Gaussien sur une surface avec un angle α est encore un faisceau Gaussien avec la même taille de spot, mais il a un décalage du centre, qui est proportionnel à la turbidité du milieu, la taille du spot, et inversement proportionnelle à la cotangente de l'angle α .»

Pour évaluer les performances de l'algorithme, plusieurs simulations et expérimentations sont réalisées. Le résultat montre que le nouvel algorithme permet d'obtenir une meilleure résolution (0,035 pixels) que l'algorithme classique (0,078 pixels) en milieu claire. La résolution du nouvel algorithme est 2 fois plus grande que celle de l'algorithme classique.

Plusieurs expérimentations sont réalisées pour évaluer notre méthode de mesure de la turbidité. Les expérimentations ont été menées avec un cube et avec notre réfractomètre. La solution Formazine de 4000 NTU est diluée dans différents échantillons turbides pour calibrer le turbidimètre. Les résultats expérimentaux montrent que la résolution moyenne

de notre méthode basée sur le réfractomètre atteint 8 NTU dans une gamme de 0 NTU à 200 NTU, et 1,15 NTU dans une gamme de 0 NTU à 20 NTU. Nous avons comparé notre méthode avec le néphélomètre spécifié par le standard. Le résultat calculé par notre méthode s'adapte correctement aux résultats obtenus à partir d'un néphélomètre commercial.

Perspective: trois nouveaux prototypes

A la fin de la thèse, nous avons proposé trois nouveaux prototypes de capteur pour mesurer la salinité et la turbidité de l'eau de mer simultanément. Le premier prototype utilise un prisme monobloc pour compenser la variation de longueur d'onde du module laser provoqué par le changement de température. La résolution de la salinité absolue de ce prototype atteint $1,4 \text{ mg.kg}^{-1}$. Basés sur ce modèle, nous avons ouvert une cavité avec une longueur de 20 mm. Ce prototype a la même résolution de salinité absolue que le précédent. Cependant, la résolution de la turbidité atteint 1% de la gamme de mesure. Le dernier prototype a un miroir à 45° afin de réfléchir la lumière diffusée à 90° . Il est équipé d'une photo-diode pour mesurer l'intensité lumineuse à 90° . La résolution sur la mesure de turbidité de ce modèle atteint moins de 1% de la gamme de mesure.

Conclusion

Le réfractomètre est très bien adapté pour mesurer, avec une très grande précision, la salinité de l'eau de mer. L'utilisation du PSD, dans un premier temps, a permis de mesurer la salinité avec une résolution de 1 mg.kg^{-1} . Cependant, le PSD peut seulement travailler en milieu clair, il ne fonctionne pas dans les milieux turbides. Par rapport au PSD, le réfractomètre utilisant un CCD peut être utilisé pour mesurer la salinité et la turbidité en milieu clair et turbide, en appliquant des algorithmes différents à l'image capturée par le CCD. La résolution de mesure de la salinité en utilisant le CCD est meilleur que celle utilisant le PSD. De plus, le système utilisant un CCD a la capacité de mesurer des propriétés différentes de l'eau de mer en appliquant les algorithmes différents.

Contents

1	State of the art: the measurement of sea water salinity and turbidity	8
	Introduction	9
I	Generality	9
	I.1 Oceanography	9
	I.2 Salinity	10
	I.2.1 Definition of salinity	10
	I.2.2 Absolute Salinity and Practical Salinity	12
	I.3 Turbidity	12
	I.3.1 Definition of turbidity	12
	I.3.2 Scattering	13
	I.3.3 Turbidity Standards	15
II	Salinity measurement methods	17
	II.1 Conductivity based salinity measurement	17
	II.1.1 Definition of conductivity	17
	II.1.2 Conductivity of seawater	18
	II.1.3 Conductivity sensors	19
	II.2 Refractometer based salinity measurement	20
	II.3 Some refractive index measurement methods	21
	II.3.1 Refractometer based methods	21
	II.3.2 Interferometer based methods	23
	II.3.3 Fiber Bragg grating based methods	24
III	Turbidity measurement methods	26
	III.1 Transmissometer	27
	III.2 Backscatter method	27
	III.3 Nephelometric (90°) scatter method	28
	III.4 Multi-angle method	30
	Conclusion	32
	Bibliography	35
	Figures and tables	36
2	Design and implementation of an optical refractometer	37
	Introduction	38
I	Preliminary knowledge of modelling a refractometer	38
	I.1 Review of Snell–Descartes law	38
	I.2 Introduction of optical material	39
	I.2.1 Sellmeier coefficients	39
	I.2.2 Temperature coefficient of refractive index	40

	I.2.3	Thermal expansion coefficient	42
II		Modelling a refractometer	42
	II.1	Prototype of refractometer	42
	II.2	Relationship between refractive index and laser beam position	43
	II.3	Study of the resolution	45
III		Design and implementation of the refractometer	47
	III.1	Introduction of optoelectronics elements	47
	III.1.1	Laser source	47
	III.1.2	Position Sensitive Device/Detector	48
	III.2	Implementation of the refractometer	51
	III.2.1	Step1: adhesion of the prism	51
	III.2.2	Step2: adhesion of the laser source	52
	III.2.3	Step3: adhesion of the PSD	53
	III.2.4	Step4: verification and calibration of the refractometer . . .	53
IV		The resolution of the refractometer	54
		Conclusion	56
		Bibliography	58
		Figures and tables	59
3		CCD-based refractometer: ready to build a multi-functional sensor	60
		Introduction	61
I		CCD-based position detection	61
	I.1	Review the principle and limitation of PSD	61
	I.2	Principle of pixel-based image sensor	62
	I.2.1	Principle of CCD image sensor	63
	I.2.2	Compare to CMOS image sensor	64
	I.3	Image location algorithms	66
	I.3.1	General introduction	66
	I.3.2	Well-known algorithms	67
	I.3.3	Selection of the algorithm	69
II		Performance analysis of CCD- and PSD-based system	69
	II.1	Resolution	69
	II.2	Speed	71
	II.3	Saturation	72
III		Evaluate the parameters of CCD-based system	73
	III.1	Number of processed images	74
	III.2	Threshold	75
	III.3	Optimum image window size	76
	III.4	Laser beam power & Saturation	76
IV		Performance comparison of CCD and PSD-based system	77
	IV.1	Resolution	78
	IV.2	Speed	79
V		Performance trade-off of CCD-based system	80
	V.1	Number of images processed	80
	V.2	Image window	81
	V.3	Binning	82
		Conclusion	83
		Bibliography	86

Figures and tables	87
4 Turbidity measurement based on the refractometer	88
Introduction	90
I Review of the turbidity measurement methods	90
I.1 Selection of the turbidity measurement method	91
I.2 Principle of attenuation based method	91
I.3 Attenuation coefficient to turbidity	94
I.4 Sensitivity analysis	95
II Issues in measuring turbidity with refractometer	96
II.1 Measurement distance	96
II.2 Non-uniqueness of light path inside the beam	96
II.3 Light path variation caused by refractive index change	97
II.4 Interference	98
II.5 High turbidity measurement	98
III Issues in measuring refractive index in turbid medium	99
III.1 Non-uniqueness of light path inside the beam	99
III.2 Divergence and scattering caused asymmetrical spot	99
IV Invalidation of PSD	100
V Using CCD to measure the turbidity with refractometer	102
V.1 High turbidity measurement	102
V.2 Scattered light & interference elimination	102
V.3 Solution to light path related problems	103
V.3.1 Light path variation according to the refractive index	103
V.3.2 Non-uniqueness of light path inside the beam	104
V.4 New location algorithm	105
VI Experiments & Results	107
VI.1 Performance evaluation of new location algorithm	107
VI.1.1 Simulation	107
VI.1.2 Experiment	109
VI.2 Simulation & experiments with parallel slab	110
VI.2.1 Simulation	110
VI.2.2 Experiments in high turbid medium	110
VI.2.3 Experiments in low turbid medium	112
VI.3 Simulation & experiments with refractometer	113
VI.3.1 Simulation	113
VI.3.2 Experiments in high turbid medium	113
VI.3.3 Experiments in low turbid medium	115
VI.4 Comparison with nephelometer	115
Conclusion	117
Bibliography	119
Figures and tables	120
5 Perspective: improvements of refracto-turbidi-meter performance	121
Introduction	122
I Issues and Possible improvements	122
I.1 Issues in our methods	122
I.2 Improvements for refractometer	123

I.3	Improvements for turbidi-meter	124
I.4	Other improvements	125
II	Prototype II: new model of refractometer	125
II.1	New model	126
II.2	Performance analysis	126
III	Prototype III: new model of refracto-turbidi-meter	127
III.1	Turbidi-meter based on prototype II	128
III.2	Futher improvement	129
	Conclusion	131
	Bibliography	132
	Figures and tables	133
General Conclusion		134
A Algorithm of Seaver & Millard		139
B Resolution analysis of refractometer prototype I		141
C Resolution analysis of refractometer prototype II		145
D Specifications for different prototypes		149
I	Specifications for refracto-turbidi-meter prototype I	150
II	Specifications for refracto-turbidi-meter prototype II	151
III	Specifications for refracto-turbidi-meter prototype III	152
IV	Specifications for refracto-turbidi-meter prototype IV	153

General Introduction

The researches included in this thesis are under the frame of oceanography, which is linked to understanding global climate changes, potential global warming and related biosphere concerns. As a branch of the oceanography, the physical oceanography, which studies the ocean from its physical properties, attracts us the most. Among these oceanographic physical properties, temperature and salinity are two most important ones. In fact, temperature, salinity, and pressure are used to calculate density which is directly related to the distribution of horizontal pressure gradients and ocean currents. Another physical property that is important for oceanography is turbidity, which is useful for the oceanographers to study the microorganisms that will participate in the carbon cycle and oxygen production. Changes in temperature, salinity and turbidity help the oceanographers to track the movement of the seawater. For these reasons, we need to know the distribution of temperature, salinity, density, and turbidity in the ocean. This requires different high-resolution measurement instruments to measure these oceanographic physical properties. Current studies have found that all these physical properties are tightly connected to each other to influence the different oceanographic phenomena, which make the study of *in situ* multi-functional sensor valuable. Based on these requirements, our research interests is the design of a high resolution multi-functional *in situ* oceanographic sensor to measure these physical properties, especially salinity and turbidity. Recent researches have built the relationship between salinity and refractive index of seawater. To measure the salinity, a high resolution refractometer is needed. For the turbidity measurement, the scattering property of seawater are studied by different researches and is defined as a represent of turbidity.

The objective of the work described in this document includes the design, modelling, implementation, and improvement of an *in situ* optical refractometer, which measures refractive index of seawater and light attenuation caused by the scattering simultaneously. Specifically, this work is part of a cooperation launched in 2006 between the school TELECOM Bretagne through the Department optics (UMR FOTON 6082), SHOM (Service Hydrographique et Océanographique de la Marine) and the project NOSS (NkeElectronics Optical Salinity Sensor). The goal is to develop a high resolution and compact optical refractometer to measure the refractive index and light scattering properties of seawater to determine the physico-chemical parameters of the ocean, especially salinity and turbidity. The salinity and turbidity measurement must meet the oceanographic needs, e.g. the measure of salinity must achieve a measurement uncertainty of a few milligrams of salt per litre of seawater. To achieve these resolution requirements, a high resolution refractometer was designed first to measure the refractive index of seawater. Based on the configuration of the refractometer, the possibility of measuring turbidity with the refractometer is discussed and a feasible solution is introduced in this thesis as well. At the end of this thesis, we discuss several methods to improve the performance of the multi-functional *in situ* optical

sensor.

The first chapter is for the objective of introducing several necessary definitions to understand the application described in this thesis, different technologies used to measure the physico-chemical ocean parameters, and the state-of-the-art salinity and turbidity measurement methods. More precisely, we first introduce the physical oceanography and the principal physico-chemical parameters, especially salinity, conductivity, and turbidity. The Practical Salinity is associated with the conductivity and temperature of seawater, while turbidity is related to the scattering property of seawater. Different salinity and turbidity measurement methods are presented in this chapter as well. Some of these methods can reach high resolution but are hard to integrate into a compact *in situ* multi-functional sensor, others meet the requirement of integration but have low resolution. That's why a new high resolution compact *in situ* multi-functional sensor is studied in this thesis. Our research method is to design a high-resolution salinity sensor first and then add the turbidity measurement functionality into the salinity sensor. By comparing these state-of-the-art salinity measurement methods, the method of refractometer based on the laser beam deviation most fits our requirement and is selected as our basis for the design.

The objective of the second chapter is to introduce the study of design, modelling, and implementation of a high resolution refractometer based on the laser beam deviation measurement. We start from presenting some preliminary knowledge of modelling a refractometer, among which we pay special attention to the temperature coefficients of the optical material. Based on these preliminary knowledges, we model the refractometer in both a differential method and a geometrical method to build the relationship between refractive index and laser beam deviation. More important, from this relationship we obtain the performance requirements for the geometric parameters and optoelectronic elements in order to reach the desired refractive index resolution (in an order of 10^{-7}). To fulfil these requirements, we introduce a high resolution position detection detector (PSD) with a measurement resolution of $0.3 \mu m$ to measure the laser beam deviation. With the optimized parameters, a detailed operation procedure is included in chapter 2 to guide the fabrication of the refractometer. The last step of the modelling is the verification of the resolution, which recalls an experiment to evaluate the actual resolution of the PSD. According to the experimental result, the resolution of refractive index calculated is about 3×10^{-7} , equals to the absolute salinity of $1 \times 10^{-3} g.kg^{-1}$.

The third chapter discuss the needed preparation in order to upgrade the high resolution refractometer that we designed into a multi-functional sensor. The transmitted beam carries not only the refractive index related beam deviation information but also the other information associated to the intensity distribution. To obtain these intensity distribution related informations, a pixel-based image sensor is needed to be used to replace PSD, which is designed to calculate the light position. To make this replacement reasonable, it is necessary to prove that by using a pixel-based image sensor, the resolution of laser beam deviation measurement can reach at least the same resolution as the one provided by using a PSD. This chapter first introduces two well-known image sensors, CCD and CMOS. By comparing the technical characteristics of the two image sensors, CCD is selected to be used in the multi-functional sensor. In order to retrieve the laser beam deviation information from the captured images, the centroid algorithm is used to calculate the gravity center of the laser spot. A performance comparison between PSD and CCD combined with a centroid algorithm are discussed with special attention paid to the CCD-based system. According to the operating principle of CCD-based system, several experiments were carried out to evaluate five factors of CCD-based system: image window size, number of processed

images, threshold, binning and saturation. By applying the optimized parameters, several experiments were made to compare CCD-based system with the state-of-the-art PSD-based system in terms of two performance indicators, namely resolution and speed. It is shown that, by applying the optimized parameters, the performance of a CCD-based system is comparable to that of a PSD-based system in measuring laser beam deviation.

The fourth chapter is aimed at demonstrating the benefits brought from the use of CCD instead of PSD. The measurement of turbidity is one of the best choices for this purpose. In order to best demonstrate the advantages of CCD-based system, we introduce a CCD-based turbidity measurement method in measuring the transmitted light intensity without modifying the configuration of refractometer. By analysing the principle of the turbidity measurement method from measuring the transmitted light intensity, we study the interference between the turbidity measurement and the refractive index measurement. Due to the interference, we further prove that PSD is not suitable to correctly measure neither the refractive index nor the transmitted light intensity in a turbid medium. On the contrary, CCD can overcome the interference and correctly provide both the laser beam deviation information and the transmitted light intensity information in a turbid medium due to the recorded light intensity distribution. To prove the benefits from CCD, a new algorithm and several techniques are proposed to eliminate the interference. Several simulations and experiments are carried out to verify the performance of the method proposed in the same chapter.

The last part of the thesis introduces the perspective in the near future and addresses the problem of the turbidity measurement resolution. For this purpose, a new refracto-turbidi-meter is designed under the consideration of both the laser beam deviation measurement and the transmitted light intensity measurement. We start from the proposition of several possible ways to improve the performance of the refractive index measurement and the turbidity measurement in a compact sensor. Based on these proposed improvement methods, we introduce a new compact *in situ* double-functional sensor for the salinity and turbidity measurement of seawater, which has the absolute salinity resolution of $1 \times 10^{-3} g.kg^{-1}$ and the turbidity resolution, 1% of the measurement range.

Chapter 1

State of the art: the measurement of sea water salinity and turbidity

Contents

Introduction	9
I Generality	9
I.1 Oceanography	9
I.2 Salinity	10
I.2.1 Definition of salinity	10
I.2.2 Absolute Salinity and Practical Salinity	12
I.3 Turbidity	12
I.3.1 Definition of turbidity	12
I.3.2 Scattering	13
I.3.3 Turbidity Standards	15
II Salinity measurement methods	17
II.1 Conductivity based salinity measurement	17
II.1.1 Definition of conductivity	17
II.1.2 Conductivity of seawater	18
II.1.3 Conductivity sensors	19
II.2 Refractometer based salinity measurement	20
II.3 Some refractive index measurement methods	21
II.3.1 Refractometer based methods	21
II.3.2 Interferometer based methods	23
II.3.3 Fiber Bragg grating based methods	24
III Turbidity measurement methods	26
III.1 Transmissometer	27
III.2 Backscatter method	27
III.3 Nephelometric (90°) scatter method	28
III.4 Multi-angle method	30
Conclusion	32
Bibliography	35
Figures and tables	36

Introduction

The objective of the work described in this document includes the design, modelling, implementation, and improvement of an *in situ* optical refractometer, which measures the refractive index of seawater and the light attenuation caused by the scattering simultaneously. The measurement of refractive index is aimed at measuring the salinity, while the measurement of light attenuation is for the measure of turbidity.

This chapter introduces some useful physiochemical properties in the domain of oceanography, especially salinity and turbidity of seawater. Different principles and methods to measure these two properties, including the most state of the art methods are mentioned in this chapter as well.

At the beginning of this chapter, we give a general introduction of the oceanography and introduce several important seawater properties. Among them, we pay special attention to two of the properties, salinity and turbidity, by describing their definitions and discussing several methods with their basic principles to measure these two seawater properties. For the introduction of the salinity measurement, the state of the art refractometer are introduced as well. To link the measurement of refractive index to the measurement of salinity, the relationship between seawater refractive index and salinity is illustrated.

The second part of this chapter introduces the state of the art turbidity measurement. The scattering theory, which explained the turbidity phenomenon, is firstly reviewed. Based on the theory, several industry turbidity standards are introduced to illustrate the turbidity unit. At the end of this part, we introduce different state of the art turbidity measurement methods.

I Generality

I.1 Oceanography

Oceanography is a branch of earth science that studies the ocean. It covers a wide range of topics and is divided into several sub-branches, eg. biological oceanography, chemical oceanography, geological oceanography, and physical oceanography. The study of the oceans is linked to understanding global climate changes, potential global warming and related biosphere concerns. Among these sub-branches, we pay special attention to the physical oceanography, which studies the physical properties and dynamics of the ocean. The primary interests are the interaction of the ocean with the atmosphere, the oceanic heat budget, water mass formation, currents, and coastal dynamics[1].

Among the physical properties, four of them, named as temperature, pressure, salinity, and density, are very important to the oceanography. Heat fluxes, evaporation, rain, river inflow, and freezing and melting of sea ice all influence the distribution of temperature and salinity at the ocean's surface. The changes in temperature and salinity can change the density of the water, which can lead to convection. In addition, temperature, salinity, and pressure are used to calculate density. The distribution of density inside the ocean is directly related to the distribution of horizontal pressure gradients and ocean currents. Density currents are produced where gravity acts upon a density difference between one fluid and another. Besides these four properties, another property named turbidity, which is related to the suspended particles in seawater is very important for oceanography, especially the biological researches. In this thesis, we introduce a double optical sensor to measure salinity and turbidity of seawater.

I.2 Salinity

Salinity is a very important property to describe sea water, especially associated to the measurement of temperature. Different seas have quite different salinities, for example, the Mediterranean (38-39), the Red Sea (36-47), the Baltic Sea (<15), and the Black Sea (18-22). The salinity map Fig 1.1 shows the areas of high salinity (36) in green, medium salinity in blue (35), and low salinity (34) in purple. Salinity is rather stable but areas in the North Atlantic, South Atlantic, South Pacific, Indian Ocean, Arabian Sea, Red Sea, and Mediterranean Sea tend to be a little high (green). Areas near Antarctica, the Arctic Ocean, Southeast Asia, and the West Coast of North and Central America tend to be a little low (purple).

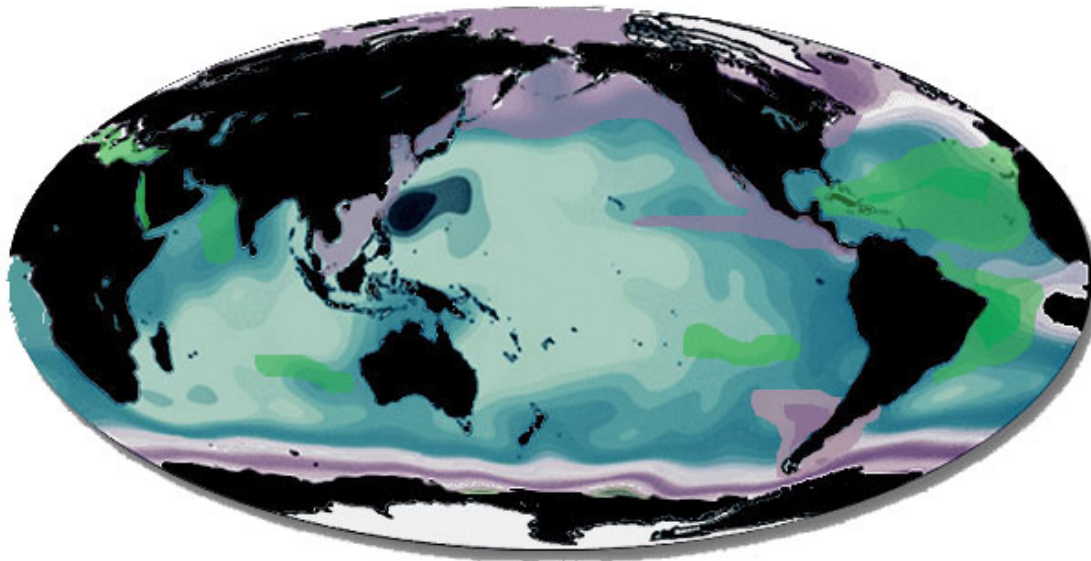


Figure 1.1: Salinity map of the world

The accuracy of measuring salinity depends on the application. To understand the circulation of seawater in coastal and offshore by measuring the dissolved substances, the accuracy of salinity measurement need to be compatible to the study. For the coastal seawater salinity measurement (less then 600 meters), the required accuracy of salinity in the range of 0 and 38 PSU is ± 0.02 PSU. For the offshore measurement, the expected accuracy reaches ± 0.003 PSU in a range from 10 to 38 PSU with the depth more than 2500 meters.

I.2.1 Definition of salinity

In 1865, Fochhammer[2] first introduced the term salinity[3]. In his paper, the salinity is represented as the dissolved salt content of a parcel of water. However, this quantity is not precise enough to measure in practice. With the evolution of the measurement technology, other definitions of salinity were proposed. The first precise definition of salinity of seawater is given by Forch, Knudsen and Sørensen[4] in 1902.

“Salinity is the total amount of solid materials in grams contained in one kilogram of seawater when all the carbonate has been converted to oxide, the

bromine and iodine replaced by chlorine, and all organic matter completely oxidized”[5]

This definition is called *absolute salinity* with the unit of *g/kg*. Although this definition is much more precise, it is not possible to measure this quantity directly. Based on the premise of the constancy of ionic ratios in seawater, the International Council for the Exploration of the Sea defined a “chlorinity” that could be determined by a simple volumetric titration using silver nitrate, to be used as a measure of salinity[6]. Chlorinity was defined as:

“the weight in grams (in vacuo) of the chlorides contained in one gram of seawater (likewise measured in vacuo) when all the bromides and iodides have been replaced by chlorides.”

Based on the measurements on samples of seawater from the surface of the Baltic, Mediterranean, Red Seas, and North Atlantic Ocean, salinity can be calculated with the formula:

$$S_a = 0.03 + 1.805 Cl, \quad (1.1)$$

where S_a is the salinity and Cl expresses the chlorinity. This equation was used from 1902 to 1962. The major inconvenience of this definition shown in Eq 1.1 is the inconsistency to the definition of salinity. A sample of seawater with no chlorinity has salinity of 0.03‰. As a result, the Joint Panel on Oceanographic Tables and Standards (JPOTS) proposed a redefinition of *absolute salinity* as:

$$S_a = 1.80655 Cl \quad (1.2)$$

This definition suffered from the fact that still there was no method for coping with the varying chlorinity-salinity-density relationship under conditions of ionic change. It was used since 1962. In 1978, the salinity was redefined another time. To solve the problem of directly measuring the absolute salinity, the *Practical Salinity Scale* was defined in 1978. It measures the practical salinity with three other properties: temperature, pressure, and seawater conductivity. The precise definition of *practical salinity* is:

“The Practical Salinity, symbol S , of a sample of sea water, is defined in terms of the ratio K_{15} of the electrical conductivity of the seawater sample at the temperature of 15 deg C and the pressure of one standard atmosphere, to that of a potassium chloride (KCl) solution, in which the mass fraction of KCl is 32.4356×10^{-3} , at the same temperature and pressure. The K_{15} value exactly equal to 1 corresponds, by definition, to a Practical Salinity exactly equal to 35.”[7]

The relation between practical salinity and the ratio K_{15} is given by:

$$S = 0.0080 - 0.1692K_{15}^{1/2} + 25.3851K_{15} + 14.0941K_{15}^{3/2} - 7.0261K_{15}^2 + 2.7081K_{15}^{5/2} \quad (1.3)$$

This equation is valid for a Practical Salinity from 2 to 40. From the definition, it is obvious that practical salinity is a ratio and strictly no unit should be used but often PSU (Practical Salinity Unit) is added to that value. In this document, we add “PSU” after the value of practical salinity for clearly expressing the physical meaning of the value.

I.2.2 Absolute Salinity and Practical Salinity

It is very important to emphasize that the practical salinity does not directly reflect the dissolved salt material in seawater. The total mass of dissolved material, absolute salinity S_a with the unit of g/kg , can be calculated from the equation $S_a = a + b S$, where a and b are two coefficients obtained from the seawater samples over the world. In 2006, Jackett and his colleagues[8] gives a more accurate expression of the relationship between absolute salinity and practical salinity by comparing different ocean seawaters as shown in Eq. 1.4.

$$S_a = (1.0045 \pm 0.0005) S \quad (1.4)$$

The difference between S and S_a is approximately $0.45 \pm 0.05\%$; for example, a seawater parcel with $S = 35$ PSU has an absolute salinity S_a of between 35.140 and 35.175 ‰, a difference of approximately 0.16 ‰, which is between 50 and 100 times as large as the accuracy with which we can determine salinity at sea.

In 2009, the Intergovernmental Oceanographic Commission adopted TEOS-10[9] (Thermodynamic Equation Of Seawater - 2010) to replace EOS-80 as the official description of seawater and ice properties in marine science. The Absolute Salinity is redefined in TEOS-10 as “Density Salinity” S_A^{dens} , which is:

“the value of the salinity argument of the TEOS-10 expression for density which gives the sample’s actual measured density at the temperature $t = 25^\circ C$ and at the sea pressure $p = 0$ dbar”.

When there is no risk of confusion, “Density Salinity” is also called Absolute Salinity with the label S_A , which can be calculated using Practical Salinity, temperature, pressure and the computer algorithm of McDougall, Jackett and Millero:

$$S_A = S_R + \delta S_A = S_A(S_P, \phi, \lambda, p), \quad (1.5)$$

where ϕ is latitude (degree North), λ is longitude (degree east, ranging from $0^\circ E$ to $360^\circ E$), S_P is the Practical Salinity, while p is sea pressure and δS_A is the salinity anomaly. Notation S_R here stands for the reference composition of seawater, which is defined as:

$$S_R \approx u_{PS} S_P \quad \text{where} \quad u_{PS} \equiv (35.16504/35) g.kg^{-1} \quad (1.6)$$

According to this definition shown in Equation 1.5, the Absolute Salinity can be accurately measured in laboratory. For the applications, which need the highest accuracy, long-term stability and world-wide comparability of the measured values, the only way to obtain high reliability is by traceability of the measurement results to the primary standards of the International System of Units (SI). From these primary standards, the salinity can be computed via an empirical relation that is very precisely known. The UNESCO/IOC SCOR/IAPSO working group 127 (WG127) proposed several potential candidates for this purpose, one of which is the refractive index.

I.3 Turbidity

I.3.1 Definition of turbidity

Besides the salinity, another important property of seawater is the presence of dispersed, suspended solids - particles not in true solution and often including silt, clay, algae and

other micro-organisms, organic matter and other minute particles. These particles obstruct the transmittance of light through water and impart a qualitative characteristic, called turbidity. The American Public Health Association (APHA) defines turbidity as:

“Turbidity is an expression of the optical property that causes light to be scattered and absorbed rather than transmitted in straight line through the sample.”
[10]

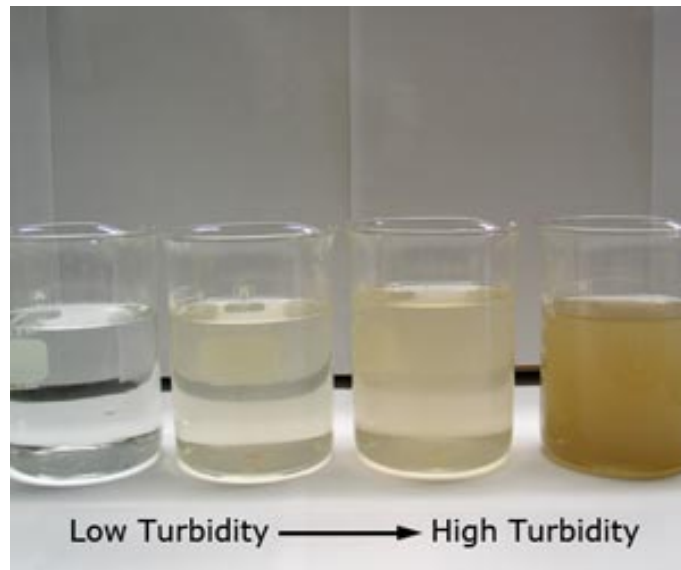


Figure 1.2: Samples of turbidity

Visually, turbidity affects the clarity of water, the measurement of turbidity is a measure of the relative clarity of water. Fig 1.2 shows the different clarity of water with different turbidity. From the definition of turbidity, it is easy to find out the measurement of turbidity is not a direct measure of suspended particles but, instead, a measure of the scattering effect such particles have on light[11]. The scattering effect is the interaction between light and suspended particles. When light is incident on a particle, several processes occur, including reflection, refraction, diffraction and absorption. For particles that are of the order of the wavelength in size or smaller, these processes are referred to as “scattering”. Scattering exists not only in the suspended particles but also the molecules of water. Therefore, there is no solution has a zero turbidity, that’s why the measurement of turbidity is a measure of relative clarity of water rather than the absolute clarity.

I.3.2 Scattering

The basic scattering is the scattering of one single particle. When a directed light meets a particle, one portion of the light is absorbed by the particle, while another portion of light is diffused in all directions. The portion of light flux diffused in different directions is defined by the phase function, denoted as $p(\hat{s}', \hat{s})$, which represents the portion of light flux diffused from direction \hat{s} to direction \hat{s}' . The phase function is related to the size, shape and composition of the particle and to the wavelength of the incident light. Since the phase function is related to the size of the particle and the wavelength of the incident

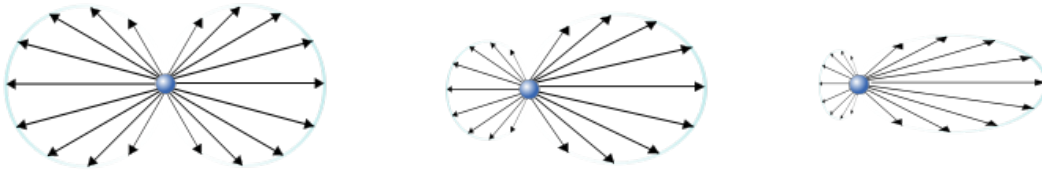


Figure 1.3: Profile of scattered intensity from particles of three sizes

light, a normalized radius $R = \frac{2\pi r}{\lambda}$ was introduced to define the size of the particle r with respect to the wavelength λ . The different scattering patterns from particles of three sizes are depicted in Fig 1.3. The left diagram shows the scattering pattern when the normalized radius $R \ll 1$. In this case, the scattered lights are symmetrically identical in forward and backward. As normalized radius R of particle increases, light scattered from different points of the particle create interference patterns that are additive in the forward direction. This makes the forward-scattered light greater than the backward-scattered light. The middle diagram of Fig 1.3 shows the scattering pattern of a large particle, while the right one is the scattering pattern of a larger particle.

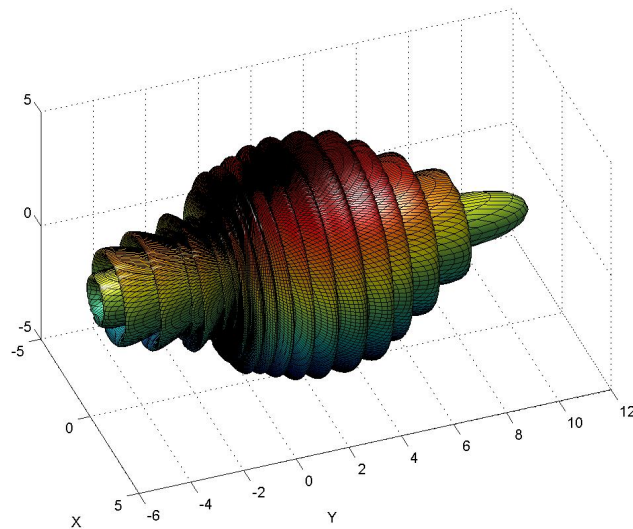


Figure 1.4: Example of 3D Mie scattering angular pattern

Beside the size of particle, the shape and refractive index of particle affect the shape function as well. The scattering distribution of spherical particle is well studied by Gustav Mie[12], who gave an analytical solution of Maxwell's equations for the scattering of electromagnetic radiation by a single spherical particle. This theory is then called the Mie theory. Fig 1.4 is the 3D Mie scattering angular pattern of a particle with radius $2 \mu m$, when a 633 nm incident light passing through it from the left. Special case of the Mie

scattering is the Rayleigh scattering, named after the British physicist Lord Rayleigh, is the elastic scattering of light or other electromagnetic radiation by particles much smaller than the wavelength of the light. The particles may be individual atoms or molecules[13]. The left diagram of Fig 1.3 is one example of Rayleigh scattering. In order for scattering to occur, the refractive index of particle must be different than the refractive index of sample liquid. Since the particle's refractive index determines how it redirects the light passing through it, the scattering becomes more intense when the difference between the particle's refractive index and the refractive index of sample liquid increases.

Another coefficient that impacts the scattering effect is the color of the suspended solids and the sample liquid, because the colored suspended solids and sample liquid absorb light in certain bands of the visible spectrum. This results in the decrease of both the transmitted light and scattered light.

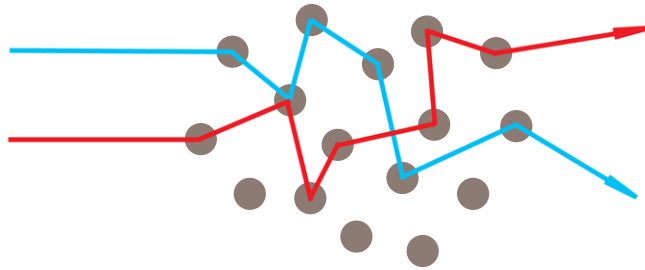


Figure 1.5: Multiscattering example

In a volume of water, the scattering happens in all the suspended particles that interact with the light, thus the total scattered light increases as the number of particle increases. However, this rule is broken when the number of particles exceeds a certain point. For a volume of water with high particle concentration, a scattered light has a high chance to meet another particle to scatter again. This phenomenon is called multi-scattering, shown in Fig 1.5. Multi-scattering acts to reduce the distance traversed by the scattered rays, so that the total scattered light decreases.

1.3.3 Turbidity Standards

Practical attempts to quantify turbidity date to 1900 when Whipple and Jackson[14] developed a standard suspended fluid using 1000 parts per million (ppm) of diatomaceous earth in distilled water. Dilution of this reference suspension resulted in a series of standard suspensions used to derive a ppm-silica scale for calibrating contemporary turbidimeters[11].

Jackson invented a turbidimeter with a special candle and a flat-bottomed glass tube, and calibrated it in graduations equivalent to ppm of suspended silica turbidity. This turbidimeter is then called the Jackson Candle Turbidimeter. The usage of the Jackson Candle Turbidimeter is shown in Fig 1.6. A burned candle is putted under the flat-bottomed tube. The measurement is made by slowly pouring a turbid sample into the tube until the visual image of the candle flame, viewed from the open top of the tube, diffused to a uniform glow. The visual image of the flame disappears when the intensity of the scattered light equalled that of transmitted light. The depth of the sample in the

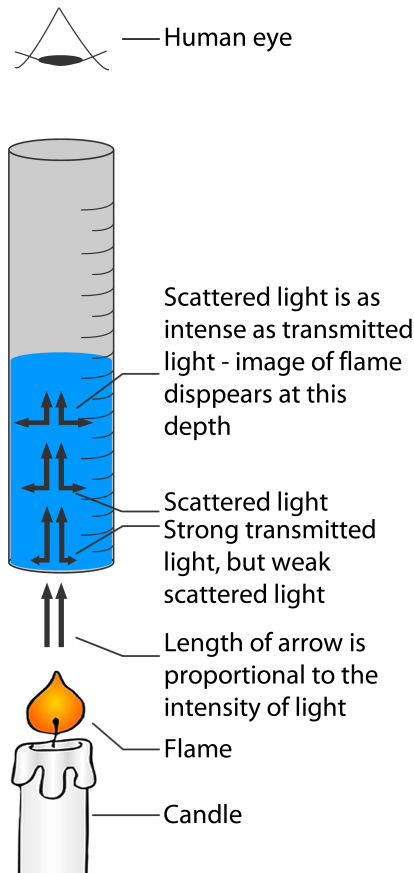


Figure 1.6: Jackson Candle Turbidimeter

tube was then read against the ppm-silica scale, and turbidity was referred to in terms of Jackson Turbidity Units (JTU).

Jackson Candle Turbidimeter was firstly based on standards prepared from material found in nature, such as Fuller's earth, kaolin and stream-bed sediment, making consistency in formulation difficult to achieve. To improve the consistency in formulation, a new suspension for turbidity standards named formazin was developed by Kingsbury and Clark[15] in 1926. It is prepared by accurately weighing and dissolving 5.00 g of hydrazine sulfate and 50.0 g of hexamethylenetetramine in one liter of distilled water. Formazin can be reproducibly prepared from assayed raw materials. Under ideal environmental conditions of temperature and light, this formulation can be prepared repeatedly with an accuracy of $\pm 1\%$. Formazin was first adopted by the APHA and American Water Works Association (AWWA) as the primary turbidity standard material in the 13th edition of *Standard Methods for the Examination of Water and Wastewater* and units of turbidity measurement became known as Formazin Turbidity Units (FTU) .

Even though the consistency of formazin improved the accuracy of the Jackson Candle Turbidimeter, it was still limited in its ability to measure extremely high or low turbidity. What is more, it is dependent on human judgement to determine the exact extinction point, which makes it not practical. In addition, the light source of the Jackson Candle

Turbidimeter is a candle flame, incident light emitted is in the longer wavelength end of the visible spectrum (yellow-red), where wavelength are not scattered as effectively by small particles. The Jackson Candle Turbidimeter is also incapable of measuring turbidity due to black particles such as charcoal because light absorption is so much greater than light scattering that the field of view became dark before enough sample could be poured into the tube to reach an image extinction point.

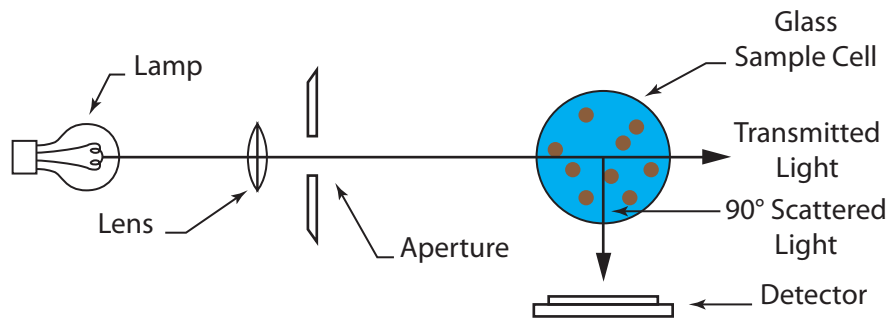


Figure 1.7: Principle of nephelometer

Finally, turbidity measurement standards changed in the 1970's when the nephelometric turbidimeter, or nephelometer, was developed which determines turbidity by the light scattered at an angle of 90° from the incident beam (Fig 1.7). Nephelometry has been adopted by *Standard Methods* as the preferred means for measuring turbidity because of the method's sensitivity, precision, and applicability over a wide range of particle size and concentration. Likewise, the preferred expression of turbidity is in Nephelometric Turbidity Units (NTU).

Other turbidity units include FNU (Formazin Nephelometric Unit) and FAU (Formazin Attenuation Unit) are defined in the international standard ISO 7027[16]. FNU is a unit that applies to nephelometric measurement and FAU refers to a transmitted (or absorbed) measurement. NTUs, FTUs, FNUs and FAUs are all based on the same formazin primary standard.

II Salinity measurement methods

II.1 Conductivity based salinity measurement

The definition of Practical Salinity introduces the salinity measurement from the measurement of electrical conductivity of seawater. To understand this method, it is necessary to study the movement of ions in water and the conductivity.

II.1.1 Definition of conductivity

Conductivity is the ability of a material to conduct electric current. In water, the dissolved ions are conductors. The major positively charged ions are sodium, (Na^+) calcium (Ca^{+2}), potassium (K^+) and magnesium (Mg^{+2}). The major negatively charged ions are chloride (Cl^-), sulfate (SO_4^{-2}), carbonate (CO_3^{-2}), and bicarbonate (HCO_3^-). Nitrates

(NO_3^{-2}) and phosphates (PO_4^{-3}) are minor contributors to conductivity, although they are very important biologically. The measurement of conductivity can therefore evaluate the amount of dissolved salts in water.

The units of conductivity are siemens per meter (S/m), which is identical to the old unit of mho/m. For studying the salinity of the water, the conductivity is usually measured in terms of its resistivity ρ , in the units of ohm meter (Ωm). The conductance G is the inverse of the resistance, $G = \frac{1}{R}$, where R is the resistance. In practice, the measurement of conductivity is the capacity of water to conduct electric current between two electrodes. The conductance of the sample water is inversely proportional to the distance of the two electrodes and proportional to the cross section of the electrodes. We can write:

$$G = \frac{\kappa \tau}{l}, \quad (1.7)$$

where κ represents the conductivity in units of $S.m^{-1}$, τ is the cross section of the electrodes in units of m^2 . The conductivity of a solution depends on the concentration of the electrolytes. Therefore it is convenient to divide the conductivity by concentration. This quotient is termed molar conductivity, is denoted by Λ_m , which equals to

$$\Lambda_m = \frac{\kappa}{c}, \quad (1.8)$$

where c is the concentration of electrolytes. The molar conductivity is in units of siemens meter-squared per mole ($S.m^2.mol^{-1}$)

II.1.2 Conductivity of seawater

As the definition of Practical Salinity, the salinity is calculated from the conductivity C , the temperature t and the pressure p_r :

$$S = f(C, t, p_r) \quad (1.9)$$

However, the calculation of salinity with this equation needs to measure temperature and pressure simultaneously, especially temperature, because the value of conductivity strongly depends on temperature. Due to this dependence, the calculated salinity should be treated by a correction algorithm[17]. The accuracy of salinity calculated from this method depends on the error of the measurement of temperature in unit of $^{\circ}C$, conductivity in unit of mS/cm and pressure in unit of bar.

To follow the specification offered by the WOCE HPO (World Ocean Circulation Experiment Hydrographic Programme Office), several *in situ* measurement instruments were invented, whose performances reach the limit achieved in laboratory. These instruments measure Conductivity, Temperature and Depth of seawater simultaneously, thus called CTD. Despite the name, all CTDs actually measure pressure, which is not quite the same thing as depth. The relationship between pressure and depth is a complex one involving water density and compressibility as well as the strength of the local gravity field. With the CTD data, the practical salinity can be calculated. Some CTDs contain a water sampler to collect water samples for later analysis in the lab. Table 1.1 lists the performance of the state-of-the-art CTD made by SeaBird Electronics. Within the range between 0 and 40 PSU, the uncertainty given by the CTD SBE 9⁺ is about 0.002 PSU, according to Practical Salinity Scale defined in 1978.

The thermosalinometer gives the temperature and salinity of water pumped under the surface, accurate to about a hundredth [18]. It is composed of a cell with electrodes which

Table 1.1: Characteristic of CTD SBE 9⁺ made by SeaBird Electronics, Inc

	Range	Initial Accuracy	Resolution	Time Response
Temperature	-5 to +35°C	0.001°C	0.0002°C	0.065 s
Conductivity	0 to 7 S/m	0.0003 S/m	0.00004 S/m	0.065 s
Pressure	0 to full scale	0.015% of full scale	0.001% of full scale	0.015 s

determine sea water's conductivity. Thermistors measure the water temperature in the cell and near the hull. This instruments allows us to calculate the salinity of surface seawater with an accuracy of a hundredth for each parameter. Other instruments like the *expendable bathythermograph* (XBT) can obtain a record of temperature as a function of depth from a moving ship. Some XBTs also measure conductivity, allowing salinity to be computed, is termed an XCTD[19]. Such devices can provide an accuracy of 0.01 *mS/cm* for conductivity and 0.01 °C for temperature[20].

The biggest problem of conductivity sensor is long time measuring under seawater: the fouling, which can consist of either living organisms (biofouling) or a non-living substance (inorganic or organic). This phenomenon influences the accuracy of the conductivity sensor and can not be easily corrected.

II.1.3 Conductivity sensors

For measuring the conductivity of electrolytic solutions, there are, in principle, three groups of sensor[21]:

1. classical conductivity cells containing two or more electrodes
2. inductive conductivity sensors containing one or two transformers
3. capacitive conductivity sensors

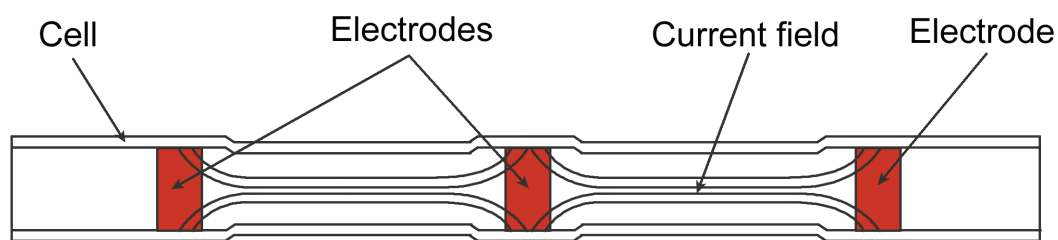


Figure 1.8: Conductivity sensor SBE 4 (SeaBird Electronics, Inc.)

In oceanography, the third type is not used, whereas the first and second type have found broad applications.

Among the classical conductivity cells with electrodes, the SBE 4 series conductivity sensors from SeaBird Electronics are the most advanced ones (Fig.1.8). These sensors consist of a glass tube with three platinum rings, deposited at 50 mm distance and forming the electrodes. Fig.1.8 shows a two-terminal cell in which the electrode resistances are in series with (and indistinguishable from) the cell resistance proper. Because the electrode resistances are low and the cell resistance high, errors resulting from changes in the electrode

resistances are small. The outer electrodes are connected together to confine electric fields inside the cell, making the measured resistance (and instrument calibration) independent of calibration bath size or proximity to protective cages or other objects. The fouling has a big impact to this kind of conductivity sensor. The deposit caused by fouling reduces the internal diameter of the cell, and modifies the cell constant K (a constant to calculate the electrical resistance R [20]).

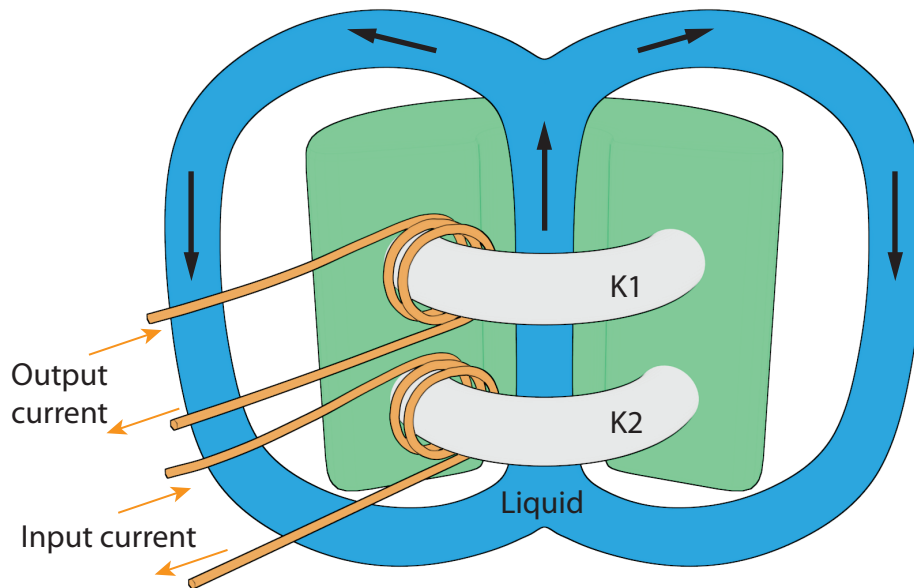


Figure 1.9: Principle of inductive conductivity sensor

Other than the classical conductivity cells with electrodes, inductive conductivity is based upon the creation of a magnetic field that results in an electrical voltage in a liquid. This method (Fig 1.9) has advantages since it requires no direct contact with the liquid. This type of conductivity sensor is based upon the creation of a magnetic field between two parallel electric coils. The coils are sealed in a doughnut-shaped housing. The transmitting coil $K1$ generates an alternating field that results in voltage in the liquid. The ionic content allows the current to flow to drive the current in the receiving coil $K2$.

II.2 Refractometer based salinity measurement

Since optic technology has been developed for years, it has been widely used in different applications, one of which is to measure physical parameters. The seawater refractive index varies proportionally to density, which is strongly correlated with salinity; therefore, the measurement of seawater refractive index can be used to measure its absolute salinity. In oceanography, several pioneers tried to study the the refractive index of seawater[22, 23, 24]. Based on the statistic of different seawater refractive indexes, they built the expression for the refractive index of seawater in a function of seawater temperature t , pressure p_r , salinity S , and wavelength λ . This makes the measurement of seawater salinity from its refractive index possible. Based on this theory, several optical salinity sensors have been studied.

Modern refractive index based salinity sensors are based on the publication of R.C. Millard and G. Seaver[24] in 1990. They studied the refractive index of seawater in 428

places and built the relationship between the refractive index and the salinity from an optimal mathematical model that fits the experimental data as the following equation:

$$n(T, p_r, S, \lambda) = n_I(T, \lambda) + n_{II}(T, S, \lambda) + n_{III}(T, p_r, \lambda) + n_{IV}(T, p_r, S), \quad (1.10)$$

which has 27 terms, grouped to 4 groups labelled n_I , n_{II} , n_{III} , and n_{IV} . A full form of this equation can be found in appendix A. This equation describes the refractive index of seawater as a function of seawater temperature t , pressure p_r , salinity S , and wavelength λ . This equation is valid under the condition: $0 < T < 30^\circ C$, $0 < p < 100 Mpa$, and seawater density ρ is in the range of 0 and $1045 kg.m^{-3}$. With a light source of wavelength from 0.5 to $0.7 \mu m$, the uncertainty of refractive index n calculated by this equation varies from 4×10^{-7} to 8×10^{-5} .

Since the equation 1.10 is an optimized fitting result of the sample refractive indexes (for example, the Least Squares Regression (LSR)), it might vary when new seawater sample data is added into the sample set. For instance, considering the exploitation of experimental data on the refractive index (N) obtained originally by Mehu and Johannin-Gilles (1968)[25] and extrapolated by Austin and Halikas[26] in 1979, the absolute standard deviation on the refractive index obtained with this algorithm is not constant with the various studied parameters (T, p_r, S, λ) and can vary from 4×10^{-7} for distilled water at atmospheric pressure to 8×10^{-5} for seawater at high pressure. As a consequence, in order to obtain a high accurate salinity sensor, it is necessary to improve equation 1.10, which requires a more accurate refractive index measurement.

II.3 Some refractive index measurement methods

The study of refractive index measurement has been carried out for many years[22, 27, 28, 29, 30, 31]. They can be categorized into four categories:

1. refractometer based methods
2. interferometer based methods
3. fiber Bragg grating based methods
4. surface plasmon based methods

II.3.1 Refractometer based methods

Ernst Abbé firstly designed his refractometer in 1869[32]. In 1874, he published a comprehensive booklet[33] where he discusses the theory and describes instruments for the measurement of refractive index using prisms and by total reflection. But it didn't become commercially available from Carl Zeiss before 1881. It's original design was so successful that even as of today it is over 141 years old, it is still used and copied in new devices. The principle of abbé refractometer is shown in Fig 1.10 (a). Basically, the abbé refractometer is based on the critical angle. Sample is put into the illuminating prism and the measuring prism. The light source emits the light, which enter the sample from the illuminating prism. These lights are refracted at critical angle at the bottom surface of measuring prism, and then a telescope is used to measure position of the border between bright and light areas. With the border position, the angle and the refractive index of the prism, the refractive index of the sample can be calculated easily. Fig 1.10 (b) is the abstract principle of abbé

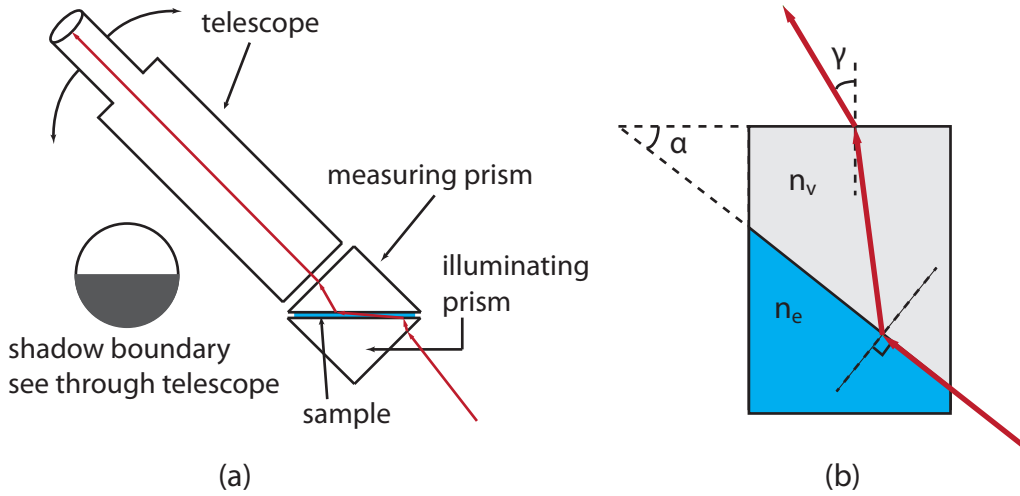


Figure 1.10: Principle of abbé refractometer

refractometer. According to this configuration, the refractive index of the sample n_e is a function of the refractive index of prism n_v , the angle of the prism α , and the observation angle γ .

$$n_e = \sin(\alpha) \sqrt{n_v^2 - \sin^2(\gamma)} + \cos(\alpha) \times \sin(\gamma) \quad (1.11)$$

A variety of other instruments have been derived from the original Abbé design. K.H. Mahrt and C. Waldmann[34] used a CCD (Charge-Coupled Device) to measure the angle α in equation 1.11. They put all the optics and electronics into a 53.6 cm long cylinder with a diameter of 5 cm. According to this paper, The accuracy of measured refractive index n reaches 1×10^{-6} with a sampling rate of 1000 times per second. Although this method provides a high resolution, it highly depends on the dimension of the sensor, which can not fulfil the requirement of a compact *in situ* sensor.

In 1987, Seaver[24] began developing a critical wavelength refractometer (CWR) to measure the absolute index of refraction of seawater to 2×10^{-5} . This invention was applied to Seaver's well-known equation of refractive index. In 1989, Minato[23] has made a laboratory instrument for measuring the refractive index value. According to his study, a remote refractive index difference meter was designed and tested for use as a salinity sensor.

The principle of Minato's method is to measure the difference between the real seawater's index and the standard seawater's as shown in Fig.1.11. The beam from a laser diode transmits through an optical fiber cable and is incident almost normally on the front window of the sample cell. The sample cell is divided into two partitions; one contains the reference, the other the sample seawater. The laser beam that passes through the reference water in the sample cell finally refracted out of the sample cell at the surface of the reference and sample seawater. A Position Sensitive Device (PSD) is used to detect the laser beam deviation caused by the refraction. This method achieves a refractive index resolution of 4×10^{-6} , which is not sufficient in our case.

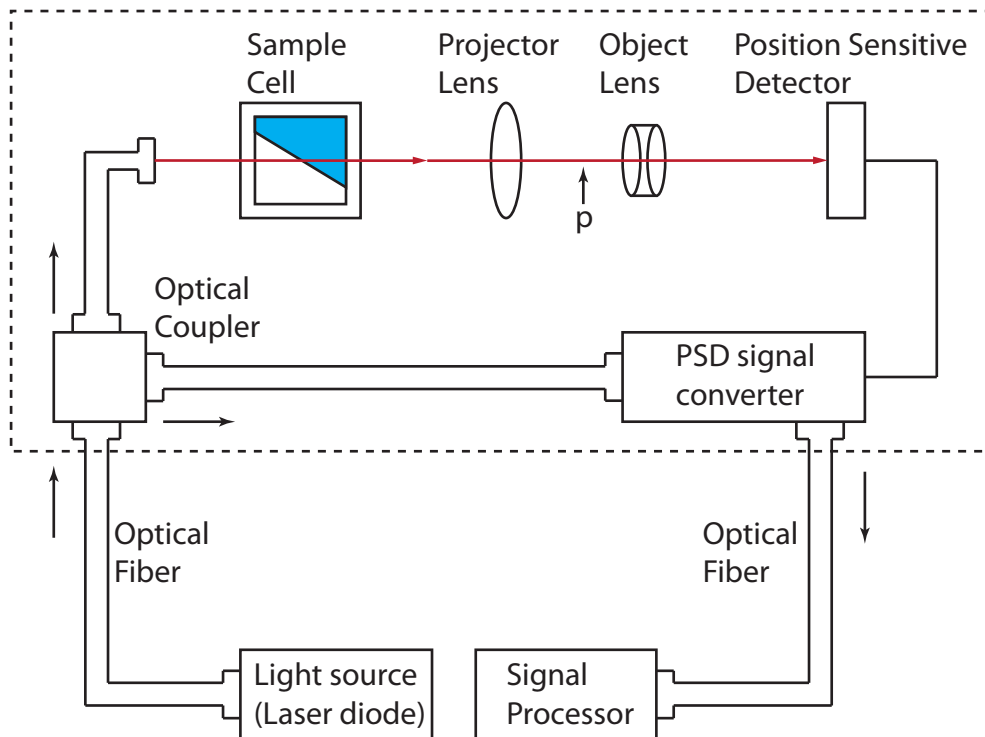


Figure 1.11: Setup for remote measurement of difference of refractive index

II.3.2 Interferometer based methods

The refractometer based methods refract light to make the measurement, in contrary, there exists another popular refractive index measurement method which measures the difference in speed of the light in different media - interferometer based refractive index measurement. Interferometric measurement has been developed for several years and has been used to measure the refractive index. The interferometer based refractive index measurement methods have a great advance in measurement accuracy compared to the refractometer based on measuring the critical angle or the one relying on detecting the laser beam displacement[35]. However, this method is very sensible to the variation of temperature and vibration.

In 1989, Barn *et al.*[27] have developed a grating interferometer with extremely high stability and applied the interferometer to measure the refractive index. Moosmuller[28] developed a novel two-beam Jamin interferometer for the measurement of a refractive index in 1996. Both of these two methods reached a high accuracy of refractive index (1×10^{-8}).

Marc Le Menn[36, 37] developed another interferometer based on the cube-capillary. By applying this technology to the refractive index measurement, it obtained a standard deviation in an order of 5×10^{-6} .

Singer[38] used a new method which measures the phase change on translation normal to the beam propagation in one arm of a Michelson interferometer of a compensating double wedge filled with the two liquids. The resolution of his method to measure the refractive index is in an order of 10^{-6} . Richerzhagen[39] measured the absolute refractive index of liquid water as a function of temperature at a wavelength of $1.064 \mu\text{m}$ by using

Michelson interferometer as well. His method obtained an accuracy of 2×10^{-4} when the temperature is in the range of 20°C and 60°C . The principle of this interferometer based refractive index measurement is shown in Fig 1.12.

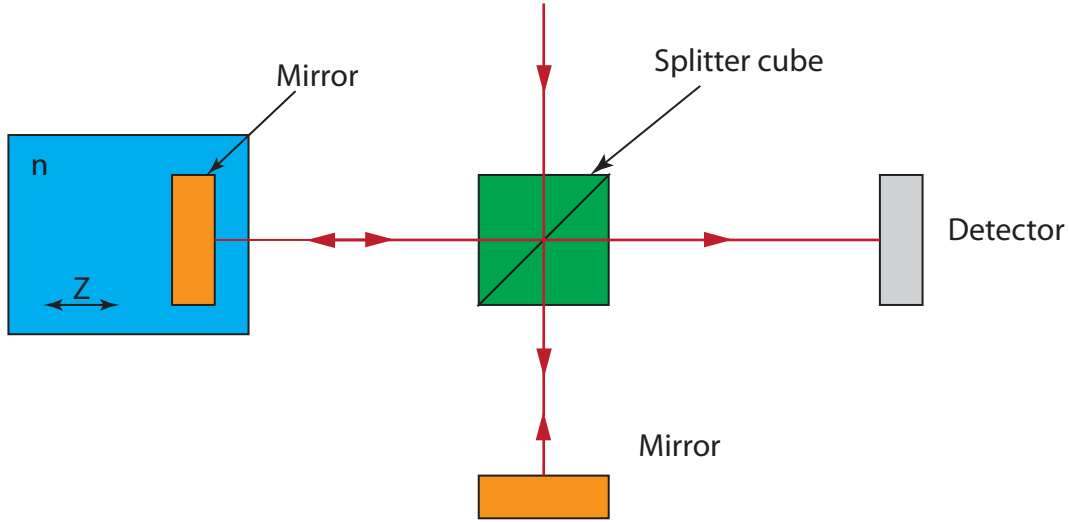


Figure 1.12: Principle of the refractive index measurement based on the Michelson interferometer

The most recent interferometer based refractometer obtain a high resolution on refractive index (10^{-7}). Suhadolnik[40] developed a new type of optical fibre interferometric refractometer consists of an optical fibre Mach-Zehnder interferometer and a Michelson interferometer. The Mach-Zehnder interferometer was used to measure the optical path length difference of the moving sample, while the Michelson interferometer measures the liquid sample displacement in air.

II.3.3 Fiber Bragg grating based methods

The Fiber Bragg Grating has been proved to be efficient for passively detecting the environment change caused by distortion or temperature[41]. The advantages of grating-based sensors are well known. High sensitivity, intrinsic codify of the measured parameter in an absolute parameter, multiplexing capabilities and very low cost are only few of them. The principle of operation relies on the dependence of the Bragg resonance on effective refractive index and the grating pitch. Fig 1.13 shows this operation principle. A fiber Bragg grating is a periodic or aperiodic perturbation of the effective refractive index in the core of an optical fiber. The refractive index perturbation leads to the reflection of light (propagating along the fiber) in a narrow range of wavelengths, for which a *Bragg condition* is satisfied:

$$\lambda_B = 2n_e\Lambda, \quad (1.12)$$

where Λ is the grating period, λ_B is the vacuum wavelength, and n_e is the effective refractive index of light in the fiber. Essentially, the condition means that the wave number

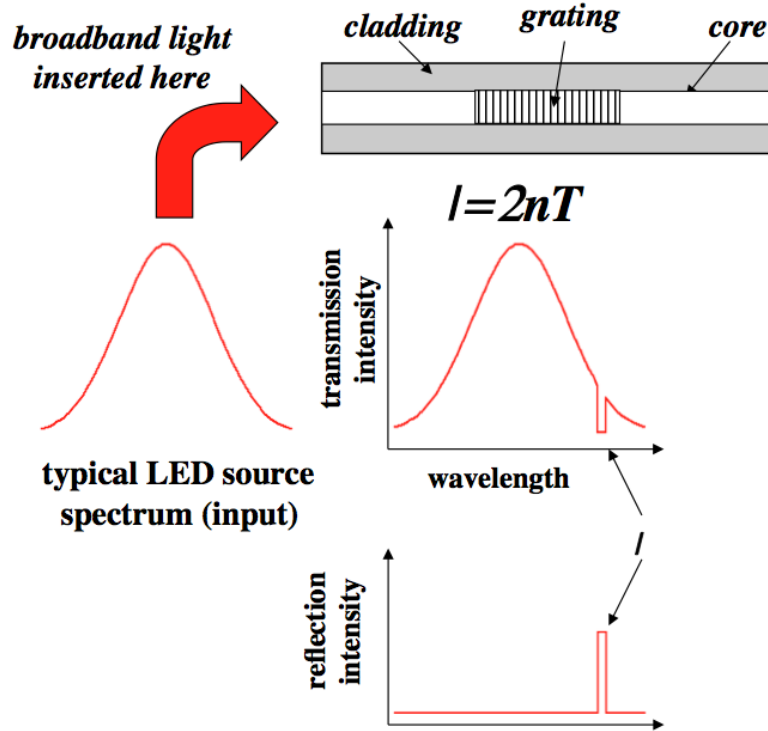


Figure 1.13: Principle of Fiber Bragg Grating

of the grating matches the difference of the (opposite) wave vectors of the incident and reflected waves.

Since the effective refractive index is not influenced by the external one for standard optical fibers, no sensitivity to external refractive index is expected. However, if fiber cladding diameter is reduced along the grating region, the effective refractive index is significantly affected by external refractive index. As a consequence, shifts in the Bragg wavelength combined with a modulation of the reflected amplitude are expected. Based on this principle, A. Iadicco *et al.*[42] developed a method to measure the refractive index with the resolution of 10^{-5} . In their method, three layer model for the thinned optical fiber has been used to identify the dependence of the effective refractive index from the external one.

Another method to make the refractive index influenced by the external one is to tilt the grating, so that the portion of light wave will transmit into cladding as shown Fig 1.14. This method is thus called Tilted Fiber Bragg Grating (TFBG). TFBGs are spectrally sensitive to the refractive index of the medium surrounding the fiber's cladding, therefore they are used for refractometry[43].

A. Iadicco[44] developed a new refractometer by utilising the micro-structured fiber Bragg grating. The proposed structure relies on a partial and localized etching of the cladding layer along a standard grating. The main spectral changes of the structured grating are the increasing of the stopband and the formation of a narrow allowed band strongly dependent on the etching features and the surrounding refractive index. The resolution of this method reaches 4×10^{-5} .

In conclusion, the measurement of refractive index based on the fiber Bragg grating

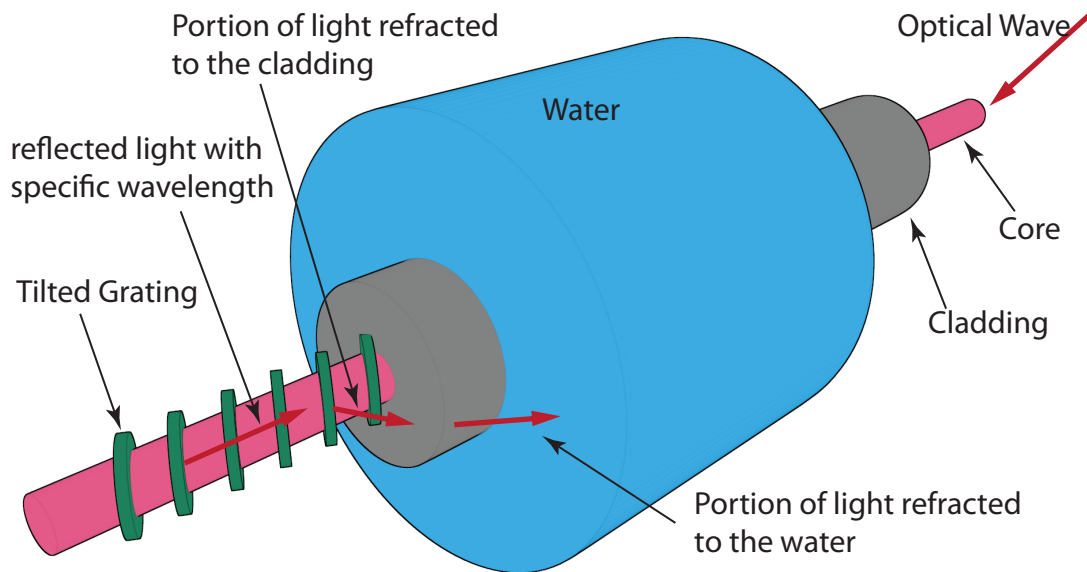


Figure 1.14: Measurement of refractive index with Tilted Fiber Bragg Grating (TFBG)

have been used in a variety of environmental and chemical applications. However, the resolution of the fiber Bragg grating based methods reaches about 10^{-5} , which is not sufficient for our seawater salinity measurement.

III Turbidity measurement methods

Turbidity can be interpreted as a measure of the relative clarity of water. It is not a direct measure of suspended particles in water but, instead, a measure of the scattering and attenuation effects these particles have on light. The higher the intensity of the scattered or attenuated light, the higher the value of turbidity. Since the light is scattered to all the direction, the scattered light can be measured at different angle. According to the measurement angle, the turbidity measurement methods can be categorized into four categories: transmissometer, backscatter, nephelometric scatter, and multi-angle measurement. Fig 1.15 shows the different kinds of measurement method.

Two factors highly affect the scattering, which might further affect the measurement of turbidity:

Absorption: samples containing particles that strongly absorb incident light will prevent a significant portion of this light from reaching the detection system. This will result in an artificially low turbidity value.

Wavelength: light scatter depends on the size of the particle and the wavelength of light interacting with that particle.

In this section, we introduce several state-of-the-art turbidity measurement method in different categories.

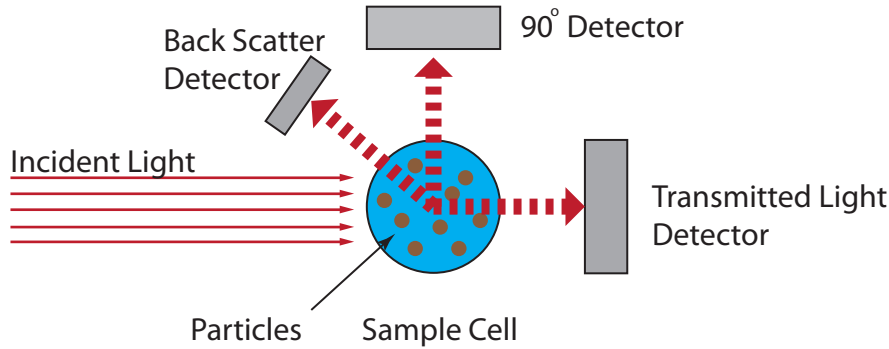


Figure 1.15: Different turbidity measurement methods

III.1 Transmissometer

The first practical turbidimeter, Jackson Candle Turbidimeter, measures the light extinction caused by the scattering. Based on the Jackson Candle Turbidimeter, several visual extinction turbidimeters were developed with improved light source and high sensitivity photoelectric detectors. All these turbidimeters measure the light intensity at an angle called attenuated detection angle, which is geometrically oriented at an angle that is 180-degrees relative to the incident light beam. These kinds of device has another name, called transmissometer. The transmitted intensity measured at the attenuation detection angle is not only depending on scattering but also absorption. This relationship can be expressed as:

$$I_{tran} = I_{inc} e^{-\rho(\sigma_{abs} + \sigma_{scatt})l}, \quad (1.13)$$

where I_{tran} , I_{inc} are the transmitted light intensity and incident light intensity respectively, while σ_{abs} and σ_{scatt} are absorption coefficient and scattering coefficient. l here stands for the distance the light passed in the medium and ρ is the density of the particles. The absorption coefficient σ_{abs} represents the portion of light absorbed by a particle and the scattering coefficient σ_{scatt} is the portion of light that scattered by the particle. According to this equation, this detection angle measures the attenuation of the incident light beam due to both light scattering and absorption, so that it has the greatest susceptibility to absorbance and color interferences[45]. Another drawback of this method is its limitation in measuring high or extremely low turbidity. At low scattering intensities, the change in transmitted light was so small that it is virtually undetectable by any means. Typically, the signal was lost in the electronic noise. At high concentrations, multiple scattering results in the equation 1.13 no longer stands, which makes this method lead to large error. In Fig. 1.16, curve marked solid diamond shows the relationship between the transmitted light intensity and the turbidity.

III.2 Backscatter method

To solve the limitation of measuring the turbidity in high turbidity, another angle called the backscatter detection angle has been used, which is geometrically centered at an angle of between 0 and 45 degrees relative to the directional centerline of the incident light beam as shown in Fig. 1.15. This angle is sensitive to scattering light that is reflected back in the

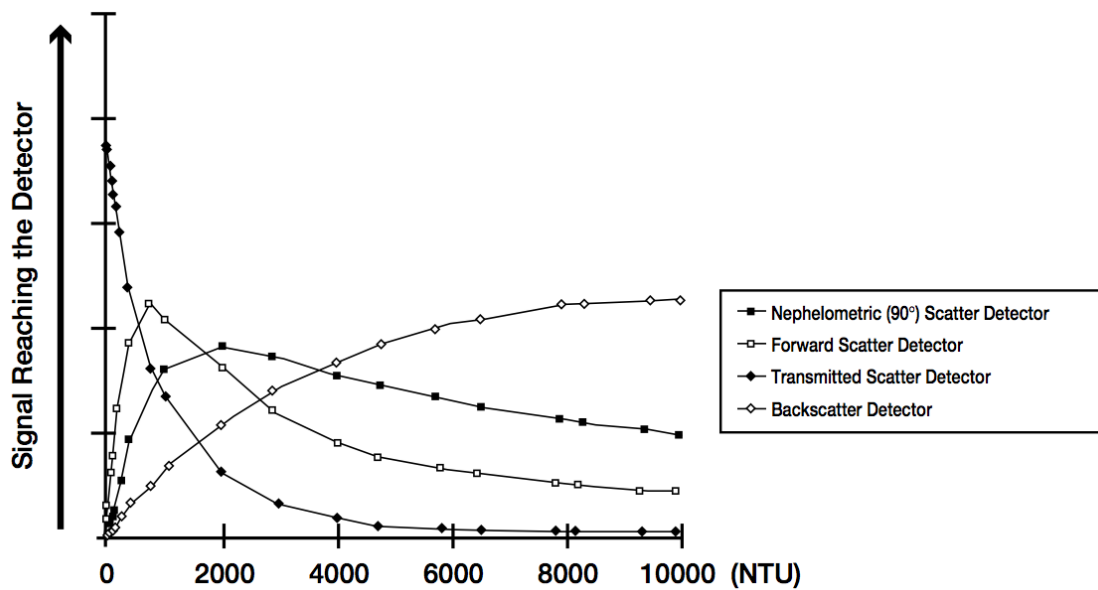


Figure 1.16: The relationship of turbidity and scattered light at different angles

direction of the incident light source. As the reflected light is more easily detected in the extremely high turbidity samples, this method is specially useful in a high turbid medium. However, it is not an appropriate technique for low level turbidity monitoring because it has inherent poor sensitivity at these levels.

III.3 Nephelometric (90°) scatter method

Besides the limitation of measuring high turbidity, the transmissometer is not sensitive in ultra low turbidity. To solve these problems, a 90-degree detection angle (90°) is used. This angle is often referred to as the nephelometric detection angle and is the most common detection angle because of its sensitivity to a broad range of particle sizes. The turbidimeter based on this method is called the Nephelometer. Due to the advantage of nephelometric scatter method, it is adopted as the turbidity measurement standard. Two sets of design criteria have been generally accepted for performing turbidity measurement. These methods, USEPA Method 180.1 and ISO Method 7027, have been used as part of the measurement requirement guidelines for regulatory compliance.

USEPA Method 180.1

USEPA Method 180.1 is the most common regulatory method used in the world. It is referenced to Standard Methods for the Examination of Water and Wastewater Method 2130B. The following design criteria are required with USEPA Method 180.1:

- The primary detector must be for nephelometric (90 degree) measurement ± 30 degrees.
- The light source must be a tungsten filament lamp with a color temperature between 2200 and 3000 K.

- The spectral response peak for the detector must be between 400 and 600 nm, the primary wavelengths of light.
- The measurement range is from 0 to 40 NTU. Any sample above this range must be diluted until it is within this range.

Method 180.1 has several advantages:

- The method uses short wavelengths of light that are more sensitive to scattering by small particles.
- Tungsten lamps emit light that is nine times more effectively scattered by small particles than the 860 nm light source.
- The method is most applicable in clean water samples, below 1.0 NTU.
- Tungsten lamps are readily available and inexpensive.
- The method is well-documented and widely understood.

Two drawbacks to this method exist. First, it is sensitive to interference from color that absorbs light in the wavelength range of 400-600 nm. Second, the tungsten light sources require lengthy warm-up times in order to achieve short term stability and must be calibrated frequently. Compliance with the drinking water regulations using USEPA Method 180.1 require only the measurement of low turbidity levels. In the past, the final effluent water in drinking water plants must have a turbidity less than 0.5 NTU 95% of the time, with a maximum level of 2 NTU. In 1998, this regulation tightened to a turbidity of 0.3 NTU 95% of the time, with a 1.0 NTU maximum turbidity level. Many water treatment plants have subscribed to the Partnership for Safe Drinking Water, which imposes a maximum turbidity level of 0.1 NTU. At these levels, instruments must measure accurately, and discrepancies between instruments should be known.

ISO 7027

ISO Method 7027 originated in the brewing industry and is commonly used in Europe. The method has been accepted for regulatory reporting in water since the 1980s. The following design criteria are required with ISO Method 7027:

- The primary detector must be for nephelometric (90 degree) measurement, ± 1.5 degrees.
- The light source must be at a wavelength of 860 nm. An LED or a combination of tungsten filament lamps with filters can be used to achieve this wavelength.
- The spectral bandwidth of the light must be within 860 nm ± 30 nm. The wavelength at this range is less susceptible to color interferences, makes this method good for samples with color and low level monitoring.
- The measurement range is from 0 to 40 NTU. Any sample above 40 NTU must be diluted until the measurement is within this range.

The strengths of ISO Method 7027 include the use of a near-monochromatic light source that is stable, has low absorbance interference with samples, and results in low stray light. The major drawback of using the long wavelength source is its reduced sensitivity to small

particle sizes. The reduced sensitivity can be amplified but this will result in increased measurement noise at low turbidity levels. At the low end of the measurement range, instruments using this method tend to read slightly lower than those using USEPA Method 180.1. Regulatory compliance for water treatment plants requires accurate measurements at the very low turbidity range.

No matter which standard is used, the turbidity value can be obtain from the measured light intensity at 90° by following equation:

$$T = a_0 I_{90}, \quad (1.14)$$

where T is the turbidity in NTU units, a_0 is the calibration coefficient, and I_{90} is the light intensity measured at 90° .

III.4 Multi-angle method

As discussed before, the measurement of turbidity at different angles has different benefits and drawbacks. The method based on the transmitted light is simple, efficient, and wide measurement range, however, it is impacted by the absorption so that insensitive in ultra low level turbidity and high level turbidity case. The backscatter method is suitable for the high turbidity case, but not a proper method for low level turbidity monitoring. Although the 90-degree measurement is very sensitive to particle scatter and provides the ability to measure low level turbidity, its performance is still influenced by the sample color.

According to the introduction of the two nephelometer standard USEPA Method 180.1 and ISO 7027, the performance dependent is primarily due to the light source. To avoid the effects caused by the light source, a new design of turbidimeter, which is based on a nephelometer and measures the scattering at multiple angles, is developed and called the ratio turbidimeter. Fig 1.17 shows the state-of-the-art ratio turbidimeter 2100AN of Hach.

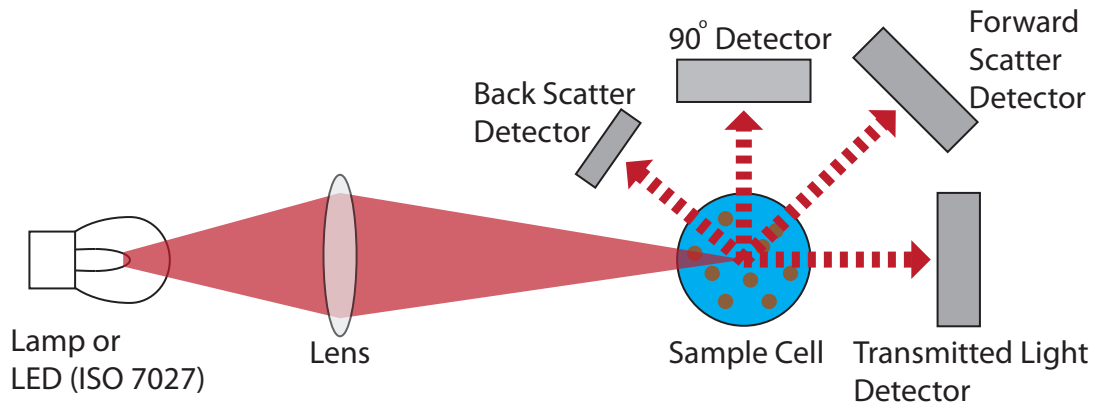


Figure 1.17: Optical design of Hach ratio turbidimeter 2100AN

The turbidity value is derived by ratioing the nephelometric signal against a weighted sum of the transmitted and forward-scattered signals. Some design also includes a backscattering signal to improve the performance in ultra high turbid medium. In this case, the turbidity can be obtained by a calibration algorithm defined as:

$$T = \frac{I_{90}}{d_0 I_t + d_1 I_{fs} + d_2 I_{bs} + d_3 I_{90}}, \quad (1.15)$$

where T is the turbidity in NTU units, d_0, d_1, d_2 and d_3 are calibration coefficients need to be calibrated. I_t is the transmitted light intensity, I_{fs} is the forward scatter light intensity, I_{bs} is the backscatter light intensity, and I_{90} is the light intensity captured at 90° .

At low or moderate turbidity levels, the forward-scattered signal is negligible in comparison to the transmitted signal, so that the calibration coefficient d_1 is set to 0. Similarly, The back-scattered signal can be ignored in low turbidity level. Thus, the turbidity value can be measured only by the light intensity of 90° and the transmitted one. Equation 1.15 thus can be expressed as:

$$T = \frac{I_{90}}{d_0 I_t + d_3 I_{90}}, \quad (1.16)$$

As the turbidity increases, the effect of multiple scattering can not be ignored any more. This multiple scattering acts to reduce the distance traversed by the scattered rays, while it can only increase the distance traversed by transmitted rays. The results is that the transmitted light is more attenuated than the scattered light at high turbidities, causing the calculated turbidity value turns to be larger than the actual value. In this case, the forward-scattered light is used to compensate the lose of transmitted light. Another algorithm for high turbidity case is written as:

$$T = \frac{I_{90}}{d_0 I_t + d_1 I_{fs} + d_3 I_{90}}, \quad (1.17)$$

Since back scatter method is specially suitable for ultra high turbidity level. A back scatter detector is used for measuring the ultra high turbidity, when the other detector go blind, which forms the equation 1.15.

Conclusion

As a branch of oceanography, physical oceanography studies the physical properties and dynamics of the ocean. The study of physical oceanography requires different high-resolution measurement instrument to measure different physical properties of seawater, e.g. turbidity, salinity, temperature, and pressure, etc. Current researches have found that all these physical properties are tightly connected to each other to affect the different oceanographic phenomenons. This makes the research of *in situ* multi-sensors valuable. Under this context, the integration of the salinity and turbidity measurement into one compact *in situ* sensor is a very interesting topic in oceanography. This chapter introduces state of the art technologies in salinity and turbidity measurement.

The first part of this chapter summarizes the research interests of physical oceanography and its methodology. Among the physical properties that interest physical oceanography, we pay special attention to two of them: salinity and turbidity. The definition of both salinity and turbidity are reviewed at the beginning of this part, e.g. the conductivity of seawater associated with the temperature defines the Practical Salinity Scale and The chemical material Formazin became the primary standard of turbidity. This part emphasises the importance of measuring the refractive index of seawater to calculate the seawater practical salinity. For the introduction of turbidity, the standard method - nephelometer, is highlighted at the end of this part.

The second part of this chapter reviews different methods of measuring seawater refractive index and turbidity. The sensors based on the fiber Bragg grating and the sensors based on surface plasmon have improved the sensibility of measuring refractive index, however, they are still not sensible enough to achieve the requirement of the *in situ* measurement. Interferometer based refractive index measurement can reach the highest accuracy, but it is very sensible to the variation of temperature and vibration as well. What is more, this kind of method requires a very sophisticated signal processing technique. All these issues make this methods hard to integrate with other sensors. Compared to these methods, refractometer based on the measurement of laser beam displacement can be designed to have a high refractive index measurement resolution in a compact optical system. For the turbidity measurement, transmissometer with modern photoelectric detectors became popular to measure the attenuation of transmitted light. It is easy to integrate into a compact sensor and provides high precision except in extremely low and extremely high situation. Based on the fact that the scattered light is much more stable than the transmitted light, nephelometer, the standard methods defined by USEPA Method 180.1 and ISO 7027 measure the diffused light at 90°. Although nephelometer standard improved the accuracy, it still meets large uncertainty at high turbidity level. Another issue of nephelometer standard is that the requirement of the standard makes it not easy to integrate the standard into a compact sensor. A more sophisticated method, ratio nephelometer, further improves the adapted measurement range of nephelometer. However, this method needs multiple photoelectric detectors, which results in the difficulty to integrate into a compact *in situ* sensor as well.

Bibliography

- [1] R.H. Stewart. *Introduction to Physical Oceanography*. University Press of Florida, 2009.
 - [2] Forchhammer and Georg. On the composition of sea-water in the different parts of the ocean. *Philosophical Transactions of the Royal Society of London*, 155:pp. 203–262, 1865.
 - [3] William J. Wallace. *The development of the chlorinity/salinity concept in oceanography*. Elsevier Science Ltd, 1974.
 - [4] M. Knudsen, C. Forch, and S.P.L. Sørensen. *Bericht über die chemische und physikalische Untersuchung des Seewassers und die Aufstellung der neuen hydrographischen Tabellen*. 1902.
 - [5] L.D. Talley, G.L. Pickard, W.J. Emery, and J.H. Swift. *Descriptive Physical Oceanography*. Elsevier Science, 2011.
 - [6] E. L. Lewis. The practical salinity scale of 1978 and its antecedents. *Marine Geodesy*, 5(4):350–357, 1982.
 - [7] Unesco. The international system of units (si) in oceanography. *Marine Science*, 45:133, 1985.
 - [8] Jackett, David R., Trevor J. McDougall, Rainer Feistel, Daniel G. Wright, and Stephen M. Griffies. Algorithms for density, potential temperature, conservative temperature, and the freezing temperature of seawater. *J. Atmos. Oceanic Technol*, 23:1709–1728, 2006.
 - [9] IOC, SCOR, and IAPSO. The international thermodynamic equation of seawater – 2010: Calculation and use of thermodynamic properties. 2010.
 - [10] APHA, AWWA, and WPCF. Standard methods for the examination of water and wastewater. pages 2–12, 1989.
 - [11] Michael J. Sadar. Turbidity science. *Technical Information Series, Booklet 11, Hach Company*, 1998.
 - [12] G. Mie. Beiträge zur optik trüber medien, speziell kolloidaler metallösungen, leipzig. *Ann. Phys.*, page 377, 1908.
 - [13] Victor Twersky. Rayleigh scattering. *Appl. Opt.*, 3(10):1150–1150, Oct 1964.
 - [14] Whipple and Jackson. *M.I.T. Quarterly*, 13:274, 1900.
 - [15] Williams Kingsbury, Clark and Post. *J. Lab. Clin. Med*, 11:981, 1926.
 - [16] Iso7027: Water quality - determination of turbidity. *International Standard*, 1999.
 - [17] J-P. Girardot. Capteur et instrumentation utilisés en océanographie physique. Nov. 2002.
 - [18] Ifremer. Thermosalinometer, 2011. http://www.ifremer.fr/fleet/equipements_sc/eq/thermosalinometre.htm.
-

- [19] Wikipedia. Expendable bathythermograph, 2011. http://en.wikipedia.org/wiki/Expendable_bathythermograph.
 - [20] M.L. Menn. *Instrumentation et métrologie en océanographie physique*. Collection Capteurs et instrumentation. Hermès science publications-Lavoisier, 2007.
 - [21] A. Hyldgard, I. Olafsdottir, M. Olesen, T. Hedegaard, O. Hansen, and E.V. Thomsen. Fish amp; chips: Four electrode conductivity / salinity sensor on a silicon multi-sensor chip for fisheries research. In *Sensors, 2005 IEEE*, pages 1124 –1127, 30 2005-nov. 3 2005.
 - [22] G. Seaver. The optical determination of temperature, pressure, salinity and density in physical oceanography. *Marine Technology Society journal*, (2):69–79, 1987.
 - [23] H. Minato, Y. Kakui, A. Nishimoto, and M. Nanjo. Remote refractive index difference meter for salinity sensor. *Instrumentation and Measurement, IEEE Transactions on*, 38(2):608 –612, apr 1989.
 - [24] G. Seaver R. C. Millard. An index of refraction algorithm for seawater over temperature, pressure, salinity, density, and wavelength. *Deep-sea research. Part A. Oceanographic research papers*, (12):1909–1926, 1990.
 - [25] A. Mehu and A. Johannin-Gilles. Variation de la réfraction spécifique de l'eau de merétalon de copenhagen et de ses dilutions en fonction de la longuerr d'onde, de la température et de la chlorinité. *Deep Sea Research and Oceanographic Abstracts*, 16(6):605 – 611, 1969.
 - [26] G.Halikas R. W. Austin. The index of refraction of seawater. *SIO Ref 76-11 Scripp Institution of Oceanography*, 1979.
 - [27] Thomas H. Barnes, Kenji Matsumoto, Tomoaki Eiju, Kyofumi Matsuda, and Noatake Ooyama. Grating interferometer with extremely high stability, suitable for measuring small refractive index changes. *Appl. Opt.*, 30(7):745–751, Mar 1991.
 - [28] H. Moosmüller and W. P. Arnott. Folded jamin interferometer: a stable instrument for refractive-index measurements. *Opt. Lett.*, 21(6):438–440, Mar 1996.
 - [29] M C Phan Huy, G Laffont, Y Frignac, V Dewynter-Marty, P Ferdinand, P Roy, J-M Blondy, D Pagnoux, W Blanc, and B Dussardier. Fibre bragg grating photowriting in microstructured optical fibres for refractive index measurement. *Measurement Science and Technology*, 17(5), 2006.
 - [30] Claes Nylander, Bo Liedberg, and Tommy Lind. Gas detection by means of surface plasmon resonance. *Sensors and Actuators*, 3(0):79 – 88, 1982-1983.
 - [31] Wei Liang, Yanyi Huang, Yong Xu, Reginald K. Lee, and Amnon Yariv. Highly sensitive fiber bragg grating refractive index sensors. *Applied Physics Letters*, 86(15):151122 –151122–3, apr 2005.
 - [32] Joachim Wittig. Earnst abbe. bsb b. g. teubner verlagsgesellschaft. *Leipzig*, page 60, 1989.
-

-
- [33] E. Abbe. Neue apparatus zur bestimmung des brechungs - und zerstreungsvermögens fester und flüssiger körper. *Mauke's Verlag, Jena*, 1874.
- [34] K.-H. Mahrt and C. Waldmann. Field proven high speed micro optical density profiler sampling 1000 times per second with 10^{-6} precision. In *OCEANS '88. 'A Partnership of Marine Interests'. Proceedings*, pages 497 –504 vol.2, oct-2 nov 1988.
- [35] Shojiro Nemoto. Measurement of the refractive index of liquid using laser beam displacement. *Appl. Opt.*, 31(31):6690–6694, Nov 1992.
- [36] M. Le Menn. Instrument de mesure de l'indice de réfraction d'un fluide. *French Patent N°9809747*, July 1998.
- [37] M Le Menn and J Lotrian. Refraction index measurement by a laser-cube-capillary technique. *Journal of Physics D: Applied Physics*, 34, 2001.
- [38] K. D. Singer, M. S. Merlin, S. J. Lalama, and A. F. Garito. Interferometric refractometer for measuring the relative refractive index of two liquids. *Review of Scientific Instruments*, 53(2):202 –204, feb 1982.
- [39] Bernold Richerzhagen. Interferometer for measuring the absolute refractive index of liquid water as a function of temperature at $1.064 \mu\text{m}$. *Appl. Opt.*, 35(10):1650–1653, Apr 1996.
- [40] A Suhadolnik. An optical fibre interferometric refractometer. *Measurement Science and Technology*, 18, 2007.
- [41] A.D. Kersey, M.A. Davis, H.J. Patrick, M. LeBlanc, K.P. Koo, C.G. Askins, M.A. Putnam, and E.J. Friebele. Fiber grating sensors. *Lightwave Technology, Journal of*, 15(8):1442 –1463, aug 1997.
- [42] A. Iadicicco, A. Cusano, G.V. Persiano, A. Cutolo, R. Bernini, and M. Giordano. Refractive index measurements by fiber bragg grating sensor. In *Sensors, 2003. Proceedings of IEEE*, volume 1, pages 101 – 105 Vol.1, oct. 2003.
- [43] G. Laffont and P. Ferdinand. Tilted short-period fiber-bragg-grating-induced coupling to cladding modes for accurate refractometry. *Measurement Science and Technology*, 12:765–770, 2001.
- [44] A. Iadicicco, S. Campopiano, A. Cutolo, M. Giordano, and A. Cusano. Refractive index sensor based on microstructured fiber bragg grating. *Photonics Technology Letters, IEEE*, 17(6):1250 –1252, june 2005.
- [45] Mike Sadar. Turbidity measurement: A simple, effective indicator of water quality change, 2011. http://www.hachhydromet.com/web/ott_hach.nsf/wcms/688194E7BB964DF7C125777C004F737E/\protect\T1\textdollarfile/Turbidity_AppNote_LowRes.pdf.
-

Figures and tables

Figures

1.1	Salinity map of the world	10
1.2	Samples of turbidity	13
1.3	Profile of scattered intensity from particles of three sizes	14
1.4	Example of 3D Mie scattering angular pattern	14
1.5	Multiscattering example	15
1.6	Jackson Candle Turbidimeter	16
1.7	Principle of nephelometer	17
1.8	Conductivity sensor SBE 4 (SeaBird Electronics, Inc.)	19
1.9	Principle of inductive conductivity sensor	20
1.10	Principle of abbé refractometer	22
1.11	Setup for remote measurement of difference of refractive index	23
1.12	Principle of the refractive index measurement based on the Michelson interferometer	24
1.13	Principle of Fiber Bragg Grating	25
1.14	Measurement of refractive index with Tilted Fiber Bragg Grating (TFBG)	26
1.15	Different turbidity measurement methods	27
1.16	The relationship of turbidity and scattered light at different angles	28
1.17	Optical design of Hach ratio turbidimeter 2100AN	30

Tables

1.1	Characteristic of CTD SBE 9 ⁺ made by SeaBird Electronics, Incs	19
-----	--	----

Chapter 2

Design and implementation of an optical refractometer

Contents

Introduction	38
I Preliminary knowledge of modelling a refractometer	38
I.1 Review of Snell–Descartes law	38
I.2 Introduction of optical material	39
I.2.1 Sellmeier coefficients	39
I.2.2 Temperature coefficient of refractive index	40
I.2.3 Thermal expansion coefficient	42
II Modelling a refractometer	42
II.1 Prototype of refractometer	42
II.2 Relationship between refractive index and laser beam position .	43
II.3 Study of the resolution	45
III Design and implementation of the refractometer	47
III.1 Introduction of optoelectronics elements	47
III.1.1 Laser source	47
III.1.2 Position Sensitive Device/Detector	48
III.2 Implementation of the refractometer	51
III.2.1 Step1: adhesion of the prism	51
III.2.2 Step2: adhesion of the laser source	52
III.2.3 Step3: adhesion of the PSD	53
III.2.4 Step4: verification and calibration of the refractometer	53
IV The resolution of the refractometer	54
Conclusion	56
Bibliography	58
Figures and tables	59

Introduction

As discussed in the last chapter, the refractometer based on the measurement of laser beam displacement meets the requirement of high resolution *in situ* salinity measurement. This chapter is aimed to introduce the study of design, modelling, implementation of a high resolution refractometer. Our further work are all based on the configuration of the refractometer discussed in this chapter.

At the beginning of this chapter, several preliminary knowledges of modelling a refractometer are reviewed. Snell's law, the theory behind refractometer, is first reviewed in this part. Three material coefficients, wavelength, temperature and thermal-expansion, are emphasised to guide the choice of the optical material.

Based on the consideration of these preliminary knowledges, the modelling of our optical refractometer is presented in the second part of this chapter. By using a geographic method, the relationship between the refractive index and the laser beam position is established. According to this relationship, the optimized optico-geometric parameters of refractometer are determined to reach the necessary refractive index resolution.

In the third part of this chapter, we introduce the conception and the implementation of the modelled refractometer. According to the modelling, the optoelectronics elements and optical material are chosen to fulfil the resolution requirements. A detailed operation procedure is also included in this part to guide the fabrication of the refractometer.

At the end of this chapter, the experiments are presented to evaluate the performance of the refractometer. The experimental results are also included in this part.

I Preliminary knowledge of modelling a refractometer

Before the introduction of modelling refractometer, some preliminary knowledge need to be reviewed. According to our previous study and research[1, 2], the refractive index of seawater highly depends on the temperature, thus the relationship between refractive index and temperature need to be studied first. As the refractive index measurement is achieved by measuring the laser beam displacement, the temperature caused optical material expansion must be considered as well.

I.1 Review of Snell–Descartes law

Refraction is the bending of a wave when it enters a medium where it's speed is different. The refraction of light when it passes from a fast medium to a slow medium bends the light ray toward the normal to the boundary between the two media. The term refractive index is a measure of the speed of light in medium. It is expressed as a ratio of the speed of light in vacuum relative to that in the considered medium[3]. In 1621, a Dutch physicist named Willebrord Snell, derived the relationship between the different angles of light as it passes from one transparent medium to another[4]. This relationship is then called Snell–Descartes Law.

Fig. 2.1 illustrates the Snell–Descartes law. When an incident light beam meets the separation of two mediums with refractive index n_1 and n_2 respectively, it changes speed, and bends. We call this phenomenon *refraction*. A more strict definition of this law is given as:

“ Snell–Descartes law gives the relationship between angles of incidence and refraction for a wave impinging on an interface between two media with different

indices of refraction. The law follows from the boundary condition that a wave be continuous across a boundary, which requires that the phase of the wave be constant on any given plane, resulting in: ”[5]

$$n_1 \times \sin(\theta_1) = n_2 \times \sin(\theta_2), \quad (2.1)$$

where θ_1 and θ_2 are the angles from the normal of the incident and refracted waves, respectively.

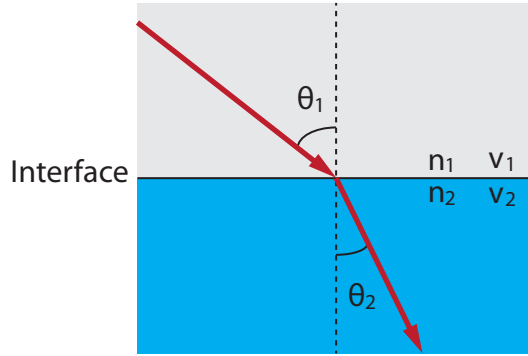


Figure 2.1: Illustration of Snell–Descartes law

I.2 Introduction of optical material

One of the most important part in an optical refractometer is the reference of refractive index, which is usually made from glasses. To obtain high resolution, the refractive index of the reference glass must be independent to the change of external environment during the measurement. This requirement is especially important for the *in situ* sensors due to their working environments. For *in situ* seawater sensors, pressure and temperature are two main parameters that might affect the refractive index of the prism. From the literature[6], we don't have the reliable information of the influence of the pressure to the refractive index of prism, but we know that this effect is much smaller than the effect of refractive index variation caused by temperature variation. Besides the temperature, the refractive index of prism is sensitive to the light wavelength, which needs to be considered in the refractometer design as well.

I.2.1 Sellmeier coefficients

The relationship between refractive index and wavelength for a particular transparent medium is described by the Sellmeier equation[7], which is first proposed by Wolfgang Sellmeier in 1871. The usual form of the equation is expressed as:

$$n^2(\lambda) = 1 + \frac{B_1\lambda^2}{\lambda^2 - C_1} + \frac{B_2\lambda^2}{\lambda^2 - C_2} + \frac{B_3\lambda^2}{\lambda^2 - C_3}, \quad (2.2)$$

where n is the refractive index, λ is the wavelength, and B_1, B_2, B_3 and C_1, C_2, C_3 are experimentally determined *Sellmeier coefficients*[8]. The determination of the coefficients was performed for all glass types on the basis of precision measurements by fitting the dispersion equation to the measurement values. The sellmeier coefficients for a particular

glass can be found in the Schott Glass catalogue[9]. Table 2.1 lists the coefficients for several Schott glasses.

Table 2.1: Sellmeier coefficients for special glasses

	K7	N-BAK2	N-K5	N-KF9
B_1	1.1273555	1.01662154	1.08511833	1.19286778
B_2	0.124412303	0.319903051	0.199562005	0.0893346571
B_3	0.827100531	0.937232995	0.930511663	0.920819805
C_1	0.00720341707	0.00592383763	0.00661099503	0.00839154696
C_2	0.0269835916	0.0203828415	0.024110866	0.0404010786
C_3	100.384588	113.118417	111.982777	112.572446

Since the refractive index of prism changes according to different wavelengths, the light source of refractometer need to be selected carefully to avoid the dispersion. Laser is an idea light source to work in a refractometer due to its narrow band of wavelength.

I.2.2 Temperature coefficient of refractive index

The refractive indices of the glasses only depend on wavelength, but also upon temperature. In the environment where exists the variation of temperature, the study of the impact to glass refractive index due to the variation of temperature is needed. This is necessary for choosing the right optical glass as the reference medium in a refractometer. The relationship of refractive index variation and temperature change is called the *temperature coefficient of refractive index*. This relationship can be derived from the equation 2.2 and expressed as:

$$\frac{dn_{abs}(\lambda, T)}{dT} = \frac{n^2(\lambda, T_0) - 1}{2n(\lambda, T_0)} (D_0 + 2D_1\Delta T + 3D_2\Delta T^2 + \frac{E_0 + 2E_1\Delta T}{\lambda^2 - \lambda_{TK}^2}), \quad (2.3)$$

where T_0 presents the reference temperature ($20^\circ C$), T is the temperature in the unit of $^\circ C$, ΔT is the temperature difference versus the reference temperature T_0 . Symbol λ here standards for the wavelength of the light, D_0 , D_1 , D_2 , E_0 , E_1 , and λ_{TK} are constants depending on the glass type. $dn(\lambda, T)$ is the temperature coefficients of the relative refractive indices apply for an air pressure of 0.10133×10^6 Pa. To study the change of the absolute refractive index $n_{abs}(\lambda, T_0)$ according to the change of temperature, equation 2.3 can be deduced to the following form:

$$dn_{abs}(\lambda, T) = \frac{n^2(\lambda, T_0) - 1}{2n(\lambda, T_0)} (D_0\Delta T + D_1\Delta T^2 + D_2\Delta T^3 + \frac{E_0\Delta T + E_1\Delta T^2}{\lambda^2 - \lambda_{TK}^2}), \quad (2.4)$$

The temperature coefficient of absolute refractive index $\frac{dn_{abs}(\lambda, T)}{dT}$ can be positive or negative with the same temperature change for different types of glass. Fig 2.2 shows the temperature coefficients for different Schott glasses when the wavelength is $632.8 \mu m$ and the temperature is in a range of $-2^\circ C$ and $40^\circ C$, which contains the range of the seawater temperature. To minimize the refractive index variation caused by the temperature, the temperature coefficients should be small under all possible environment temperatures. From this figure, we can find out that the glasses N-BK10, K10, and N-BK7 have the

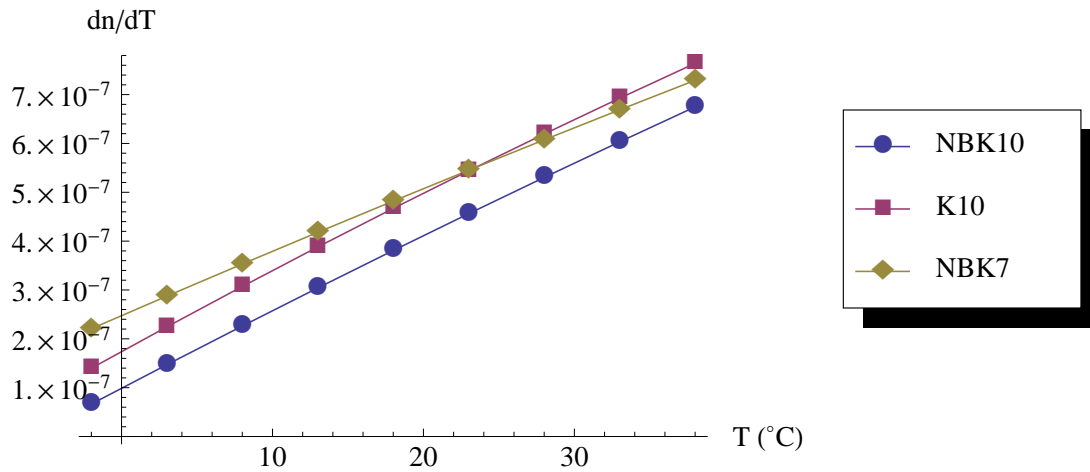


Figure 2.2: The positive temperature coefficient of absolute refractive index for several Schott glasses

temperature coefficients in an order of 10^{-7} , which is very small, so that they are good candidate for the material of the prism.

Another phenomenon that we can observe from the Fig. 2.2 is that the temperature coefficient increases as the temperature increases and maintains a positive value. There exists the prisms, whose temperature coefficients decrease as the temperature raise and maintain a negative value. Fig 2.3 depicts several prisms that own this characteristic. The temperature coefficients of these glasses shown in this figure are in an order of 10^{-6} .

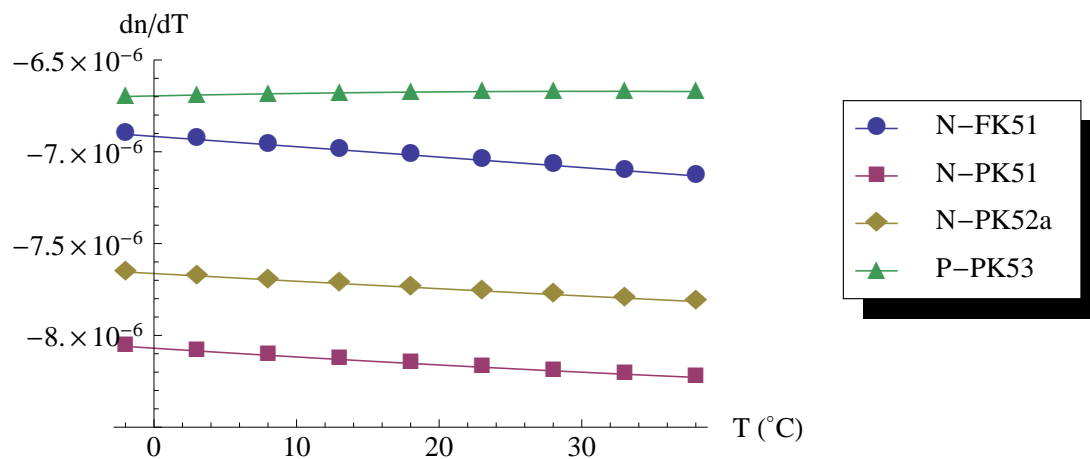


Figure 2.3: The negative temperature coefficient of absolute refractive index for several Schott glasses

In our refractometer design, if we use two prisms, one with the positive temperature coefficient as shown in Fig. 2.2, another one with the negative temperature coefficient as shown in Fig. 2.3, such pair of two glasses with positive and negative temperature coefficients can be used to compensate the deviation of laser beam caused by the thermal

change of prism refractive index[10].

I.2.3 Thermal expansion coefficient

Another impact of the temperature change is caused by the geometrical expansion or contraction when temperature changes. This dimensional variation will cause the light spot position measurement inaccurate.

Thermal expansion is the tendency of matter to change in volume in response to a change in temperature[11]. It is usually expressed as a fractional change in length or volume per unit temperature change. For solid materials, a linear expansion coefficient is usually employed. If a crystalline solid is isometric (has the same structural configuration throughout), the expansion will be uniform in all dimensions of the crystal. If it is not isometric, there may be different expansion coefficients for different crystallographic directions, and the crystal will change shape as the temperature changes. In our case, we consider the linear isometric expansion for our prisms. Thus, the expansion follows the equation:

$$\Delta l = \alpha_l l_0 \Delta T, \quad (2.5)$$

where α_l is the thermal expansion coefficient in the unit of $^{\circ}C^{-1}$, Δl is the variation of the size due to the temperature change ΔT . l_0 here stands for the original size. Table 2.2 lists the thermal expansion coefficients for different SCHOTT glasses in a range of -30 and 70 $^{\circ}C$.

Table 2.2: Thermal expansion coefficients for different glasses in a range of -30 and 70 $^{\circ}C$

	K7	N-BAK2	N-KF9	N-FK51a	N-PK51	N-PK52a	P-PK53
$\alpha_l(\times 10^{-6} \text{ }^{\circ}C^{-1})$	8.4	8.0	9.6	12.7	12.4	13.0	13.3

II Modelling a refractometer

II.1 Prototype of refractometer

The basic principle of our refractometer is to transfer the measurement of refractive index to the measurement of laser beam displacement. Based on our previous refractometer prototype[2], a new prototype was proposed and depicted in Fig. 2.4. This refractometer consists of two prisms with different refractive indices to compensate the influence caused by temperature change. Based on the simulation in ZEMAX, we chose K7¹ ($n = 1.50934$ at wavelength of 632.8 nm) as the material of left hand side prism and N-FK51² ($n = 1.48534$ at wavelength of 632.8 nm) as the material for right hand side prism. The laser beam first illuminates the left hand side prism and reaches a mirror AB . After the reflection at AB , the laser beam is redirected to the surface between the medium and the prism, CO , with an incident angle that is very close to the critical angle. It is then refracted and propagates a distance d in the medium. At surface OE , the laser beam is refracted again and enters the right hand side prism. The mirror FG finally reflects the laser beam to the top of the prism, where a laser beam position detection device is used to detect the position of the laser spot x_p . The blue area contains the seawater.

¹In practice, the material H-K9L of Foctec is used as an alternative of K7

²In practice, the material H-QK3L of Foctec is used as an alternative of N-FK51

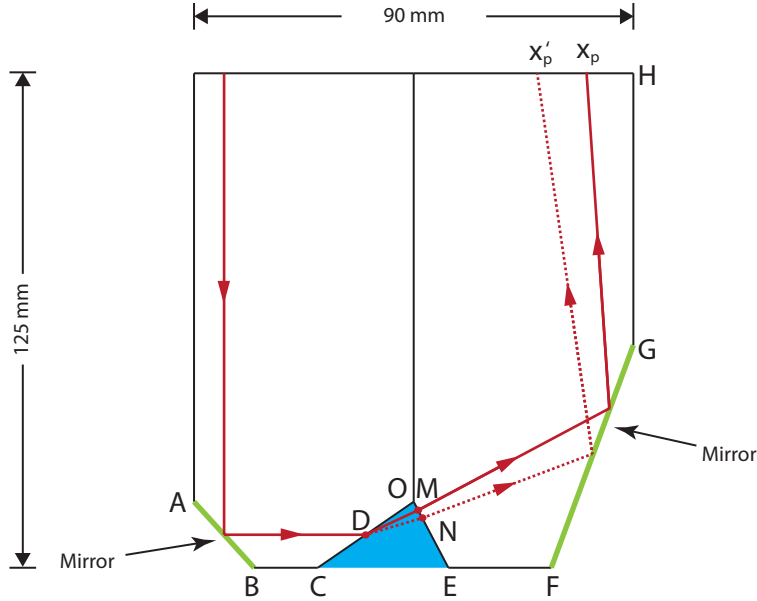


Figure 2.4: The prototype of the optical design of the refractometer

The change of the water refractive index results in the difference of refraction at surface CO , which leads the laser beam from DM to DN as shown in Fig. 2.4. This deviation of laser beam further brings the refraction changes at surface OE , which finally makes the laser beam spot moves to the position x'_p . The laser spot displacement $\Delta x_p = x'_p - x_p$ can be used to calculate the change of refractive index.

II.2 Relationship between refractive index and laser beam position

The resolution of this refractometer depends on the parameters of the prism and the photo-electronic devices used in this configuration. The parameters of the photoelectric devices can be determined according to the desired performance and the optical parameters of the prism. Thus, to test and improve the performance of this refractometer, the relationship between the water refractive index and the laser spot position must be discussed at first to confirm the optical parameters of the prism.

The analysis of the relationship is carried out by a geometrics method, which is illustrated in Fig 2.5. To simplify the discussion, the reflection in the mirror AB and FG are equivalent to the direct propagation into its image, so that the laser spot position P is equivalent to the laser spot position P' in Fig 2.5. Since the laser spot position P' moves along the line $H'P'$ according to the refractive index change, the position can be presented as the distance between the point H' and P' , noted as $\overline{H'P'}$. If we put the system into a Cartesian coordinate system with point O as the original point and the horizontal direction is the x axis, the laser spot position $\overline{H'P'}$ can be written as:

$$\overline{H'P'} = \sqrt{(P'_x - H'_x)^2 + (P'_y - H'_y)^2} = \frac{P'_x - H'_x}{\cos(2\beta)}, \quad (2.6)$$

where the subscript x and y standard for the coordinate of x and y for the corresponding point, while β is the angle between the the mirror FG and the y axis. From the geometrics, the coordinate of point H' can be calculated using the following group of equations: φ

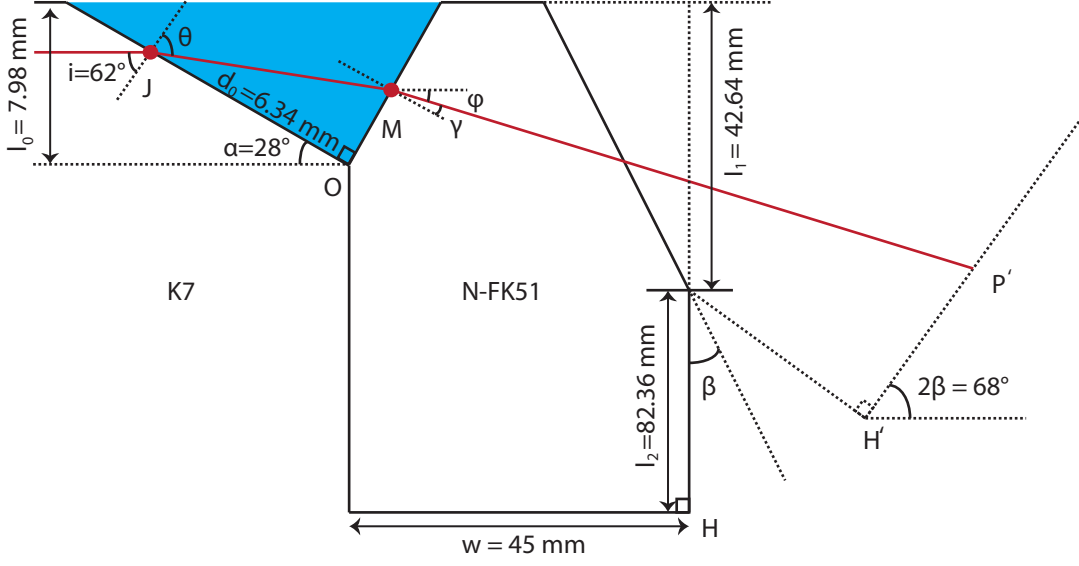


Figure 2.5: Principle of geometric method

$$H'_x = w + l_2 \sin(2\beta) \quad (2.7)$$

$$H'_y = l_0 - l_1 - l_2 \cos(2\beta) \quad (2.8)$$

The symbol w is the width of the prism, l_0 , l_1 and l_2 describe the size of the prism. The point P' is the intersection of the line $H'P'$ and the line MP' . These two lines can be presented as:

$$MP' : y = \tan(\pi - \alpha + \gamma)x + b_{MP'} \quad (2.9)$$

$$H'P' : y = \tan(2\beta)x + b_{H'P'} \quad (2.10)$$

where $b_{MP'}$ is the intersection point of line MP' and y axis while $b_{H'P'}$ is the intersection point of line $H'P'$ and y axis. From the these two equations, the point P' can be derived as:

$$P'_x = \frac{b_{H'P'} - b_{MP'}}{\tan(\pi - \alpha + \gamma) - \tan(2\beta)} \quad (2.11)$$

$$P'_y = \tan(2\beta) \frac{b_{H'P'} - b_{MP'}}{\tan(\pi - \alpha + \gamma) - \tan(2\beta)} + b_{H'P'} \quad (2.12)$$

Since point H' is in the line $H'P'$, $b_{H'P'}$ can be derived by using the coordinate of H' to substitute the x and y in equation 2.10. Thus, $b_{H'P'}$ can be expressed as:

$$b_{H'P'} = l_0 - l_1 - l_2 \cos(2\beta) - \tan(2\beta)[w + l_2 \sin(2\beta)] \quad (2.13)$$

Similarly to $b_{H'P'}$, $b_{MP'}$ can be calculated by substituting point $M(M_x, M_y)$ into the function of line MP' , where M_x and M_y are function of incident light position d_0 , prism angle α and the first refraction angle θ :

$$M_x = \frac{d_0 \cos(\frac{\pi}{2} - \alpha)}{\tan(\theta)} \quad (2.14)$$

$$M_y = \frac{d_0 \sin(\frac{\pi}{2} - \alpha)}{\tan(\theta)} \quad (2.15)$$

With equation 2.10, 2.14 and 2.15, $b_{MP'}$ is expressed as:

$$b_{MP'} = \frac{d_0 \sin(\frac{\pi}{2} - \alpha)}{\tan(\theta)} - \tan(\pi - \alpha + \gamma) \frac{d_0 \cos(\frac{\pi}{2} - \alpha)}{\tan(\theta)} \quad (2.16)$$

Combined all the equations above, we can write the laser spot position $\overline{H'P'}$ as a function of the angle θ , γ and some geometric parameters of prism.

$$\begin{aligned} \overline{H'P'} &= f(\theta, \gamma, \alpha, \beta, d_0, l_0, l_1, l_2, w) \\ &= \frac{1}{\cos(2\beta)}(-w - l_2 \sin(2\beta)) - \frac{l_0 - l_1 - l_2 \cos(2\beta)}{\tan(2\beta) + \tan(\alpha - \gamma)} + \frac{d_0 \cos(\alpha) \cot(\theta)}{\tan(2\beta) + \tan(\alpha - \gamma)} \\ &+ \frac{(w + l_2 \sin(2\beta) \tan(2\beta))}{\tan(2\beta) + \tan(\alpha - \gamma)} + \frac{d_0 \cot(\theta) \sin(\alpha) \tan(\alpha - \gamma)}{\tan(2\beta) + \tan(\alpha - \gamma)} \end{aligned} \quad (2.17)$$

The relationship between the angles i , θ , and γ can be easily built from the Snell's law:

$$n_1 \sin(i) = n_e \sin(\theta) \quad (2.18)$$

$$n_e \sin(\frac{\pi}{2} - \theta) = n_2 \sin(\gamma) \quad (2.19)$$

Hence, the laser spot position $\overline{H'P'}$ is a function of incident angle i , incident position d_0 , the refractive index n_e , n_1 , n_2 , and some geometric parameters of prism.

$$\overline{H'P'} = f(i, \alpha, \beta, d_0, n_e, n_1, n_2, l_0, l_1, l_2, w) \quad (2.20)$$

The appendix B includes the full details of the deduction for this relationship.

II.3 Study of the resolution

The resolution of the refractometer depends on the sensitivity and the range of measurement. The sensitivity of the refractometer S_t is expressed as:

$$S_t = \frac{\partial n_e}{\partial p} = \frac{\partial n_e}{\partial \gamma} \frac{\partial \gamma}{\partial p} \quad (2.21)$$

According to equation 2.18 and 2.19, the relationship between the refractive index variation ∂n_e and variation of the refraction angle $\partial \gamma$ can be written as:

$$\frac{\partial n_e}{\partial \gamma} = \frac{\cos(\gamma) n_e}{\sin(\gamma) [1 + \tan^2(\theta)]} \quad (2.22)$$

The relationship between the position variation ∂p and variation of the refraction angle $\partial \gamma$ can be obtained from the derivative of equation 2.17, which is:

$$\frac{\partial \gamma}{\partial p} = \cos(2 * \beta) / \left[\frac{d_0 \cot(\theta) \sin(\alpha) / \cos^2(\alpha - \gamma)}{-\tan(2\beta) - \tan(\alpha - \gamma)} - \frac{(l_0 - l_1 - l_2 \cos(2\beta) - d_0 \cos(\alpha) \cot(\theta) - (w + l_2 \sin(2\beta)) \tan(2\beta) - d_0 \cot(\theta) \sin(\alpha) \tan(\alpha - \gamma))}{\cos^2(\alpha - \gamma) (-\tan(2\beta) - \tan(\alpha - \gamma))^2} \right] \quad (2.23)$$

Thus, the sensibility of the refractive index measurement is:

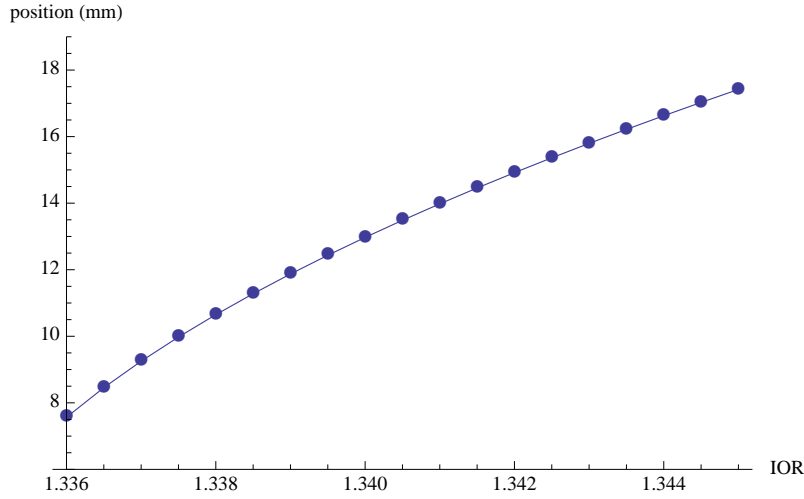


Figure 2.6: The relationship between the laser spot position and the index of refraction (IOR)

$$S_t = \frac{\partial n_e}{\partial p} = \frac{\partial n_e}{\partial \gamma} \frac{\partial \gamma}{\partial p} = \cos(2 * \beta) \cos(\gamma) n_e / \left[\sin(\gamma) [1 + \tan^2(\theta)] \left[\frac{d_0 \cot(\theta) \sin(\alpha) / \cos^2(\alpha - \gamma)}{-\tan(2\beta) - \tan(\alpha - \gamma)} - \frac{(l_0 - l_1 - l_2 \cos(2\beta) - d_0 \cos(\alpha) \cot(\theta) - (w + l_2 \sin(2\beta)) \tan(2\beta) - d_0 \cot(\theta) \sin(\alpha) \tan(\alpha - \gamma))}{\cos^2(\alpha - \gamma) (-\tan(2\beta) - \tan(\alpha - \gamma))^2} \right] \right] \quad (2.24)$$

The angle γ and θ in this equation can be calculated from the equations:

$$\theta = \arcsin\left(\frac{n_1}{n_e} \sin(i)\right) \quad (2.25)$$

$$\gamma = \arcsin\left(\frac{n_e}{n_2} \sin(\theta)\right) \quad (2.26)$$

Combined with the three equations above, the sensibility of the refractometer is a function of incident angle i , incident position d_0 , the refractive index n_e , n_1 , n_2 , and some geometric parameters of prism.

$$S_t = f_s(i, \alpha, \beta, d_0, n_e, n_1, n_2, l_0, l_1, l_2, w) \quad (2.27)$$

With these equations, the resolution of the refractometer can be computed according to different dimensional parameters. Fig. 2.6 plots the laser beam position versus different seawater refractive indices from 1.3360 to 1.3450 with the dimensional parameters as follows: $\alpha = 28^\circ$, $\beta = 34^\circ$, $i = 62^\circ$, $w = 45 \text{ mm}$, $d_0 = 6.34 \text{ mm}$, $l_0 = 7.98 \text{ mm}$, $l_1 = 42.64 \text{ mm}$, and $l_2 = 82.36 \text{ mm}$.

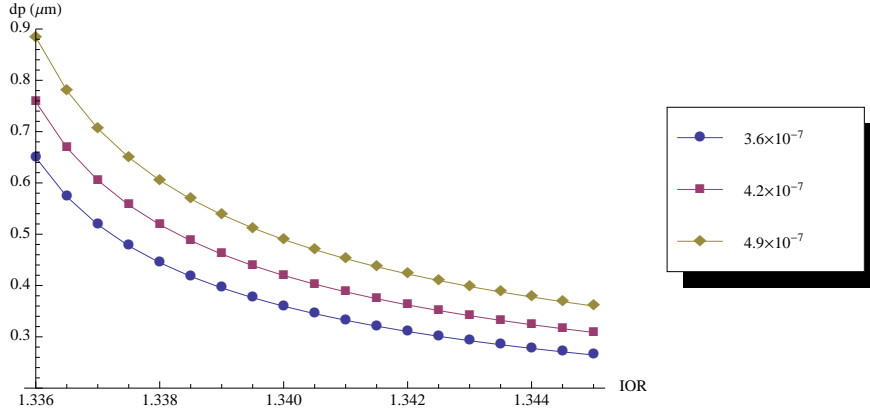


Figure 2.7: The required laser spot position sensitivity for different refractive index sensitivity requirement

From this figure, we can find that the laser spot moves a distance of about 10 mm from 7.57 mm for refractive index 1.3360 to 17.42 mm for refractive index 1.3450. This requires the optoelectronic sensor has at least an active area of 10 mm to achieve the requirement of refractive index measurement range. With the same configuration, fig 2.7 lists the required laser spot position detection sensitivity for three different refractive index measurement sensitivity requirement: 3.6×10^{-7} , 4.2×10^{-7} , and 4.9×10^{-7} .

From this figure, to reach the desired refractive index measurement resolution, the sensitivity of laser spot position detector must reach $0.3 \mu\text{m}$.

III Design and implementation of the refractometer

The fabrication of the refractometer is the process to integrate the optical prism and the optoelectronic elements, including light source and position detection device. The fabrication must guarantee that the modelling configuration is well implemented to avoid the error caused by the assembling process.

III.1 Introduction of optoelectronics elements

III.1.1 Laser source

As we discussed in section I.2.1 the refractive index is sensitive to the light wavelength, and it is necessary to use a light source with narrow band of wavelength. Laser is a good choice for the light source of our system. The laser source used for the prototype is a laser module equipped with a 0.2 mW diode laser[12] at a wavelength of $635 \mu\text{m}$. A two-lens-collimator is equipped at the exit of the module to produce a collimated beam with the divergence of 1.5 mrad . Fig 2.8 shows the photo and the structure of the laser module used in our refractometer.

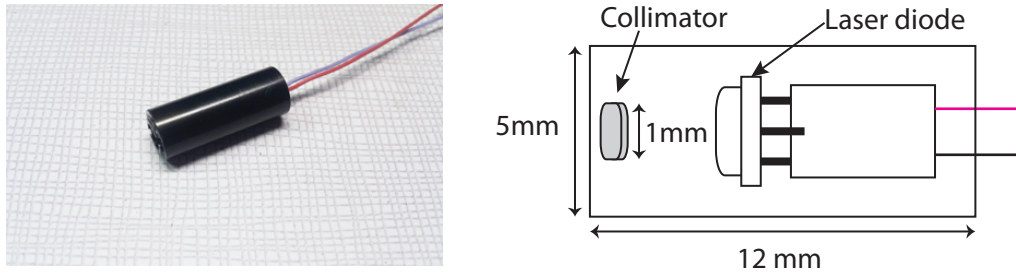


Figure 2.8: The structure of the laser module

III.1.2 Position Sensitive Device/Detector

According to the principle of our refractometer, the measurement of refractive index is transferred to measure the laser spot position. In this section, we introduce one of the devices, Position Sensitive Device, used in the prototype to measure the laser spot position, and discuss its resolution.

Definition

The Position Sensitive Device or Position Sensitive Detector (PSD) is an optical position sensor that can measure a position of a light spot in one or two-dimensions on a sensor surface. From this general definition, it is obvious to conclude that PSD is not specific to a particular optical device, any optical device provides the capability to measure the light spot position can be categorized as PSD.

In our situation, a one-dimension (1-D) lateral-effect PSD is used to measure the laser spot position. The lateral-effect PSD[13] provides high sensitivity, short response time and independence from spot light size, shape and intensity. Due to these advantages, it is widely used in the high accuracy light spot detection applications. In this document, the term PSD is used to present the lateral-effect PSD.

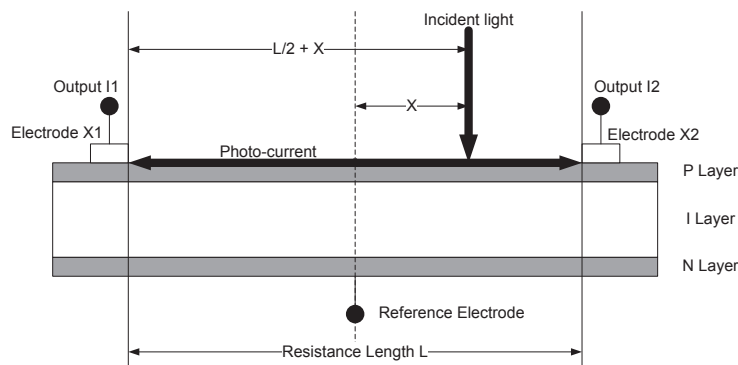


Figure 2.9: The principle of 1-D lateral-effect PSD

A PSD basically consist of a uniform resistive layer formed on one or both surfaces of a high-resistivity semiconductor substrate, and a pair of electrodes formed on both ends of the resistive layer for extracting position signals. The active area, which is also a resistive layer has a P-N junction that generates photo-current by means of the photovoltaic effect.

Principle

The principle of 1-D PSD is shown in Fig. 2.9. PSD has a single active area formed by a P-N junction. The two parts that originated from the laser spot to the two electrodes form two lateral resistances, (R_1, R_2) , for the photo-currents running towards the electrodes. When a light strikes the PSD, electric charges, which are proportional to the intensity of light, are generated and form two photo currents. Under the driven of voltage, the two photo currents are running from the laser spot to the two electrodes, X_1 and X_2 . The photo currents are then collected through the resistances by the output electrodes, which are inversely proportional to the distance between the electrode and the center of the incoming light beam. The two photo currents, labelled as I_1 and I_2 are expressed as:

$$I_1 = \frac{\frac{L}{2} + x}{L} I_0 \quad (2.28)$$

$$I_2 = \frac{\frac{L}{2} - x}{L} I_0 \quad (2.29)$$

where L is the length of the PSD active area, I_0 is the total photo current generated by the incident light. From the equation 2.28 and 2.29, the position of the incident light x can be retrieved from the following equation[14]:

$$x = \frac{L I_2 - I_1}{2 I_1 + I_2} \quad (2.30)$$

According to the principle, the center given by 1-D PSD is the gravity center of incident light. The post-processing process, which is typically implemented by the external processing circuit, first amplify each of the photo-currents, transfers them into voltages, and then calculates the subtraction, addition and division operations in equation 2.30.

Resolution of PSD

The resolution of PSD is the minimum detectable displacement of a spot light on PSD, expressed as a distance on the PSD surface. Suppose the light spot moves a distance Δx on the PSD surface, the difference of the photo currents I_1 and I_2 can be express as following according to equation 2.28 and 2.29.

$$\Delta I_1 = I_0 \frac{(\frac{L}{2} + (x + \Delta x))}{L} - \frac{\frac{L}{2} + x}{L} I_0 = I_0 \frac{\Delta x}{L} \quad (2.31)$$

$$\Delta I_2 = I_0 \frac{(\frac{L}{2} - (x + \Delta x))}{L} - \frac{\frac{L}{2} - x}{L} I_0 = -I_0 \frac{\Delta x}{L} \quad (2.32)$$

With these two equations, we can express the change of laser spot position Δx in a function of photo current change ΔI :

$$\Delta x = L \frac{\Delta I}{I_0} \quad (2.33)$$

When the laser spot displacement is very small, the noise is the main contribution to the change of the photo current. The resolution of PSD is mainly depending on the photo current I_n caused by noise. The noise contains not only the shot noise and thermal noise inside the PSD but also the noise in external post-processing circuit, such as the noise in operational amplifier. The currents caused by these noise form the noise current I_n [15]:

$$I_n = \sqrt{I_s^2 + I_j^2 + I_{en}^2}, \quad (2.34)$$

where I_s is the noise current caused by the shot noise, the thermal noise results in the noise current I_j , and I_{en} stands for the noise current from the equivalent noise input voltage of operational amplifier. From the principle of PSD, several methods can be adapted to improve the resolution:

- Increasing the signal photo current I_0
- Increasing the interelectrode resistance
- Shorten the resistance length L
- Use a low noise operational amplifier

Selection of PSD

According to the resolution discussion in last section, to reach the refractive index resolution of 10^{-7} , the PSD should have an active area more than 10 mm with a resolution better than 0.3 μm . Based on this consideration, we chose the 12 mm Hamamatsu PSD S3932[16]. By connecting to the signal processing card C5923, the reported resolution of this PSD reaches 0.3 μm . Since this resolution is very important for calculating the actual refractive index resolution, we designed an experiment to test the actual resolution of PSD at the end of this chapter.

Limitation of PSD

Although PSD has the advantage of high sensitivity, short response time (3 μs), and independence from light spot size, shape and intensity, it still has same limitations. This limitation should be considered as well when choosing the position detection device.

The first limitation is due to the design purpose of PSD. PSD is designed to measure the incident light position, which makes it not proper to be applied to a multi-functional sensor. For those applications which are not only sensitive to the light spot position but also the light distribution or light spot shape, PSD cant be used for detecting both the variations.

Furthermore, as an analogue device, the PSD analogue output signal makes it hard to benefit from modern post-processing techniques. This limitation can be proved from the 4 methods to improve the PSD resolution. Except increasing the signal photo current I_0 , the other methods involves hardware or device modification, eg. the PSD interelectrode resistance or operational amplifier. The modern digital post-processing methods cant be easily applied to PSD signals.

Another drawback of PSD-based systems is that the high resolution of such systems relies on the assumption that the two analogue photo-currents should be amplified with two identical amplifiers, which is difficult to be achieved at a low cost.

One of the advantage of PSD is its independence from light spot size, shape and intensity. However, as we know that PSD actually measures the gravity center of the incident light. That's to say, this advantage is only hold when the light spot size, shape and intensity don't change during the movement. For those applications, in which the light spot shape and intensity change according to the position, the position provided by PSD will cause a large error. This limitation will be discussed further in chapter 4.

Despite these limitations, for a uni-functional refractometer as discussed in this chapter, PSD is qualified to provide high performance in locating the light position.

III.2 Implementation of the refractometer

In this part of the section, we will explicate the different steps of the fabrication of the refractometer, including the adhesion of the prism, the laser source, and the PSD.

III.2.1 Step1: adhesion of the prism

The first step is the adhesion of the two prisms. Since the sensor need to work in deep sea, the two prisms must be well aligned to avoid the rupture by high pressure. This requires not only the two prisms are placed in the same plane but also the border of the prism are well aligned. Fig. 2.10 shows the unaligned prism, which is caused by the prism shift during the adhesion. To avoid this non-alignment, a supporter in stainless steel is fabricated, which is shown in Fig. 2.11(a). The size of the supporter is exactly the same as the prism size so that the collage can be processed in the supporter. Fig. 2.11(b) depicts the mounting of the collage.

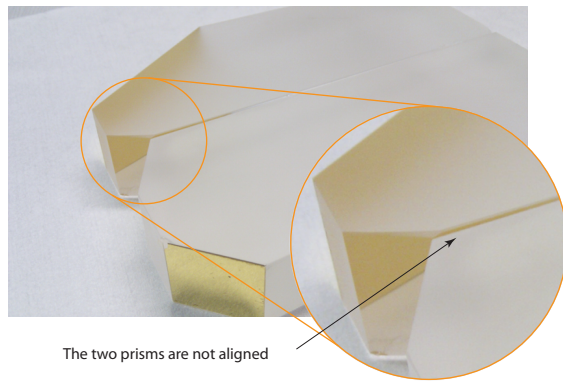
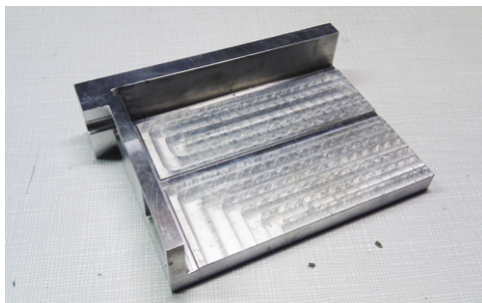
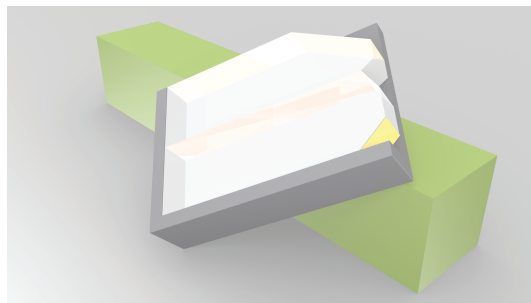


Figure 2.10: The unaligned prism

The two prisms are well aligned and put into the supporter, which is tilted as shown in Fig. 2.11(b). With this configuration, the gravity of the prisms will drive the prism aligned in the same plane and the border of the two prisms will be aligned as well. We use a photosensitive resin NOA63[17] (Norland Optical Adhesive 63), which is a transparent optical adhesive. This kind of adhesive will be polymerized under the light UV. We place a UV lamp near the mounting of the prisms and wait for the polymerization for about 1800 seconds to make sure the two prisms are well adhered. The adhesive might flow to the supporter so that the light UV will make the supporter and the prism adhered as well. A knife can be used to easily separate the adhered prism and the supporter.



(a)



(b)

Figure 2.11: The mounting for the prism collage

III.2.2 Step2: adhesion of the laser source

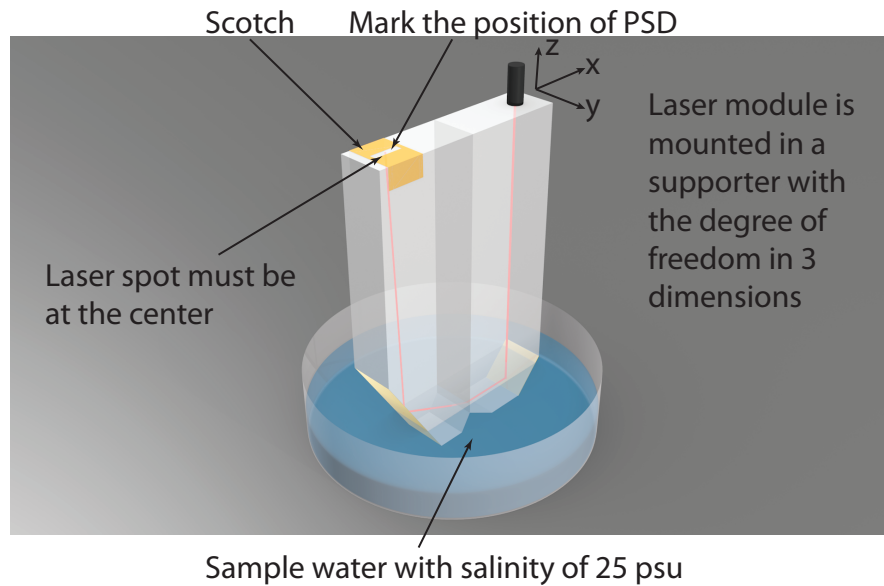


Figure 2.12: The mounting for the adhesive of laser module

The second step is to adhere the laser source to the prism. The mounting for the adhesive of laser module is shown in Fig. 2.12. The ailight laser module is mounted in a supporter with the degree of freedom in 3 dimensions. The adhered prism are fixed into a container. The salinity sample of 25 PSU is poured into this container to help fix the position of the laser module. At the position of the PSD, a white paper is adhered by adhesive plaster to mark the desired PSD position.

The adhesive used for the adhesion of laser module is NOA63 as well. It is important to avoid contacting the collimator of the laser module when daubing the NOA63 on the laser module. Fig.2.13 (a) depicts the right way to daub the adhesive on the laser module, all the adhesive are daubed at the border.

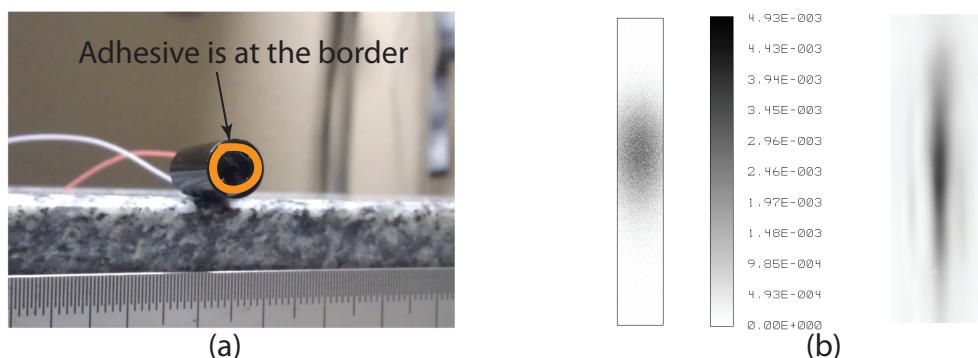


Figure 2.13: Some important notion of mounting laser module

Another issue is that the laser spot shape of diode laser is not a circle but an ellipse. In our prototype of refractometer, the refraction changes the size of the laser spot. Fig. 2.13

(b) gives several laser spot image captured at the position of PSD. The left sub-diagram in Fig. 2.13 (b) is a simulation laser spot by ZEMAX, while the right sub-diagram is a real laser spot captured by a CCD (Charge-Coupled Device). Apparently, this extension of the laser spot, reduced the measurement range. To reduce this effect, the diode laser need to be rotated to make sure that the short diameter of the laser spot is in the refraction plane. Both the position and the rotation of the laser can be determined by observing the laser spot displayed in the white paper. When the laser spot is in the middle of the marked PSD position and the spot size reaches the minimum, a UV lamp is used to polymerize the NOA63.

III.2.3 Step3: adhesion of the PSD

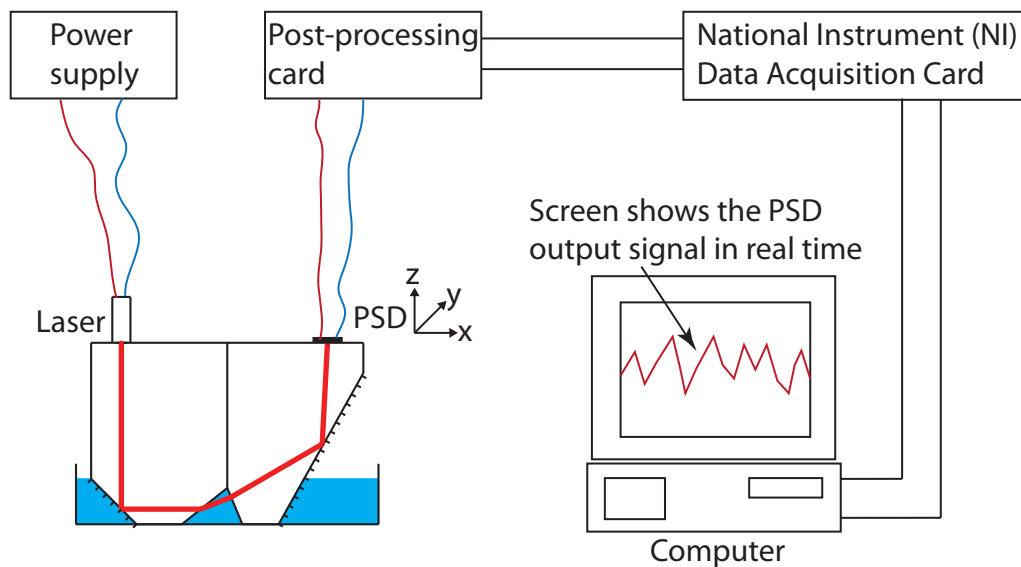


Figure 2.14: The mounting for the adhesion of PSD

The last step is the adhesion of PSD as shown in Fig. 2.14. The prism adhered with the laser module is fixed into a container. The laser module is lighted by a 5 volt power supply. The PSD is mounted in a 3 dimension supporter and connected to a Hamamatsu post-signal-processing card[18]. A National Instrument DAQ card is used to collect the position signal from the Hamamatsu post-signal-processing card. The collected voltages are display in the screen of a computer in real time.

The adhesive NOA63 is first daubed on the PSD active area surface and then pressed onto the prism to avoid the large bubbles inside the adhesive. 35 PSU salinity water sample is poured into the container to help find the right position of the PSD. By adjusting the 3-dimension supporter, we can find the place where the output of post-signal-processing card is 0 volt. A UV lamp is used to polymerize the adhesive NOA63.

III.2.4 Step4: verification and calibration of the refractometer

After the fabrication of the refractometer, a verification is needed to verify the fabrication process. To achieve this, an experiment is designed and illustrated in this part. The

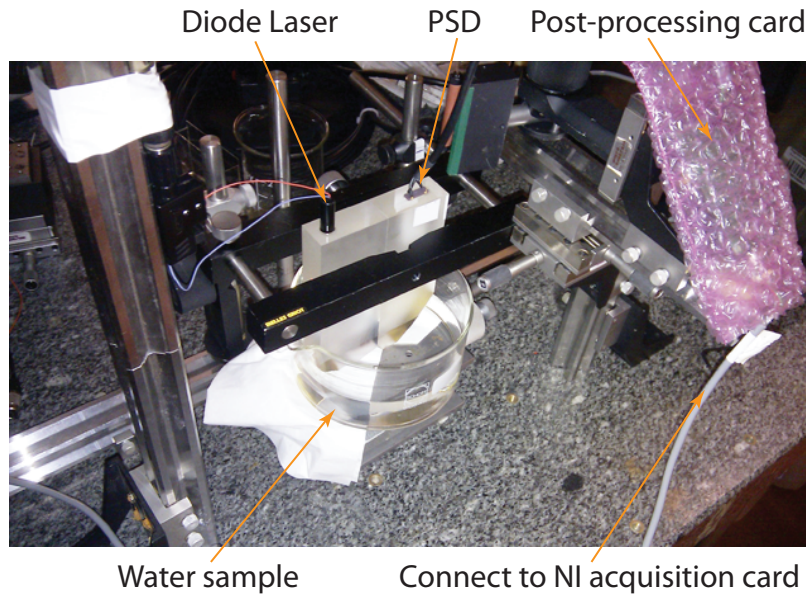


Figure 2.15: The mounting for verifying the fabrication process

verification includes the the test of the PSD output in the measurement range boundaries, that is 10 PSU and 40 PSU in our case. Fig. 2.15 is the mounting of verifying the fabricated refractometer.

The refractometer is fixed in a container, and the laser module is connected to a 5 volt power supply, while the PSD is connected to the Hamamatsu post-signal-processing card. The position signal is collected by a National Instrument daq card and displayed in a computer screen. Three experiments need to be carried out with different water samples, 10 PSU, 35 PSU, and 40 PSU. The position signals (voltage value) for the three different water samples need to be recorded to calibrate the calculation.

IV The resolution of the refractometer

The resolution of the refractometer is verified from equation 2.17 by testing the actual PSD resolution, which is obtained from an experiment. The set up of this experiment is shown in Fig.2.16 (a). The laser module is mounted on motorized micro-positioner. The laser beam is vertically pointing to the PSD active surface. The PSD connected to the Hamamatsu post-signal-processing card generates the position signals, which are collected and recorded by a computer.

By moving the motorized micro-positioner with a step of $0.1 \mu m$, which is considered to be the reference measure to evaluation the PSD resolution, the PSD signals are collected. During each step, 10000 samples of PSD signals were captured in 1 second. The laser beam position was then calculated by averaging the 10000 PSD signal samples. The laser beam is first pointed at the center of the PSD (position voltage is 0 volt), and then move the motorized micro-positioner for 50 steps along the length of PSD. The averaged position signal are recorded and plotted in Fig. 2.16 (b).

The resolution of the PSD is evaluated by a linear fitting of the experimental results. As expected, the results shows a good linearity and the standard uncertainty to the fitting

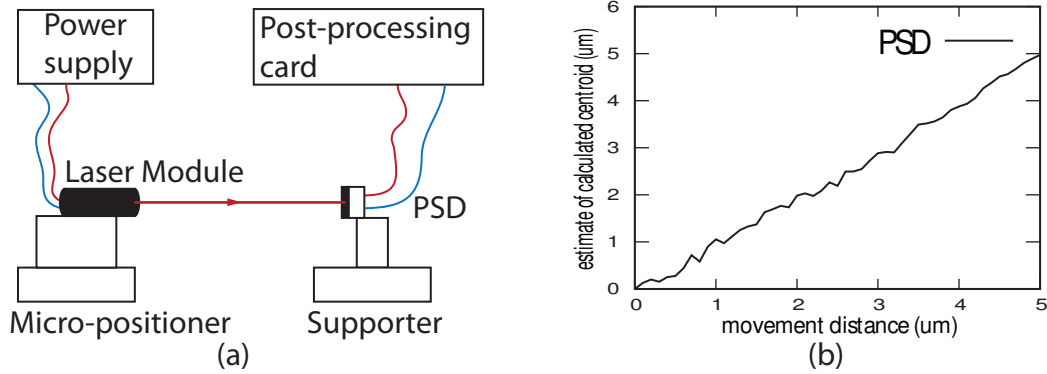


Figure 2.16: The set up for verifying the resolution of PSD

line reaches $\delta_x = 0.11 \mu m$. With this PSD resolution, the resolution of refractive index for the refractometer can be calculated from equation 2.24, reaches 2.94×10^{-7} , equivalent to the absolute salinity of $1 \times 10^{-3} g.kg^{-1}$.

Conclusion

By comparing the state-of-the-art refractive index measurement techniques, the refractometer based on the laser beam deviation measurement is adopted as our principle of design, which can reach high resolution and can be easily integrated into a compact *in situ* sensor. The modelling, design, fabrication of the refractometer are introduced in this chapter.

The first thing to design a refractometer is the chose of the optics in order to minimize the influence caused by the external environment especially the temperature. The expansion of the material caused by the temperature variation is also studied in this part. Based on these studies, a refractometer consist of two prisms is modelled. By using the differential and geometric method, the relationship between the seawater refractive index and the laser spot position is built. The measurement range and sensitivity of the refractometer are discussed as well. With the refractometer configuration that we used, the laser spot moves about 10 *mm* when the refractive index measurement range is between 1.3360 and 1.3450. To reach the refractive index measurement sensitivity in an order of 10^{-7} , the laser spot measurement sensitivity must reach at least 0.3 μm .

The next step is the selection of the optoelectronic devices, including the light source and the light position detector. Since the refractive index is sensitive to the wavelength, a red dot laser module at 635 *nm* is used as the light source due to its narrow band of wavelength. For the light position detector, an analogue device, PSD, is used in our refractometer because of its high sensitivity, short response time and independence from spot light size, shape and intensity. According to the resolution requirement, a 12 *mm* Hamamatsu PSD with the resolution of 0.3 μm is used in our refractometer. Although PSD can reach the requirement of measuring the refractive index, it is not suitable for the multi-functional sensors due to its limitations. We paid special attention to these limitations for further improving the performance and broadening the applications of our sensor.

At the third part of this chapter, we presented the fabrication process of the refractometer. We used a photosensitive resin NOA63 combined with the lamp UV to adhere different parts of the refractometer. Several special problems that need to pay attention were illustrated in this part. In order to work in high pressure environment, the two prisms must be well aligned, which is achieved by putting the prisms into a tilted support. The refraction changes the size of the laser spot. To avoid the extended laser spot reduce the measurement range, the diode laser need to be rotated to make sure that the short diameter of the laser spot is in the refraction plane. At the end of the fabrication process, the refractometer need to be verified by measuring the position of three salinity samples: 10 *PSU*, 35 *PSU*, and 40 *PSU*.

The resolution of the refractometer is determined by the sensitivity of PSD and the refractometer configuration. To verify the actual resolution of our refractometer, the actual sensitivity of PSD must be studied. To achieve this, an experiment was carried out to evaluate the actual PSD resolution. From the experimental results, it is believed that the actual PSD resolution reaches $\delta_x = 0.11 \mu m$. According to our refractometer configuration, the corresponding refractive index resolution is 2.94×10^{-7} , equivalent to the absolute salinity of $1 \times 10^{-3} g.kg^{-1}$.

Bibliography

- [1] Damien Malardé. *Étude et développement d'un salinomètre de haute résolution basé sur la réfractométrie*. PhD thesis, Télécom Bretagne, 2009.
 - [2] D Malardé, Z Y Wu, P Grosso, JL de Bougrenet de la Tocnaye, and M Le Menn. High-resolution and compact refractometer for salinity measurements. *Measurement Science and Technology*, 20(1), 2009.
 - [3] H.D. Young, R.A. Freedman, A.L. Ford, and F.W. Sears. *Sears and Zemansky's university physics: with modern physics*. Pearson Addison Wesley, 2008.
 - [4] K B Wolf and G Krotzsch. Geometry and dynamics in refracting systems. *European Journal of Physics*, 16(1), 1995.
 - [5] Eric W. Weisstein. Snell's law, 2007. <http://scienceworld.wolfram.com/physics/SnellsLaw.html>.
 - [6] K.-H. Mahrt and C. Waldmann. Field proven high speed micro optical density profiler sampling 1000 times per second with 10^{-6} precision. 2:497–504, oct-2 nov 1988.
 - [7] G. Ghosh. *Handbook of thermo-optic coefficients of optical materials with applications*. Handbook of Optical Constants of Solids. Academic Press, 1998.
 - [8] Schott AG. Tie-19: Temperature coefficient of the refractive index, 2008. http://www.lumonics.com/Materials/schott_tie-19_temperature_coefficient_of_refractive_index.pdf.
 - [9] Schott AG. Data and tools for optical designers, 2011. http://www.schott.com/advanced_optics/english/our_products/materials/data_tools/index.html?so=france&lang=french.
 - [10] Zong Yan Wu, Jean-Louis De Bougrenet De La Tocnaye, Marc Le Menn, and Philippe Grosso and. Optical refractometer for measuring seawater salinity and corresponding salinity sensor. *Patent 7821622*, 2010.
 - [11] P.A. Tipler and G. Mosca. *Physics for Scientists and Engineers*. Number vol. 1 in Physics for Scientists and Engineers. W.H. Freeman, 2008.
 - [12] Huanic Optoelectronic. Reddot laser module type: Di635-2-3. [http://huanic.com/webs/laser-module/red/pdf/reddot/DI635-2-3\(5x12\).pdf](http://huanic.com/webs/laser-module/red/pdf/reddot/DI635-2-3(5x12).pdf).
 - [13] J.T. Wallmark. A new semiconductor photocell using lateral photoeffect. *Proceedings of the IRE*, 45(4):474–483, april 1957.
 - [14] I. Edwards. Using photodetectors for position sensing. *Sensors Magazine*, Dec 1988.
 - [15] Hamamatsu Corporation. Characteristics and use of psd. http://sales.hamamatsu.com/assets/pdf/catsandguides/psd_technical_information_eng_2.pdf.
 - [16] Hamamatsu Corporation. One-dimensional psd s3931, s3932, s3270. http://sales.hamamatsu.com/assets/pdf/parts_S/s3931_etc_kpsd1002e06.pdf.
-

- [17] Norland Products Inc. Norland optical adhesive 63. <https://www.norlandprod.com/adhesives/NOA%2063.html>.
 - [18] Hamamatsu Corporation. Signal processing circuit for 1-d psd c3683-01. http://sales.hamamatsu.com/assets/pdf/parts_C/C3683-01.pdf.
-

Figures and tables

Figures

2.1	Illustration of Snell–Descartes law	39
2.2	The positive temperature coefficient of absolute refractive index for several Schott glasses	41
2.3	The negative temperature coefficient of absolute refractive index for several Schott glasses	41
2.4	The prototype of the optical design of the refractometer	43
2.5	Principle of geometric method	44
2.6	The relationship between the laser spot position and the index of refraction (IOR)	46
2.7	The required laser spot position sensitivity for different refractive index sensitivity requirement	47
2.8	The structure of the laser module	48
2.9	The principle of 1-D lateral-effect PSD	48
2.10	The unaligned prism	51
2.11	The mounting for the prism collage	51
2.12	The mounting for the adhesive of laser module	52
2.13	Some important notion of mounting laser module	52
2.14	The mounting for the adhesion of PSD	53
2.15	The mounting for verifying the fabrication process	54
2.16	The set up for verifying the resolution of PSD	55

Tables

2.1	Sellmeier coefficients for special glasses	40
2.2	Thermal expansion coefficients for different glasses in a range of -30 and $70\text{ }^{\circ}\text{C}$	42

Chapter 3

CCD-based refractometer: ready to build a multi-functional sensor

Contents

Introduction	61
I CCD-based position detection	61
I.1 Review the principle and limitation of PSD	61
I.2 Principle of pixel-based image sensor	62
I.2.1 Principle of CCD image sensor	63
I.2.2 Compare to CMOS image sensor	64
I.3 Image location algorithms	66
I.3.1 General introduction	66
I.3.2 Well-known algorithms	67
I.3.3 Selection of the algorithm	69
II Performance analysis of CCD- and PSD-based system	69
II.1 Resolution	69
II.2 Speed	71
II.3 Saturation	72
III Evaluate the parameters of CCD-based system	73
III.1 Number of processed images	74
III.2 Threshold	75
III.3 Optimum image window size	76
III.4 Laser beam power & Saturation	76
IV Performance comparison of CCD and PSD-based system	77
IV.1 Resolution	78
IV.2 Speed	79
V Performance trade-off of CCD-based system	80
V.1 Number of images processed	80
V.2 Image window	81
V.3 Binning	82
Conclusion	83
Bibliography	86
Figures and tables	87

Introduction

In last chapter, we introduced the modelling, design, implementation of a refractometer based on the measurement of laser beam deviation by a 1-D PSD. This method obtains a high resolution in measuring the refractive index of seawater. However, the requirement of multi-functional sensor and the limitation of PSD determine that a single PSD is not a good candidate to measure multiple quantities.

To overcome the limitation of PSD, a new light position detection method based on Charge-Coupled Device (CCD) is introduced in this chapter and compared with the PSD-based method. CCD, which records the distribution of the incident light, provides not only the ability to calculate the light position information but also the possibility to retrieve other useful information from the light distribution.

The first part of this chapter presents the basic principle of the CCD-based location method. The limitation of PSD is reviewed at the beginning of this chapter. As an optoelectronic device, CCD and its similar alternative CMOS image sensor are introduced. Both of these two devices do not directly provide information on position but rather on laser spot shape and intensity distribution. The position information is retrieved by different post-processing algorithms, which are also introduced in the first part of this chapter.

To compare the CCD- and PSD-based method. Centroid algorithm, which computes the gravity center of the incident light as the PSD does, is chosen as the post-processing algorithm. The second part of this chapter analyses the performance of PSD-based method and CCD-based method combined with centroid algorithm in two aspects: resolution and speed. An important phenomenon for optical sensor, named saturation, is specially discussed in this part as well.

In the third part, several experiments were carried out to evaluate five factors of CCD-based system combined with centroid algorithm: image window size, number of processed images, threshold, binning and saturation. By applying the optimized parameters, several experiments were made to compare CCD-based system with the state-of-the-art PSD-based system in terms of two performance indicator, namely resolution and speed.

At the end, we provide several possible ways to improve the performance of CCD-based system combined with centroid algorithm.

I CCD-based position detection

I.1 Review the principle and limitation of PSD

The principle of 1-D PSD is showed in Fig 3.1. PSD has a single active area formed by a P-N junction. The two parts that originated from the laser spot to the two electrodes form two lateral resistances for the photo-currents running towards the electrodes. The photo currents are collected through the resistances by the output electrodes, which are inversely proportional to the distance between the electrode and the center of the incoming light beam. This relationship is expressed as follows:

$$x = \frac{L}{2} \frac{I_2 - I_1}{I_2 + I_1} \quad (3.1)$$

where I_1 and I_2 are the electrode photo-currents, L is the length of the PSD active area and x stands for the laser spot position.

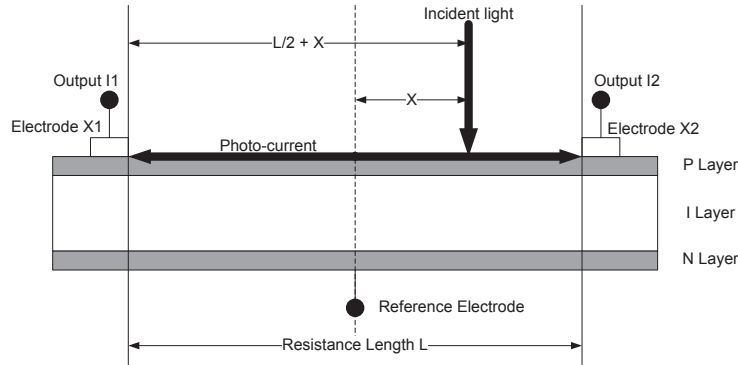


Figure 3.1: Principle of 1-D PSD

As an analogue device, PSD provides high sensitivity, short response time and independence from light spot size, shape and intensity. However, PSD has its own limitations as well, which have been discussed in chapter 2:

1. PSD is designed to measure light position, which makes it not proper to be applied to a multi-functional sensor
2. The PSD analogue output signal makes it hard to benefit from modern post-processing techniques
3. External circuit needs two identical operational amplifiers to amplify the analogue signal, which is hard to achieve.
4. Light intensity distribution must not change during the light movement.

As we discussed in chapter 1, the study of multi-functional *in situ* sensor is a valuable topic for the physical oceanography. Since the limitation of PSD makes it not a good candidate to measure multiple quantities at the same time, it is necessary to find out another optoelectronic device which can be used to compute not only the laser beam deviation but also other quantities we are interested in. Before we discuss the measurement of other quantities with new optoelectronic device, it is necessary to prove that the new device can obtain at least the same resolution of measuring the laser beam deviation as PSD does. In this chapter, we propose to measure the laser beam deviation by using a Charge-Coupled Device (CCD) and we prove that CCD-based light position detection system obtains better performance than PSD-based system.

I.2 Principle of pixel-based image sensor

One drawback of PSD is its simple analogue output signals. The output of PSD is two photo-currents, implying the light position information. In a multi-functional sensor the light intensity distribution contains much more information, including the light position information. These information are difficult to be retrieved from the two photo-currents generated by PSD. A better way is to record the light intensity distribution in a 2-dimension space, which recalls the pixel-based image sensor. In modern technology, there exists two different types of pixel-based image sensor: Charge-Coupled Device (CCD) and Complementary Metal-Oxide-Semiconductor (CMOS).

I.2.1 Principle of CCD image sensor

In 1969, the Charge-Coupled Device (CCD) was invented by W. Boyle and G. E. Smith[1], recording illumination in a pixel-based image. Both types of image sensors, CCD or CMOS, convert light into electric charge and process it into electronic signals. A CCD image sensor consists of a large number of light-sensing elements arranged in a two-dimensional array on a thin silicon substrate. The semiconductor properties of silicon allow the CCD chip to trap and hold photon-induced charge carriers under appropriate electrical bias conditions. The fundamental light-sensing unit (or pixel) of the CCD is a metal oxide semiconductor (MOS) capacitor operated as a photodiode and storage device. A single MOS device of this type is illustrated in Figure 3.2, with reverse bias operation causing negatively charged electrons to migrate to an area underneath the positively charged gate electrode[2]. Electrons liberated by photon interaction are stored in the depletion region up to the full well reservoir capacity. When multiple detector structures are assembled into a complete CCD, individual sensing elements in the array are segregated in one dimension by voltages applied to the surface electrodes and are electrically isolated from their neighbors in the other direction by insulating barriers, or channel stops, within the silicon substrate.

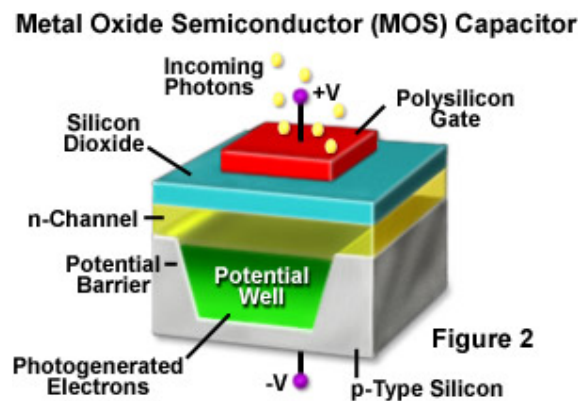


Figure 3.2: Principle of Metal Oxide Semiconductor (MOS) Capacitor

The light-sensing photo diode elements of the CCD respond to incident photons by absorbing much of their energy, resulting in liberation of electrons, and the formation of corresponding electron-deficient sites (holes) within the silicon crystal lattice. One electron-hole pair is generated from each absorbed photon, and the resulting charge that accumulates in each pixel (usually called photoelectrons) is linearly proportional to the number of incident photons. External voltages applied to each pixel's electrodes control the storage and movement of charges accumulated during a specified time interval.

Image generation with a CCD camera can be divided into four primary stages or functions: charge generation, collection and storage of the liberated charge, charge transfer, and charge measurement. Fig 3.3 is the structure of a typical CCD image system. The charge generation stage is the process that the light-sensing photo diode element absorb the photons and resulting photoelectrons. These photoelectrons generated in the depletion region are initially collected into electrically positive potential wells associated with each pixel.

Before the stored charges can be measured to determine photo flux on the pixel, the charge must first be transferred to a readout node while maintaining the integrity of the charge packet. The readout process is operated line by line as shown in Fig 3.3. A line

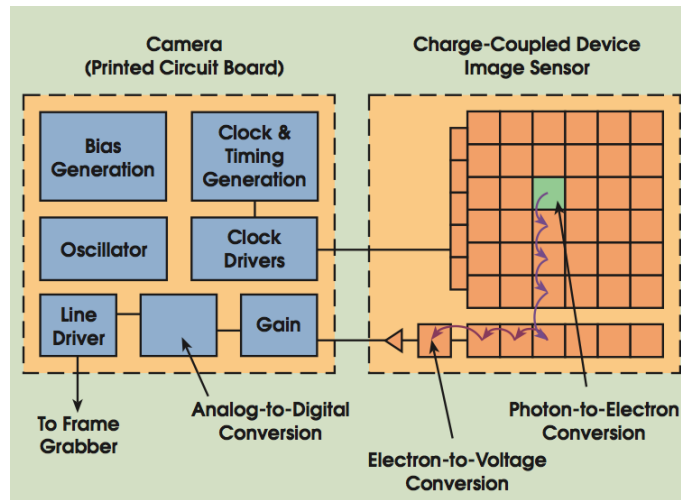


Figure 3.3: Principle of CCD image sensor (DALSA tech. paper)

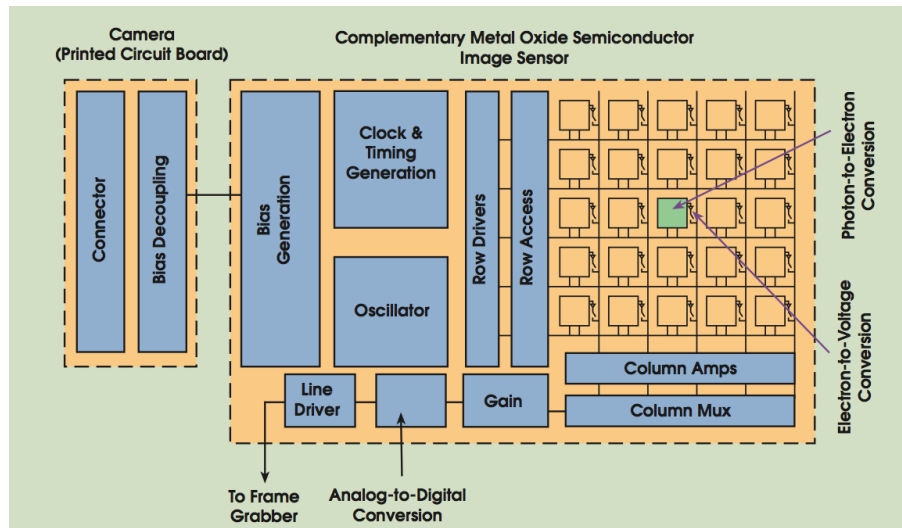


Figure 3.4: Principle of CMOS image sensor (DALSA tech. paper)

of stored charges transfer into a special structure called serial register at the same time. This line of stored charges are then shifted into an unique output node to be amplified and converted to voltage, buffered and send off-chip as an analogue signal. This analogue signal is then pass through the Analog-Digital Converter (ADC) in order to be transferred as a digital signal and stored in the storage device, eg. hard disk or memory. This process continues line by line until all the pixels of the CCD have been transferred and measured.

I.2.2 Compare to CMOS image sensor

Both CMOS and CCD chips sense light through similar mechanisms, by taking advantage of the photoelectric effect, which occurs when photons interact with crystallized silicon to promote electrons from the valence band into the conduction band. The difference between these two types of image sensor is the way they transfer the photoelectrons charges into voltage. Fig 3.4 shows the principle of CMOS image sensor. After the conversion from

photon to electron, CMOS image sensor directly convert the charges into voltage inside the pixel rather than transfer them to a unique readout node like CCD does, because in CMOS sensor, each diode contains its own electron-to-voltage converter, while CCD has only one read out node to do the same function. This difference is depicted in Fig 3.5.

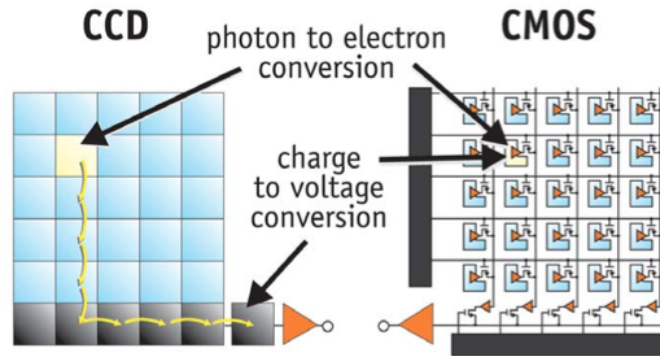


Figure 3.5: The difference between CCD and CMOS

Based on the difference, the performance of these two types of image sensor is different. The comparison between these two methods are carried out in 7 aspects: responsivity, dynamic range, uniformity, shuttering, speed, windowing, and antiblooming[3].

Responsivity is the amount of signal the sensor delivers per unit of input optical energy. CMOS imager sensors are marginally superior to CCDs in this aspect, because gain elements are easier to place on a CMOS image sensor.

Dynamic range refers to the maximum signal level with respect to noise. CCD has an advantage by about a factor of two in comparable circumstance, because CCD has less on-chip circuitry, which has less on-chip noise compared to CMOS.

Uniformity is the consistency of response for different pixels under identical illumination conditions. CMOS image sensors are traditionally much worse than CCDs in this aspect. Each pixel has an open-loop output amplifier, and the offset and gain of each amplifier varied considerably because of wafer processing variations, making both dark and illuminated non-uniformities worse than those in CCDs.

Shuttering refers to the ability to start and stop exposure arbitrarily. This is a standard feature of virtually all consumer and most industrial CCDs, while implementing uniform electronic shuttering in CMOS image sensors requires a number of transistors in each pixel. Usually, CMOS image sensor use a rolling shutter exposes different lines of an array at different times.

Speed is an area, in which CMOS arguably has the advantage over CCDs because all camera functions can be placed on the image sensor.

Windowing is the ability to read out a portion of image sensor. This capability is natural to CMOS image sensors, but limited in CCDs.

Antiblooming refers to the ability to drain localized overexposure without compromising the rest of the image in the sensor. The blooming phenomenon is first discovered

in CCD, thus it requires specific engineering to achieve this capability. On contrary, CMOS generally has natural blooming immunity.

Table 3.1 lists the performance comparison of the CCD image sensor and CMOS image sensor. From this table, we can find that both CCD and CMOS have their own advantages and disadvantages. Since the light distribution is especially important in our situation, the performance of uniformity and dynamic range are significant for our application, thus we chosen CCD as our image sensor. It should be noticed that CMOS image sensor is also a good candidate to measure the light distribution for the laser beam deviation and other quantities. For instance, Peter F. I. Scott *et al.*[4] designed a laser beam deviation measurement system based on a CMOS image sensor and obtained very high resolution.

Table 3.1: Comparison between CCD image sensor and CMOS image sensor

Performance/Feature	CCD image sensor	CMOS image sensor
Responsivity	Moderate	Slightly better
Dynamic range	High	Moderate
Uniformity	High	Low to Moderate
Uniform Shuttering	Fast, common	Poor
Speed	Moderate to High	Higher
Windowing	Limited	Extensive
Antiblooming	High to none	High
System Noise	Low	Moderate
System Complexity	High	Low

I.3 Image location algorithms

Although the image captured by CCD records the distribution of laser spot intensity, it cant directly provide the position information, instead, an image location algorithm is needed to retrieve the laser spot position. This part introduces several popular image location algorithms to calculate the laser spot position.

I.3.1 General introduction

There are two tasks to be performed in the process of computing the locations of target images: recognition and location[5]. The detection of the target images is required to unambiguously identify targets within a scene. The location of the target image is generally a second process which precisely and accurately determines the target image position within the digital image frame. In our situation, the recognition task can be ignored because there is only one target, the laser spot, need to be located. It should be noticed that the position of the light spot depends on its definition in different applications. Thus these location algorithms are also depending on different position definitions.

As we discussed in last chapter, to reach the requirement of refractive index measurement resolution, the accuracy of laser beam deviation measurement should reach to $0.3 \mu m$. However, the size of the modern CCD pixel is usually larger than $3 \mu m$. This requires that the location algorithm has a sub-pixel resolution.

I.3.2 Well-known algorithms

Before processing the algorithms, the light distribution need to be captured. The image-capture process of a CCD-based system contains sampling, amplification and quantization. It first samples the optical intensity and then converts the sample into signal charge, which is transformed into voltage through a common output. After voltage quantization, all signals are processed by the post-processing algorithm to calculate the position. For a incident light with the light intensity distribution $f(x, y)$, the sampled signal $p(x, y)$ can be expressed as:

$$p(x, y) = f(x, y)s(x, y) = \sum_{j_1=-\infty}^{\infty} \sum_{j_2=-\infty}^{\infty} f(j_1\Delta x, j_2\Delta y)\delta(x - j_1\Delta x, y - j_2\Delta y), \quad (3.2)$$

where $p(x, y)$ is the sampled signal, and $s(x, y)$ is the sampling function. δ here stands for the dirac function. Δx and Δy are the pixel width and height respectively. All the location algorithms process the discrete sampled signal, and calculate the location according to their location definition.

Centroid method

The most famous location algorithm is the centroid algorithm, which calculates the gravity center of the target. For a target $f(x, y)$, the center (x_c, y_c) given by the centroid algorithm is expressed as:

$$x_c = \frac{\int_{x=-\infty}^{\infty} \int_{y=-\infty}^{\infty} x f(x, y) dx dy}{\int_{x=-\infty}^{\infty} \int_{y=-\infty}^{\infty} f(x, y) dx dy} \quad (3.3)$$

$$y_c = \frac{\int_{x=-\infty}^{\infty} \int_{y=-\infty}^{\infty} y f(x, y) dx dy}{\int_{x=-\infty}^{\infty} \int_{y=-\infty}^{\infty} f(x, y) dx dy} \quad (3.4)$$

When applying this algorithm to the sampled signal, the image captured by the CCD, this algorithm is written as follows:

$$x_c = \frac{\sum_{i=-\infty}^{\infty} \sum_{j=-\infty}^{\infty} i p_{i,j}}{\sum_{i=-\infty}^{\infty} \sum_{j=-\infty}^{\infty} p_{i,j}} \quad (3.5)$$

$$y_c = \frac{\sum_{i=-\infty}^{\infty} \sum_{j=-\infty}^{\infty} j p_{i,j}}{\sum_{i=-\infty}^{\infty} \sum_{j=-\infty}^{\infty} p_{i,j}} \quad (3.6)$$

in which $p_{i,j}$ stands for the pixel value in the i th column and j th row of the image. Another form of the equation 3.3 can be found in the form of Fourier transformation, which is very useful to study the systematic error of the centroid algorithm[6]:

$$x = -\frac{F'_u(0, 0)}{2\pi j F(0, 0)}, \quad (3.7)$$

where $F_u(x, y)$ is the Fourier transform of $f(x, y)$, and $F'_u(x, y)$ is the derivative of F_u . The reported accuracy of centroid algorithm is about 0.1 pixel.

Squared centroid method

Another famous algorithm, the squared centroid algorithm is originated from the centroid algorithm. The invention of this algorithm is to improve accuracy of centroid algorithm in a noisy image. The principle of this algorithm is expressed by this equation:

$$x_c = \frac{\int_{x=-\infty}^{\infty} \int_{y=-\infty}^{\infty} x f^2(x, y) dx dy}{\int_{x=-\infty}^{\infty} \int_{y=-\infty}^{\infty} f^2(x, y) dx dy} \quad (3.8)$$

$$y_c = \frac{\int_{x=-\infty}^{\infty} \int_{y=-\infty}^{\infty} y f^2(x, y) dx dy}{\int_{x=-\infty}^{\infty} \int_{y=-\infty}^{\infty} f^2(x, y) dx dy} \quad (3.9)$$

Several studies have compared the accuracy of squared centroid algorithm and the centroid algorithm. The squared centroid algorithm obtains nearly the same accuracy (about 0.1 pixel) as the centroid algorithm does. What is more, the squared centroid method has better performance than centroid algorithm in high noise image.

Fourier transform method

Both the centroid and squared centroid algorithm try to calculate the gravity center of the image. Apart from this definition, another method, the Fourier transform based method, measures the position of the laser spot from the frequency domain rather than the space domain. The Fourier transform of the laser spot $f(x, y)$ is expressed as:

$$F(u, v) = \int \int_{-\infty}^{\infty} f(x, y) e^{-j2\pi(ux+vy)} dx dy \quad (3.10)$$

If the laser spot moves a distance x_c in the x direction, the Fourier transform for the new laser spot $f(x - x_c, y)$ is (let $t = x - x_c$):

$$\begin{aligned} F_1(u, v) &= \int \int_{-\infty}^{\infty} f(x - x_c, y) e^{-j2\pi(ux+vy)} dx dy \\ &= \int \int_{-\infty}^{\infty} f(t, y) e^{-j2\pi(u(t+x_c)+vy)} dt dy \\ &= \int \int_{-\infty}^{\infty} f(t, y) e^{-j2\pi(ut+vy)} e^{-j2\pi(ux_c)} dt dy \\ &= e^{-j2\pi ux_c} F(u, v) \end{aligned} \quad (3.11)$$

Equation 3.11 shows that the laser spot deviation x_c can be calculated in the case when the laser spot distribution does not change during the displacement. If this requirement is fulfilled, the accuracy of this method can reach at least 0.1 pixel.

Edge detection method

Besides the gravity center, the geometric center is another possible definition for the laser spot position. The algorithms based on this definition are categorized as the edge detection methods. This kind of method is based on the fact that the shape of the target is known, usually circle or ellipse. To locate the target, two steps are needed. First, an edge detection algorithm is used to highlight the edge of the target. With the edge, the geometric center is then calculated.

In 1986, the Canny edge detection operator[7] was developed by John F. Canny and uses a multi-stage algorithm to detect a wide range of edges in images. The further research have improved the accuracy of this method to sub-pixel level. Another famous edge detection operator is the sobel operator. Technically, it is a discrete differentiation operator, computing an approximation of the gradient of the image intensity function. The algorithm based on sobel operator reaches sub-pixel accuracy as well.

For laser spot, the detected edge is an ellipse, usually in the following form:

$$\frac{(x - x_c)^2}{r_x} + \frac{(y - y_c)^2}{r_y} = 1 \quad (3.12)$$

With the detected ellipse edge, a Hough transform is made to evaluate the center of the ellipse (x_c, y_c) and the two diameters r_x, r_y . This method can also reach sub-pixel accuracy, but it has higher time complexity than the other algorithms.

I.3.3 Selection of the algorithm

As we discussed above, many algorithms can be used for laser beam position calculation. Algorithm selection is based on the definition of laser beam position, which highly depends on the applications. To compare with PSD, the definition of the laser beam position should be defined as the same as the PSD-based system, which is the gravity center of laser spot. Therefore, the centroid algorithm has been used here to calculate the gravity center due to its simplicity. It should be noted that centroid algorithm is not the most suitable algorithm in our application. The limitation of centroid algorithm will be discussed in chapter 4, in which a new algorithm is proposed. In this chapter, since our purpose is to compare the CCD-based method with the PSD-based method, and try to prove that the CCD-based method can obtain better performance, thus the centroid algorithm which measures the same quantity as PSD does is a proper algorithm for our discussion.

II Performance analysis of CCD- and PSD-based system

In this section, we analyse the performance of the CCD-based system and compare it with the PSD-based one. Two performance indicators, named resolution and speed, are discussed for both of them. Since saturation is a common issue for the photoelectronic devices, the impacts of saturation to both of CCD- and PSD-based system are studied at the end of this chapter.

II.1 Resolution

The resolution of a CCD-based laser beam deviation measurement system depends on three aspects: systematic error caused by sampling, quantization and centroid algorithm, systematic error due to noise, and their corresponding uncertainties. We assume here that the laser spot moves a distance d from position X_0 to position X_d along the x axis. Let e_c be the systematic error caused by sampling, quantization and centroid method, the following relationship exists:

$$x_d = \bar{x}_0 + d + e_c \quad (3.13)$$

The systematic error e_c caused by sampling, quantization and centroid algorithm could be calculated by substituting equations 3.7 and 3.13 and used for correcting the resolution in the post-processing phase. The resolution of the centroid algorithm is also determined by

the noise of the image sensor, which includes three types of noises: the readout noise N_r , the signal photon noise N_p and the background noise N_b . The background noise and the readout noise impinge all the pixels in the image window; in contrast, the signal photon noise just impacts the pixels illuminated by the laser spot. Since the centroid algorithm processes all the pixels of the image, the centers of both the laser spot and noises are calculated. If the laser spot moves a distance d from x_0 , the calculated center x_d' is:

$$x_d' = \frac{x_r M_{rn} + x_b M_{bn} + x_p M_{pn} + (x_0 + d + e_c) M_s}{M_{rn} + M_{bn} + M_{pn} + M_s}, \quad (3.14)$$

where x_r , x_b , x_p are the centers of readout noise, background noise and light photon noise, respectively, while M_{rn} , M_{bn} , M_{pn} , M_s respectively represent the mass of readout noise, background noise, light photon noise and laser spot. As a reference, in a noisy environment, the equation that expresses the original position x_0' is listed below:

$$x_0' = \frac{x_{r_0} M_{rn} + x_{b_0} M_{bn} + x_{p_0} M_{pn} + x_0 M_s}{M_{rn} + M_{bn} + M_{pn} + M_s}, \quad (3.15)$$

in which x_{r_0} , x_{b_0} , x_{p_0} are the original centers of readout noise, background noise and light photon noise. The background noise and the readout noise follow the Poisson distribution which can be approximately considered as a Gaussian distribution. Since these two noises impact all the image pixels, the center of noises is independent of the laser spot. That's to say, the following relationship holds: $x_{r_0} = x_r$ and $x_{b_0} = x_b$. On the other hand, the signal photon noise is related to the laser spot intensity, thus the assumption could be made that the moved distance of light photon noise approximately equals the moved distance of laser spot d or $x_p = x_{p_0} + d$. By substituting equation 3.14 and 3.15, the systematic error e is shown as:

$$e = \frac{e_c M_s - d(M_{rn} + M_{bn})}{M_{rn} + M_{bn} + M_{pn} + M_s} \quad (3.16)$$

Fig 3.6 shows the relationship between the original position x_0' , and the gravity center of the noises. The size of the circle presents the mass of the light intensity, while the point inside the circle is the gravity center of the portion of light. From this figure, we can find that the calculated laser spot position is the mass center of the original laser spot and the noises.

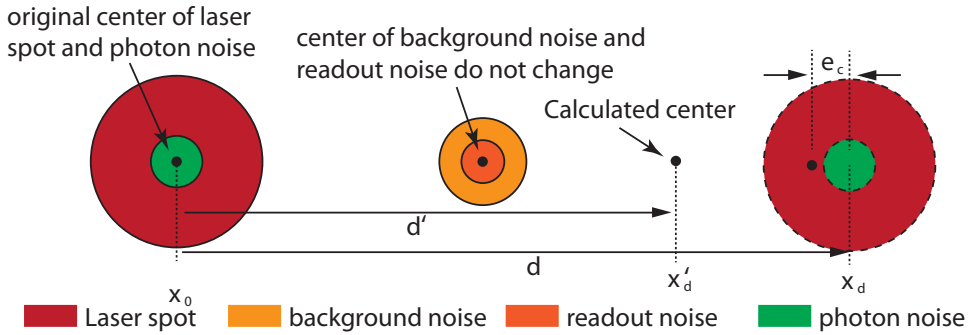


Figure 3.6: The relationship between the calculated spot center and the noise center

The ratio between the calculated distance d' and the moved distance of the laser spot

could be expressed as follows:

$$\frac{d'}{d} = 1 + \frac{e}{d} = \frac{M_{pn} + M_s + \frac{e_c}{d} M_s}{M_{rn} + M_{bn} + M_{pn} + M_s} \quad (3.17)$$

The systematic error caused by noise can be eliminated or at least reduced in both the capture and post-processing phases. Applying a threshold in the post-processing algorithm can efficiently eliminate the readout noise and background noise. Another post-processing way to increase the signal to noise ratio (SNR) is to average it using multiple images. If N images are used for the calculation, the SNR increases \sqrt{N} times. Temperature also has a very close relationship with the noise. Typically, the CCD temperature should be reduced as much as possible. In the laser deviation measurement system, the temperature increase caused by the laser also increases the noise. In the capture phase, the use of pulsed laser and synchronized exposure can solve this problem. In sections III and IV, experiments applying these methods to improve the resolution are described.

The resolution of PSD have been discussed in chapter 2. For PSD-based system, the systematic error is mainly due to the amplifier asymmetry for the two current signals I_1 and I_2 , ambient light, physical construction of the detector head, and y-axis displacement [8]. Noise is also a key factor that may impact the resolution, including thermal noise current, shot noise and amplifier noise. To improve the PSD resolution, we can increase inter-electrode resistance, which results in a reduction of both amplifier and shot noise. Another way to improve the resolution is to use symmetric and low noise operational amplifiers, but it results in quite an expensive external processing circuit. The error caused by the background light can be eliminated using Pulse Amplitude Modulation, shown in [9].

II.2 Speed

Speed is another important feature for the deviation position measurement. One of the indices to judge PSD speed is response time, defined as the time during which the output signal rises from 10% to 90% of its peak value. The PSD response time depends mainly on the physical features of the PSD, for example its inter-electrode resistance and terminal capacitance. The reverse voltage also affect the response time. For most advanced PSDs, the response time can reach $3 \mu s$. In practice, the PSD output signal will be sampled and digitalized for calculation, the response time of the external circuit need to be counted as well. To reduce the error caused by noise, the average of more than one sample should be calculated. In general, the time cost for PSD-based system mainly depends on the sum of the digitalized time, number of sample, sampling frequency and the computing time. Fig 3.7 (a) depicts the cost time for acquiring one laser spot position with N PSD output samples.

Compared to PSD, the CCD image sensor cannot output a continuous signal: instead, it generates series of frames, which is a snapshot of the laser beam spot. The overall processing time t of a separate frame can be approximately calculated as:

$$t = t_e + t_r + t_s + t_l + t_p, \quad (3.18)$$

in which t_e is the exposure time, t_r is the readout time, t_s is the time used for storing the image, t_l is the image load time and t_p stands for the algorithm processing time. Fig 3.7 (b) shows the time cost of acquiring one laser spot position by using a CCD-based system. The readout time includes the time in which all the rows shift into serial register, the time in which the pixels move to the AD converter under clock control, and the time spent

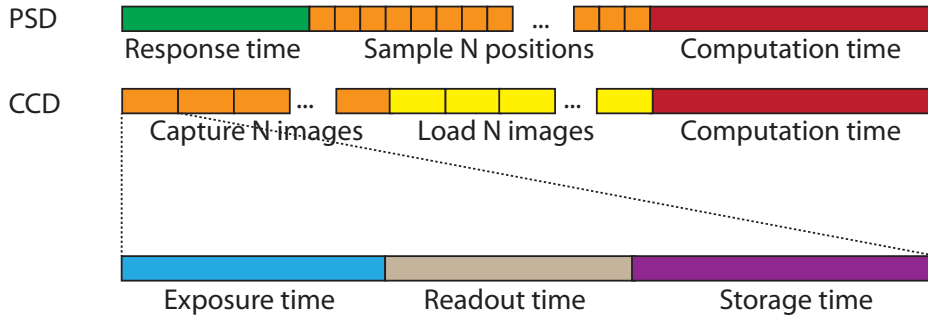


Figure 3.7: The time cost for acquiring one laser spot position with PSD- and CCD-based system

by AD conversion and digitization. Exposure time must be long enough for the image sensor capture. The readout time depends critically on the clock frequency, window size and window position. After the image is generated, the centroid of the algorithm will take time to process the image. Image size, algorithm used and processor frequency are the main factors impacting the processing time. For an image with $M \times N$ pixels, the time complexity of the centroid algorithm is $O(MN)$.

Several techniques are available to reduce the processing time of image sensors. The CCD with dual serial registers and two amplifiers can speed up the readout time. A laser with larger intensity could shorten the exposure time. The CCD with region of interest and binning features could output fewer pixels, which can also improve the post-processing speed with the cost of lowering the resolution. Implementing the algorithm in hardware is another efficient way to improve the speed of CCD-based systems.

II.3 Saturation

Usually, for optical sensors, saturation results in large error and should definitely be avoided. In practice, the PSD output current follows a good linearity with respect to the laser spot position. If the incident light power is too high and therefore the saturation occurs, the output current is no longer linear with the laser spot position. Hence, the center information cannot be retrieved as expected. The parameter “photo-current saturation” is defined as the total output current when the whole active area of PSD is illuminated, and is considered to express the saturation performance of the PSD. This value depends on the inter-electrode resistance of the PSD and the reverse voltage [10]. A direct way to avoid saturation is to reduce incident light intensity. A PSD with small inter-electrode resistance and high reverse voltage can prevent saturation from occurring.



Figure 3.8: The phenomenon of blooming

The saturation of CCD is defined as the maximum amount of charges that the image

sensor pixel can collect. This amount of charge a pixel can hold in routine operation is called its full well capacity [11]. One effect of saturation is that the linearity relationship between the number of collected charges and the received light intensity will not stand near the full well capacity, which causes the output signal to generate unexpected distortion. One possible solution to this problem is to adjust the camera gain control so that the full bit depth of the ADC does not span the linear full well capacity of the camera. This makes the image show saturation before real saturation occurs [12]. Another influence is blooming. When the image pixel full well capacity is reached, the more generated charges or the charges that cannot be transferred will pollute the adjacent image areas. A typical phenomenon of blooming is the appearance of white streak or erroneous pixel signal value near the high intensity pixels as shown in Fig 3.8. With respect to measuring the displacement of laser beams, blooming leads to unexpected and non-recoverable results, so it should be avoided at all cost. If the camera gain is carefully adjusted to limit the ADC work in the linear full well capacity, blooming will not occur when saturation is just observed. For the application discussed in this paper, the gravity center of a given laser spot is highly related to laser spot intensity, hence, saturation should be avoided in the measurement.

III Evaluate the parameters of CCD-based system

In the previous sections, the factors that might impact the resolution and speed of a CCD-based system, have been described, including the laser beam power, the number of frames used to calculate the position, the image window size, binning and threshold. To assess the impact of these parameters on system performance, different experiments have been carried out. Since the resolution and speed of PSD-based systems highly depend on the equipment and device themselves, commercial PSD (Hamamatsu S3932 [13]) and external processing circuits (Hamamatsu C3683-01 [14]) were used in the following experiments for comparing to CCD-based systems.

A diode laser at a wavelength of 635 nm was mounted on a motorized 3 dimension micro-positioner with minimum step size of $0.1 \mu\text{m}$, which moved along the x axis of the image under the control of a computer. The laser was directly pointed at a PSD or a DALSA camera [15], which offers a 1280×960 resolution and a small $3.75 \times 3.75 \mu\text{m}$ pixel size without interspace. In order to control the power of the laser, a polarizer and a filter were set up between the laser and the camera. This setup is shown in Fig. 3.9. The CCD is removable and can be replaced by a PSD.

Before comparing the CCD-based and PSD-based systems,

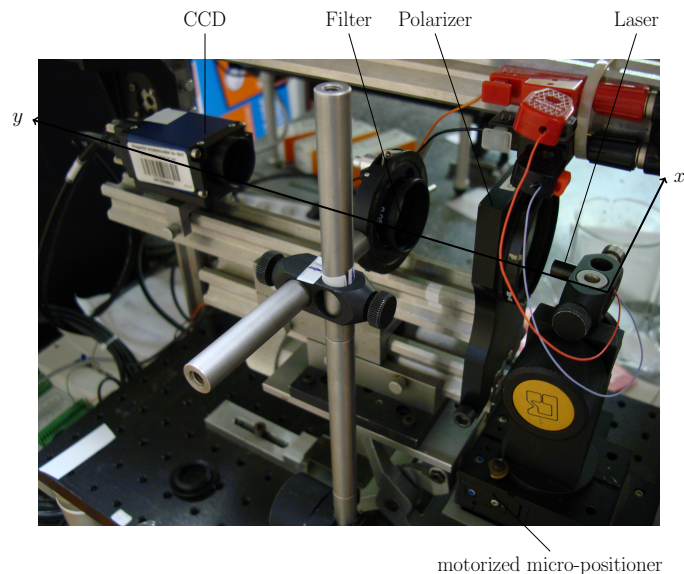


Figure 3.9: The experiment setup

the factors mentioned in the previous sections should be first considered. An experiment was carried out to analyze these factors. During the experiment, the laser was moved to a specific position and 100 full size images were taken in 4 seconds. This experiment was repeated 50 times to avoid accidental error. According to these 50 groups of images, different numbers of images were selected in each group and processed with different image window sizes and thresholds.

The resolution of the system is assessed from two aspects: systematic error and its uncertainty. For assessing systematic error and its uncertainty, the average of calculated centers (the estimate of position [16]) and standard deviations (the standard uncertainty [16]) of all the groups were plotted. The power of the laser beam was adjusted to avoid saturation and blooming, as shown in Fig 3.10. From the bottom chart in Fig 3.10, the gray-scale of the sum of background noise and readout noise reaches about 9. Since the center of ideal Gaussian spot equals the gravity center of the Gaussian spot, a Gaussian fitting was used to obtain the reference position and the laser beam waist. The average Gaussian center of the images calculated by a Gaussian fitting algorithm in the 50 experiments is 663.69 pixels and the average laser spot size¹ is about 80 pixels. With different parameters, the estimate of laser spot position and standard uncertainty were calculated. The systematic error of the CCD-based system was assessed by comparing the estimate of calculated center with the reference center, whereas the uncertainty was evaluated by the standard deviation of calculated centers. A smaller distance between calculated center and reference center gives smaller systematic error, and smaller standard uncertainty is obtained by a smaller standard deviation.

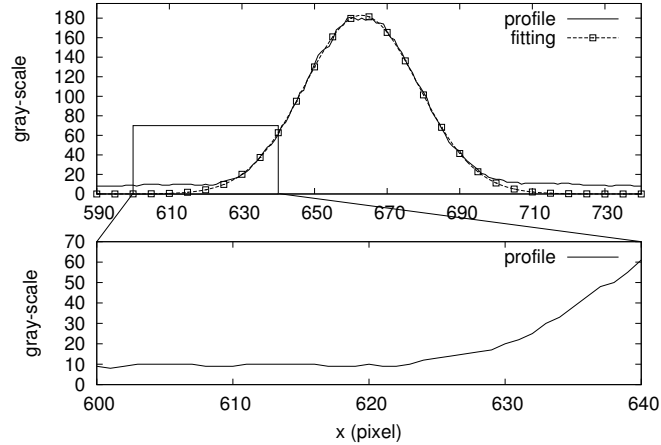


Figure 3.10: The profile of the Gaussian spot

III.1 Number of processed images

With the 50 groups of images, different numbers of images were selected in each group, and the center of each image was calculated with no threshold and full image size. The estimate of calculated center and standard uncertainty are depicted in Fig 3.11. Both the estimate of center and standard uncertainty in this chart show a trend to stabilize as more images were used. This stability could be attributed to the fact that more images give more noise samples making the center of noise more stable. The standard uncertainty remains at a level of less than 0.056 pixels, which gives a high level of precision. However, the center given by the experiment is less than 642.9 pixels, which has a large deviation from the reference center 663.69 pixels. According to equation 3.17, the large systematic error is caused by the noises that will lead to the measured distance being much less than the

¹The laser spot size is defined as the diameter of the spot. The border of the spot is defined as the place where the light intensity reduces to the noise level

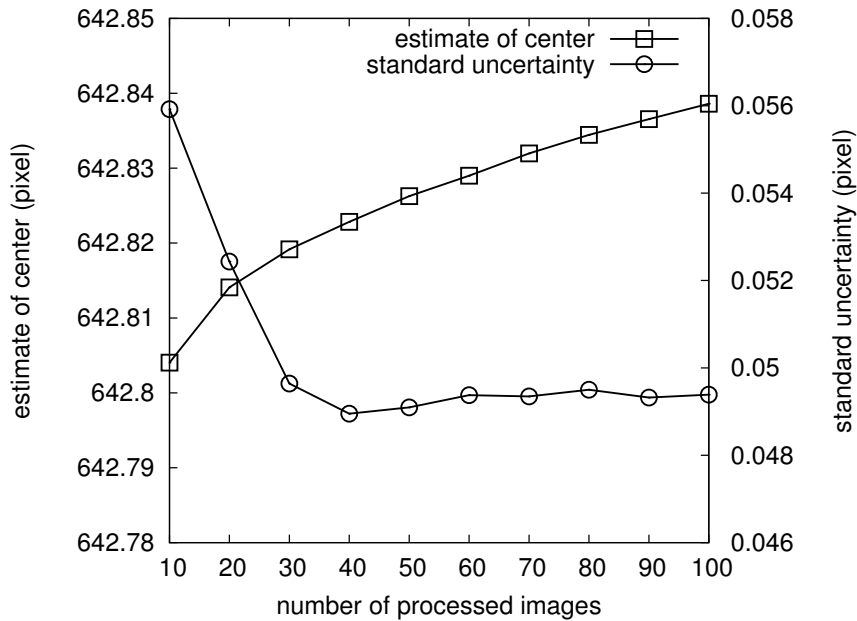


Figure 3.11: The estimate center against the number of processed image

actual distance. Although the result shows a large systematic error, the variance of both estimate of center and standard uncertainty caused by the variance of processed image number is quite small. That is to say, the resolution of CCD-based systems do not highly depend on the number of processed images. It is a good way to improve speed without greatly reducing resolution.

III.2 Threshold

As the number of processed images will not dramatically affect the resolution of a CCD-based system, 10 images were selected for the calculation in the later experiment. As illustrated in previous section, larger noise results in larger systematic error. Applying a threshold is a common method to eliminate the effect of noises. With different thresholds applied to the full-size images, the estimate of center and standard uncertainty were plotted in Fig 3.12. The behavior of estimate and standard uncertainty is quite different between applying a threshold less than the level of noise and applying a threshold larger than the level of noises. When the threshold is less

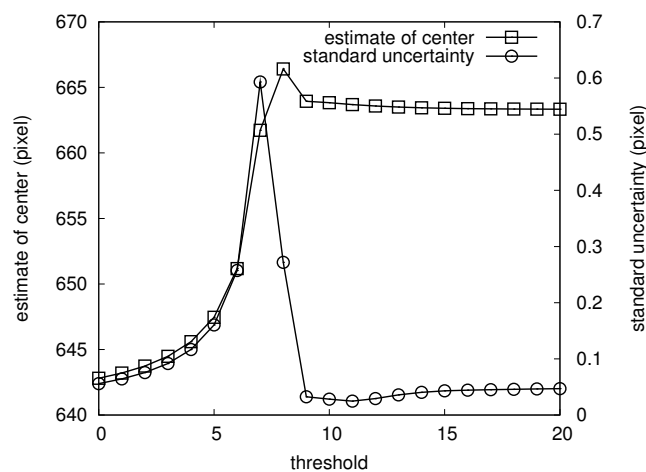


Figure 3.12: The estimate center and the standard uncertainty against the threshold

than the level of noise, the systematic error decreased but the standard uncertainty increased as the threshold gets closer to the level of noise. Once the threshold is beyond the level of noise, both the estimate of center and standard uncertainty remain steady and the system reaches high resolution (with estimate of calculated center 663.33 pixels and standard uncertainty 0.045 pixels).

III.3 Optimum image window size

Fig 3.13 describes how image window size affects resolution. The results are calculated with no threshold and 10 images. It is obvious that both of the systematic error and uncertainty are sensitive to image window size. As image window size increased, smaller uncertainty was obtained, while systematic error increased. One important reason that might lead to the larger systematic error is the fact that the mass of noises increased as the image window got larger. The effect of the image window size mainly applies to the standard uncertainty, which rises exponentially as the image window decreases linearly. To improve speed by using a smaller image window, the size of the image window should be carefully adjusted according to the performance required from the application.

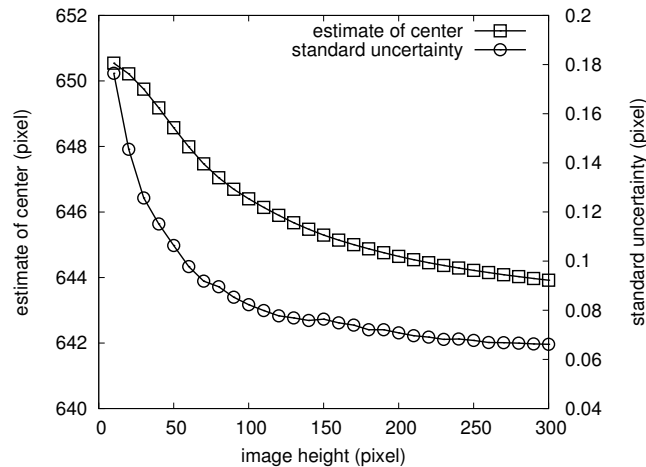


Figure 3.13: The estimate center and the standard uncertainty against the height of image

III.4 Laser beam power & Saturation

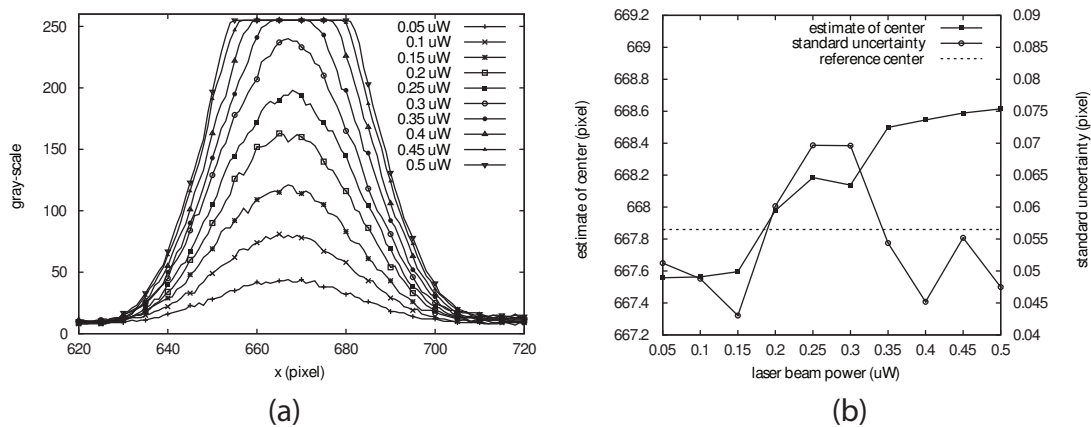


Figure 3.14: The profiles of images with different laser beam power

The power of the laser beam is related to the signal photon noises, which overlay

the Gaussian spot. An extremely high laser beam power will lead to saturation or even blooming. All the signal photon noises, saturation and blooming will interfere with the systematic error and its uncertainty of a CCD-based system. To figure out the systematic error and uncertainty according to different laser beam powers, an experiment was designed and implemented. Fig 3.14 (a) shows the profiles of images with different laser beam powers, and the estimate of centers and standard uncertainty are plotted in Fig 3.14 (b).

The curve of the estimate of centers calculated with different laser power turns out to be a transformation between two states. One state happens when the laser power is less than $0.15 \mu W$, while another occurs after a laser power larger than $0.35 \mu W$. Between these two states, the estimate of center increases quickly as the laser power increases. The slight decrease of $0.3 \mu W$ is possibly caused by accidental error. The formation of the first state is due to the low noises brought by the low laser power, which can be observed in Fig 3.15. The low standard uncertainty at

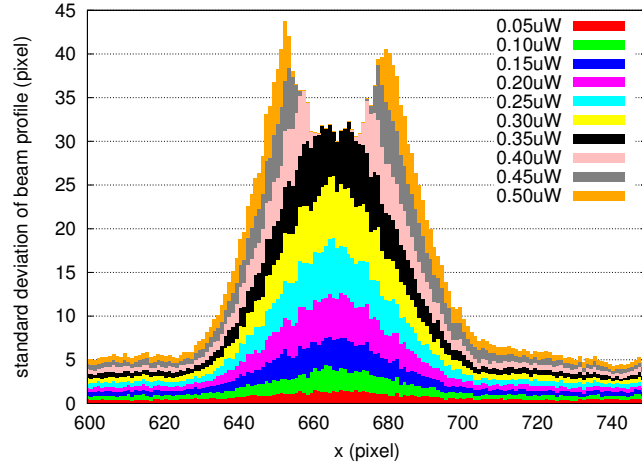


Figure 3.15: The standard deviation of the laser beam profile with different powers

The low standard uncertainty at the same phase further proves this explanation. These noises affect the systematic error in this state, which shows a difference between the reference center (obtained by Gaussian fitting to the images with different powers, 667.86 pixels) and the calculated center. With the increase in laser power, both the standard uncertainty and the estimate of center increased quickly. This trend continues until saturation occurs at the power of $0.35 \mu W$, as showed in Fig 3.14(a). From Fig 3.15, it is clear that the noise rises with the increase of laser power. This impacts the standard uncertainty of the systematic error so that it gives a larger uncertainty when the laser power increases. In addition to noise impacting the systematic error, another factor that affects the systematic error is the fact that the laser polarization might not be ideally uniform. This makes the Gaussian spot center move toward one direction when adjusting the power by polarizer. Compared with Fig 3.14 (a) and Fig 3.14 (b), it is obvious that the second state is due to saturation, which hides most of the signals and noises at the top of the laser spot intensity. Since the noises are hidden by saturation, the standard uncertainty reduced to the level of first state. Both low laser power and saturation provide the system a small uncertainty and a large systematic error. To obtain a smaller systematic error, the power of the laser should be adjusted appropriately to avoid low signal-to-noise ratio and saturation.

IV Performance comparison of CCD and PSD-based system

To compare the two different methods, the CCD image window size was cut to be the same as the size of PSD, that is $4.8 \times 1mm$ (1280×267 pixels). The response of the two methods to various factors was taken by moving the motorized micro-positioner with a step of $0.1 \mu m$, which is considered to be the reference measure to compare the two

methods. During each step, 10000 samples of PSD signals and 64 images were captured in 1 second. For PSD, the laser beam position was calculated by averaging the 10000 PSD signal samples, while the average image of 64 images was used to compute the laser beam position by the centroid algorithm with threshold 10 applied. To obtain a full-range comparison, five zones that are oriented from the center of the sensor were chosen to perform the measurement. In each zone, the micro-positioner was moved by 50 steps. To guarantee that a complete laser beam is contained in the active sensor surface, the range of the measurement is set to the range of -1mm to $+1\text{mm}$ according to the laser beam waist (46.6 pixels in this experiment). The laser was synchronized with the camera exposure by a National Instrument DAQ card in pulse mode. The CCD saturation is avoided by applying a polarizer to reduce the laser power and setting the exposure time to $13\ \mu\text{s}$. All the experiments are carried out in a dark room to obtain the best performance.

IV.1 Resolution

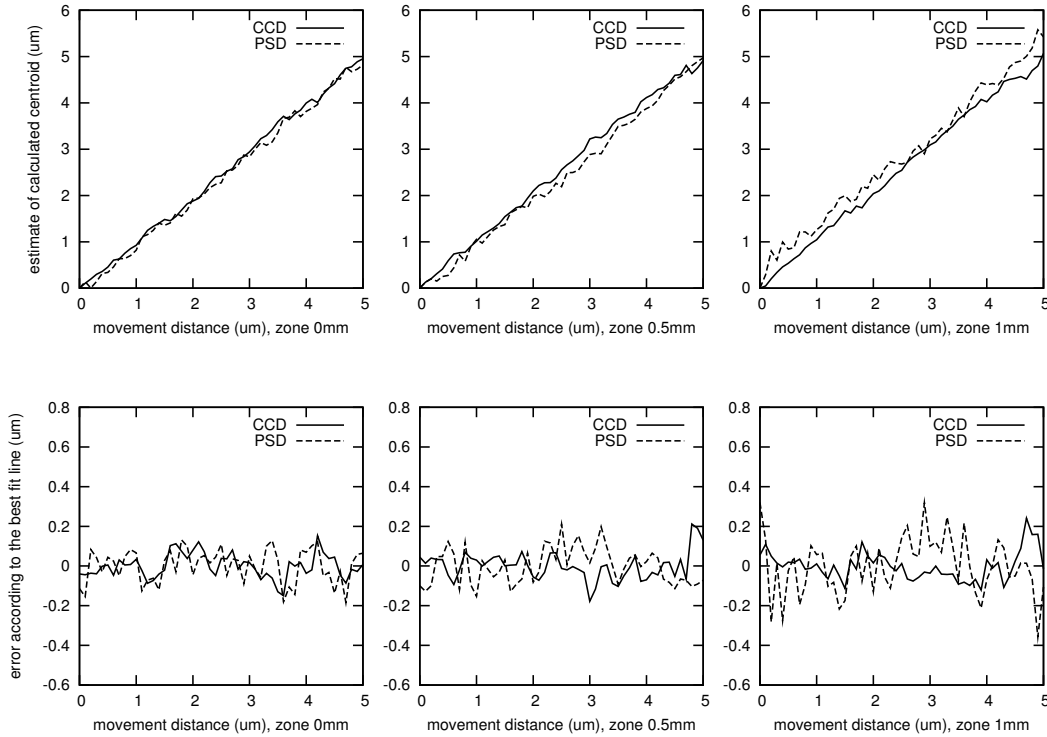


Figure 3.16: The estimated center and the error according to the best fit line against the moved distance

For comparing the resolution of both methods, these centers for PSD and CCD-based systems with different units were converted to distance. The slope of the best fit line indicates the ratio between the measurement unit and the distance. Thus the slopes are used to convert the measurement units to distances which are listed in Table 3.2. In this table, the slopes for a CCD-based system are very close to the inverse of the image pixel size ($0.267\ \text{pixel}/\mu\text{m}$), which shows that the systematic error of CCD-based system is very small according to equation 3.17. The uncertainty can be evaluated by the standard

deviation of the error according to the best fit line. The estimate of calculated centers and the error according to the best fit line of both CCD and PSD in each measurement zone are depicted by Fig 3.16, which shows good linearity for all the zones. The chart in the second row of Fig 3.16 shows that the error of the PSD-based system is larger than that of the CCD-based system.

The standard uncertainty of the errors in each zone are plotted in Fig 3.17, from which we can observe that the uncertainty of the PSD-based system will gradually increase as the laser beam leaves the center. In contrast, the CCD-based system presents a good consistency in all the positions, with an average standard uncertainty $\sigma_x = 0.07 \mu m$. It is obvious that the uncertainty of the CCD-based system is much less than the uncertainty of the PSD-based system (average standard uncertainty $\sigma_x = 0.11 \mu m$) under the same operating conditions. And the resolution of the CCD-based system is insensitive to the laser spot position compared to the PSD-based system.

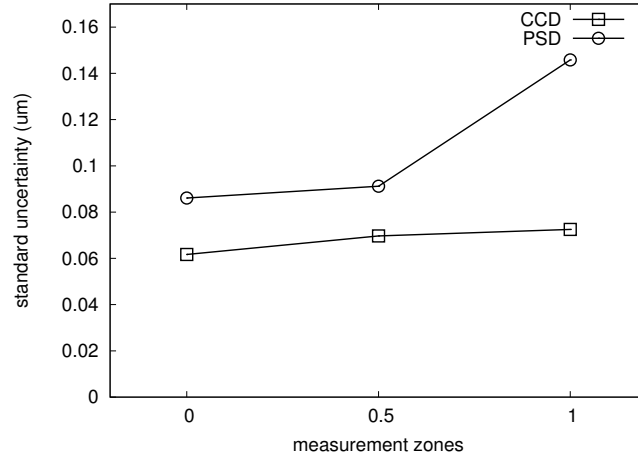


Figure 3.17: The standard uncertainty of systematic error

Table 3.2: The slopes for different zones with CCD and PSD

	0mm	+0.5mm	+1mm
CCD ($pixel/\mu m$)	0.2622	0.2462	0.2625
PSD ($V/\mu m$)	0.0019	0.0018	0.0017

IV.2 Speed

During the experiment, the duration of both capture and processing was recorded simultaneously. The program was implemented in C and was carried out in a DELL notebook LATITUDE E6500. For the PSD-based system, the duration contains not only the time used for capturing, sampling and digitalizing, but also the time elapsed for calculating the average. In addition to these, the image store and load time are also considered for CCD-based system. Fig 3.18 shows the time cost to obtain one laser beam position for both of the systems. The time cost by PSD processing is very short, with an average of $0.35 ms$, so that it can't be observed in Fig 3.18. The primary time cost of the PSD-based system is capture, which highly depends on the sample rate of the external circuit. Compared with the stability of the time cost associated with the PSD-based system, the time cost of the CCD-based system depends greatly on the storage access time (store and load), which takes 80.4% of the total time on average due to the low speed of the storage device. A possible improvement is to store all the images in memory, which is much faster than the external storage device. Furthermore, the processing time will also be reduced due to the fast readout speed of memory. Although the actual processing time reaches about $0.7 s$

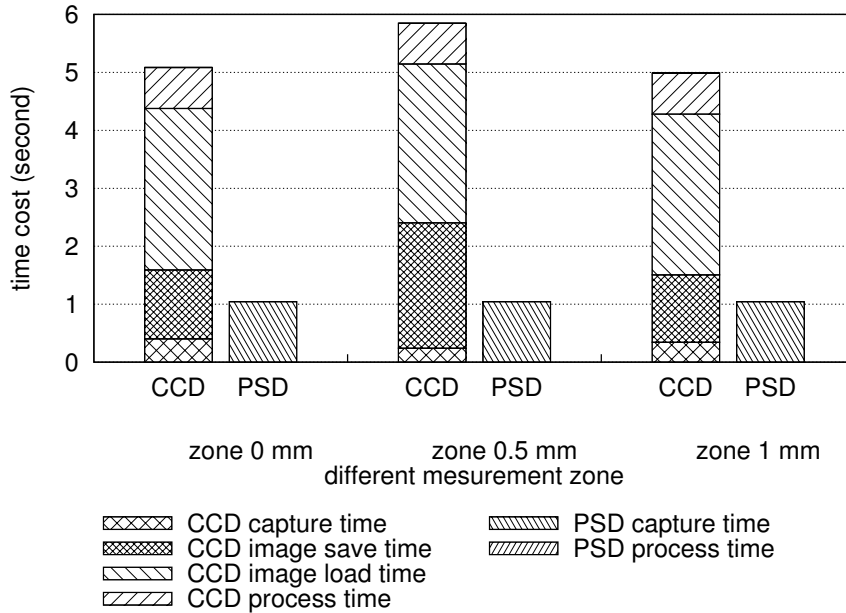


Figure 3.18: Time cost in both CCD- and PSD-based system

on average, which is much longer than the PSD-based system, it only takes 13% of the total time. The time cost on capture and processing is 1.036 s, which nearly equals the time cost of a PSD-based system (1.044 s). Thus, the critical time cost by a CCD-based system is the storage access time, which needs to be optimized in the system design and implementation.

V Performance trade-off of CCD-based system

V.1 Number of images processed

As discussed in section II.2, the time complexity of processing K images with the size of $M \times N$ is $O(KMN)$. The time cost by image processing is related to both the number of images and the image size. In previous experiments, 65 images were used to calculate the center of laser beam. With the same image set, different numbers of images were selected and used to calculate the center. The standard uncertainty of systematic errors and time costs for this processing are shown in Fig 3.19. Time cost is a position-insensitive quantity, which decreases linearly as the number of processed images is reduced. With the decrease of processed images, the calculated centers indicate a tendency toward growth. When 10 images were used for the centroid calculation, the time cost by loading and processing images decreased to 0.53 s on average and the standard uncertainty of error rise to $\pm 0.094 \mu\text{m}$, which increased by 36.2% compared with the standard uncertainty of error of processing 50 images (average standard uncertainty of error is $0.069 \mu\text{m}$). However, this uncertainty is still smaller than the uncertainty of the PSD-based system mentioned in last section. Although fewer images are processed, the uncertainty of systematic error will increased, and the number of processed images will not greatly reduce the resolution. In practical applications, reducing number of the images is a good way to improve speed without losing much resolution.

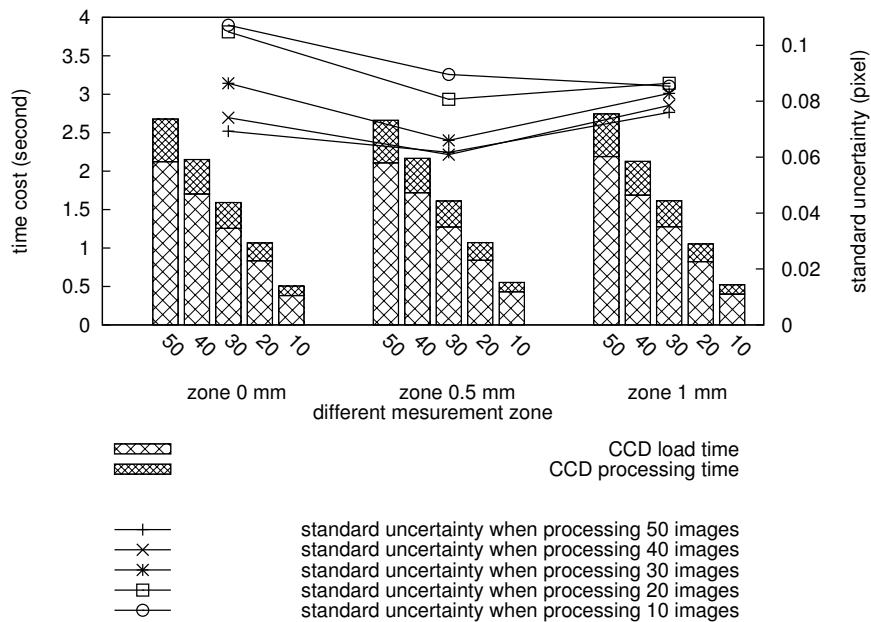


Figure 3.19: Uncertainty and time cost for processing different numbers of images

V.2 Image window

Another way to reduce the processing time is to diminish the image size. To maintain the measurement range, the length of the image window remained at 4.6mm (1280 pixels) and the width of the image window was diminished from 267 pixels to 250 pixels, 200 pixels, 150 pixels, 100 pixels, and 50 pixels. The same image set was used but preprocessed by an image window algorithm, which generates the desired image size. According to the last section, 10 images were used for calculating the position of the laser beam to obtain the worst resolution. The uncertainty and time cost are depicted in Fig 3.20.

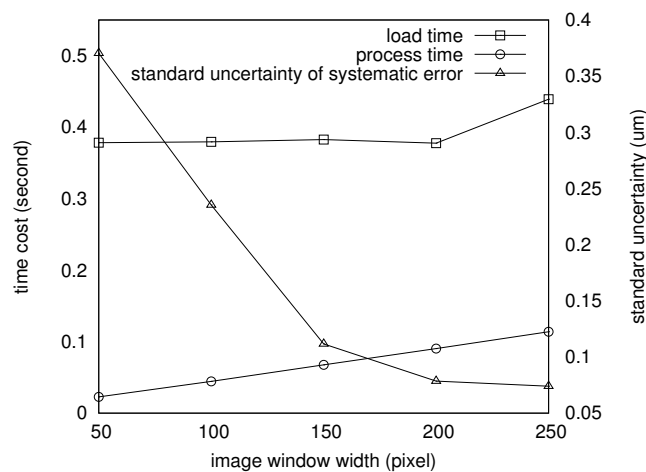


Figure 3.20: Uncertainty and time cost for processing different image windows in position 0 mm

As the image width decreased, the uncertainty of measurements rose very quickly, from $0.074\ \mu\text{m}$ to $0.37\ \mu\text{m}$. Compared with the speed improvement gained by reducing the number of processed images, a smaller image window did not improve the speed remarkably. There is only a benefit of 0.152 seconds in speed (load time and processing time), with an increase of $0.3\ \mu\text{m}$ standard uncertainty. As the image width decreases, the time cost decreases linearly, while the uncertainty of systematic error increases exponentially. This shows a clear constraint for a CCD-based system: the image

window width should be larger than the size of the laser spot; otherwise, the resolution will decrease exponentially as the image window width decreases.

V.3 Binning

Binning is the process of combining charges from adjacent pixels in a CCD during the readout phase. It will improve the readout speed at the expense of reducing the image dimension in pixels (number of image pixels). Since the charge of adjacent pixels will be readout at the same time, the readout noise of CCD working in binning mode will decrease compared to the CCD working in non-binning mode. However, the background noise will increase due to larger exposure area per pixel unit. An experiment of binning was carried out under the same environment as the previous experiments. A

2×2 binning was applied for the measurement, thus image dimension reduced to 640×133 pixels. To verify the effect of the noise, different thresholds were applied to 10 images for each position. The standard uncertainty are plotted in Fig 3.21. The threshold 10, which was applied for the previous experiments, is not effective enough in the case of 2×2 binning. The standard uncertainty ($\pm 0.2423 \mu m$) for applying threshold 10 is nearly the same as the one without applying the threshold ($\pm 0.2469 \mu m$). However, with a threshold of 19, the standard uncertainty reduced to the minimum value $\pm 0.0448 \mu m$, after which the standard uncertainty increased slightly as the threshold increased. Until applying the threshold of 85, the standard uncertainty remained at a level of less than $0.1 \mu m$. The average load time and process time reduced to 0.3 s and 0.1 s separately. Binning will lead to fast system speed with more noise when the background illumination is high. Under a high illumination situation, the binning technique should be used with a higher threshold to maintain high resolution.

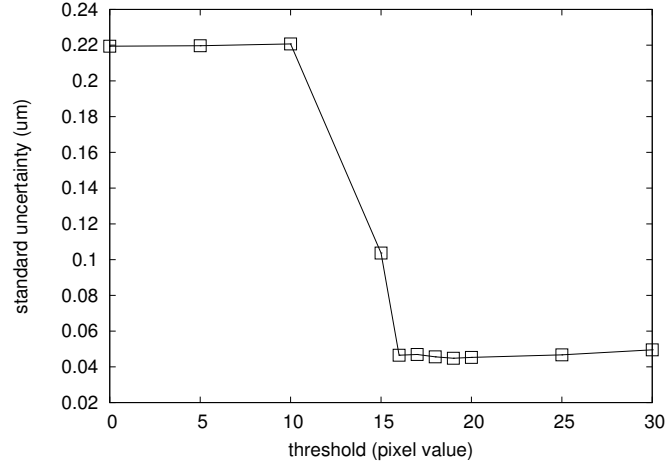


Figure 3.21: Standard uncertainty of systematic error for different thresholds

Conclusion

The limitation of PSD makes it not suitable to apply to a multi-functional *in situ* sensor. In order to implement a multi-functional sensor, the pixel-based image sensor, which utilizes a series of pixels (form a 2-D image window) to record the light intensity distribution other than position, is used to replace PSD. To make this replacement reasonable, it is necessary to prove that the pixel-based method can at least obtain the same resolution as the PSD does in measuring the laser beam deviation. This chapter introduced the pixel-based method, and compared the performance of this method to the performance of PSD-based method.

The first part of this chapter reviews the limitation of PSD. Since PSD is designed to measure the light position, its simplicity makes it not suitable for measuring the quantities other than position. In order to measure the other quantities, the light intensity distribution, which contains much more information than position, is needed to be recorded. The pixel-based image sensor is a kind of device to record the incident light intensity distribution. Two popular types of image sensor, CCD and CMOS, are compared from principle to performance. We chose CCD as our pixel-based image sensor due to its uniformity and wide dynamic range. However, CCD only records the light intensity distribution, it can not provide the laser spot position information. To achieve this, an image location algorithm must be applied to the image. At the end of this part, several popular image location algorithms are introduced. For the comparison of CCD- and PSD-based method, the centroid algorithm, which measures the gravity center as PSD does, is selected to calculate the laser spot position.

The second part of this chapter compared the performance of these two methods in two aspects: resolution and speed. Noise is one of the big influence to the resolution of both two methods. For CCD-based system, applying a threshold can effectively eliminate the readout noise and background noise. Capturing more images to compute the position can reduce the error caused by noise as well. For PSD-based method, increasing inter-electrode resistance is a good way to reduce both the amplifier and shot noise. As an analogue device, PSD has a very fast respond time ($3 \mu s$), however, to achieve high resolution several PSD output signals are needed to be processed which makes the speed of PSD-based system depending on the external sampling and digitalization process. The speed of the CCD-based system usually depends on exposure time, readout time, storage time, load time, and computation time.

Before the comparison of PSD- and CCD-based system, several parameters of CCD-based system are studied in this chapter. A small image window size is useful not only for increasing the resolution but also for improving the speed with the limitation that the laser spot should be entirely contained in the image. Applying a threshold to the noise level could efficiently reduce the systematic error. To improve the speed, binning is an alternative means, but the noise level should be reconsidered to choose a proper threshold. Saturation hides lots of laser spot information and thus should be definitely avoided. The resolution of CCD-based systems do not highly depend on the number of processed images. It is a good way to improve speed without greatly reducing resolution.

According to the analysis and experiment results provided in this chapter, CCD-based system can obtain better resolution than PSD-based system with a comparable speed to PSD-based system by adjusting these parameters. This makes CCD a better alternative to PSD in beam deviation measurement applications. Furthermore, CCD records all the power distribution information of laser spot, thus gives the capability of measuring the

power distribution sensitive quantities, such as, the turbidity of seawater. In next chapter, we will discuss the possibility of measuring turbidity with the same refractometer configuration combined with a CCD.

Bibliography

- [1] Boyle W S and Smith G E. Charge coupled semiconductor devices. *Bell Syst. Tech. J.*, 49:587–93, 1970.
 - [2] Kenneth R. Spring, Thomas J. Fellers, and Michael W. Davidson. Introduction to charge-coupled devices (ccds). <http://www.microscopyu.com/articles/digitalimaging/ccdintro.html>.
 - [3] Dave Litwiller. Ccd vs. cmos: Facts and fiction. http://www.teledynedalsa.com/public/corp/Photonics_Spectra_CCDvsCMOS_Litwiller.pdf.
 - [4] Peter F. I. Scott, Anton S. Kachatkou, Nicholas R. Kyele, and Roelof G. van Silfhout. Real-time photon beam localization methods using high-resolution imagers and parallel processing using a reconfigurable system. 48(7):073601, 2009.
 - [5] M R Shortis, T A Clarke, and T Short. A comparison of some techniques for the subpixel location of discrete target images. *Videometric III*, 2350:239–250, 1994.
 - [6] Bracewell and Ronald Newbold. *The Fourier transform and its applications*. McGraw-Hil, 1978.
 - [7] J Canny. A computational approach to edge detection. *IEEE Trans. Pattern Anal. Mach. Intell.*, 8:679–698, June 1986.
 - [8] S. Iqbal, M.M.S. Gualini, and A. Asundi. Measurement accuracy of lateral-effect position-sensitive devices in presence of stray illumination noise. *Sensors and Actuators A: Physical*, 143:286–292, May 2008.
 - [9] Wang Guanghui, Ping Shum, Xu Guoliang, and Zhang Xuping. Position detection improvement of position sensitive detector (psd) by using analog and digital signal processing. *Information, Communications & Signal Processing, 2007 6th International Conference on*, pages 1–4, 2007.
 - [10] Solid State Division HAMAMATSU PHOTONICS K.K. Characteristics and use of psd. http://sales.hamamatsu.com/assets/pdf/catsandguides/psd_technical_information.pdf.
 - [11] Steve B. Howell. *Handbook of CCD astronomy*. Cambridge University Press, 2000.
 - [12] Solid State Division HAMAMATSU PHOTONICS K.K. Ccd saturation and blooming. <http://learn.hamamatsu.com/articles/ccdsatandblooming.html>.
 - [13] Solid State Division HAMAMATSU PHOTONICS K.K. One-dimensional psd s3931, s3932, s3270. http://sales.hamamatsu.com/assets/pdf/parts_S/s3931_etc_kspd1002e05.pdf.
 - [14] Solid State Division HAMAMATSU PHOTONICS K.K. Signal processing circuit for 1-d psd c3683-01. http://sales.hamamatsu.com/assets/pdf/parts_C/C3683-01.pdf.
 - [15] DALSA Corporation. Genie m1280 datasheet, 2009. http://www.dalsa.com/prot/mv/datasheets/genie_m1280_1.3.pdf.
-

- [16] BIPM, IEC, IFCC, ISO, IUPAC, IUPAP, and OIML. Guide to the expression of uncertainty in measurement. *ISO, Geneva, 1993.*
-

Figures and tables

Figures

3.1	Principle of 1-D PSD	62
3.2	Principle of Metal Oxide Semiconductor (MOS) Capacitor	63
3.3	Principle of CCD image sensor (DALSA tech. paper)	64
3.4	Principle of CMOS image sensor (DALSA tech. paper)	64
3.5	The difference between CCD and CMOS	65
3.6	The relationship between the calculated spot center and the noise center	70
3.7	The time cost for acquiring one laser spot position with PSD- and CCD- based system	72
3.8	The phenomenon of blooming	72
3.9	The experiment setup	73
3.10	The profile of the Gaussian spot	74
3.11	The estimate center against the number of processed image	75
3.12	The estimate center and the standard uncertainty against the threshold	75
3.13	The estimate center and the standard uncertainty against the height of image	76
3.14	The profiles of images with different laser beam power	76
3.15	The standard deviation of the laser beam profile with different powers .	77
3.16	The estimated center and the error according to the best fit line against the moved distance	78
3.17	The standard uncertainty of systematic error	79
3.18	Time cost in both CCD- and PSD-based system	80
3.19	Uncertainty and time cost for processing different numbers of images .	81
3.20	Uncertainty and time cost for processing different image windows in position 0 mm	81
3.21	Standard uncertainty of systematic error for different thresholds	82

Tables

3.1	Comparison between CCD image sensor and CMOS image sensor . . .	66
3.2	The slopes for different zones with CCD and PSD	79

Chapter 4

Turbidity measurement based on the refractometer

Contents

Introduction	90
I Review of the turbidity measurement methods	90
I.1 Selection of the turbidity measurement method	91
I.2 Principle of attenuation based method	91
I.3 Attenuation coefficient to turbidity	94
I.4 Sensitivity analysis	95
II Issues in measuring turbidity with refractometer	96
II.1 Measurement distance	96
II.2 Non-uniqueness of light path inside the beam	96
II.3 Light path variation caused by refractive index change	97
II.4 Interference	98
II.5 High turbidity measurement	98
III Issues in measuring refractive index in turbid medium	99
III.1 Non-uniqueness of light path inside the beam	99
III.2 Divergence and scattering caused asymmetrical spot	99
IV Invalidation of PSD	100
V Using CCD to measure the turbidity with refractometer	102
V.1 High turbidity measurement	102
V.2 Scattered light & interference elimination	102
V.3 Solution to light path related problems	103
V.3.1 Light path variation according to the refractive index	103
V.3.2 Non-uniqueness of light path inside the beam	104
V.4 New location algorithm	105
VI Experiments & Results	107
VI.1 Performance evaluation of new location algorithm	107
VI.1.1 Simulation	107
VI.1.2 Experiment	109
VI.2 Simulation & experiments with parallel slab	110

VI.2.1	Simulation	110
VI.2.2	Experiments in high turbid medium	110
VI.2.3	Experiments in low turbid medium	112
VI.3	Simulation & experiments with refractometer	113
VI.3.1	Simulation	113
VI.3.2	Experiments in high turbid medium	113
VI.3.3	Experiments in low turbid medium	115
VI.4	Comparison with nephelometer	115
Conclusion	117
Bibliography	119
Figures and tables	120

Introduction

In last chapter, we compared the CCD- and PSD-based laser beam deviation measurement, and proved that the CCD-based system can obtain better resolution than PSD-based system with comparable speed. Further more, the CCD-based system records the laser spot intensity distribution, which provides us the possibility to retrieve the informations other than laser spot position. To prove this benefit of CCD-based system, the turbidity measurement without modifying the configuration of our refractometer is discussed in this chapter.

The different turbidity measurement methods are first reviewed in the first part of this chapter. By comparing these methods, the attenuation measurement is the most suitable one to demonstrate the advantage of CCD-based system. The principle of the attenuation based turbidity measurement is specially presented. From the principle, the factors that affect the resolution of attenuation measurement are analysed at the end of the first part.

Since our turbidity measurement is based on the refractometer, the refraction and the design of the refractometer might influence the measure of turbidity, which is discussed in the second part of this chapter. Similarly, the refractive index measurement in a turbid water is much more complex than in a clear water. In the third part of this chapter the issues in measuring refractive index in turbid medium are discussed. Due to the interference between the refractive index measurement and the turbidity measurement, the PSD is not suitable to correctly measure neither the refractive index nor the attenuation in a turbid medium. This limitation is discussed in this chapter as well.

Next, we introduce the turbidity measurement with refractometer by using a CCD instead of PSD. A new algorithm is proposed and is proved to be much more accurate than the centroid algorithm in both turbid and non-turbid medium. Several experiments and simulations are presented to evaluate the performance of the method. The experimental results are compared to the one of nephelometer at the end of this part.

At the end of this chapter, we presents the limitation caused by the configuration of the refractometer and proposes the possible solutions, which are very useful to guide the modelling and design of the new refracto-turbidi-meter.

I Review of the turbidity measurement methods

According to the introduction in chapter 1, the state-of-the-art turbidity measurements include: transmitted light measurement, backscattered measurement, 90° scatter measurement, and ratio nephelometric measurement. The advantage and disadvantage of these methods are already discussed in chapter 1. The ratio nephelometric measurement method obtains the best performance, which requires multiple light intensity sensor[1]. 90° scatter measurement or nephelometer is defined as standard (ISO7027[2], EPA method 180.1[3]). The backscatter measurement method is especially suitable for the ultra high turbidity measurement, but has poor performance in low and moderate turbid medium. The transmitted light measurement method gives high resolution except for the ultra low and high situation. To measure turbidity, the direct way is to choose one of these methods, which best fits our requirements.

I.1 Selection of the turbidity measurement method

The selection of the turbidity measurement method depends on the requirement of our application. As we expect to show the benefits gained from the usage of CCD instead of PSD in our existing refractometer, the turbidity measurement that we chose must lead to the least modification to our refractometer. This is valuable not only for the need of compact multi-functional sensor but also the need for reduction of the cost.

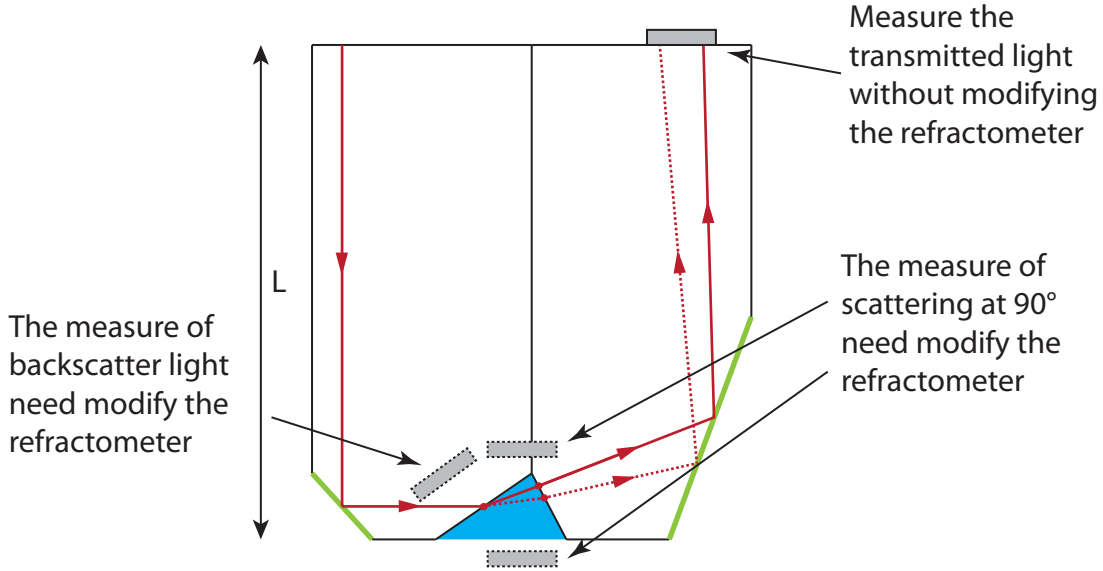


Figure 4.1: Principle of refractometer

The ratio nephelometric method requires at least two light intensity sensor, one at 90° measures the scattering, another measures the transmitted light. The transmitted light can be measured at the current position of CCD or PSD as shown in Fig 4.1. However, the sensor at 90° can not be placed into our refractometer without modifying the optical design (Fig 4.1 shows several possible position for nephelometric measurement). This makes that both the nephelometric method and ratio nephelometric method do not fulfil our requirement. The backscatter method meets the same problem, thus it is not proper for the turbidity measurement with our refractometer. From this point, the measure of transmitted light, which implies the attenuation of the light, is selected to measure turbidity.

I.2 Principle of attenuation based method

As the transmitted light method is chosen as our turbidity measurement method, it is necessary to study the principle of the turbidity measurement based on the measure of transmitted light.

The incident light is diffused in all directions when it meets the particle. The portion of light flux diffused in different directions is defined by the phase function, denoted as $p(\hat{s}', \hat{s})$, which represents the portion of light flux diffused from direction \hat{s} to direction \hat{s}' . The phase function is related to the wavelength of the incident light and the size of the particles, a normalized radius $R = \frac{2\pi r}{\lambda}$ is introduced to define the size of the particle, in which r is the radius of the particle and λ is the wavelength of the incident light. The

phase function of spherical particle is well studied by Gustav Mie[4], who gave an analytical solution of Maxwell's equations for the scattering of electromagnetic radiation by a single spherical particle. According to the Mie theory, the larger the normalized radius, the more light is scattered forward. To reduce the complexity of Mie theory, several approximations have been proposed[5, 6, 7], including Henyey and Greenstein's equation, and its further approximation by Blasi, Le Sa c, and Schlick. Since the scattering is axisymmetric along the propagation direction and the medium is isotropic, these approximation equations is a function of the angle θ between the incident direction and the scattering direction, written as $p(\cos\theta)$. The Henyey and Greenstein's equation is

$$p_{HG}(\cos\theta) = \frac{1}{4\pi} \frac{1 - g^2}{(1 + g^2 - 2g(\cos\theta))^{3/2}}, \quad (4.1)$$

where g is in the range $(-1, 1)$. Negative values of the g correspond to back-scattering, and positive values correspond to forward-scattering. When $g = 0$, it changes to be an isotropic phase function. To make the equation 4.1 more efficient in computer graphics, Blasi, Le Sa c, and Schlick introduced an other approximation to the Henyey Greenstein function as

$$p_{Schlick}(\cos\theta) = \frac{1}{4\pi} \frac{1 - k^2}{(1 - k\cos\theta)^2}, \quad (4.2)$$

where k is similar to the parameter g in Henyey Greenstein's function, and follows the relationship

$$k = 1.55g - 0.55g^3 \quad (4.3)$$

Fig 4.2 shows the scattering with different parameters g and k in these two approximations.

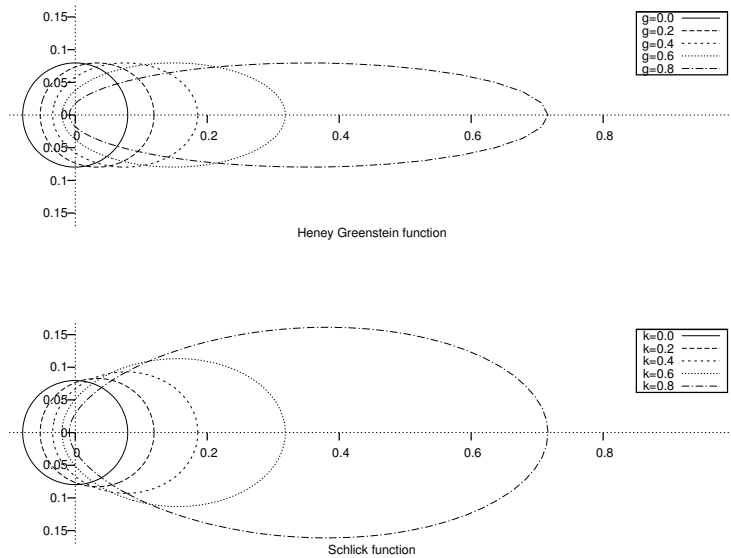


Figure 4.2: Two phase functions: Henyey Greenstein function and Schlick function.

Besides the flux diffused, another portion of light flux is absorbed by the particle, represented as $\sigma_a I_0$, where I_0 is the flux intensity of incident light. Similarly, the portion

of light diffused out of the light propagation direction, which is related to the normalized radius R of the particle is denoted as $\sigma_d I_0$. Here σ_a and σ_d are called absorption cross section and diffusion cross section, respectively, which are the functions of the incident light wavelength λ . These two coefficients associated with the phase function describe the optical properties of a single particle. For a volume of water, the density of particles should also be considered. The more particles in the medium, the more light is absorbed and scattered out of the propagation direction.

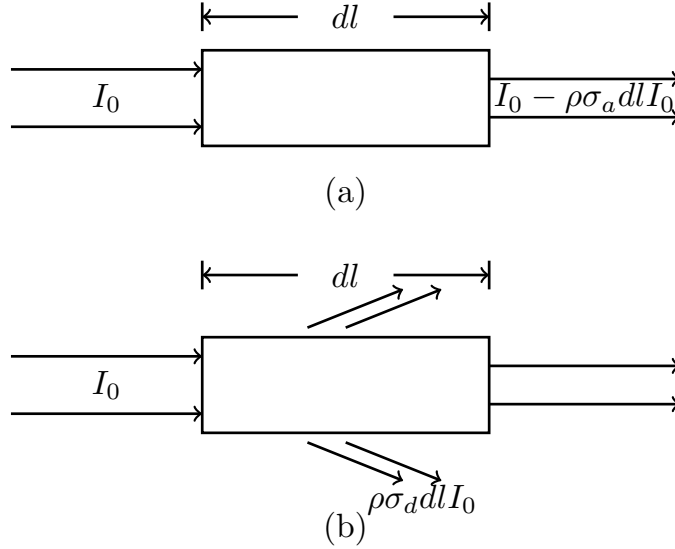


Figure 4.3: The light absorption and diffusion in a unit volume of turbid water.

Fig. 4.3 shows the absorption and diffusion of an incident light with flux intensity I_0 , upon a volume of turbid water with unit cross section, particle density ρ and length of dl . The flux that is absorbed by ρdl particles is calculated by the equation:

$$I_a = \rho \sigma_a(\lambda) dl I_0 \quad (4.4)$$

The portion of light diffused out of the propagation direction by these particles can be expressed by:

$$I_d = \rho \sigma_d(\lambda) dl I_0 \quad (4.5)$$

According to Eq.4.4 and Eq.4.5, the decrease in the incident flux intensity for the volume dl is:

$$\frac{dI}{dl} = -\frac{(I_a + I_d)}{dl} = -\rho(\sigma_a(\lambda) + \sigma_d(\lambda))I \quad (4.6)$$

This partial differential equation can be easily solved as:

$$I = I_0 e^{-\rho(\sigma_a(\lambda) + \sigma_d(\lambda))l} \quad (4.7)$$

A special form of this equation without the diffusion cross section σ_d is called the Beer-Lambert law. In equation 4.7, the part $\rho(\sigma_a(\lambda) + \sigma_d(\lambda))$ that causes the attenuation of the incident beam, is a good candidate to describe the optical properties of the volume of medium. To simplify the formula, $\rho(\sigma_a(\lambda) + \sigma_d(\lambda))$ is expressed as T , the attenuation coefficient. Therefore, the attenuation coefficient T can be calculated from:

$$T = -\frac{\ln(I_{trans}) - \ln(I_0)}{l}, \quad (4.8)$$

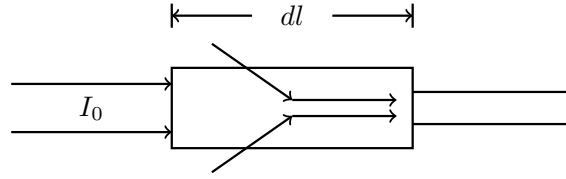


Figure 4.4: The light scattered from other parts of the medium to the incident light propagation direction

where I_{trans} is the light intensity measured in the transmission path out of the volume. Besides the attenuation of the incident beam, the light that propagates through the volume of medium increases as a portion of the light flux from other directions are scattered into the transmission direction. This phenomenon is depicted in Fig 4.4. Different from the attenuation of the incident light, this part of flux, caused by the multi-scattering in the medium increases the transmitted radiation in the transmission direction, noted as I_{ms} , which can not be easily separated from the transmitted light I_{trans} . Thus, the Eq. 4.8 should be

$$T = -\frac{\ln(I_{trans} - I_{ms}) - \ln(I_0)}{l} \quad (4.9)$$

Another part of multi-scattering light that increases the transmission radiation is caused by the reflection between the two refraction surfaces. Besides the refraction, a part of the laser beam is reflected in the second refraction surface, the reflected light is diffused by the particles in the medium and reflected again in the first refraction surface. This process continues between the two surfaces. As a result, part of the reflected light is scattered into the transmission direction as well.

The flux intensity of multi-scattered light in propagation direction is related to the density of the particles and the length of the light path. The higher the density of the particles, the more multi-scattering occurs. A longer light path gives more light scattered into the propagation direction too. The impacts caused by the multi-scattered light are evaluated in the analysis of the experiment results.

I.3 Attenuation coefficient to turbidity

Strictly speaking, the state-of-the-art turbidity measurement measures the diffusion property of the medium. That is to say, the turbidity should be proportional to the portion of diffused light, noted as:

$$Turbidity = k_t \times \rho \times \sigma_d(\lambda), \quad (4.10)$$

where k_t is a constant coefficient to convert the light intensity into turbidity units, e.g. NTU. Under this relationship, the absorption part $\rho\sigma_a(\lambda)$ in the attenuation coefficient impacts the measurement of the turbidity. This is one of the drawbacks of the attenuation based turbidity measurement - it has the greatest susceptibility to absorbance and color interferences. The absorption of the particles highly depends on the wavelength, there exists a risk that the particles absorb most of the light so that the detected light attenuation is much larger than the actual one, which leads to a large error. It should be mentioned that the measurement of absorption is very difficult to achieve. The common method is to choose a special light source which has low absorbance interference, e.g. the light source at

wavelength of 860 *nm* as defined in ISO 7027. In our discussion, we relies on the assumption that the medium that we measured has very weak absorption for the wavelength that we used. In this case, the turbidity can be treated as proportional to the attenuation coefficient T .

I.4 Sensitivity analysis

The sensitivity of the turbidity measurement can be estimated from the Eq 4.9. The multi-scattering part is ignored here and will be discussed later from the experiment results. Since the incident light intensity I_0 can be measured with non-turbid water in advance, the equation can be modified as:

$$T = -\left(\frac{\ln(I_{trans})}{l} - C\right) \quad (4.11)$$

The derivative of T can be expressed as:

$$T' = \frac{dT}{dI_{trans}} = -\frac{1}{l \times I_{trans}} \quad (4.12)$$

Thus, the sensitivity of the measurement of turbidity S_t is

$$S_t = k_t \times dT = -k_t \frac{dI_{trans}}{l \times I_{trans}}, \quad (4.13)$$

where k_t is a constant coefficient to convert the attenuation coefficient into other turbidity units, for example, NTU. As the attenuation of light intensity I_{att} equals $I_0 - I_{trans}$, the sensitivity S_t can be written as:

$$S_t = -k_t \frac{dI_{trans}}{l \times I_{trans}} = -k_t \frac{d(I_0 - I_{att})}{l \times (I_0 - I_{att})} = k_t \frac{dI_{att}}{l \times (I_0 - I_{att})}, \quad (4.14)$$

From this equation, it is obvious that the sensitivity of turbidity measurement is proportional to the sensitivity of the light intensity sensor $dI_m = -dI_{att}$, but inversely proportional to the length of the light path l in the turbid medium. A longer light path can provide better turbidity measurement sensitivity. Another interesting phenomenon resulting from this equation is the sensitivity depending on the measurement range. With the same sensitivity of the light intensity sensor and the same light path length, the larger the measured intensity, the better the sensitivity obtained. Considering that the measured light intensity decreases as the turbidity increases, it is easy to conclude that the sensibility is better in low turbid medium than in the high turbid medium when light path and sensor sensitivity are the same. Similarly to the length of the light path, the sensitivity is inversely proportional to the initiate light intensity I_0 . In conclusion, To improve the sensitivity of the turbidity measurement based on the measure of transmitted light, the following ways can be used:

1. Choose the light intensity sensor with higher sensitivity.
2. Increase the length that the light propagate in the medium
3. Increase the incident light intensity
4. Dilute the sample to a low turbidity range

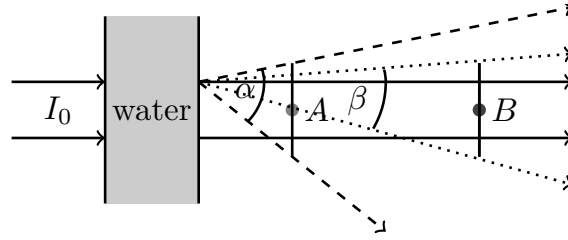


Figure 4.5: The difference of light intensity measurement by locating the light intensity sensor at different distances of the medium

II Issues in measuring turbidity with refractometer

As discussed in last section, the attenuation coefficient T can be calculated from the attenuation of the incident laser beam according to Equation 4.9. However, when applying this theory to our refractometer demonstrated in chapter 2, the two quantities to be measured, refractive index and scattering (the measurement of transmitted light is an indirect way to measure the scattering), interfere to each other so that the measurement for each of the properties differs from the stand alone measurement. In this section, we introduce the impacts to the turbidity measurement caused by the refractive index measurement, while the next section presents the inverse one.

II.1 Measurement distance

The first issue caused by the refractometer is, according to the theory, the intensity I_{trans} is measured by the sensor located far away from the medium, where the transmitted light is well separated from the scattered light. However, with the refractometer, the height L shown in Fig 4.1 limits the distance between the sensor and the medium, so that the transmitted light and scattered light are mixed together. Fig 4.5 depicts the difference of light intensity measurement while locating the light intensity sensor at different distances of the medium. Besides the light propagated along the transmission direction, another portion of light is scattered out of the medium. The sensor located near the medium, shown in position A, captures not only the transmitted radiation but also the scattered radiation with an angle α , while at the distant position B, the sensor accepts the transmitted radiation and the scattered radiation with the angle β , smaller than α . Therefore, B receives less scattered light than A.

This issue causes the light radiation measured by the sensor A mixes the transmitted radiation I_{trans} and a portion of scattered radiation I'_{scatt} . According to equation 4.8, the calculated attenuation coefficient T' is:

$$T' = -\frac{\ln(I_{trans} + I'_{scatt}) - \ln(I_0)}{l} < T_{true}, \quad (4.15)$$

where T_{true} stands for the actual turbidity of the medium. It is easy to conclude that this issue will cause the measured value smaller than the actual value of turbidity.

II.2 Non-uniqueness of light path inside the beam

Another issue is caused by the width of the laser beam. During our introduction of the turbidity measurement principle, the width of the incident light is ignored. However, in

practice, the laser beam width and space intensity distribution cannot be ignored. For a collimated laser beam with initiate intensity distribution $I_0(x, y)$, the attenuation coefficient T can be retrieved from the attenuation at any point, for instance, (x', y') . Equation 4.8 can be written as:

$$T(x', y') = \frac{\ln(I_0(x', y')) - \ln(I_{trans}(x', y'))}{l(x', y')}, \quad (4.16)$$

where $l(x', y')$ is length of light path of the medium for the light emitted from point (x', y') . This leads to another problem, the width of the collimated beam causes that the different point inside the initiate beam propagate through the medium with different lengths. As shown in Fig 4.6, for a wide beam shown as the red, light emitted from point (x', y') has shorter light paths OM than the one emitted from point (x'', y'') (labelled as $O'M'$), and this difference varies as the refractive index of the medium changes.

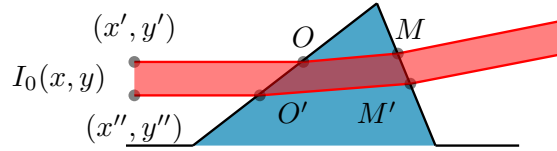


Figure 4.6: Different parts inside the beam pass different lengths in the medium

It should be noticed that, without the refraction, for any point (p_x, p_y) , the length of the light path is a constant, $l(p_x, p_y) = L_c$. Thus, the light intensity in equation 4.8 can be replaced by the light power, so that we have the following equation:

$$T = \frac{\ln(\int_{-\infty}^{\infty} \int_{-\infty}^{\infty} I_0(x, y)) - \ln(\int_{-\infty}^{\infty} \int_{-\infty}^{\infty} I_{trans}(x, y))}{L_c} = \frac{\ln(P_0) - \ln(P_{trans})}{L_c}, \quad (4.17)$$

in which P_0 is the initiate light power and P_{trans} is the transmitted light power. A possible solution to this problem is to use the maximum of the intensity, instead of the entire intensity, to calculate the attenuation coefficient T .

II.3 Light path variation caused by refractive index change

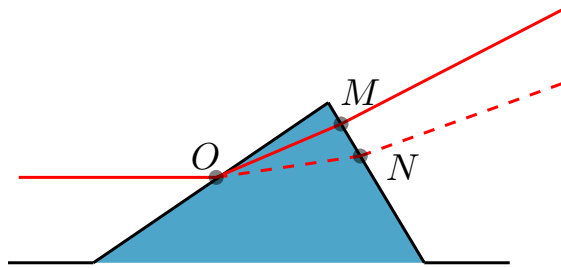


Figure 4.7: The light path varies according to different refractive index

Another issue related to the length of light path l is that it varies as the refractive index changes. In Fig 4.7, OM and ON are two different light paths according to different refraction indices of the medium. This makes the measured flux intensity quite different

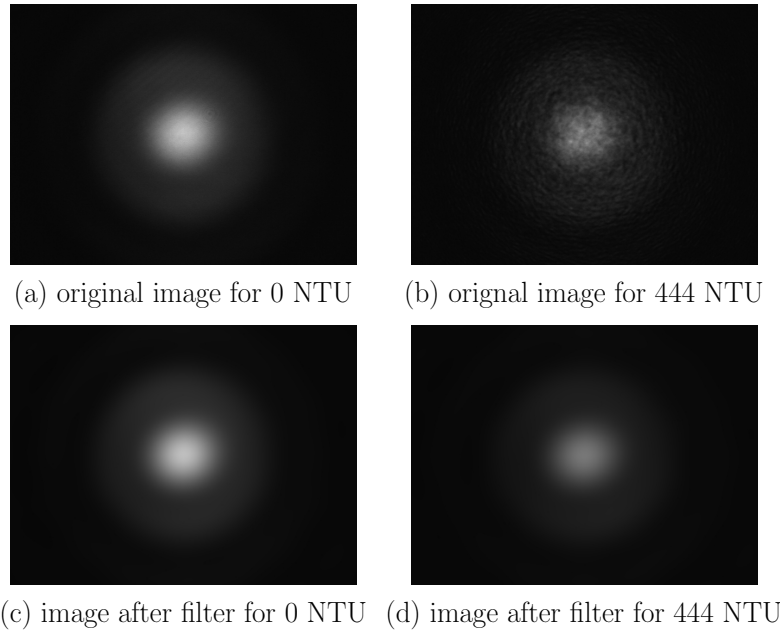


Figure 4.8: The captured scattered light and interference when camera is near to the medium

when measuring two different medium samples, which have the same turbidity but different refractive indices.

To put the refractive index into consideration, the attenuation coefficient T is a function of refractive index n_e :

$$T(x, y, n_e) = \frac{\ln(I_0(x, y)) - \ln(I_{trans}(x, y))}{l(x, y, n_e)} \quad (4.18)$$

II.4 Interference

Besides the difficulty of separating the scattered radiation and the transmission radiation, the use of laser as the source leads to interference while the laser beam propagates through the particles. As a result, speckle is observed in the sensor plane. Fig 4.8 (a) and (b) show the laser spots captured at 5 cm far from the medium along the light propagation path. Picture (a) depicts the laser spot with pure water and picture (b) shows the laser spot with the turbid water of 444.4 NTU. It is obvious that the laser spot captured with turbid water mixes the Gaussian spot and interference speckle.

The speckles caused by the interference do not change the power of the laser spot. However, since the light path inside the beam is not unique, the power of the laser spot is not suitable to represent the intensity attenuation. The existence of speckles makes the peak intensity not accurate to represent the intensity attenuation either.

II.5 High turbidity measurement

Furthermore, since our method measures the attenuation of propagated light as shown in Eq 4.9, it is easy to find out that the light intensity I_{trans} decreases when the turbidity

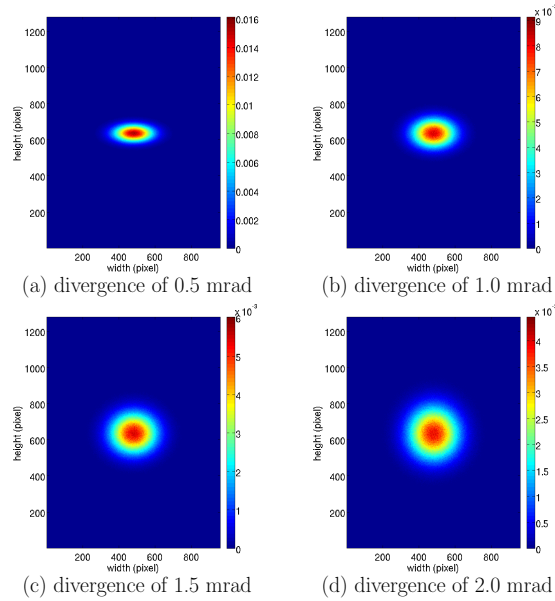


Figure 4.9: The laser spots for different laser beams with different divergence. The image is obtained from the ZEMAX simulation.

increases, which can be found by comparing the Fig 4.8 (a) and (b). This results in another issue, the light intensity becomes so weak that it can't be measured in a highly turbid case.

III Issues in measuring refractive index in turbid medium

Not only the refractive index measurement influences the turbidity measurement, the measurement of turbidity itself impacts the accuracy of the refractometer as well, which needs to be addressed in the design of the turbidi-meter. This section introduces these influences.

III.1 Non-uniqueness of light path inside the beam

The first problem related to the resolution of the refractive index measurement is caused by the light path difference as shown in Fig 4.6. According to Eq 4.9, in a turbid case, this difference of light path leads to different attenuation inside the laser spot, which further causes the intensity distribution of captured laser spot differs from the initial one. This variation of intensity distribution leads to the intensity-distribution-based location sensors not valid.

III.2 Divergence and scattering caused asymmetrical spot

One of the problems is caused by the divergence of the laser beam, which leads to the asymmetric laser spot. Both the refraction surface and the sensor surface are not perpendicular to the laser beam. When a Gaussian beam projected to the sensor surface at a non-normal angle, the Gaussian spot becomes asymmetric, while different angle changes the size of the laser spot. Fig 4.9 is generated by the simulation in ZEMAX with the configuration of our refractometer. It presents four laser spots with different laser beam divergences, but with the same refractive index of the medium. It is easy to observe that the width of the laser

spot increases as the divergence of laser spot increases. The asymmetry of the laser beam can be noticed from Fig 4.10 (a), which shows a divergent laser beam projects to a plane at an angle of 28° .



Figure 4.10: A divergent laser beam projects to a plane at an angle of 28°

Similarly with the divergence of the laser beam, the turbidity of the medium diffused the laser beam out of its propagation direction and makes the divergence of the laser beam much larger. Fig 4.10 (b) depicts a laser beam with the same divergence as in (a), but in a turbid medium, projects to a plane at an angle of 28° . It is obviously that the same laser beam in turbid medium results in more asymmetric than in clear medium.

IV Invalidation of PSD

In the modelling and design discussed in chapter 2, we used a PSD to measure the deviation of the laser beam. PSD has a single active area formed by a P-N junction. The two parts that originated from the laser spot to the two electrodes form two lateral resistances for the photo-currents running towards the electrodes. The photo currents are collected through the resistances by the output electrodes, which are inversely proportional to the distance between the electrode and the center of the incoming light beam. This relationship is expressed as follows: [8]

$$x = \frac{L}{2} \frac{I_2 - I_1}{I_2 + I_1}, \quad (4.19)$$

where I_1 and I_2 are the electrode photo-currents, L is the length of the PSD active area and x stands for the laser spot position. It should be mentioned that the incident light power P is proportional to the sum of the two photo currents.

$$P = k_p(I_1 + I_2), \quad (4.20)$$

in which k_p is a constant coefficient to convert the current into power. This means PSD can be used to measure the light power. In a non-refraction case and the PSD is placed far away from the medium so that the scattered light can be separated from the transmitted light, the power measured by PSD, P_{psd} , is exactly the transmitted light. The attenuation coefficient T thus can be calculated from the equation 4.17:

$$T = \frac{\ln(P_0) - \ln(P_{psd})}{L} \quad (4.21)$$

However, as we have discussed in section II, the turbidity measurement is influenced by the configuration of our refractometer. Under this condition, equation 4.21 no longer stands.

Firstly, the dimension limitation of refractometer makes the PSD not far enough to the medium. This leads to the mixture of transmitted light and a portion of scattered light is captured by PSD. As the illustration in equation 4.15, the measured turbidity under this condition is smaller than the actual value. It is not possible to separate these two kinds of light captured by PSD from post-processing techniques.

Second, the equation 4.21 relies on the fact that for any point in the original intensity distribution, the light emitted from that point has the same length of light path as the light emitted from the other points. Nonetheless, the refraction makes the light path inside the beam non-unique. Due to this issue, the turbidity calculated from equation 4.21 leads to large error.

Another problem is that the accuracy of laser beam deviation measured by PSD is reduced in a turbid medium. From the principle of PSD, the position it measures is the mass center of the incident light. Theoretically, the mass center of transmitted light is the position of laser spot. If the laser spot moves a distance d from position x_0 to position x_d along the x axis. The new position x_d is:

$$x_d = x_0 + d + e_c, \quad (4.22)$$

where e_c is the systematic error caused by PSD-based system. Here we ignore the noise, because it has been discussed in last chapter. Since the transmitted light is mixed with a portion of scattered light, the calculated center is no longer the exact position of the laser spot:

$$x'_d = \frac{(x_0 + d + e_c)M_s + x_{sc}M_{sc}}{M_s + M_{sc}}, \quad (4.23)$$

in which M_s is the mass of laser spot, M_{sc} is the mass of scattered light, and x_{sc} stands for the mass center of scattered light. What is more, the non-uniqueness of attenuation inside the beam makes the distribution of laser spot changes, which results in the shift of the mass center x_{sh} . The asymmetric spot caused by the divergence and scattering enhance this phenomenon and cause another mass center shift x_{ash} . The shifts impact the calculated center:

$$x'_d = \frac{(x_0 + d + e_c + x_{sh} + x_{ash})M_s + x_{sc}M_{sc}}{M_s + M_{sc}} \quad (4.24)$$

From equation 4.24, the system error of PSD in turbid medium can be obtained:

$$\begin{aligned} e = x'_d - (x_0 + d) &= \frac{(x_0 + d + e_c + x_{sh} + x_{ash})M_s + x_{sc}M_{sc}}{M_s + M_{sc}} - x_0 - d, \\ &= \frac{(e_c + x_{sh} + x_{ash})M_s + (x_{sc} - x_0 - d)M_{sc}}{M_s + M_{sc}} \end{aligned} \quad (4.25)$$

The invalidation of mass center based laser beam deviation measurement is further discussed in next chapter, where we gives an accurate expression for the center shift caused by the turbidity x_{sh} .

In conclusion, the attenuation of laser beam in a refractometer has a spatial dependence, which results in the invalidation of measuring the attenuation coefficient from the

power. This spatial dependence results in the mass center shift, which further impacts the measurement of laser beam deviation. However, PSD doesn't record the laser spot spatial information, so that it cannot deal with these problems. What is more, the mixed scattered light affects not only the accuracy of attenuation measurement but also the one of refractive index measurement, which cannot be handled by PSD as well. All these issues make PSD not a good candidate sensor in a refracto-turbidi-meter.

V Using CCD to measure the turbidity with refractometer

As we have discussed in last chapter, CCD records much more information than PSD by recording the light intensity distribution. This gives us the possibility to solve all these issues mentioned above by using a CCD instead of a PSD.

V.1 High turbidity measurement

In a high turbid medium, the transmitted light is very weak, so that the signal to noise ratio SNR turns to be very small so that the transmitted light can not be measured. Since CCD can be controlled to operate with different exposure times, the transmitted radiation in a high turbid medium can be measured with long exposure time. The attenuation coefficient T can be represented by calculating with the transmitted radiation in a unit time period, which can be expressed as:

$$T = -\frac{\ln\left(\frac{I_{trans} + N_r + N_p + N_b}{t}\right) - \ln\left(\frac{I_0}{t_0}\right)}{l}, \quad (4.26)$$

in which t is the exposure time and t_0 stands for the exposure time used to measure the incident light intensity. N_r , N_p , and N_b are the readout noise, photon noise, and background noise respectively. The readout noise is independent to the exposure time, that is to say, longer exposure time improve the signal-to-readout-noise ratio. The photo noise only impacts the illuminated pixels and it is related to the illumination in the pixel. Thus we have $N_{pt}/t \approx N_{pt'}/t'$, where N_{pt} and $N_{pt'}$ are the photon noise with the exposure time t and t' respectively. The background noise impinges all the pixels, so that it increases as the exposure time increases. However, the background noise can be eliminated by several techniques, e.g. subtracting the background image from the captured laser spot image. If the exposure time is k_t times of the original exposure time t , the new signal to noise ratio SNR' can be written as:

$$SNR' = \frac{k_t I_{trans}}{N_r + k_t N_p + k_t N_b} = \frac{I_{trans}}{\frac{N_r}{k_t} + N_p + N_b} > \frac{I_{trans}}{N_r + N_p + N_b} = SNR \quad (4.27)$$

The reduce of the readout noise increases the signal to noise ratio compared to the original signal to noise ratio SNR . Because of this, the CCD can be used in high turbidity measurement.

V.2 Scattered light & interference elimination

To separate the transmitted radiation with the scattered radiation, the Fourier transformation of the laser spot in different turbidities has been studied, depicted in Fig 4.11, and gives us the profile of the laser spot Fourier transformation in pure water and turbid water

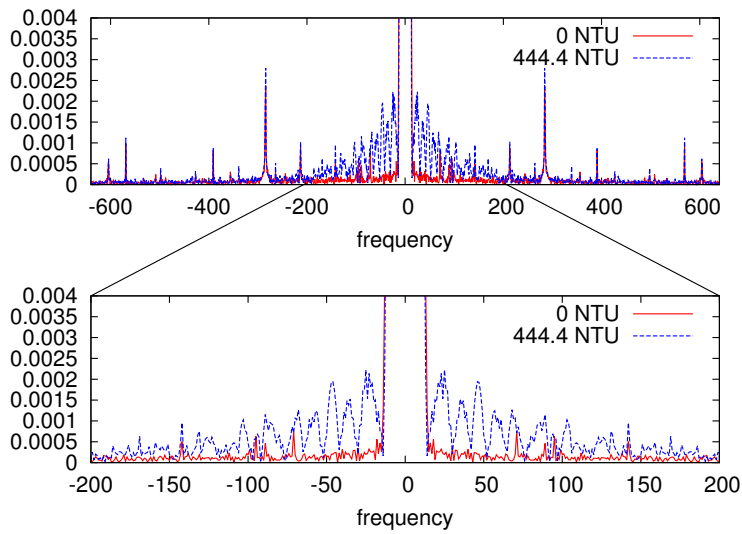


Figure 4.11: The Fourier transformation profile of the laser spot with different turbidities.

of 444.4 NTU. Since a laser is used in the refractometer, the ideal Fourier transformation of the laser spot should be Gaussian too, which can be found in the low frequency (between the spatial frequency -20 and 20 approximately). By comparing the Fourier transformation for different turbidities in Fig. 4.11, a low pass filter can be used to remove the scattered radiation. The result of a low pass filter can be found in Fig 4.8 (c) and (d). For pure water, the resulting image does not differ much from the original image, which can be foreseen since there is no scattering in this case. The image (d) shows that this method correctly retrieves the original Gaussian spot from the original image that mixed the transmitted radiation, the scattered radiation and the speckles caused by interference.

V.3 Solution to light path related problems

V.3.1 Light path variation according to the refractive index

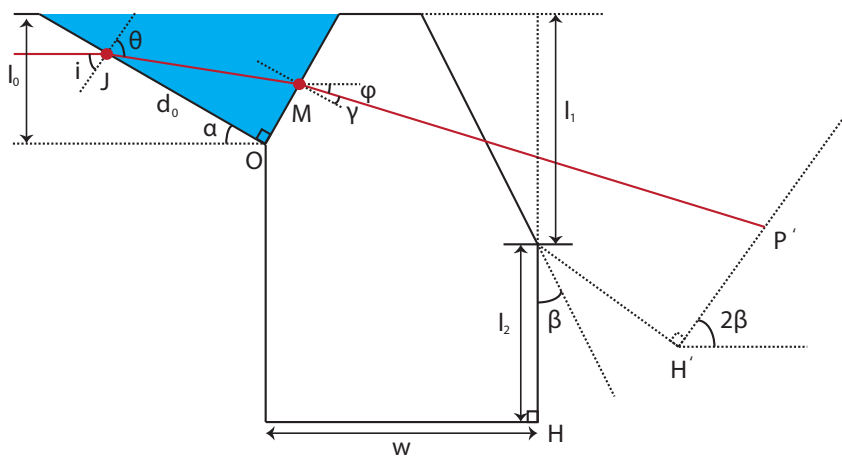


Figure 4.12: The principle of geometric method

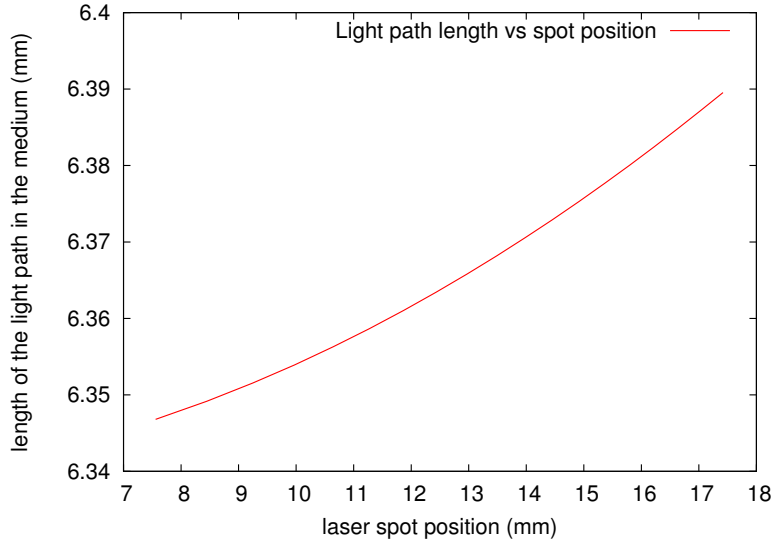


Figure 4.13: The relationship between the length of the light path in the medium and the laser spot position.

One issue discussed in section II is that the length of light path l used to calculate the attenuation coefficients varies according to the change of refractive index. As shown in Fig 4.12, because the refractive index is calculated from the laser spot position $\overline{H'P'}$, the light path length \overline{JM} in the medium from Eq 4.9 can be expressed as a function of the laser spot position. From this figure, \overline{JM} is express as:

$$\overline{JM} = \frac{d_0}{\cos(\frac{\pi}{2} - \theta)} \quad (4.28)$$

Combined with the relationship between the angle θ and $\overline{H'P'}$ discussed in chapter 2, the relationship of light path length and laser spot position can be built, which is shown in Fig 4.13.

A quadratic fitting gives us an approximate equation to calculate the length of light path according to the laser spot position, which is expressed in Eq 4.29.

$$\overline{JM} = l(\overline{H'P'}) = 6.338340 - 0.000284 \overline{H'P'} + 0.000185 \overline{H'P'}^2 \quad (4.29)$$

The light path used in the calculation of attenuation coefficient T can be corrected from this equation.

V.3.2 Non-uniqueness of light path inside the beam

Another issue related to the light path is the non-uniqueness of the light path length for the light emitted from different part of the beam. This results that in each point of the spot, the light attenuation is different. For the wide beam, the maximum value of the spot is used to avoid the non-unique attenuation caused by the different light paths inside the beam. By applying the light path related settings to Eq. 4.26, the attenuation coefficient is:

$$T = -\frac{\ln(\frac{I_{fc}}{t}) - \ln(\frac{I_{fc0}}{t_0})}{l(\overline{H'P'})}, \quad (4.30)$$

where I_{fc} is the maximum value of the filtered image, I_{fc0} is the maximum value of the original filtered image. In practice, N images will be captured for one measurement to avoid accidental errors, the attenuation coefficient can thus be obtained by the formula $\frac{\sum_1^N T_i}{N}$, in which T_i is the attenuation coefficient calculated from Eq.4.30 with the i th image.

V.4 New location algorithm

As discussed in section IV, the non-uniqueness of attenuation inside the beam, the divergence of laser beam, and the scattering change the light intensity distribution so that the gravity center based location method such as PSD and centroid algorithm lead inaccuracy in measuring the laser beam deviation.

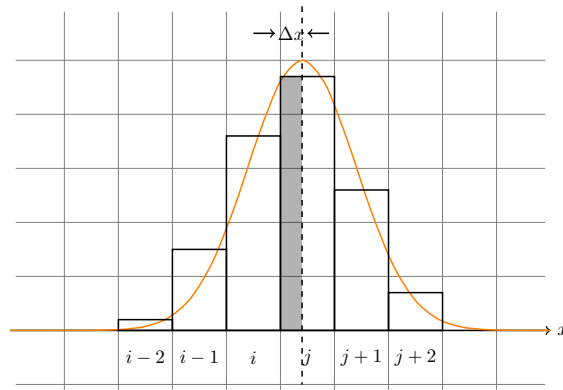


Figure 4.14: The principle of new laser spot location algorithm

To solve this problem, a new algorithm is proposed, which is insensitive to the distribution variation of the laser spot. Fig 4.14 describes this algorithm, which tracks the peak of the Gaussian source shown as the dash line. This dash line divides the divergent laser beam into two parts, named left part and right part, respectively. Since the source laser beam can be considered as a perfect Gaussian beam, the mass of the left part M_{left} is equal to the right one M_{right} and this relationship holds after the refraction of the beam, even though the shape and distribution are asymmetric. This beam is quantized into pixels, which is shown as the bars in Fig 4.14, by a CCD. The mass in the left part M'_{left} can be expressed as:

$$M'_{left} = \sum_0^i P_i + M_{\Delta x}, \quad (4.31)$$

where $M_{\Delta x}$ is the mass shown as the shadow area, P_i is the value of i th pixel. Similarly, the right part M'_{right} can be written as:

$$M'_{right} = \sum_j^{width-1} P_j - M_{\Delta x} \quad (4.32)$$

With Eq. 4.31 and 4.32, the area in the shadow is obtained by

$$M_{\Delta x} = \frac{\sum_j^{width-1} P_j - \sum_0^i P_i}{2} \quad (4.33)$$

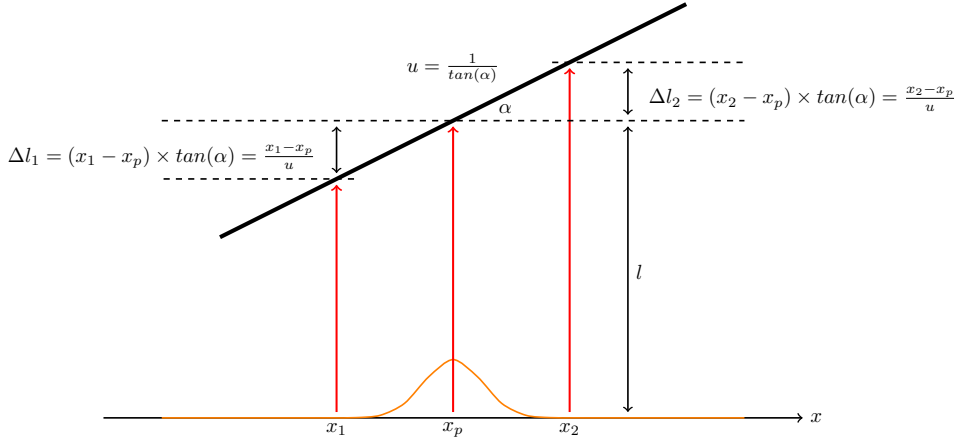


Figure 4.15: The light path inside the beam

And the sub-pixel position is calculated as:

$$x_p = \frac{M\Delta x}{P_j} + i \quad (4.34)$$

In a turbid medium, the attenuation is not uniform inside the beam as shown in Fig 4.15. For a standard Gaussian beam $f(x) = I_0 e^{-\frac{(x-x_p)^2}{2\sigma^2}}$, after the attenuation, the beam changes to:

$$I = I_0 e^{-\frac{(x-x_p)^2}{2\sigma^2}} e^{-T(x-\frac{x_p}{u}+l)} = e^{-\frac{(x-x_p+\frac{T\sigma^2}{u})^2}{2\sigma^2}} I_0 e^{\frac{T^2\sigma^2}{2u^2}-Tl}, \quad (4.35)$$

in which T is the attenuation coefficient, l is the light path of the center, u is a coefficient which describes the different attenuation inside the beam, x_p is the original peak position, and σ is the laser beam size. From this equation, it is easy to conclude that the new laser spot is still a Gaussian spot but with a peak shift of $-\frac{T\sigma^2}{u}$ compared to the original spot. The peak value of the Gaussian spot attenuates to $e^{\frac{T^2\sigma^2}{2u^2}-Tl}$ of the original one. This is shown in Fig 4.16.

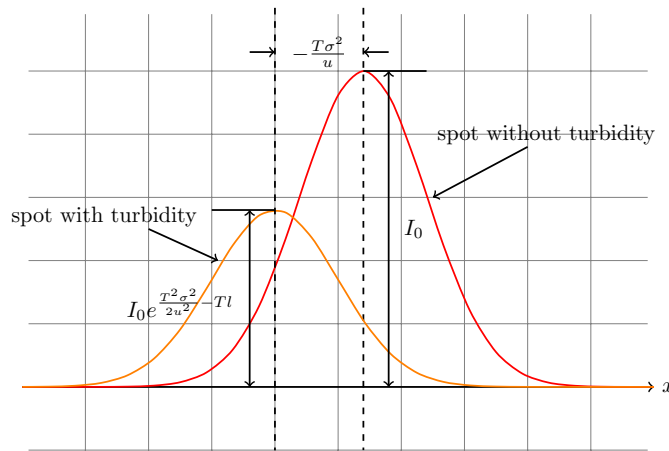


Figure 4.16: The peak shift of the Gaussian spot in a turbid medium

Thus, the mass of the left part and the right part of peak can be calculated from the following equations:

$$M''_{left} = I_0 \int_{-\infty}^{x_p - \frac{T\sigma^2}{u}} e^{-\frac{(x - x_p + \frac{T\sigma^2}{u})^2}{2\sigma^2}} e^{\frac{T^2\sigma^2}{2u^2} - Tl} dx = M''_{right} = I_0 \int_{x_p - \frac{T\sigma^2}{u}}^{+\infty} e^{-\frac{(x - x_p + \frac{T\sigma^2}{u})^2}{2\sigma^2}} e^{\frac{T^2\sigma^2}{2u^2} - Tl} dx \quad (4.36)$$

As in the divergence case, the center calculated by Eq 4.34 is $x_p - \frac{T\sigma^2}{u}$. To obtain the laser spot position x_p , the deviation part $-\frac{T\sigma^2}{u}$ needs to be calculated first. To simplify the discussion, the coefficient $\frac{\sigma^2}{2u^2}$ is noted as v , thus the maximum value measured is $I_0 e^{vT^2 - Tl}$. According to the principle discussed in section I.2, we obtain the following equation:

$$vT^2 - Tl = \ln(I_m) - \ln(I_0) \quad (4.37)$$

By solving this equation, the attenuation coefficient T is expressed as:

$$T = \frac{l - \sqrt{l^2 + 4v(\ln(I_m) - \ln(I_0))}}{2v} \quad (4.38)$$

Combined with Eq. 4.34, 4.36, and 4.38, the laser spot position x_p in turbid medium is calculated by:

$$x_p = w \left(\frac{M_{\Delta x}}{P_j} + i \right) + k \left(l - \sqrt{l^2 + 4v(\ln(I_m) - \ln(I_0))} \right), \quad (4.39)$$

where w is the size of the pixel.

VI Experiments & Results

VI.1 Performance evaluation of new location algorithm

VI.1.1 Simulation

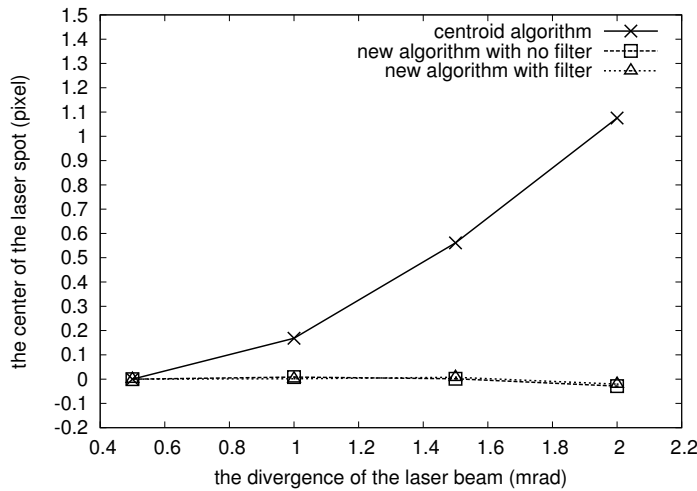


Figure 4.17: The positions obtained by the different algorithms for different divergence of laser beam. (simulated in ZEMAX)

To evaluate the performance of the new algorithm, two simulations: divergence simulation and turbidity simulation, are carried out in ZEMAX, in which the configuration of the refractometer is simulated, while the scattering model chosen for the simulation of turbidity is the Mie scattering. During the simulation, the refractive index of the medium keeps the same, so that the calculated laser spot position is expected to be the same as well. The divergence simulation takes 4 images with 4 different laser beam divergences from 0.5 mrad to 2 mrad . The new algorithm is applied to both the original image and the filtered image. The calculated center can be found in Fig 4.17. To simplify the comparison, the reference center used here is the center calculated for 0.5 mrad , which labeled as position 0. From Fig 4.17, it is clear that the new algorithm obtains better stability than the centroid algorithm when applying different divergences. Table 4.1 gives more detail of the center calculated by the new algorithm, which shows a maximum error of 0.028 pixel. The centroid algorithm turns to be invalid when divergence of laser beam is large.

Table 4.1: Center calculated with different algorithms for different divergences

Divergence (mrad)	0.5	1.0	1.5	2.0
centroid (pixel)	0	0.1684	0.5612	1.0754
new algorithm without filter (pixel)	0	0.0087	0.0014	-0.0286
new algorithm with filter (pixel)	0	0.0013	0.0078	-0.0205

The turbidity of the medium is simulated by changing the density of the particles. The reference image is the image simulated in non-turbid case here. 4 different particle densities ($2 \times 10^6/cm^3$, $4 \times 10^6/cm^3$, $6 \times 10^6/cm^3$, $8 \times 10^6/cm^3$) are simulated and the result is depicted in Fig 4.18. Since the turbid medium diffuses the light out of the beam, a threshold is used to eliminate those light intensities that are diffused out of the laser spot but captured by the CCD. Combined with the threshold, the new algorithm provides a much more accurate result than the centroid algorithm, which gives a deviation of 2.4 pixels. In Table. 4.2, the error of the new algorithm can be found as about 0.069 pixel.

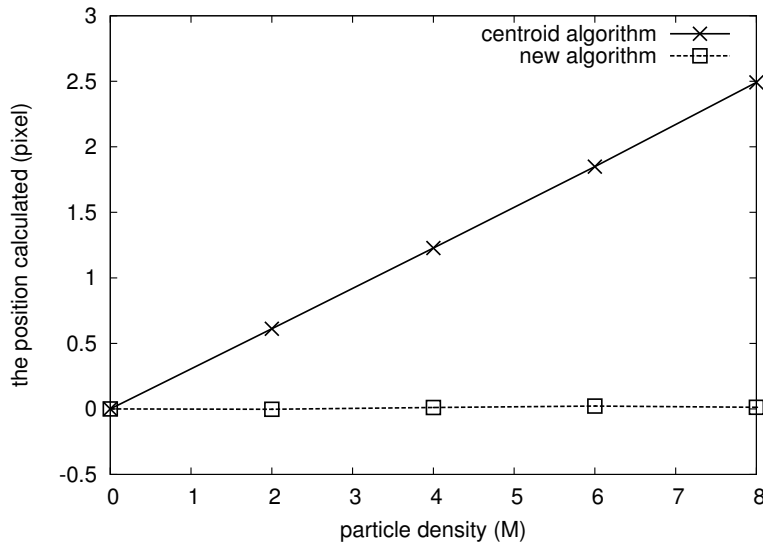


Figure 4.18: The positions obtained by the different algorithms for different density of particles in the medium. (simulated in ZEMAX)

density of particles (<i>per cm³</i>)	0×10^6	2×10^6	4×10^6	6×10^6	8×10^6
centroid algorithm (pixel)	0	0.6117	1.2273	1.8364	2.4439
new algorithm (pixel)	0	-0.0552	-0.0550	-0.0149	0.0695

It is interesting that as the particle density increases linearly, the calculated position by centroid algorithm increases linearly too. This can be explained by the equation 4.35. In turbid medium, the Gaussian spot has a peak shift of $-\frac{T\sigma^2}{u}$. Since the laser spot width σ and the coefficient u are constants, the peak shift is proportional to the attenuation coefficient T .

VI.1.2 Experiment

In chapter 3, several experiments were carried out to evaluate the performance of the centroid algorithm with a micro-positioner, which can move with a step of $0.1 \mu m$. To compare the performance of the centroid algorithm with the new algorithm, the same image set is chosen, and the two algorithms are applied. The centers calculated by these two algorithms are depicted in Fig 4.19. Furthermore, the result for the new algorithm with the filter is included in this figure too. It is obvious that the curve of the new algorithm is much smoother than the centroid algorithm. The error of these methods can be calculated by a linear fitting. Centroid algorithm obtains a maximum error of 0.1 pixel with the standard deviation of 0.0784 pixel, while the new algorithm with and without the filter get a maximum error about 0.06 pixel (the standard deviations are 0.0348 and 0.0352 pixel respectively). For an image with $M \times N$ pixels, the two algorithms have the same time complexity of $O(MN)$. All the results above make the new algorithm a good alternative to the centroid algorithm even in non-turbid case. Besides, according to the simulation results and the algorithm analysis, the new algorithm is insensitive to the light intensity distribution variation and can be applied to the turbid medium.

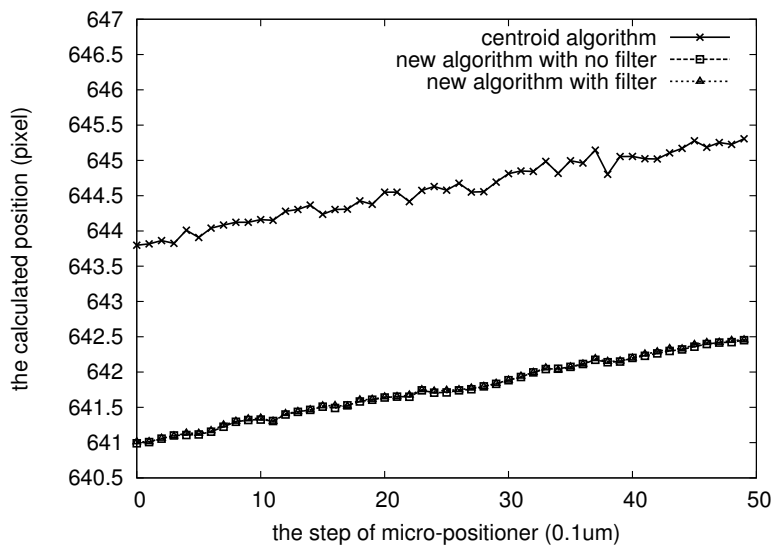


Figure 4.19: The calculated center provided by the centroid algorithm, new algorithm with and without filter.

VI.2 Simulation & experiments with parallel slab

VI.2.1 Simulation

To test the principle of turbidity measurement, the simulation in parallel slab are carried out, firstly in ZEMAX. The turbidity of the medium is changed by adjusting the density of the particles from $1 \times 10^6/cm^3$ to $1 \times 10^7/cm^3$. The scattering model used in the simulation is the Mie scattering. The dimension of the parallel slab follows the size of the parallel slab used in the real experiment. A CCD is placed 10 cm from the parallel slab along the laser beam propagation direction. Table 4.3 depicts the attenuation coefficient T calculated by Eq 4.9. By doing a linear fitting, the attenuation coefficient given by the method correctly describes the density of the particles, which is theoretically proportional to the turbidity in the simulation. The error standard deviation of the calculated attenuation coefficient T according to the line is 8.2×10^{-4} . This result means the multi-scattered light I_{ms} can be ignored in Eq 4.9 due to the short light path in the turbid water.

density of particles ($10^6/cm^3$)	attenuation coefficient
0	0
1	-0.015
2	-0.029
3	-0.044
4	-0.059
5	-0.073
6	-0.088
7	-0.104
8	-0.118
9	-0.133
10	-0.150

VI.2.2 Experiments in high turbid medium

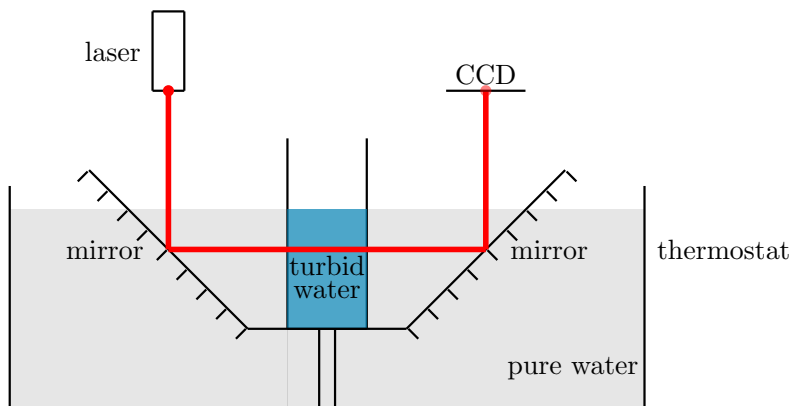


Figure 4.20: The experiment setup for the experiments carried out in a parallel slab

Besides the simulation, an experiment was carried out in the parallel slab. Fig. 4.20 shows the setup of the experiment. A red diode laser at 635 nm is mounted perpendicularly

to the horizontal plane. A 45 degree mirror redirects the laser beam to a parallel slab with a width of 16 mm. Another 45 degree mirror is used to redirect the propagating beam into a DALSA CCD camera [9], with a 1280×960 resolution and a small $3.75 \times 3.75 \mu\text{m}$ pixel size. The turbidity reference used in the experiment is the 4000 NTU Formazin standard. Since the scattering is sensitive to the size of the formazin particles, which change according to temperature, the setup was established in the presence of a thermostat to keep the temperature stable. To obtain different turbidity, 1 ml 4000 NTU Formazin standard was added N times to the parallel slab, which contained 40 ml pure water at the beginning. The turbidity of diluted turbid water can be calculated by:

$$t_i = \frac{t_{i-1} \times V_{i-1} + \Delta V \times 4000}{V_{i-1} + \Delta V}, \quad (t_0 = 0, V_0 = 40) \quad (4.40)$$

where ΔV is the added volume of 4000 NTU Formazin standard each time, t_i and V_i is the turbidity and the total volume after adding the ΔV of 4000 NTU Formazin for i th time. 10 images are captured for each turbidity with a sufficient exposure time to make sure the peak of the spot reaches more than 100 (maximum 255 for the CCD). Since the diluted formazin is not stable for long time storage, all experiments are carried out in a dark room and in less than 1 hour to obtain the best performance.

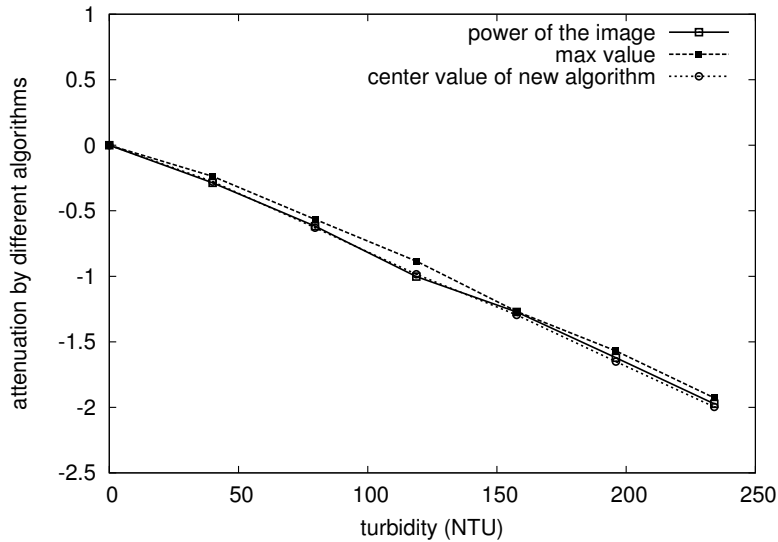


Figure 4.21: Experimental results for the parallel slab for high turbid medium.

Fig 4.21 shows the experimental result. The light intensity I_0 is pre-measured with pure water as the reference light intensity. For each turbidity, according to Eq 4.9, three attenuation coefficients are calculated by using the power of the image, the max value of the image, and the pixel value in the position obtained from the new algorithm as I_m , respectively. All these three curves show linearity to the turbidity which is in the range from 0 NTU to about 234.1 NTU as expected. The average error of these three methods is estimated by a linear fitting, which gives three similar slopes of -0.0085 , -0.0084 , -0.0086 , respectively. By using the max value of the image, the standard deviation of error is the largest of the three, which reaches ± 4.87 NTU (2% of the measurement range), while the standard deviation of error obtained by using the power of the image is ± 3.17 NTU (1.4% of the measurement range). The standard deviation of error given by the new

algorithm is the smallest: ± 2.82 NTU (1.2% of the measurement range). From Eq 4.9, it is easy to conclude that the resolution of the turbid-meter is proportional to the sensitivity of the light sensor and inversely proportional to the light path length. It is believed that the resolution in the experiment can be improved by simply extending the width of the slab.

VI.2.3 Experiments in low turbid medium

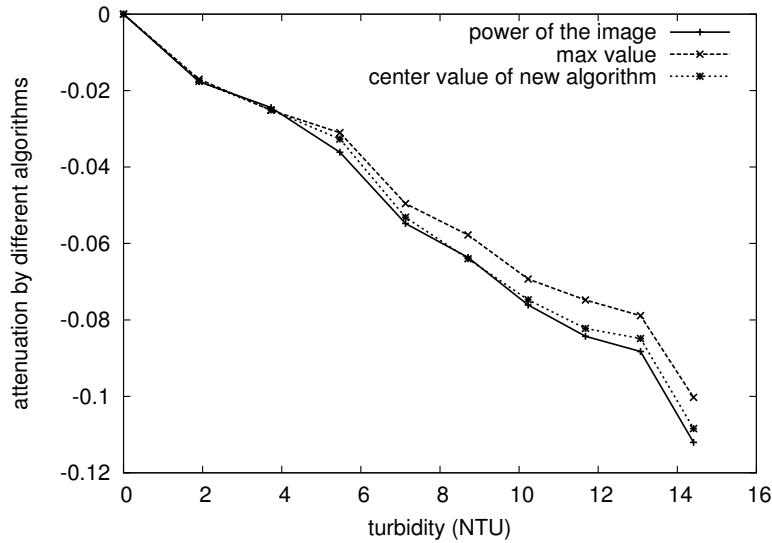


Figure 4.22: Experimental results for the parallel slab for low turbid medium.

As discussed in section I.4, the resolution of the turbid-meter is better in the low turbid medium than in the high turbid one with the same light path and light sensor sensitivity. To demonstrate that, another experiment was carried out with the same parallel slab. All the configurations in this experiment are the same as the one for the high turbid medium discussed in the last section. 40 ml pure water is poured into the slab as the base volume of water. 1 ml diluted turbid water with the turbidity of 78.43 NTU is added to the slab 9 times. For each time, 24 images are captured within 1 second. According to Eq 4.40, the range of the turbidity for the 9 media varies from 1.91 NTU to 14.41 NTU. Fig. 4.22 expresses the attenuation coefficient calculated by using the power of the image, the maximum of the image and the pixel value given by the new algorithm, respectively. All of them show a linearity with respect to the turbidity. Even in this small range of turbidity, it is clear that the higher turbid medium gives larger error than the low turbid medium. For these three methods, the maximum value gives a large deviation in higher turbidity medium than the other two. The standard deviation of error for the three methods can be estimated by a linear fitting, which shows that the standard deviation of error of using the power of the image is about ± 0.5 NTU (3.5% of the measurement range), while the new algorithm provides a standard deviation of ± 0.6 NTU (4.2% of the measurement range). Compared with the standard deviation of error obtained in the last section, the absolute sensitivity of the turbidity is better in a low turbid medium (± 0.6 NTU) than in a high turbid one (± 2.82 NTU), which well proves the previous sensitivity discussion. However, the relative turbidity sensitivity in a low turbid medium (4.2%) is worse than in a high

turbid one (1.2%). This is because that the light attenuation is much smaller in low turbid medium than in high turbid one. The attenuation signal to noise ratio (SNR) turns to be smaller in low turbid medium as well, which leads to worse relative sensitivity.

VI.3 Simulation & experiments with refractometer

VI.3.1 Simulation

The simulation of measuring the turbidity with our refractometer was carried out in ZEMAX. The turbidity of the medium was changed by modifying the particle density of the medium from $1 \times 10^6/cm^3$ to $1 \times 10^7/cm^3$. The divergence of the laser beam is set to 1 mrad, the same as the source used in the experiment. A CCD of 1280×960 pixels is simulated by a rectangular detector. Table. 4.4 expresses the attenuation coefficient calculated from the simulation. Similarly to the parallel slab case, the attenuation coefficient given by the algorithm discussed in this paper shows a good linearity to the density of the particles in the medium, which is theoretically proportional to the turbidity of the medium.

density of particles ($10^6/cm^3$)	attenuation coefficient
0	0
1	-0.018
2	-0.036
3	-0.053
4	-0.071
5	-0.090
6	-0.107
7	-0.126
8	-0.144
9	-0.165
10	-0.185

VI.3.2 Experiments in high turbid medium

Fig 4.23 shows the set up of the experiment with the refractometer. The refractometer is used instead of the parallel slab. The diode laser and CCD used in this experiment are the same as those used in the parallel slab experiment. The refractometer is set-up in a small tank, in which 100 ml pure water is used as the base water. 0.5 ml 4000 NTU formazin solution was added to the small tank 11 times and is diluted to different turbid water levels. The turbidity can be calculated according to the Eq 4.40. All the experiments are carried out in the presence of a thermostat to make sure the temperature of the turbid medium does not change.

The experimental results are shown in Fig 4.24. The attenuation coefficients are calculated by two different quantities, the power of the image and the pixel value given by the new algorithm, as the measured intensity I_m in Eq 4.38. The reference light intensity I_0 is pre-measured in pure water with the same configuration. As the turbidity increases, both methods give a trend of decrease for the attenuation coefficient. The average error of these two methods can be evaluated by a linear fitting. The method using the power of the image as the measured intensity provides an error with standard deviation of ± 8.09

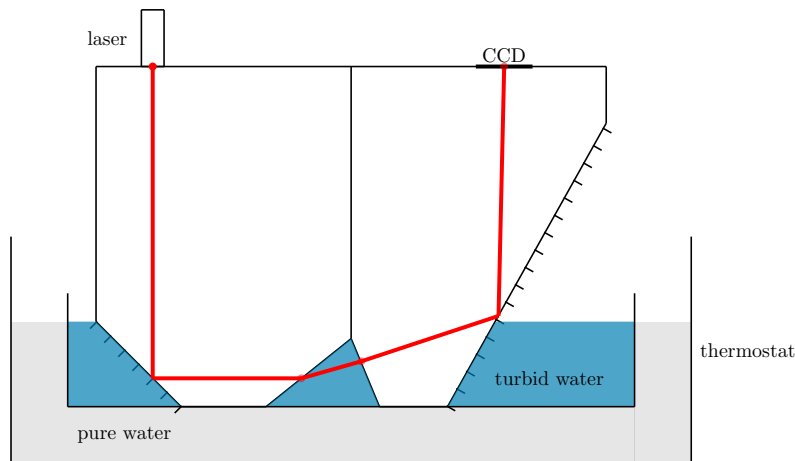


Figure 4.23: Experiment setup for the experiments carried out with the refractometer

NTU (3.4% of measurement range), while the standard deviation of error for the method using the new algorithm is about ± 7.96 NTU (3.4% of measurement range). As we have discussed in Section I.4, the sensitivity of the measurement of turbidity is inversely proportional to the light path in the medium. Compared to the error obtained in the parallel slab with 15.91 mm, the error obtained with the refractometer fits this analysis. From the Eq 4.29, the light path distance can be calculated as about 6.36 mm. The ratio of the errors between parallel slab and refractometer is about 2.7, while the ratio between the light path in parallel slab and the one in refractometer is about 2.5. It is believed that the difference between both ratios is caused by the set-up error of the laser source, which makes the laser beam not exactly perpendicular to the horizontal plane. This set-up error makes the actual light path distance shorter than the theoretical one.

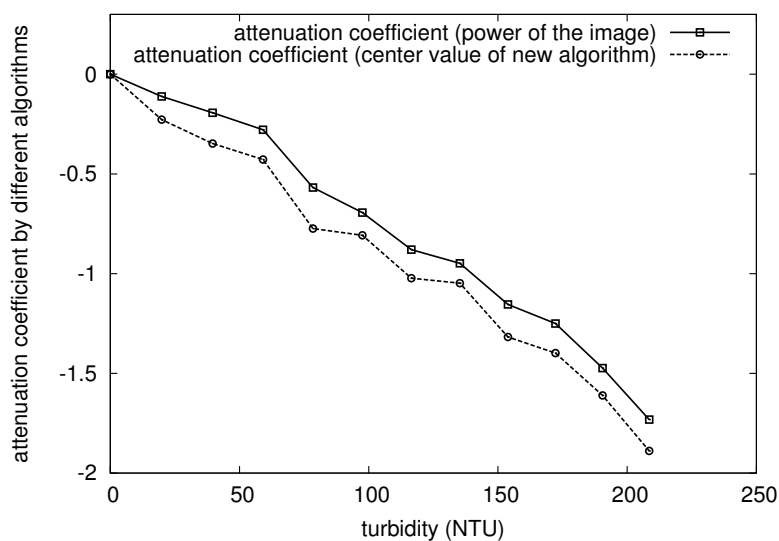


Figure 4.24: Experimental results with the refractometer in high turbid medium

VI.3.3 Experiments in low turbid medium

The performance of the turbidity measurement with the refractometer in a low turbid medium is tested with another experiment. The experiment set up is the same as the experiment in high turbid medium discussed in last section. 100 ml pure water is used as the base medium, while diluted formazin of 190 NTU is added into the base medium 11 times to generate different turbid water from 0 NTU to about 19 NTU. The attenuation coefficients calculated from the power of the image and the pixel value obtained by the new algorithm are plotted in Fig 4.25. The power of the image shows a better linearity than the new algorithm. The reason is that in a low turbid case, the attenuation of the light is very small so that the non-uniqueness of the attenuation inside the beam is not significant. Thus, the more pixels of the spot used as the measured intensity I_{trans} , the more accurate the result is. However, the new algorithm only tracks the intensity in one location, which divides the mass of the spot into two identical parts. Therefore, it highly depends on the sensitivity of the light intensity sensor. In a low turbid case, the attenuation of the light intensity for one pixel is so small that the CCD cannot detect it, this explains that in the low turbid case shown in Fig 4.25, the attenuation coefficient calculated from the new algorithm does not hold linearity, especially in ultra low turbid mediums. The experimental results with parallel slab prove this as well, in which the standard deviation of new algorithm (± 0.6 NTU, 4.2% of measurement range) is larger than the standard deviation of using the image power (± 0.5 NTU, 3.5% of measurement range). With the refractometer, the standard deviation of using the power of the image is obtained from a linear fitting, which is about ± 1.15 NTU (6% of measurement range). The ratio between this error and the error obtained in the parallel slab (± 0.5 NTU) is 2.3, which fits the ratio between the light paths (about 2.5).

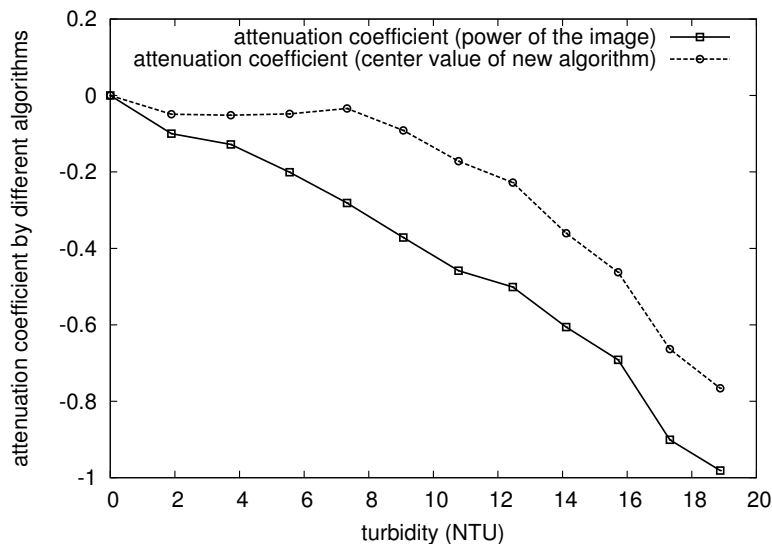


Figure 4.25: Experimental results with the refractometer in low turbid medium

VI.4 Comparison with nephelometer

Nephelometer, which measures the diffusion of the light at 90 degree from the light propagation direction, is a stationary or portable instrument for measuring suspended particulates

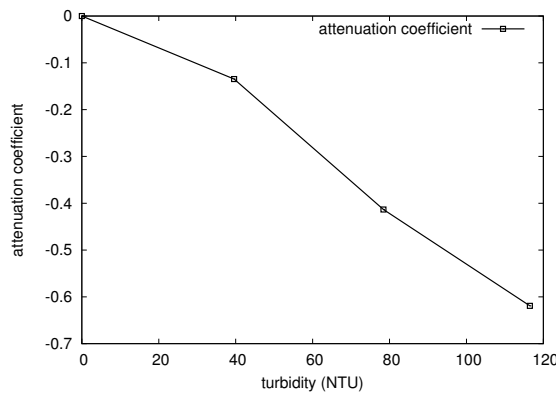


Figure 4.26: Experimental results with the refractometer

in a liquid or gas colloid. It has been proved to be an accurate and reliable method to measure turbidity from scattering. To test the performance of our method mentioned in this paper, the experimental result is compared to the result obtained from a nephelometer. The test sample is 100 ml diluted formazin turbidity solution. The turbidity of the sample is firstly measured in the nephelometer HACH 2100N[10], which gives a result of 109 ± 2 NTU. The experiment setup is the same in section VI.3.2. The turbidi-meter is firstly calibrated by adding 1ml 4000 NTU formazin turbidity solution into 100 ml pure water for 3 times. For each time, 24 images are captured by the CCD within 1 second. Since the test sample is not in low turbid range, the new algorithm is used to calculate the attenuation coefficient. The attenuation coefficients calculated for the calibration are shown in Fig 4.26. A linear fitting is made from the calibration results, which has a slope of -0.0055 . With this calibrated configuration, the experiment with test sample is carried out as well. The attenuation coefficient obtained by the new algorithm is -0.6054 . According to the slope of the fitting line, the turbidity of the test sample can be calculated as $t = \frac{T}{k} = \frac{-0.6054}{-0.0055} = 110.07$ NTU, which fits the result obtained from the nephelometer.

Conclusion

CCD records the light intensity distribution rather than the light position as PSD does, thus it can provide much more information than PSD. We have proved that the CCD-based system obtains better performance than PSD-based system in laser beam deviation measurement. This makes the use of CCD instead of PSD valuable. To show more advantages of CCD-based system, the measure of the quantities other than laser beam deviation without modifying the refractometer is necessary. Under our subject background, turbidity measurement is a good choice. In this chapter, we introduced how to measure turbidity with our current refractometer by using a CCD.

At the beginning of this chapter, we shortly reviewed the state of the art turbidity measurement methods. The attenuation based method is the only one that can be used without modifying the refractometer configuration. By analysing its principle, the attenuation coefficient, which is proportional to the absorption, diffusion, and particle density of the medium, is chosen as a descriptor of turbidity. This method has the susceptibility to absorbance and color interferences, which are related to the wavelength of the light source. According to the analysis of the attenuation coefficient computation, the resolution of this method is proportional to the sensitivity of the light intensity sensor, and inversely proportional to the light path in the medium and the measurement range.

With the configuration of our refractometer, the measurement of turbidity has to face several issues. The interference of the laser is observed in turbid medium, which forms speckles that lead to unexpected result. In our configuration of the refractometer, different refractive index will result in a different light paths. The width of the laser beam and the refraction result in the non-uniform attenuation inside the beam, which disturbs measurement of the attenuation from the laser spot power. In contrast to refractive index measurement, the attenuation measurement requires that the laser intensity is stable during the measurement as a reference intensity. Besides the laser beam, the light diffused out of the beam is received by the light intensity sensor as well, which disturbs the power of the spot. Furthermore, attenuation makes the light intensity too weak to be measured, which causes bad performance in high turbid medium. All these problems determine that a simple light intensity sensor such as PSD cannot afford to measure the turbidity in a refractometer. To overcome these problems, a CCD is used to deal with these issues. With recording the light intensity distribution, an image captured by CCD can be treated with a low pass filter to eliminate speckle, and the diffused light can be eliminated by applying a proper threshold. The laser intensity is automatically controlled to keep it stable during all the measurement. By playing with a longer exposure time, weak light can be captured as well. To avoid the non-uniform light path inside the laser beam, only one ray of light is traced and used to calculate turbidity.

In addition to the issues of measuring the turbidity with a refractometer, the turbid medium impacts the measurement of the refractive index as well. Due to the convergence of the laser beam, the laser spot becomes asymmetric, when it is captured by a CCD that is non-perpendicular to the laser beam. What is more, turbidity makes this phenomenon much more obvious. Besides the asymmetric of the laser spot, the turbidity results in a shift of the laser spot peak, which is proportional to the attenuation coefficient. This shift needs to be corrected when applying mass-center-based algorithm to locate the laser spot. A CCD records all the distribution information of the laser spot, which makes it possible to retrieve the position information more accurately. A new algorithm, which tracks the location that divides the mass of the spot into two equal parts, is introduced in this paper,

and is proved to be more accurate than the centroid algorithm in both the non-turbid environment and turbid environment.

We also presented several simulations and experiments to evaluate the method mentioned in this chapter. Through the simulations and experiments, the average accuracy of our method based on the current refractometer reaches 8 NTU in a range from 0 NTU to 200 NTU and 1.15 NTU in a range from 0 NTU to 20 NTU. We compared our method with the nephelometer specified by the NTU standard. The result computed by our method well fits the result obtained from a nephelometer.

The method illustrated in this chapter is not the optimized solution to measure the refractive index and turbidity in a compact *in situ* sensor. If we take off the restrictions of building the double sensor based on our current refractometer, it is possible to design a new CCD-based refracto-turbidi-meter with better performance. By choosing a light source at wavelength 860 *nm*, the absorbance can be avoided. A unique-prism design instead of two-prisms design decreases the complexity of fabrication. The sensitivity can be improved by increasing the length of the light path in the medium, which requires a new modelling of the optics. Before the light beam enter the prism, the light power can be measured as the reference for attenuation based turbidity measurement to improve the accuracy of turbidity computation. One more light intensity sensor could be introduced to measure the scattered light at 90°, which can improve the turbidity measurement performance in ultra low and ultra high turbidity case. All these possible improvements were discussed in the next chapter ‘perspective’.

Bibliography

- [1] Michael J. Sadar. Turbidity science. *Technical Information Series, Booklet 11, Hach Company*, 1998.
 - [2] Iso7027: Water quality - determination of turbidity. *International Standard*, 1999.
 - [3] APHA, AWWA, and WPCF. Standard methods for the examination of water and wastewater. pages 2–12, 1989.
 - [4] G. Mie. Beiträge zur optik trüber medien, speziell kolloidaler metallösungen, leipzig. *Ann. Phys.*, page 377, 1908.
 - [5] L. C. Henyey and J. L. Greenstein. Diffuse radiation in the galaxy. *Astrophys*, 93:70, 1941.
 - [6] W. M. Cornette and J. G. Shanks. Physically reasonable analytic expression for the single-scattering phase function. *Appl. Opt.*, 31:3152, 1992.
 - [7] W. M. Irvine. Multiple scattering by large particles. *Astrophys*, 4:1563, 1956.
 - [8] I. Edwards. Using photodetectors for position sensing. *Sensors Magazine*, Dec. 1988.
 - [9] DALSA Corporation. Genie m1280 datasheet, 2009. http://www.dalsa.com/prot/mv/datasheets/genie_m1280_1.3.pdf.
 - [10] Hach Company. 2100 series laboratory turbidimeters data sheet.
-

Figures and tables

Figures

4.1	Principle of refractometer	91
4.2	Two phase functions: Heney Greenstein function and Schlick function.	92
4.3	The light absorption and diffusion in a unit volume of turbid water.	93
4.4	The light scattered from other parts of the medium to the incident light propagation direction	94
4.5	The difference of light intensity measurement by locating the light intensity sensor at different distances of the medium	96
4.6	Different parts inside the beam pass different lengths in the medium	97
4.7	The light path varies according to different refractive index	97
4.8	The captured scattered light and interference when camera is near to the medium	98
4.9	The laser spots for different laser beams with different divergence. The image is obtained from the ZEMAX simulation.	99
4.10	A divergent laser beam projects to a plane at an angle of 28°	100
4.11	The Fourier transformation profile of the laser spot with different turbidities.	103
4.12	The principle of geometric method	103
4.13	The relationship between the length of the light path in the medium and the laser spot position.	104
4.14	The principle of new laser spot location algorithm	105
4.15	The light path inside the beam	106
4.16	The peak shift of the Gaussian spot in a turbid medium	106
4.17	The positions obtained by the different algorithms for different divergence of laser beam. (simulated in ZEMAX)	107
4.18	The positions obtained by the different algorithms for different density of particles in the medium. (simulated in ZEMAX)	108
4.19	The calculated center provided by the centroid algorithm, new algorithm with and without filter.	109
4.20	The experiment setup for the experiments carried out in a parallel slab	110
4.21	Experimental results for the parallel slab for high turbid medium.	111
4.22	Experimental results for the parallel slab for low turbid medium.	112
4.23	Experiment setup for the experiments carried out with the refractometer	114
4.24	Experimental results with the refractometer in high turbid medium	114
4.25	Experimental results with the refractometer in low turbid medium	115
4.26	Experimental results with the refractometer	116

Tables

4.1	Center calculated with different algorithms for different divergences	108
4.2	Center calculated with different algorithms for different turbidity	109
4.3	Simulation results with the parallel slab	110
4.4	Simulation results with the refractometer	113

Chapter 5

Perspective: improvements of refracto-turbidi-meter performance

Contents

Introduction	122
I Issues and Possible improvements	122
I.1 Issues in our methods	122
I.2 Improvements for refractometer	123
I.3 Improvements for turbidi-meter	124
I.4 Other improvements	125
II Prototype II: new model of refractometer	125
II.1 New model	126
II.2 Performance analysis	126
III Prototype III: new model of refracto-turbidi-meter	127
III.1 Turbidi-meter based on prototype II	128
III.2 Futher improvement	129
Conclusion	131
Bibliography	132
Figures and tables	133

Introduction

With the discussion in chapter 4, we have designed a high resolution refracto-turbidi-meter based on a refractometer by using a CCD. As we can see, there exists several issues in simultaneously measuring the laser beam attenuation and the laser beam deviation based on our refractometer. In this chapter, we propose three new models to improve the performance of both refractive index and turbidity measurement.

In the first part of this chapter, several possible improvements are discussed, including the one for refractometer and the one for turbidi-meter. What is more, the interference between these two measurements are also considered in our discussion.

Based on the discussion, in the second part of the chapter, a new prototype of refractometer is first presented with a short performance analysis, including the mathematical calculation and simulation. The method discussed in chapter 4 can be used to measure turbidity with this new refractometer as well. However, with the new refractometer configuration, it is possible to make several modifications to improve the performance of turbidity measurement without influencing the refractive index measurement.

In the third part of the chapter, we first introduce a new refracto-turbidi-meter, which has a resolution of 0.3 NTU in the range from 0 NTU to 20 NTU by modifying the new refractometer. A further improvements, in which one more photo-diode is used to measure the scattered light at 90° , is also included in this part. The resolution of this model is expected to at least reach 1% measurement range and obtain better performance in low turbidity measurement.

I Issues and Possible improvements

The methods that we presented in this document has been proved to have a high resolution in measuring refractive index of seawater, which further gives us the salinity information in high resolution. Furthermore, it provides the capability of measuring seawater turbidity simultaneously. However, during our discussion, there exists several issues in both the refractive index measurement and turbidity measurement, which need to be solved or at least improved in the future model. In this part, we review these issues and propose several possible methods to improve them.

I.1 Issues in our methods

In chapter 2, we introduced one refractometer, which uses two prisms with different temperature coefficients to compensate refractive index change caused by temperature variation. However, in order to work in deep sea, this two-prism configuration requires them to be well aligned in fabrication, which increased the complexity of assembling the sensor. Due to this issue, a one-prism design is expected, however, as a consequence, the temperature compensation need to be reconsidered.

Another issue for the refractometer is related to the thermal expansion coefficient, which is one of the aspects that influence the system resolution. Since the expansion caused by temperature variation is proportional to the original size of prism, a smaller prism reduces the expansion caused by temperature variation. However, according to the resolution analysis in chapter 2, the resolution is also proportional to the length of light path after the second refraction, which works as an amplifier to amplify the refractive index

variation to a detectable laser spot displacement. A smaller prism need to be well designed to make sure this length is long enough to reach the desired resolution.

In last chapter, we also introduced several issues in measuring the refractive index and turbidity simultaneously, including:

1. The combination of attenuated light and scattered light caused by the measurement distance
2. None uniqueness of light path inside the beam
3. Light path variation caused by different refractive indices
4. Interference caused by laser source and particles
5. Asymmetrical spot caused by divergence and scattering
6. Non-stable reference of laser source power
7. Absorbance and color interference in measuring turbidity

These issues are caused by two reasons: first, the refractometer that we used is not designed to be a multi-functional sensor. During the modelling of refractometer, the possible problems that might occur in a turbid medium were not under consideration. Another reason is that the method we used in last chapter to measure turbidity is only for proving the benefits of using a CCD instead of a PSD in a multi-functional sensor. With this purpose, the method we chose is the one which requires the least modification to the refractometer configuration.

In this chapter, we try to break these restrictions, and design a new refracto-turbidimeter which has better performance and less the issues mentioned above.

I.2 Improvements for refractometer

One possible improvements for refractive index measurement is to use a unique prism rather than two prisms in order to avoid the complexity in assembling process. We use another method to compensate the glass refractive index change caused by temperature variation, rather than two prisms with different temperature coefficients. As studied in chapter 2, the refractive index is not only associated to temperature but also the wavelength, which is illustrated by Sellmeier equation:

$$n^2(\lambda) = 1 + \frac{B_1\lambda^2}{\lambda^2 - C_1} + \frac{B_2\lambda^2}{\lambda^2 - C_2} + \frac{B_3\lambda^2}{\lambda^2 - C_3}, \quad (5.1)$$

When the temperature increases, the wavelength of the laser rises as well, which further results in the decrease of glass refractive index, according to equation 5.1. The variation caused by the wavelength change $\Delta n_\lambda < 0$ (*when* $\Delta T > 0$) can be used to compensate the refractive index variation induced by temperature change Δn_T (*when* $\Delta T < 0$). To choose a glass with this feature, we plotted two functions, $\frac{dn}{dT} = f_1(T)$ and $\frac{dn}{d\lambda} = f_2(T)$, for several Schott glasses at a wavelength of 635 nm in 20 °C, and found that the glass N-ZK7 best fits our requirements. Fig. 5.1 plots the two functions and the refractive index variation from 0 °C and 40 °C for N-ZK7. As shown in this figure, the refractive index variation of N-ZK7 from 0 °C and 40 °C is only 7.5×10^{-7} .

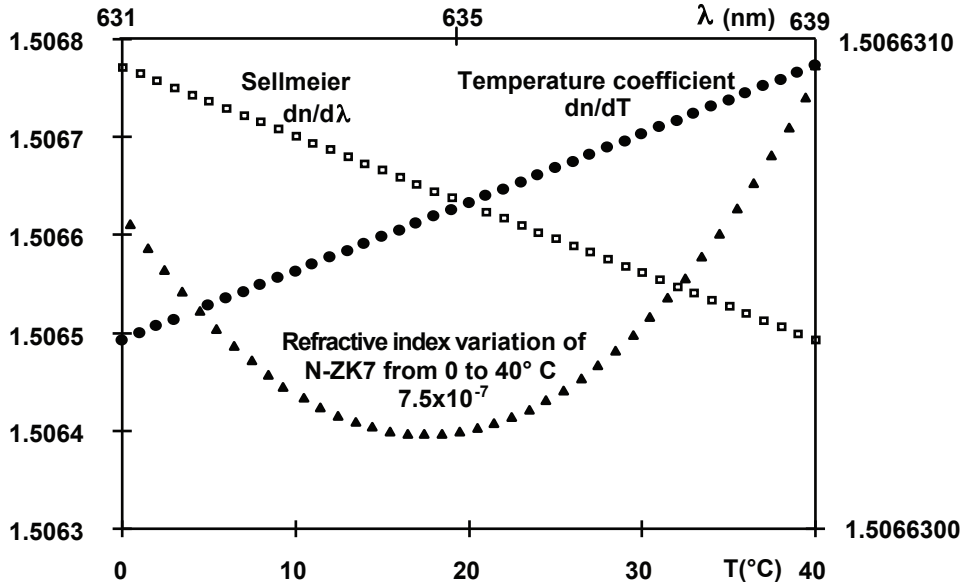


Figure 5.1: The temperature coefficient and sellmeier coefficient of glass N-ZK7 when temperature varies from 0 °C to 40 °C

Another improvement is to reduce the thermal expansion led by temperature variation. The principle is to reduce the prism size, which is proportional to the thermal expansion, and meanwhile keep the length of light path after the second refraction in order to obtain the same resolution. To meet this requirement, more reflections need to be introduced to the prism after the second refraction to keep the light path inside the prism long enough.

I.3 Improvements for turbidi-meter

For turbidity measurement, one improvement is the selection of light source. The diode laser that we used is good for the refractive index measurement, but it has the greatest susceptibility to absorbance and color interferences, which impacts the turbidity measurement by measuring the light attenuation. What is more, the laser is easy to generate interference in turbid medium. One possible solution to the problem is to use the LED at 860 nm as the light source. The particles in the nature nearly do not absorb the light at this wavelength. An issue of LED is the divergence - the light emitted from laser is much more focus than the one emitted from LED. This might impacts the refractive index measurement. The use of CCD can solve this problem due to the advanced post-processing techniques.

Another importance quantity for the transmitted light based turbidity measurement is the initial light intensity I_0 , which is the reference for the calculation. In our current refractometer, the laser beam directly enter the prism after it leaves the laser module. This makes the measurement of the light intensity difficult. In the new design of the refracto-turbidi-meter, the laser module does not directly contact the prism. An optical splitter is used to separate the laser beam into two, one enters the prism for the measurement of refractive index and turbidity, another is measured by a photo-diode as the initial light power I_0 .

Since the resolution of transmitted-based turbidity measurement highly depends on the

length of light path in the medium, the new design can improve the turbidity resolution by prolonging this length. The prolongation of the distance between the two refraction surface is one of the possible solution. Another solution is to open a groove for water in the prism after the second refraction. This groove is designed long enough to fulfil the required turbidity resolution. Besides the improvement of resolution, another advantage of prolonging the length is that the prolongation of the distance reduces the impacts of the refraction-caused light path non-uniqueness inside the beam.

The ratio nephelometric method can be adopted into our new design as well. Another light intensity sensor e.g. photo-diode can be introduced to measure the scattered light at 90° . This will further improve the performance of turbidity measurement in the medium with ultra low and ultra high turbidity.

I.4 Other improvements

For the post-processing method, the new location algorithm has been proved to be more efficient than the centroid algorithm in both the clear and turbid medium. It can be used to measure the laser beam deviation. Besides the transmitted based turbidity measurement, some new methods can be studied. As discussed in last chapter, the scattered light captured by CCD affects the high frequency parts. This part of signal contains the scattering information of the medium. A possible improvement is to retrieve the turbidity from this parts of frequency. To improve the speed of the post-processing algorithms, it is possible to implement them in a FPGA chip, which is much faster than the software implementation. The images captured by CCD can be temporally stored in memory for being processed other than in hard disk.

II Prototype II: new model of refractometer

According to the possible improvements presented in last section, we first introduce our new model of refractometer which has a uni-prism design and smaller size. Based on this refractometer, in next section, two modifications are made to make it capable to simultaneously measure turbidity in high resolution.

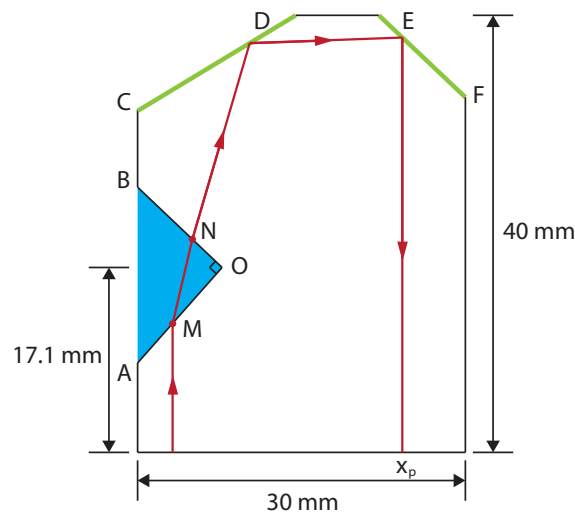


Figure 5.2: The optical design for the prototype II

II.1 New model

Fig. 5.2 depicts the optical design for the new model of refractometer[1]. This new model only has one piece of prism. As we discussed in last section, N-ZK7 is selected as the material of the prism, which has the temperature compensation characteristic. The light beam first enters the prism from the left corner of the prism and reaches the first refraction surface AO . It is then refracted into the medium and refracted again at the refraction surface BO . This refraction leads the beam to a mirror CD , which redirects the upwards beam to the right side of the prism, where it meets the second mirror EF and redirects to the right bottom corner of the prism. A light position detection device, eg. CCD or PSD, can be used to obtain the beam deviation caused by the water refractive index variation. This design makes the prism much smaller ($40\text{ mm} \times 30\text{ mm}$) than our first prototype ($125\text{ mm} \times 90\text{ mm}$) illustrated in chapter 2. According to the discussion in last section, this design has smaller expansion than the first prototype. Fig. 5.3 shows the sizes of both the two prototypes.

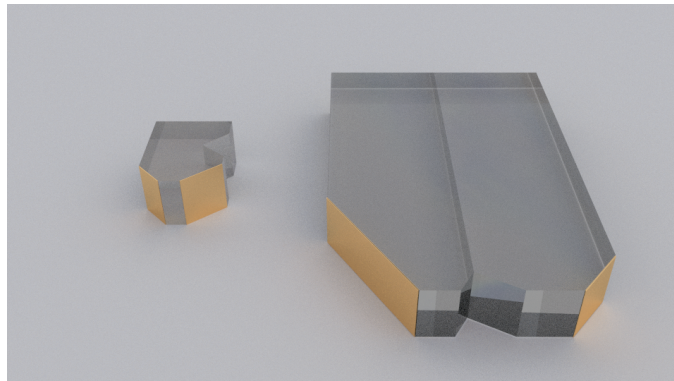


Figure 5.3: The size comparison between prototype I (right) and II (left)

II.2 Performance analysis

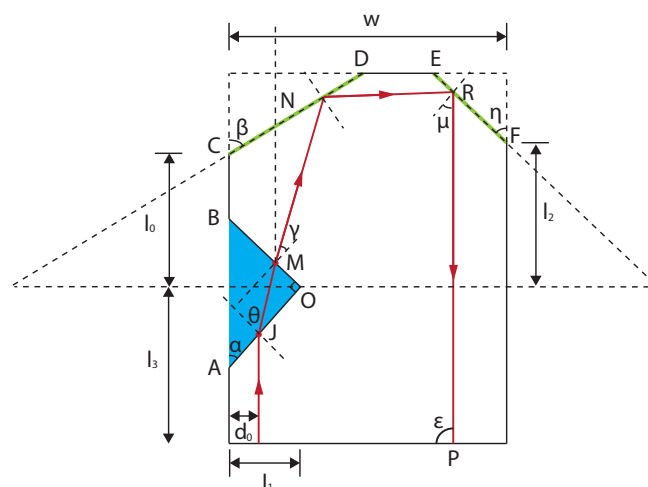


Figure 5.4: The geometric method to study the refractometer resolution

The resolution of this prototype can be calculated by using the same method illustrated in chapter 2. Fig. 5.4 shows the geometric method used to build the relationship between seawater refractive index n_e and the spot position P . Actually, the spot position P can be written as a function of seawater refractive index n_e , prism refractive index n_v , incident light position d_0 , and several geometric parameters:

$$P = f(n_e, n_v, d_0, w, l_0, l_1, l_2, l_3, \alpha, \beta, \eta), \quad (5.2)$$

where w is the width of the prism, $l_0, l_1, l_2, l_3, \alpha, \beta$, and η are the labelled in Fig. 5.4. The details of the deduction for equation 5.2 can be found in Appendix C. For the prototype II, the geometric parameters are as follows: $d_0 = 7 \text{ mm}$, $w = 40 \text{ mm}$, $l_0 = 12.113 \text{ mm}$, $l_1 = 9 \text{ mm}$, $l_2 = 13.786 \text{ mm}$, $l_3 = 17.1 \text{ mm}$, $\alpha = 39^\circ$, $\beta = 52^\circ$, and $\eta = 44.6^\circ$. With this configuration, the relationship between the spot position and the refractive index (in a range from 1.330 to 1.350) can be plotted in Fig. 5.5. The position for a refractive index of 1.340 is considered to be the reference position (position 0).

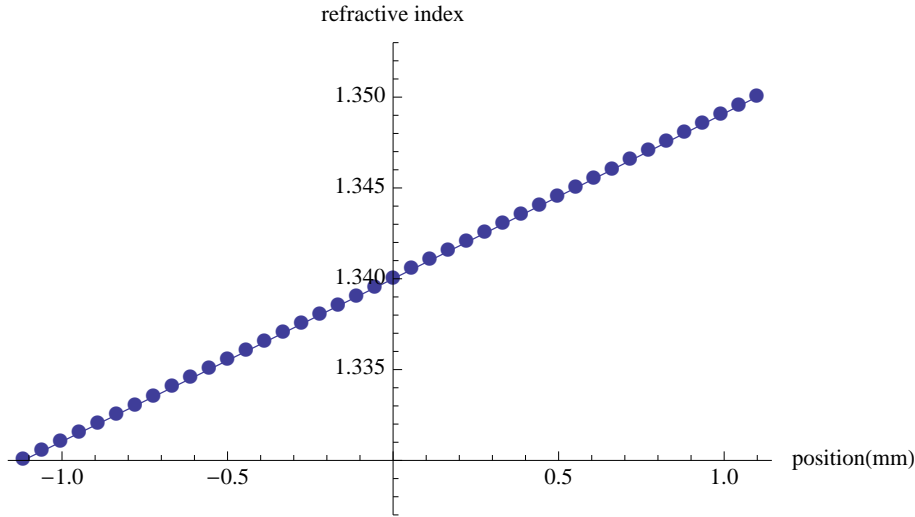


Figure 5.5: The relationship between the spot position and the refractive index for prototype II

From this figure, a good linear relationship exists between the spot position and seawater refractive index. The equation of the fitting line can be obtained from a second order polynomial fitting, with a standard deviation of 4.86×10^{-7} .

$$n_e = 1.34 + 0.006 P + 0.000032 P^2 \quad (5.3)$$

When the refractive index changes from 1.330 to 1.350, the spot moves a distance of 2.2 mm from -1.1 mm to $+1.1 \text{ mm}$. According to the spot location resolution (better than $0.1 \mu\text{m}$) discussed in chapter 3 by using a CCD, the resolution of measuring seawater refractive index reaches 0.9×10^{-6} ($\approx 1 \text{ ppm}$) which is equivalent to the absolute salinity of 2 mg.kg^{-1} .

III Prototype III: new model of refracto-turbidi-meter

The second prototype of refractometer has smaller size and temperature compensation characteristics. Based on this prototype, several modifications are made to measure tur-

bidity simultaneously.

III.1 Turbidi-meter based on prototype II

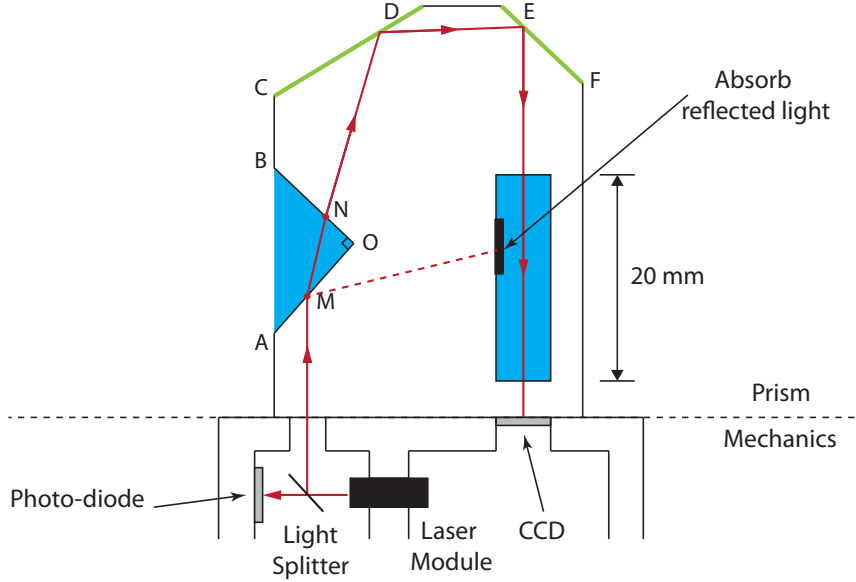


Figure 5.6: The first refracto-turbidi-meter prototype

The first refracto-turbidi-meter based on the prototype II is shown in Fig. 5.6. As we discussed in chapter 4, the turbidity measurement resolution is proportional to the length of light path propagated in the medium. In our first prototype, this distance is limited by the two refraction surface, which is about 6.35 mm . With this length, the turbidity resolution is about 1.15 NTU in the range from 0 NTU and 20 NTU . In this new prototype, we open a new groove with the length of 20 mm in the right part of the prism as shown in Fig. 5.6. The beam redirected by the second mirror enters this groove, in which it fills the seawater as the groove between two refracted surface OA and OB , and captured by a CCD in another end of the groove. At the inner surface of the opened groove, some special materials are used to absorb the reflected light to avoid them influence the scattering inside the groove.

The turbidity measurement resolution of this prototype can be calculated as: $R_t = 1.15 \times \frac{6.35}{20+MN}$, in which MN is the length of light path between the two refraction surfaces. This distance is directly affected by the incident light position d_0 shown in Fig. 5.5. The light path distance between two refraction surface decreases from 11 mm to 1.8 mm , when the incident beam position moves from 3 mm to 8 mm , while the refractive index resolution becomes better from 2.13×10^{-6} to 1.03×10^{-6} . If we use 7 mm as the incident beam position d_0 , the expected turbidity measurement resolution would be $R_t = 1.15 \times \frac{6.35}{20+MN} = 0.31 \text{ NTU}$ in the range from 0 NTU and 20 NTU . From Fig. 5.6, it is possible to further improve the resolution by increase the length of this groove. For a groove with length of 30 mm , the resolution is 0.217 NTU .

This design also reduces the impacts caused by the light path difference with different seawater refractive indices. The variation of the light path length between two refraction surfaces is about 0.054 mm , which is only 0.23% of the entire light path, so that it can

be ignored when calculating turbidity. Similarly, the non-uniqueness of light path inside the beam can be ignored as well compared to the entire light path. The length of the beam varies in the newly opened groove too. This variation is resulted by the refraction when beam enters and leaves the groove. This refraction will further impact the light spot position. To reduce these impacts, our design makes the beam enters the groove at an angle of $90 \pm 0.865^\circ$ with the range of refractive index from 1.330 to 1.350.

Another improvement of the new prototype is the set-up of light source. In the first prototype discussed in chapter 2, light source directly contacts to the prism, which makes it difficult to measure the reference light intensity I_0 . In the new model, light source is installed with the mechanics, a light splitter is used to separate the beam into two: one enters into the prism for the measurement, another is measured by a photo-diode as the reference light intensity I_0 . This design also makes it possible to use different light source other than laser. The laser module shown in Fig. 5.6 can be replaced by a LED at wavelength 860 nm , which is not absorbed by the natural particles.

III.2 Futher improvement

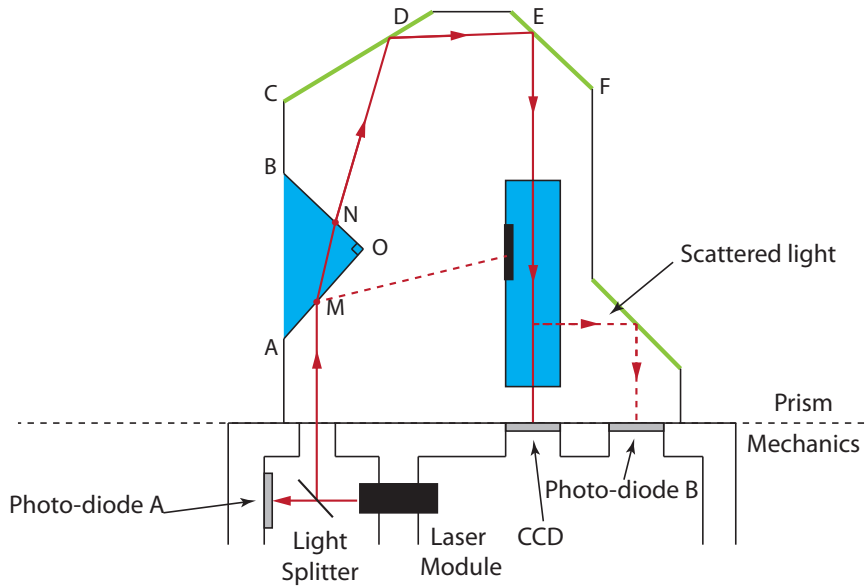


Figure 5.7: The second refracto-turbidi-meter prototype

In chapter 1, we studied the limitation of attenuation based turbidity measurement - it is not sensitive in ultra low and ultra high turbid medium. For seawater turbidity measurement, the ultra low turbid case is much more interesting. To improve the performance of our refracto-turbidi-meter in this environment, a new photo-diode is introduced to measure the scattered light at 90° . Fig. 5.7 is the design of the new refracto-turbidi-meter[2]. Based on the refracto-turbidi-meter illustrated in last section, a mirror at 45° to the light beam is placed at the right side of the groove, which reflects the diffused light to a second photo-diode placed inside the mechanics. The turbidity T is calculated by the read of photo-diode B (I_{90}) and the light intensity obtained by the CCD (I_{ccd}) as:

$$T = \frac{I_{90}}{a_1 I_{90} + a_2 I_{ccd}}, \quad (5.4)$$

in which a_1 and a_2 are two constant coefficients. It should be noticed that the reference light intensity I_{ref} given by the photo-diode A is not used in the calculation. The reason for this is that equation 5.4 is a ratio between the 90° scattered light and the weighted sum of transmitted light and scattered light, which is independent of the incident light intensity. However, both the nephelometer standard ISO 7027 and USEPA Method 180.1 only have a measurement range from 0 to 40 NTU. The photo-diode B introduced in this design is used to improve the performance in ultra low turbid medium, for the moderate turbidity measurement, the attenuation based measurement can be used. Based on this reason, we keep the photo-diode A in this design to measure the reference intensity for the attenuation based turbidity measurement. This turbidi-meter is expected to have the same resolution as the one proposed in last section (1% of the measurement range), but possess better performance in ultra low turbidity medium.

Besides all these improvements mentioned in this chapter, it should be mentioned that the light spot intensity distribution recorded by CCD contains not only the position information and the attenuation information. It is possible to retrieve other useful information which might be used to calculate turbidity. As discussed in last chapter, the scattered light captured by CCD affects the high frequency parts. This part of signal contains the scattering information of the medium. A possible improvement is to retrieve the turbidity from this parts of frequency. To improve the speed of the post-processing algorithms, it is possible to implement them in a FPGA chip, which is much faster than the software implementation. The images captured by CCD can be temporally stored in memory for being processed other than in hard disk.

Conclusion

The previous chapters presented a refracto-turbidi-meter for simultaneous *in situ* seawater salinity and turbidity measurements. It has a salinity resolution of 1 mg.kg^{-1} and turbidity resolution of 1.15 NTU in a range from 0 NTU to 20 NTU. During the discussion, we illustrated several issues in designing the refracto-turbidi-meter. In this chapter, we proposed three new models which improves the refractive index and turbidity measurement performance.

At the beginning of this chapter, we reviewed the issues existed in our current design and introduced the possible improvement methods for both the refractive index measurement and turbidity measurement. For the refractometer design, the two-prism design has a temperature compensation characteristic, but it is impacted by the wavelength shift caused by temperature variation. In our second prototype, we used a uni-prism design and chosen Schott glass N-ZK7 as the prism material because it has a positive temperature coefficient and negative sellmeier coefficient, which compensates the refractive index variation led by the temperature change. We also reduced the size of prism by using two mirrors after the second refraction in order to reduce the thermal expansion. With the new configuration, the resolution of refractive index measurement was studied in this chapter, which reaches 0.9×10^{-6} ($\approx 1 \text{ ppm}$), equivalent to the absolute salinity of 2 mg.kg^{-1} .

Based on this new refractometer, we opened a 20 mm long groove to increase the sensitivity of turbidity. The design of the new refractometer allows the light beam enters the groove at an angle of $90 \pm 0.865^\circ$, which has very small impact to the light path length in the medium. Compared to the length of the groove, the light path variation resulted by different refractive index and the non-uniqueness of light path inside the beam can be ignored. Besides these improvements, the light source is placed into the mechanics rather than directly contacts the prism. A light splitter is used to separate the beam into two: one enters the prism for the measurements, and another is measured by a photo-diode as the reference light intensity for turbidity measurement. The salinity resolution of this prototype is the same as the second refractometer prototype but it has the ability to measure turbidity in a resolution of 0.3 NTU in the range from 0 NTU to 20 NTU. The separation of prism and light source allows us to change the light source other than laser. A LED at wavelength of 860 nm is a good candidate to replace laser module as the light source since it was not absorbed by most of the natural particles.

To further improve the turbidity measurement performance in low turbid medium, a new 45° mirror was introduced into our new refracto-turbidi-meter to reflect the scattered light in the groove into the mechanics, where another photo-diode is used to capture the scattered light intensity. With this configuration, the turbidity can be calculated by the ratio between the 90° light intensity and the weighted sum of transmitted light intensity and scattered light intensity. The expected turbidity resolution of this model is better than 1% of the measurement range.

There exists other ways to improve the performance of the refracto-turbidi-meter. The usage of CCD makes it possible to apply different post-processing algorithms in order to retrieve the information contained in the captured images. These algorithms can be implemented in FPGA to accelerate the post-processing speed. The images can be stored in the memory rather than hard disk to reduce the image load time.

Bibliography

- [1] Philippe Grosso. Enveloppe soleau n 420210: Réfractomètre à bi-prismes monobloc. *Enveloppe soleau*, Jun. 2011.
 - [2] Philippe Grosso, Bo Hou, and Jean Louis de Bougrenet de La Tocnaye. Enveloppe soleau n 432414: double capteur de turbidité et salinité de l'eau de mer en zones côtières. *Enveloppe soleau*, Nov. 2011.
-

Figures and tables

Figures

5.1	The temperature coefficient and sellmeier coefficient of glass N-ZK7 when temperature varies from 0 °C to 40 °C	124
5.2	The optical design for the prototype II	125
5.3	The size comparison between prototype I (right) and II (left)	126
5.4	The geometric method to study the refractometer resolution	126
5.5	The relationship between the spot position and the refractive index for prototype II	127
5.6	The first refracto-turbidi-meter prototype	128
5.7	The second refracto-turbidi-meter prototype	129

General Conclusion

The development of fundamental knowledge concerning the oceanic heat budget, water mass formation, currents and coastal dynamics is driven by the development of techniques for measuring physico-chemical parameters of the ocean, which requires different high-resolution measurement instrument to measure different physical properties of seawater, e.g. salinity, temperature, pressure, and turbidity, etc. Current researches have found that these physical properties are tightly connected to each other to influence different oceanographic phenomenons. This characteristic makes the research of *in situ* multi-functional sensor valuable. Among these physico-chemical parameters, temperature and salinity are two most important ones to study the physico-chemical parameters of the ocean, while turbidity is another significant oceanic property, which is associated to the particles in suspension. Under this background, the study of a double sensor for sea water salinity and turbidity measurements is reasonable and valuable.

Our study starts from the difference between the two salinity definitions, the practical salinity defined as a function of seawater conductivity and temperature, and the absolute salinity, which is the essential parameter to access the physico-chemical properties of the ocean. Other than salinity, which describes the physico-chemical properties of the dissolved materials in the ocean, turbidity is a description of the optical property of the undissolved suspended materials. Based on the study, our work comes from the following two factors: on the one hand, the development of physical oceanography requires more high-resolution salinity and turbidity measurement instruments; on the other hand, the developed optic technology has been widely used in the physical property measurement. The new sensor technologies on the basis of optical components used to design alternatives of equivalent or superior performance is very competitive in terms of cost.

The work presented in this thesis is in the objective of design, modelling, implementation, and improvement of an *in situ* optical salino-turbidi-meter, which measures the salinity and turbidity of seawater simultaneously. Under the cooperation between the school TELECOM Bretagne through the Department optics (UMR FOTON 6082), SHOM (Service Hydrographique et Océanographique de la Marine) and the project NOSS (Nke-Electronics Optical Salinity Sensor), the feasibility of developing a high-resolution salino-turbidi-meter based CCD has been demonstrated through research over the past three years.

The first research involves the state-of-the-art salinity and turbidity measurements (in chapter 1). According to the definition of practical salinity, it is measured by a conductivity sensor combined with a temperature sensor. Millard and Seaver built a relationship between seawater salinity and refractive index, which forms the theoretical basis of measuring seawater salinity through the measure of refractive index. We compared several state-of-the-art refractive index measurement methods, from the current laboratory used technologies to the commercial ones, in order to choose the best solution for the require-

ment of *in situ* compact sensor. From the comparison, it allows us to show the advantage of combining these two main physical topics: the refractometer and laser beam deviation measurement: high resolution, less susceptible to interference and easy to integrate to compact sensor. We also studied the turbidity measurement methods, from the earliest Jackson candle turbidi-meter to the most advanced ratio nephelometer. The study of these methods allows us to understand the methodology of modelling, design and verify a turbidi-meter and guides us to choose the right method in order to integrate the turbidi-meter into the refractometer.

According to these researches, we first designed a high-resolution optical refractometer based on the measurement of laser beam deviation, and configured it to reach the requirement of the seawater salinity measurement (chapter 2). The work was started from studying the choose of the optical material in terms of the effects caused by the temperature variation, known as the temperature coefficient and the thermal expansion coefficient. Based on the study, a refractometer consist of two prisms with different temperature coefficients (K7 and N-BAK2), which are used to compensate the temperature influence for the refractive index measurement was modelled. For optimizing the geometric parameters of the refractometer, we analysed the relationship between the refractive index and laser beam deviation in both differential method and geometric method. According to the analysis, the requirements for the measurement range and sensitivity of the position detection sensor were discussed as well. To measure the refractive index from 1.3360 to 1.3450 with a resolution in the order of 10^{-7} , the measurement range of position detection sensor must reach 11 mm and the corresponding resolution must be at least 0.3 μm . Besides the configuration of the optics for the sensor, the selection of the optoelectronic devices include the light source and position detection sensor was also discussed in this thesis. Since the refractive index is sensitive to the wavelength, a laser module at 635 nm was used as the light source due to its narrow wavelength band. A 12 mm commercial Position Sensitive Device (PSD) with resolution of 0.3 μm was selected to measure the laser beam deviation because of its high sensitivity, short response time, and independence from spot light size, shape, and intensity.

Before we evaluated the performance of the refractometer, we presented its fabrication process step by step, and paid special attention to the issues in assembly that might affect the performance. The actual resolution of the refractometer was evaluated by an experiment, which verifies the actual resolution of the PSD. From the experimental results, it is believed that the actual standard uncertainty of PSD reaches $\pm 0.11 \mu m$. According to the refractometer configuration, the corresponding refractive index resolution is 2.94×10^{-7} , equivalent to the absolute salinity of $1 \times 10^{-3} g.kg^{-1}$.

The transmitted beam carries not only the refractive index related beam deviation information but also the other information associated to the intensity distribution. As an analogue device, PSD is designed to measure the incident light position and works well in a uni-functional refractometer. However, it is not sensitive to the change of the light intensity distribution, so that it is not suitable for retrieving the intensity distribution related information, e.g turbidity. At the beginning of chapter 3, we discussed the limitation of PSD for a multi-functional sensor. The requirement of a new *in situ* multi-functional sensor recalls a new photonic sensor, which can retrieve not only the laser spot displace information but also the light intensity distribution information. To achieve this, we studied two of the most state-of-the-art pixel-based image sensors, named Charge-Coupled Device (CCD) and Complementary Metal-Oxide-Semiconduct (CMOS), and compared them from the 7 important aspects. According to the comparison, CCD is the best choice for

our application due to its uniformity and wide dynamic range.

Before we used CCD to measure multiple seawater properties instead of PSD, it is reasonable to prove that CCD-based laser beam deviation method can at least reach the same resolution as PSD-based method. Different from PSD, CCD does not directly provide the position information but records the light intensity distribution, which is further processed by a location algorithm to retrieve the position information. We researched several well-known image location algorithms, and used the centroid algorithm for our comparison of PSD- and CCD-based laser beam deviation measurement because it measures the gravity center of the incident light as PSD does. A theoretical performance analysis of the two methods are first carried out in terms of two performance indicators, namely resolution and speed. Both PSD- and CCD-based system relies on the high signal to noise ratio to improve their resolution, however, CCD can benefit from variety of post-processing techniques while PSD mainly depends on the its structure. The speed of PSD-based system depends on its response time and external sampling and digitalization process, while the speed of CCD-based system relies on exposure time, readout time, storage time, load time, and computation time.

As the CCD-based system is much more complex than the PSD-based system, several factors that impacts the performance of CCD-based system were studied to optimize the performance. A small image window size is useful not only for increasing the resolution but also for improving the speed with the limitation that the laser spot should be entirely contained in the image. Applying a threshold to the noise level could efficiently reduce the systematic error. To improve the speed, binning is an alternative means, but the noise level should be reconsidered to choose a proper threshold. Saturation hides lots of laser spot information and thus should be definitely avoided. The number of processed image does not highly depend on the resolution, so that it is a good way to improve speed without greatly reducing resolution. By applying the optimized parameters, several experiments were made to compare CCD-based system with the state-of-the-art PSD-based system. It is shown that, by applying the optimized parameters, the performance of a CCD-based system (standard uncertainty $\pm 0.068 \mu\text{m}$ to 1 Hz) is comparable to that of a PSD-based system (standard uncertainty $\pm 0.1077 \mu\text{m}$ to 1 Hz) in measuring laser beam deviation.

Once the CCD-based system is proved to be qualified in measuring the laser beam deviation, it is time to show more advantage of CCD-based system, for example, the measurement of light intensity distribution related properties. Turbidity is one of the best choices for this purpose. As we expect to show the benefits gained from the use of CCD instead of PSD in our existing refractometer, the turbidity measurement that we chose must lead to the least modification to our refractometer. Under this consideration, we reviewed and compared the turbidity measurement methods introduced in chapter 1. The attenuation based method is the only method that can be used without modifying our current refractometer configuration. Based on this method, we studied its principle and analysed its resolution, which depends on light path length in medium, incident light intensity, measurement range, and sensitivity of light intensity sensor. We paid special attention to the interference between the turbidity measurement and the refractive index measurement and further proved that PSD is not a suitable detector for measuring the light intensity distribution related quantities. By applying a threshold, a low pass filter, and enough exposure time, the impacts to turbidity measurement caused by the refractometer can be well eliminated. In a turbid medium, the position of laser spot peak has a shift according to the turbidity of the medium. This shift impacts the gravity center based location method, e.g. centroid algorithm, and PSD. To overcome this problem, a new

algorithm, which tracks the location that divides the mass of the spot into two equal parts, was introduced in chapter 4, and was proved to be more accurate than the centroid algorithm in both the non-turbid environment and turbid environment.

For evaluating the performance of the turbidity measurement method, we carried out several simulations and experiments. Through these simulations and experiments, the average accuracy of our method based on the current refractometer reaches 8 NTU in a range from 0 NTU to 200 NTU and 1.15 NTU in a range from 0 NTU to 20 NTU. We also compared our method with the nephelometer specified by the NTU standard. The result computed by our method well fits the result obtained from a nephelometer.

The CCD-based refracto-turbidi-meter illustrated in this thesis have been proved to be effective in measuring salinity and turbidity of seawater. However it is not the optimized solution to measure the refractive index and turbidity in a compact in situ sensor. If we take off the restrictions of building the multi-functional sensor based on our current refractometer, it is possible to design a new CCD-based refracto-turbidi-meter with better performance. In the last chapter, we first studied the possible improvements for designing a high resolution refracto-turbidi-meter. A unique-prism design instead of two-prisms design decreases the complexity of fabrication. The sensitivity can be improved by increasing the length of the light path in the medium, which requires a new modelling of the optics. Before the light beam enter the prism, the light power can be measured as the reference for attenuation based turbidity measurement to improve the accuracy of turbidity computation. One more light intensity sensor could be introduced to measure the scattered light at 90° , which can improve the turbidity measurement performance in ultra low and ultra high turbidity case. At the end of this thesis, we introduced a new compact in situ double-functional sensor for seawater salinity and turbidity measurement, which has the absolute salinity resolution of $1 \times 10^{-3} \text{ g.kg}^{-1}$ and the turbidity resolution, 1% of the measurement range.

Appendix A

Algorithm of Seaver & Millard

The publication of R.C Millard and G. Seaver is a essential reference. The algorithm they developed consists of 27 terms that have been determined from 428 data points and covers the field of temperature, salinity and pressure usually encountered in oceanography: $0 < T < 30^\circ$, $0 < S < 40$, and $0 < p_r < 11000 \text{ dbar}$. It can be used for $0.5 < x < 0.7 \mu m$ and its accuracy is also variable, depending on the sub-areas of study: the standard deviation of absolute n varies from 4×10^{-7} to 8×10^{-5} . It is presented in the following form:

$$n(T, p_r, S, \lambda) = n_I(T, \lambda) + n_{II}(T, S, \lambda) + n_{III}(T, p_r, \lambda) + n_{IV}(T, p_r, S), \quad (\text{A.1})$$

where

$$n_I(T, \lambda) = A_0 + L_2 \cdot \lambda^2 + LM_2 / \lambda^2 + LM_4 / \lambda^4 + LM_6 / \lambda^6 + T_1 \cdot T + T_2 \cdot T^2 + T_3 \cdot T^3 + T_4 \cdot T^4 + TL \cdot T \cdot \lambda + T_2 L \cdot T^2 \cdot \lambda + T_3 L \cdot T^3 \cdot \lambda \quad (\text{A.2})$$

with

$$\begin{aligned} A_0 &= 1.3280657 & T_2 &= -0.0000030738272 \\ L_2 &= -0.0045536802 & T_3 &= 0.000000030124687 \\ LM_2 &= 0.0025471707 & T_4 &= -2.08831178 \times 10^{-10} \\ LM_4 &= 0.000007501966 & TL &= 0.000010508621 \\ LM_6 &= 0.000002082632 & T_2 L &= 0.00000021282248 \\ T_1 &= -0.0000052883909 & T_3 L &= -0.000000001705881 \end{aligned}$$

$$n_{II}(T, \lambda, S) = S_0 \cdot S + S_1 \cdot LM_2 \cdot S / \lambda^2 + S_1 T \cdot S \cdot T + S_1 T_2 \cdot S \cdot T^2 + S_1 T_3 \cdot S \cdot T^3 + STL \cdot S \cdot T \cdot \lambda \quad (\text{A.3})$$

with

$$\begin{aligned} S_0 &= 0.00019029121 & S_1 T_2 &= 0.0000000089818478 \\ S_1 LM_2 &= 0.0000024239607 & S_1 T_3 &= 1.2078804 \times 10^{-10} \\ S_1 T &= -0.00000073960297 & STL &= -0.0000003589495 \end{aligned}$$

$$n_{III}(p_r, T, \lambda) = P_1 \cdot p_r + P_2 \cdot p_r^2 + P \lambda M_2 \cdot p_r / \lambda^2 + PT \cdot p_r \cdot T + PT_2 \cdot p_r \cdot T^2 + P_2 T_2 \cdot p_r^2 \cdot T^2 \quad (\text{A.4})$$

$$\begin{aligned}
P_1 &= 0.0000015868384 & PT &= -0.0000000094834486 \\
P_2 &= -1.574074 \times 10^{-11} & PT_2 &= 1.0100326 \times 10^{-10} \\
P\lambda M_2 &= 0.000000010712063 & P_2T_2 &= 5.8085198 \times 10^{-15}
\end{aligned}$$

with

$$n_{IV}(S, p_r, T) = P_1S.p_r.S + PTS.p_r.T.S + PT_2S.p_r.T^2.S \quad (\text{A.5})$$

with

$$\begin{aligned}
P_1S &= -0.0000000011177517 & PT_2S &= -1.5460458 \times 10^{-12} \\
PTS &= 5.7311268 \times 10^{-11}
\end{aligned}$$

Appendix B

Resolution analysis of refractometer prototype I

The resolution of the refractometer depends on the resolution of the spot displacement measurement. To study the refractometer resolution, the relationship between the seawater refractive index and the light spot position need to be analysed. This relationship depends on not only the prism model but also the geometrical parameters of the prism. The parameter of the prototype I shown in Fig. B.1 is listed below:

Table B.1: Parameters of the prism

Parameters	Notation	Value
refractive index of K7 (left prism)	n_1	1.50934
refractive index of N-FK51 (right prism)	n_2	1.48534
refractive index of seawater	n_e	1.336 – 1.345
resolution of PSD	Δp	0.3 μm
angle of first refraction surface	α	28°
angle of second reflection surface	β	34°
width of one prism	w	45 mm
incident point position	d_0	6.34 mm
height of the refraction surface	l_0	7.98 mm
height of the second reflection surface	l_1	42.64 mm
height of the prism	$l_1 + l_2$	125 mm

1st step: Relationship between refractive index n_e and light spot position P

The light spot position P can be expressed by the distance between point H' and P' :

$$P = \overline{H'P'} = \frac{P_x' - H_x'}{\cos(2\beta)} \quad (B.1)$$

If we choose the point O as the original point of the coordinate, the point H' can be expressed by the following group of equations:

$$H_x' = w + l_2 \sin(2\beta) \quad (B.2)$$

$$H_y' = l_0 - l_1 - l_2 \cos(2\beta) \quad (B.3)$$

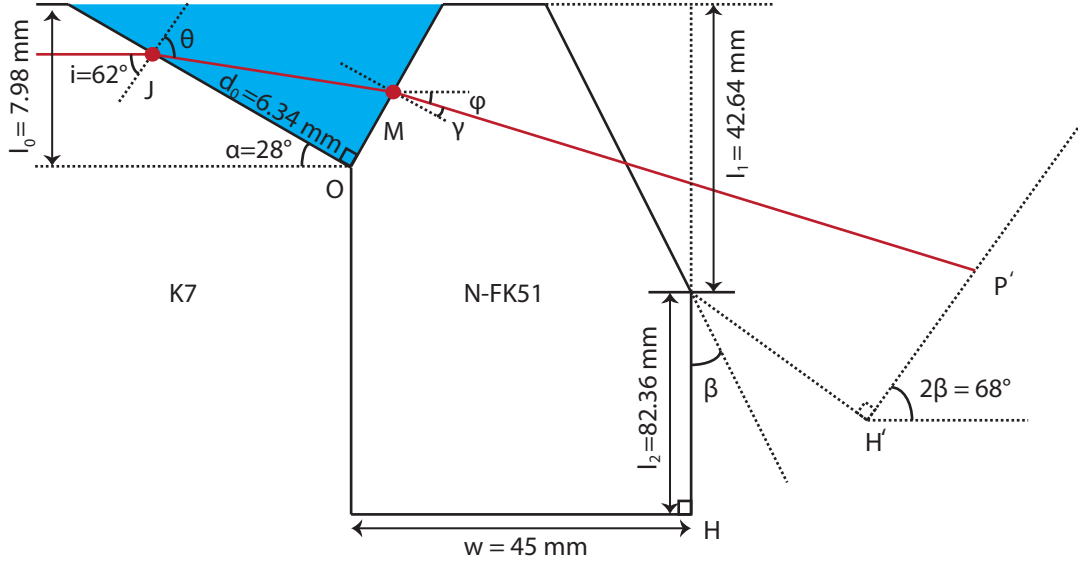


Figure B.1: Principle of the refractometer prototype I

The point P' is the intersection of line $H'P'$ and line MP' . These two lines can be expressed as:

$$MP' : \quad y = \tan(\pi - \alpha + \gamma)x + b_{MP'} \quad (\text{B.4})$$

$$H'P' : \quad y = \tan(2\beta)x + b_{H'P'} \quad (\text{B.5})$$

where $b_{MP'}$ is the intersection of the line MP' and the y axis, $b_{H'P'}$ is the intersection of line $H'P'$ and the y axis. From these two equations, the point P' can be derived as:

$$P'_x = \frac{b_{H'P'} - b_{MP'}}{\tan(\pi - \alpha + \gamma) - \tan(2\beta)} \quad (\text{B.6})$$

$$P'_y = \tan(2\beta) \frac{b_{H'P'} - b_{MP'}}{\tan(\pi - \alpha + \gamma) - \tan(2\beta)} + b_{H'P'} \quad (\text{B.7})$$

Since point H' is in the line $H'P'$, $b_{H'P'}$ can be derived by using the coordinate of H' to substitute the x and y in equation B.5. Thus, $b_{H'P'}$ can be expressed as:

$$b_{H'P'} = l_0 - l_1 - l_2 \cos(2\beta) - \tan(2\beta)[w + l_2 \sin(2\beta)] \quad (\text{B.8})$$

Similarly to $b_{H'P'}$, $b_{MP'}$ can be calculated by substituting point $M(M_x, M_y)$ into the function of line MP' , where M_x and M_y are function of incident light position d_0 , prism angle α and the first refraction angle θ :

$$M_x = \frac{d_0 \cos(\frac{\pi}{2} - \alpha)}{\tan(\theta)} \quad (\text{B.9})$$

$$M_y = \frac{d_0 \sin(\frac{\pi}{2} - \alpha)}{\tan(\theta)} \quad (\text{B.10})$$

With equation B.5, B.9 and B.10, $b_{MP'}$ is expressed as:

$$b_{MP'} = \frac{d_0 \sin(\frac{\pi}{2} - \alpha)}{\tan(\theta)} - \tan(\pi - \alpha + \gamma) \frac{d_0 \cos(\frac{\pi}{2} - \alpha)}{\tan(\theta)} \quad (\text{B.11})$$

Combined all the equations above, we can write the laser spot position $\overline{H'P'}$ as follows:

$$\begin{aligned} P = \overline{H'P'} &= f(\theta, \gamma, \alpha, \beta, d_0, l_0, l_1, l_2, w) \\ &= \frac{1}{\cos(2\beta)} (-w - l_2 \sin(2\beta)) - \frac{l_0 - l_1 - l_2 \cos(2\beta)}{\tan(2\beta) + \tan(\alpha - \gamma)} + \frac{d_0 \cos(\alpha) \cot(\theta)}{\tan(2\beta) + \tan(\alpha - \gamma)} \\ &\quad + \frac{(w + l_2 \sin(2\beta)) \tan(2\beta)}{\tan(2\beta) + \tan(\alpha - \gamma)} + \frac{d_0 \cot(\theta) \sin(\alpha) \tan(\alpha - \gamma)}{\tan(2\beta) + \tan(\alpha - \gamma)} \end{aligned} \quad (\text{B.12})$$

2nd step: Refractive index resolution Δn_e

The resolution of the refractometer depends on the sensitivity and the range of measurement. The sensitivity of the refractometer S_t is expressed as:

$$S_t = \frac{\partial n_e}{\partial p} = \frac{\partial n_e}{\partial \gamma} \frac{\partial \gamma}{\partial p} \quad (\text{B.13})$$

The relationship between the angles i , θ , and γ can be easily built from the Snell's law:

$$n_1 \sin(i) = n_e \sin(\theta) \quad (\text{B.14})$$

$$n_e \sin(\frac{\pi}{2} - \theta) = n_2 \sin(\gamma) \quad (\text{B.15})$$

According to equation B.14 and B.15, the relationship between the refractive index variation Δn_e and variation of the refraction angle $\Delta \gamma$ can be written as:

$$\frac{\Delta n_e}{\Delta \gamma} = \frac{\cos(\gamma) n_e}{\sin(\gamma) [1 + \tan^2(\theta)]} \quad (\text{B.16})$$

The relationship between the position variation Δp and variation of the refraction angle $\Delta \gamma$ can be obtained from the derivative of equation B.12, which is:

$$\begin{aligned} \frac{\Delta \gamma}{\Delta p} &= \cos(2 * \beta) / \left[\frac{d_0 \cot(\theta) \sin(\alpha) / \cos^2(\alpha - \gamma)}{-\tan(2\beta) - \tan(\alpha - \gamma)} - \right. \\ &\quad \left. \frac{(l_0 - l_1 - l_2 \cos(2\beta) - d_0 \cos(\alpha) \cot(\theta) - (w + l_2 \sin(2\beta)) \tan(2\beta) - d_0 \cot(\theta) \sin(\alpha) \tan(\alpha - \gamma))}{\cos^2(\alpha - \gamma) (-\tan(2\beta) - \tan(\alpha - \gamma))^2} \right] \end{aligned} \quad (\text{B.17})$$

Thus, the sensibility of the refractive index measurement is:

$$\begin{aligned} S_t &= \frac{\partial n_e}{\partial p} = \frac{\partial n_e}{\partial \gamma} \frac{\partial \gamma}{\partial p} = \\ &= \cos(2\beta) \cos(\gamma) n_e / [\sin(\gamma) [1 + \tan^2(\theta)] \left[\frac{d_0 \cot(\theta) \sin(\alpha) / \cos^2(\alpha - \gamma)}{-\tan(2\beta) - \tan(\alpha - \gamma)} - \right. \\ &\quad \left. \frac{(l_0 - l_1 - l_2 \cos(2\beta) - d_0 \cos(\alpha) \cot(\theta) - (w + l_2 \sin(2\beta)) \tan(2\beta) - d_0 \cot(\theta) \sin(\alpha) \tan(\alpha - \gamma))}{\cos^2(\alpha - \gamma) (-\tan(2\beta) - \tan(\alpha - \gamma))^2} \right]] \end{aligned} \quad (\text{B.18})$$

in which the refraction angle θ and γ can be calculated from the equation B.14 and B.15 in the following forms:

$$\theta = \arcsin\left[\frac{n_1}{n_e} \sin(i)\right] \quad (\text{B.19})$$

$$\gamma = \arcsin\left[\frac{n_e}{n_2} \sin\left(\frac{\pi}{2} - \theta\right)\right] \quad (\text{B.20})$$

Appendix C

Resolution analysis of refractometer prototype II

1st step: geometric parameters

Table C.1: Parameters of the prism

Parameters	Notation	Value
refractive index of N-ZK7	n_v	1.5066
refractive index of seawater	n_e	1.330 – 1.350
resolution of CCD	Δp	0.1 μm
angle of first refraction surface	α	39°
angle of first reflection surface	β	52°
angle of second reflection surface	β	44.6°
width of one prism	w	30 mm
incident point position	d_0	7 mm
height of the prism	h	40 mm

2st step: relationship between refractive index and light spot

If we choose point O as the original point of the coordinate, the light spot position p can be expressed as the y coordinate of the point P , which is in the line PR :

$$p = P_y = \tan(\eta + \pi/2 + \mu)(-l_3) + b_{pr}, \quad (C.1)$$

where constant coefficient b_{pr} can be obtained by substituting point R into the equation of line PR :

$$b_{pr} = R_y - \tan(\eta + \pi/2 + \mu)(-l_3)R_x \quad (C.2)$$

According to Fig. C.1, the first refraction point J and second refraction point M can be expressed as:

$$J_x = -d_0 \cos(\alpha) \quad (C.3)$$

$$J_y = d_0 \sin(\alpha) \quad (C.4)$$

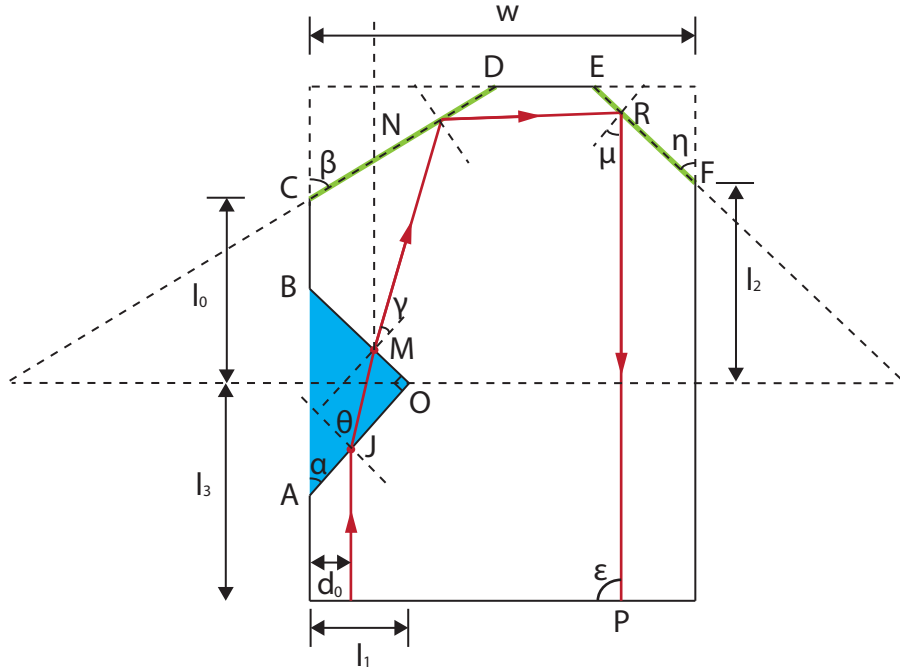


Figure C.1: Principle of the refractometer prototype II

$$M_x = \overline{OM} \sin(\alpha) = \frac{\overline{OJ}}{\tan(\theta)} \sin(\alpha) = \frac{l_1 - d_0}{\sin(\alpha) \tan(\theta)} \sin(\alpha) \quad (\text{C.5})$$

$$M_y = \overline{OM} \cos(\alpha) = \frac{\overline{OJ}}{\tan(\theta)} \cos(\alpha) = \frac{l_1 - d_0}{\sin(\alpha) \tan(\theta)} \sin(\alpha) \quad (\text{C.6})$$

The refracted beam intersects with the first mirror CD at point N , which can be given by the intersection of line MD and line CD . The equations of the two lines can be found as follows:

$$y_{cd} = \tan(\pi - \beta)x_{cd} + b_{cd} \quad (\text{C.7})$$

$$y_{mn} = \tan(\pi - (\alpha - \gamma))x_{mn} + b_{mn} \quad (\text{C.8})$$

The constant coefficient b_{cd} in equation C.7 can be calculated by:

$$b_{cd} = l_0 \tan(\beta) + l_1, \quad (\text{C.9})$$

while the constant coefficient b_{mn} for line MN can be obtained by substituting y_{mn} and x_{mn} in equation C.8 with point $M(M_x, M_y)$.

$$b_{mn} = M_y - \tan(\pi - (\alpha - \gamma))M_x \quad (\text{C.10})$$

With these equations, the coordinates of point N is:

$$N_x = \frac{(M_y - \tan(\pi - (\alpha - \gamma))M_x) - (l_0 \tan(\beta) + l_1)}{\tan(\pi - \beta) - \tan(\pi - (\alpha - \gamma))} \quad (\text{C.11})$$

$$N_y = \tan(\pi - \beta)N_x + b_{cd} \quad (\text{C.12})$$

Similarly with point N , the second reflection point R is the intersection of two lines NR and EF , which can be express as following equations:

$$y_{nr} = \tan(\pi - (\beta - (\alpha - \gamma) + \beta))x_{nr} + b_{nr} \quad (\text{C.13})$$

$$y_{ef} = \tan(\eta)x_{ef} + b_{ef} \quad (\text{C.14})$$

where $b_{ef} = -(l_1)\tan(\eta) + (w - l_1)$ and b_{nr} can be derived because line NR pass through the point N :

$$b_{nr} = N_y - \tan(\pi - (\beta - (\alpha - \gamma) + \beta))N_x \quad (\text{C.15})$$

Equation C.13, C.14, and C.15 can be used to derive the coordinates of point R :

$$R_x = \frac{(N_y - \tan(\pi - (\beta - (\alpha - \gamma) + \beta))N_x) - (-(l_1)\tan(\eta) + (w - l_1))}{\tan(\eta) - \tan(\pi - (\beta - (\alpha - \gamma) + \beta))} \quad (\text{C.16})$$

$$R_y = \tan(\eta)R_x + b_{ef} \quad (\text{C.17})$$

Combined with equation C.16, C.17, C.2, and C.1, we get the following equation:

$$\begin{aligned} P_y = & l_1 - w - l_2 \tan(\eta) + l_3 \tan(\alpha - 2\beta - 2\eta - \gamma) + \frac{\tan(\eta) + \tan(\alpha - 2\beta - 2\eta - \gamma)}{\tan(\eta) - \tan(\alpha - 2\beta - \gamma)} \\ & \times [w + l_0 \tan(\beta) + l_2 \tan(\eta) - \frac{\tan(\beta)(-l_1 - l_0 \tan(\beta))}{-\tan(\beta) + \tan(\alpha - \gamma)} + \\ & \frac{\tan(\beta)((-d_0 + l_1)\cot(\alpha)\tan(\theta))}{-\tan(\beta) + \tan(\alpha - \gamma)} + \frac{\tan(\beta)((-d_0 + l_1)\tan(\alpha - \gamma)\tan(\theta))}{-\tan(\beta) + \tan(\alpha - \gamma)} - \\ & \frac{\tan(\alpha - 2\beta - \gamma)(-l_1 - l_0 \tan(\beta))}{-\tan(\beta) + \tan(\alpha - \gamma)} + \frac{\tan(\alpha - 2\beta - \gamma)((-d_0 + l_1)\cot(\alpha)\tan(\theta))}{-\tan(\beta) + \tan(\alpha - \gamma)} + \\ & \left. \frac{\tan(\alpha - 2\beta - \gamma)((-d_0 + l_1)\tan(\alpha - \gamma)\tan(\theta))}{-\tan(\beta) + \tan(\alpha - \gamma)} \right] \end{aligned} \quad (\text{C.18})$$

The angle θ and γ can be substituted by an expression of refractive index n_e and n_v from the following two equations:

$$\theta = \arcsin\left[\frac{n_v}{n_e} \sin(i)\right] \quad (\text{C.19})$$

$$\gamma = \arcsin\left[\frac{n_e}{n_v} \sin\left(\frac{\pi}{2} - \theta\right)\right] \quad (\text{C.20})$$

3st step: refractive index resolution

The resolution of the refractometer depends on the sensitivity and the range of measurement. The sensitivity of the refractometer S_t is expressed as:

$$S_t = \frac{\partial n_e}{\partial p} = \frac{\partial n_e}{\partial \gamma} \frac{\partial \gamma}{\partial p} \quad (\text{C.21})$$

The relationship between the angles i , θ , and γ can be easily built from the Snell's law:

$$n_v \sin(i) = n_e \sin(\theta) \quad (\text{C.22})$$

$$n_e \sin\left(\frac{\pi}{2} - \theta\right) = n_v \sin(\gamma) \quad (\text{C.23})$$

According to equation C.22 and C.23, the relationship between the refractive index variation Δn_e and variation of the refraction angle $\Delta\gamma$ can be written as:

$$\frac{\Delta n_e}{\Delta\gamma} = \frac{\cos(\gamma)n_e}{\sin(\gamma)[1 + \tan^2(\theta)]} \quad (\text{C.24})$$

The relationship between the position variation Δp and variation of the refraction angle $\Delta\gamma$ can be obtained from the derivative of equation C.18, which is:

$$\begin{aligned} \frac{\Delta\gamma}{\Delta p} = & (4\cos^2(\alpha - 2\beta - 2\eta - \gamma)\cos(\theta)\sin(\alpha))/[-w\cos(\alpha - 2\eta - \theta) + \\ & (2d_0 - 3l_1)\cos(\alpha - 2\beta - 2\eta - \theta) + w\cos(\alpha + 2\eta - \theta) + l_1\cos[\alpha + 2\beta + 2\eta - \theta) - \\ & w\cos(\alpha - 2\eta + \theta) - 2d_0\cos(\alpha - 2\beta - 2\eta + \theta) + l_1\cos(\alpha - 2\beta - 2\eta + \theta) + \\ & w\cos(\alpha + 2\eta + \theta) + l_1\cos(\alpha - 2\beta - 2\eta + \theta) - 2l_2\sin(\alpha - \theta) - 2l_3\sin(\alpha - \theta) - \\ & l_0\sin(\alpha - 2\eta + \theta) + l_2\sin(\alpha - 2\eta + \theta) + l_0\sin(\alpha - 2\beta - 2\eta + \theta) - \\ & l_0\sin(\alpha + 2\eta - \theta) + l_2\sin(\alpha + 2\eta - \theta) + l_0\sin(\alpha + 2\beta + 2\eta - \theta) - \\ & 2l_2\sin(\alpha + \theta) - 2l_3\sin[\alpha + \theta) - l_0\sin(\alpha - 2\eta + \theta) + l_2\sin(\alpha - 2\eta + \theta) + \\ & l_0\sin(\alpha - 2\beta - 2\eta + \theta) - l_0\sin(\alpha + 2\eta + \theta) + l_2\sin(\alpha + 2\eta + \theta) + \\ & l_0\sin(\alpha + 2\beta + 2\eta + \theta)] \end{aligned} \quad (\text{C.25})$$

Thus, the sensibility of the refractive index measurement is:

$$\begin{aligned} S_t = \frac{\partial n_e}{\partial p} = \frac{\partial n_e}{\partial \gamma} \frac{\partial \gamma}{\partial p} = & \frac{\cos(\gamma)n_e}{\sin(\gamma)[1 + \tan^2(\theta)]} (4\cos^2(\alpha - 2\beta - 2\eta - \gamma)\cos(\theta)\sin(\alpha))/[-w\cos(\alpha - 2\eta - \theta) + \\ & (2d_0 - 3l_1)\cos(\alpha - 2\beta - 2\eta - \theta) + w\cos(\alpha + 2\eta - \theta) + l_1\cos[\alpha + 2\beta + 2\eta - \theta) - \\ & w\cos(\alpha - 2\eta + \theta) - 2d_0\cos(\alpha - 2\beta - 2\eta + \theta) + l_1\cos(\alpha - 2\beta - 2\eta + \theta) + \\ & w\cos(\alpha + 2\eta + \theta) + l_1\cos(\alpha - 2\beta - 2\eta + \theta) - 2l_2\sin(\alpha - \theta) - 2l_3\sin(\alpha - \theta) - \\ & l_0\sin(\alpha - 2\eta + \theta) + l_2\sin(\alpha - 2\eta + \theta) + l_0\sin(\alpha - 2\beta - 2\eta + \theta) - \\ & l_0\sin(\alpha + 2\eta - \theta) + l_2\sin(\alpha + 2\eta - \theta) + l_0\sin(\alpha + 2\beta + 2\eta - \theta) - \\ & 2l_2\sin(\alpha + \theta) - 2l_3\sin[\alpha + \theta) - l_0\sin(\alpha - 2\eta + \theta) + l_2\sin(\alpha - 2\eta + \theta) + \\ & l_0\sin(\alpha - 2\beta - 2\eta + \theta) - l_0\sin(\alpha + 2\eta + \theta) + l_2\sin(\alpha + 2\eta + \theta) + \\ & l_0\sin(\alpha + 2\beta + 2\eta + \theta)] \end{aligned} \quad (\text{C.26})$$

Appendix D

Specifications for different prototypes

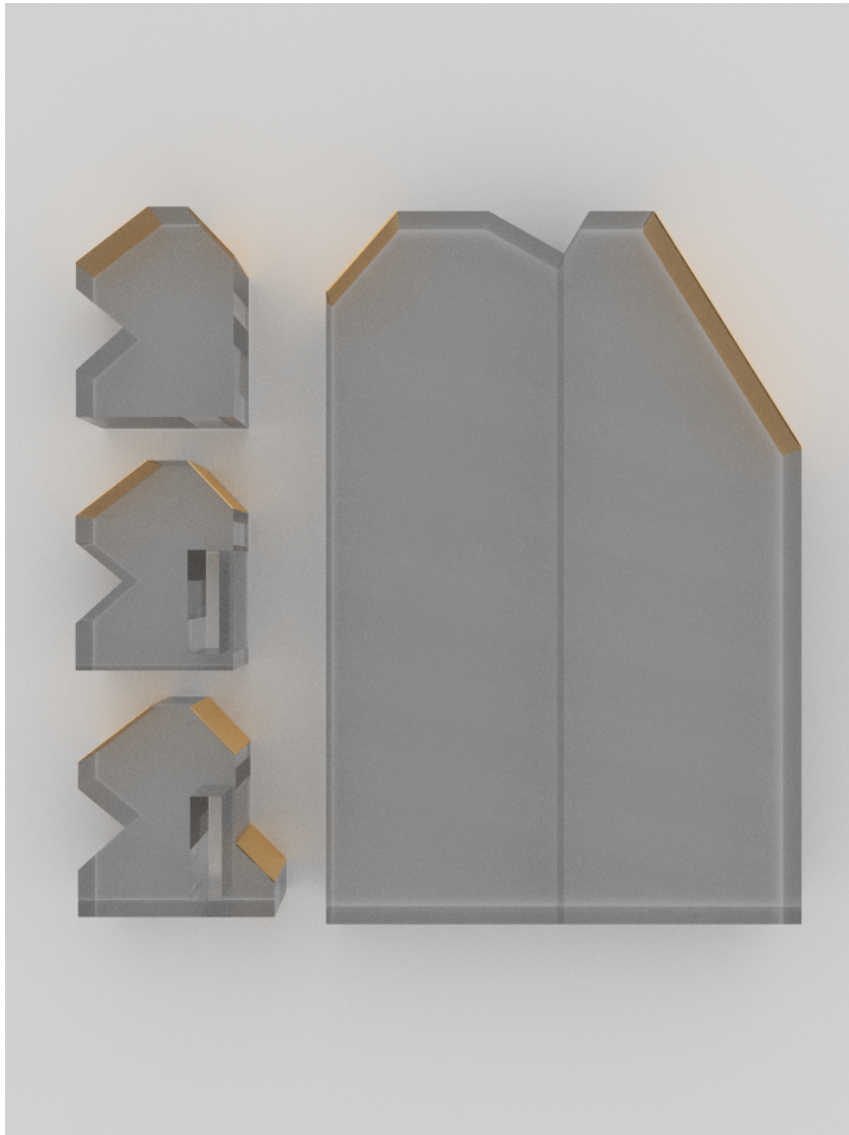
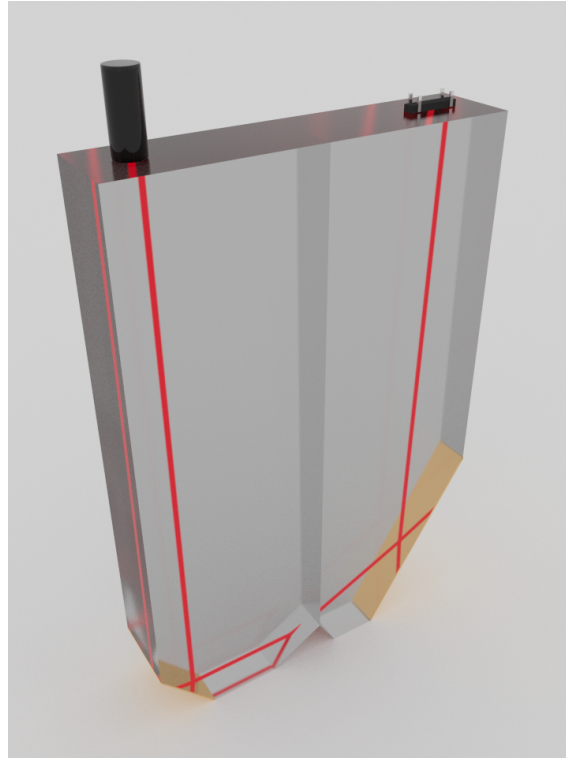


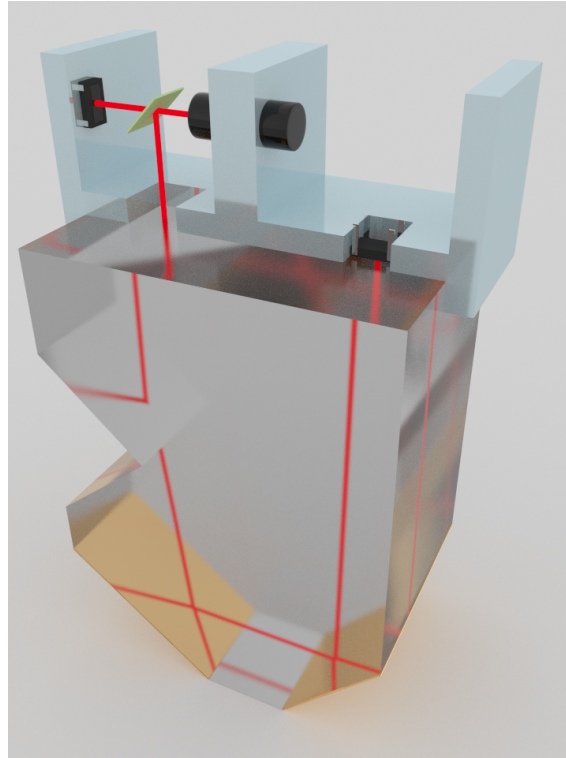
Figure D.1: Prisms for the four different prototypes

I Specifications for refracto-turbidi-meter prototype I



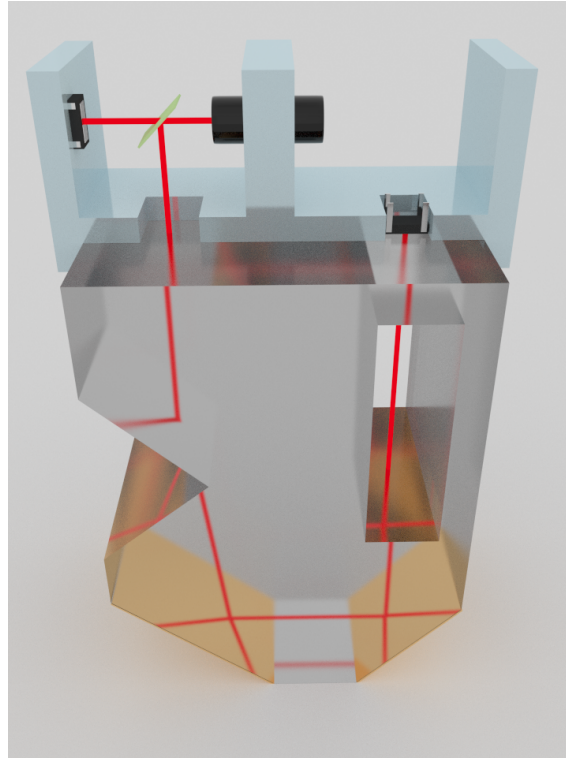
Parameters	Notation	Value
width of the sensor	w	90 mm
height of the sensor	h	125 mm
refractive index measurement range	R_n	1.336 – 1.345
refractive index resolution	Δn	2.94×10^{-7} (0.3 ppm)
absolute salinity resolution	ΔS_t	1 mg.kg ⁻¹
turbidity resolution (0 – 20 NTU)	Δt	1.15 NTU (5.75%)
turbidity resolution (0 – 200 NTU)	Δt	8 NTU (4%)
position sensor	–	CCD or PSD
position sensor length	l	> 10 mm
turbidity sensor	–	CCD
light source wave length	λ	635 nm
temperature compensation	–	yes

II Specifications for refracto-turbidi-meter prototype II



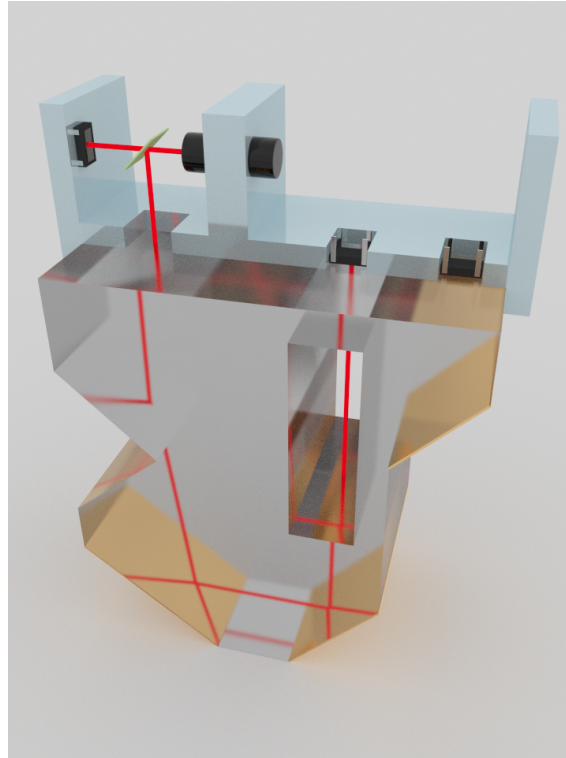
Parameters	Notation	Value
width of the sensor	w	30 mm
height of the sensor	h	40 mm
refractive index measurement range	R_n	1.330 – 1.350
refractive index resolution	Δn	1.15×10^{-6} (1 ppm)
absolute salinity resolution	ΔS_t	2 mg.kg^{-1}
turbidity resolution (0 – 20 NTU)	Δt	1.83 NTU (9%)
turbidity resolution (0 – 200 NTU)	Δt	12.7 NTU (6%)
position sensor	–	CCD or PSD
position sensor length	l	$> 2 \text{ mm}$
turbidity sensor	–	CCD
light source wave length	λ	635 nm
wavelength compensation	–	yes

III Specifications for refracto-turbidi-meter prototype III



Parameters	Notation	Value
width of the sensor	w	30 mm
height of the sensor	h	40 mm
refractive index measurement range	R_n	1.330 – 1.350
refractive index resolution	Δn	1.15×10^{-6} (1 ppm)
absolute salinity resolution	ΔS_t	2 mg.kg^{-1}
turbidity resolution (0 – 20 NTU)	Δt	0.31 NTU (1.5%)
turbidity resolution (0 – 200 NTU)	Δt	2.15 NTU (1%)
position sensor	–	CCD or PSD
position sensor length	l	$> 2 \text{ mm}$
turbidity sensor	–	CCD
light source wave length	λ	635 nm
wavelength compensation	–	yes

IV Specifications for refracto-turbidi-meter prototype IV



Parameters	Notation	Value
width of the sensor	w	30 mm
height of the sensor	h	40 mm
refractive index measurement range	R_n	1.330 – 1.350
refractive index resolution	Δn	1.15×10^{-6} (1 ppm)
absolute salinity resolution	ΔS_t	2 mg.kg^{-1}
turbidity resolution (0 – 20 NTU)	Δt	< 1% of measurement range
turbidity resolution (0 – 200 NTU)	Δt	< 1% of measurement range
position sensor	–	CCD or PSD
position sensor length	l	> 2 mm
turbidity sensor	–	CCD
light source wave length	λ	635 nm
wavelength compensation	–	yes